Karlsruhe Institute of Technology

A FLUID DYNAMICS APPROACH FOR SOLID-LIQUID PHASE CHANGE IN BINARY AND ELEMENTAL MELTS

Zur Erlangung des akademischen Grades
Doktor der Ingenieurwissenschaften
der Fakultät für Maschinenbau
Karlsruher Institut für Technologie (KIT)

genehmigte
Dissertation
von

Dipl.-Phys. Stefan Meyer

Hauptreferent:	Prof. Dr.-Ing. Xu Cheng
Korreferent:	Prof. Dr.-Ing. Thomas Schulenberg
Tag der mündlichen Prüfung:	20. Juni 2016

Acknowledgements

First of all, I would like to thank Prof. Dr. Xu Cheng and Dr. Ivan Otic for giving me the opportunity to prepare this thesis at the Institute of Fusion and Reactor Technology after I had already left the area of university and entered working life.

My special gratitude goes to Dr. Ivan Otic, who supported my research with valuable clues and fruitful discussions during the last three years.

I would also like to thank Prof. Dr. Thomas Schulenberg for his agreement to conduct the second assessment of this thesis.

I am much obliged to my colleagues at the institute for their help in many ways.

Last but not least, I would like to thank my wife as well as my parents for their constant support not only during the last three years, but from the beginning of my studies.

Karlsruhe, April 2016

Stefan Meyer

Abstract

In the area of severe accident management in nuclear reactors, the influence of solid-liquid phase change processes, especially of solidification, on the heat transport in binary core melts is an important issue. A necessary requirement for the correct modelling of this influence is an appropriate description of the phase change processes as well as of the flow field affected by them.
Existing codes from the nuclear field treat phase change indirectly by assuming a linear increase of the liquid volume fraction with temperature from zero at the solidus temperature to a value of one at the liquidus temperature. Aside from the arbitrariness of the linearity assumption and the neglection of compositional effects, an additional shortcoming of this methodology is that the phase state will in general not adapt instantaneously to the specifications of the temperature field, but will follow its own dynamics. Furthermore, in one of the most widely spread approaches, a solution of the Navier-Stokes equations is circumvented by using correlation-based characteristic velocities.
In this thesis, a simulation model is developed which couples the Navier-Stokes equations as well as transport equations for the temperature and composition field with an independent phase change model based on the phase-field method in a thermodynamic consistent manner. In particular, a phenomenological free energy functional is constructed and the governing equations for the phase volume fractions and their coupling with the other transport equations are obtained by using the formalism of irreversible thermodynamics. A dynamic calculation procedure based on free energy minimization is proposed for a parameter appearing in the free energy functional, which characterizes the width of the smooth transition regions of the phase volume fractions between pure phases. The final set of coupled evolution equations can describe convective binary eutectic alloy solid-liquid phase change with sharp as well as diffuse interfaces and contains the representation of elemental materials as a special case. In particular, the model is able to describe the detailed solidification microstructure if it is applied on sufficiently small length scales.
The model equations have been implemented in the computational fluid dynamics toolbox OpenFOAM and the code is verified by comparisons with analytical predictions as well as with neighbouring modelling approaches in suitable scenarios.
A validation is conducted with the help of three experimental test cases treating

- the sharp-interface solidification of the binary eutectic alloy $CBr_4 - C_2Cl_6$ on a micrometer length scale
- the sharp-interface melting of elemental gallium under thermal natural convection on a centimeter length scale
- the mushy-interface solidification of the binary eutectic alloy $NH_4Cl - H_2O$ under thermosolutal natural convection on a centimeter length scale.

The three validation cases illustrate that the newly developed model can describe experimental observations successfully and that it can improve numerical simulation results of existing modelling approaches.

Kurzfassung

Im Bereich der Schwerunfallbeherrschung in Kernreaktoren stellt der Einfluss fest-flüssiger Phasenumwandlungen, insbesondere von Verfestigungsprozessen, auf den Wärmetransport in binären Kernschmelzen einen wichtigen Gesichtspunkt dar. Eine notwendige Bedingung für die korrekte Modellierung dieses Einflusses besteht in einer angemessenen Beschreibung sowohl der Phasenumwandlungsprozesse als auch des durch letztere beeinträchtigten Strömungsfeldes.
Bestehende Rechenprogramme aus dem nuklearen Bereich behandeln die Phasenumwandlung indirekt durch die Annahme, dass der Volumenbruchteil der flüssigen Phase linear mit der Temperatur vom Wert null bei der Solidustemperatur zum Wert eins bei der Liquidustemperatur zunimmt. Abgesehen von der Beliebigkeit der Linearitätsannahme und der Vernachlässigung kompositioneller Effekte besteht eine weitere Unzulänglichkeit dieser Vorgehensweise darin, dass sich der Phasenzustand im Allgemeinen nicht instantan an die Vorgaben des Temperaturfeldes anpassen, sondern seiner eigenen Dynamik folgen wird. Außerdem wird bei einem der am weitesten verbreiteten Ansätze auf eine Lösung der Navier-Stokes Gleichungen verzichtet und stattdessen werden korrelationsbasierte charakteristische Geschwindigkeiten verwendet.
In dieser Arbeit wird ein Simulationsmodell entwickelt, welches die Navier-Stokes Gleichungen sowie Transportgleichungen für das Temperatur- und Kompositionsfeld auf thermodynamisch konsistente Weise mit einem unabhängigen, auf der Phasenfeldmethode basierenden Phasenumwandlungsmodell koppelt. Insbesondere wird ein phänomenologisches Funktional für die freie Energie konstruiert und die Evolutionsgleichungen für die Volumenbruchteile der verschiedenen Phasen und ihre Kopplung mit den anderen Transportgleichungen werden auf der Grundlage der Thermodynamik irreversibler Prozesse abgeleitet. Für einen im freien Energiefunktional auftauchenden Parameter, welcher die Breite der glatten Übergangsbereiche der Phasenvolumenbruchteile zwischen den reinen Phasen charakterisiert, wird eine dynamische Berechnungsprozedur basierend auf einer Minimierung der freien Energie vorgeschlagen. Der letztlich resultierende Satz gekoppelter Gleichungen kann fest-flüssige Phasenumwandlungen binärer eutektischer Systeme unter konvektiven Bedingungen sowohl mit scharfen als auch mit diffusen Phasengrenzen beschreiben und enthält die Darstellung elementarer Materialien als Spezialfall. Insbesondere kann das Modell die detaillierte Mikrostruktur der Verfestigung wiedergeben, wenn es auf hinreichend kleiner Längenskala angewendet wird.
Die Modellgleichungen wurden im strömungsmechanischen Simulationssoftwarepaket OpenFOAM implementiert und das Rechenprogramm wird durch Vergleiche mit analytischen Vorhersagen sowie benachbarten Modellierungsansätzen in geeigneten Szenarien verifiziert. Mit Hilfe dreier experimenteller Testfälle, welche

- die Verfestigung des binären eutektischen Materials $CBr_4 - C_2Cl_6$ mit scharfen Phasengrenzen auf einer Mikrometer-Längenskala
- das Schmelzen elementaren Galliums mit scharfer Phasengrenze bei thermischer natürlicher Konvektion auf einer Zentimeter-Längenskala

- die Verfestigung des binären eutektischen Materials $NH_4Cl - H_2O$ mit diffuser Phasengrenze bei thermischer und kompositioneller natürlicher Konvektion auf einer Zentimeter-Längenskala

beschreiben, wird eine Validierung durchgeführt. Die drei Validierungsfälle verdeutlichen, dass das neu entwickelte Modell experimentelle Beobachtungen erfolgreich beschreiben und dass es numerische Simulationsergebnisse existierender Modellierungsansätze verbessern kann.

Contents

1. Introduction **1**
1.1. Motivation 1
1.2. Objective 1

2. Review of Existing Modelling Approaches **5**
2.1. Models for Melt Pool Heat Transfer Simulation 5
2.2. Phase-Field Modelling of Solid-Liquid Phase Change 11
2.3. Conclusions 31

3. Model Development **35**
3.1. Free Energy Functional for Isothermal Binary Eutectic Alloys 35
3.2. Generalization to Macroscopic Length Scales 47
3.3. Coupled Governing Equations for Non-Isothermal Conditions 52
3.4. Thin-Interface Analysis 66

4. Model Verification **75**
4.1. Surface Part of Free Energy Density 75
4.2. Bulk Part of Free Energy Density 81
4.3. Transition to a Sharp-Interface Model 85
4.4. Relationship to the Volume-of-Fluid Method 88

5. Model Validation **95**
5.1. Microscopic Lamellae Solidification of $CBr_4 - C_2Cl_6$ 95
5.2. Melting of Gallium Under Thermal Natural Convection 98
5.3. Solidification of $NH_4Cl - H_2O$ Under Thermo-Solutal Natural Convection 101

6. Conclusion and Outlook **105**
6.1. Conclusion 105
6.2. Outlook 107

7. Appendix **117**
A. Derivatives of Individual Phase Compositions ξ_i 117
B. Derivatives of Chemical Potential μ 119
C. Derivatives of Internal Energy per Mass e_m 119
D. Derivatives of Entropy per Mass s_m 121
E. Material Properties of $CBr_4 - C_2Cl_6$ 123
F. Material Properties of Gallium 124
G. Material Properties of $NH_4Cl - H_2O$ 124

List of Figures

1.1. Generic phase diagram of a binary eutectic alloy with components A and B 2

2.1. Smooth phase indicator function around a sharp phase boundary Γ 12
2.2. Symmetric double well $g(\varphi)$ 13
2.3. Tangens hyperbolicus equilibrium profile of the phase indicator function . . 14
2.4. Qualitative effect of f_{bulk} on the symmetric double well 15
2.5. Anisotropic solidification pattern obtained by the phase-field method 16
2.6. Gibbs simplex for three phase-fields 29

3.1. Profile of phase-field functions around a sharp interface 37
3.2. Composition profile for a phase boundary with finite thickness 72
3.3. Composition profile for a sharp interface 72

4.1. Simulation setup with initial values 75
4.2. Equilibrium Profile of the phase-field φ_1 76
4.3. Dependence of transition layer width on δ 76
4.4. Calculated Δ-values at different times along $x = 50\mu m$ 77
4.5. Profiles of the phase-field functions at $t = 1s$ 77
4.6. Curved α-l mixture used as initial state 77
4.7. Final equilibrium state due to the action of $f_{surface}$ 77
4.8. Equilibrium state of Φ_2 for $\delta = 10^{-6}m$ 78
4.9. Equilibrium state of Φ_2 for dynamically calculated Δ 78
4.10. Calculated Δ-values along $x = 0.05m$ in Figure 4.9 78
4.11. Equilibrium profile of Φ_1 along $x = 0.05m$ in Figure 4.9 78
4.12. Simulation setup 79
4.13. Phase-field Φ_2 at $t = 600s$ with dynamically calculated values of Δ 80
4.14. Calculated values of Δ at $t = 600s$ 80
4.15. Phase-field Φ_2 at $t = 600s$ with $\Delta = 3mm$ 80
4.16. Phase-field Φ_2 at $t = 600s$ with $\Delta = 8mm$ 80
4.17. Simulation setup with initial values and boundary conditions 81
4.18. Phase-field φ_2 indicating solid phase α for $(T_0 = 360.0K, \xi_0 = 0.086)$ at $t = 4s$ 82
4.19. Composition profile in y-direction at $t = 4s$ 82
4.20. Comparison of simulated equilibrium compositions with the liquidus and solidus lines of $CBr_4 - C_2Cl_6$ for $\xi_0 < \xi_e$ 83
4.21. Comparison of simulated equilibrium compositions with the liquidus and solidus lines of $CBr_4 - C_2Cl_6$ for $\xi_0 > \xi_e$ 83
4.22. Steady-State at eutectic composition $\xi_0 = \xi_e = 0.118$ 84
4.23. Steady-State at composition $\xi_0 = 0.09$ 84
4.24. Profiles of the phase-fields in Figure 4.23 along the line $x = 0.05m$ 84
4.25. Comparison of simulation results with the liquidus and solidus lines of the phase diagram for $\xi_0 < \xi_e$ 84

4.26. Comparison of simulation results with the liquidus and solidus lines of the phase diagram for $\xi_0 > \xi_e$ . . . 84
4.27. Comparison of the phase volume fractions in the solid resulting from mass conservation with simulation results . . . 85
4.28. Simulation Setup . . . 86
4.29. Equilibrium phase boundary for $\sigma_{22} = \sigma_{12}$ . . . 87
4.30. Equilibrium phase boundary for $\sigma_{22} = 1.5\sigma_{12}$ . . . 87
4.31. Equilibrium phase boundary for $\sigma_{22} = 1.95\sigma_{12}$ . . . 87
4.32. PFM at $t = 0.0s, t = 0.1s$ and $t = 0.3s$ . . . 92
4.33. VOF at $t = 0.0s, t = 0.1s$ and $t = 0.3s$ . . . 92
4.34. PFM at $t = 0.5s, t = 0.75s$ and $t = 1.0s$ . . . 93
4.35. VOF at $t = 0.5s, t = 0.75s$ and $t = 1.0s$ . . . 93

5.1. Sketch of Ginibre's experiment . . . 96
5.2. Solidification pattern of the sample moving with $V = 0.5\frac{\mu m}{s}$ . . . 96
5.3. Solidification pattern for dynamically calculated values $\Delta(\vec{x}, t)$ . . . 97
5.4. Solidification pattern for a constant $\delta = 3 \cdot 10^{-7} m$ . . . 97
5.5. Dynamically calculated $\Delta(\vec{x}, t)$ corresponding to Figure 5.3 . . . 97
5.6. Comparison of the experimental result with the simulation result from Figure 5.3 . . . 98
5.7. Experimental setup from Gau and Viskanta with the heated wall in red . . . 98
5.8. Experimentally determined position of the sharp phase boundary at different points in time . . . 99
5.9. Comparison of simulation results with experiment . . . 99
5.10. Simulated temperature field after 17 minutes . . . 100
5.11. Simulated velocity field (magnitude) after 17 minutes . . . 100
5.12. Experimental setup in two dimensions . . . 101
5.13. Experimentally determined solidification behaviour . . . 102
5.14. Comparison of experimental results with numerical simulations (1) . . . 102
5.15. Comparison of experimental results with numerical simulations (2) . . . 103
5.16. Temperature at $x = 0.0022m$, $y = 0.09m$ . . . 104
5.17. Temperature at $x = 0.0044m$, $y = 0.09m$ . . . 104
5.18. Temperature at $x = 0.0066m$, $y = 0.09m$ . . . 104
5.19. Temperature at $x = 0.0087m$, $y = 0.065m$ . . . 104
5.20. Temperature at $x = 0.0022m$, $y = 0.045m$ . . . 104
5.21. Temperature at $x = 0.0044m$, $y = 0.045m$ . . . 104

E.1. Phase diagram of $CBr_4 - C_2Cl_6$ . . . 124
G.2. Phase diagram of $NH_4Cl - H_2O$ . . . 126

List of Tables

2.1. Comparison between the simulations of Zhang et al. and LIVE-L4 experiment for selected quantities at steady state 9

4.1. Initial values of composition ($\xi_0 < \xi_e$) for different constant temperatures T_0 81
4.2. Initial values of composition ($\xi_0 > \xi_e$) for different constant temperatures T_0 82
4.3. Volume fraction of water at the beginning and at the end of the simulations 91

E.1. Material properties of $CBr_4 - C_2Cl_6$ 123
F.2. Material properties of gallium 124
G.3. Material properties of $NH_4Cl - H_2O$ 125

Nomenclature

List of Abbreviations

Abbrev.	Description
CFD	Computational Fluid Dynamics
IVR	In-Vessel Retention Concept
MELCOR	Method for Estimation of Leakages and Consequences of Releases
OECD	Organization for Economic Cooperation and Development

List of Symbols

Symbol	Description	Units
α	hypoeutectic solid phase of a binary eutectic alloy	
β	hypereutectic solid phase of a binary eutectic alloy	
β_ξ	linear compositional expansion coefficient	1
β_k	linear kinetic coefficient of a solid-liquid phase boundary of an elemental material	Ksm^{-1}
β_T	linear thermal expansion coefficient	K^{-1}
$\boldsymbol{\tau}$	viscous stress tensor	Nm^{-2}
$\boldsymbol{m}$	stress tensor	Nm^{-2}
δ	free input length governing the transition width of phase indicator functions	m
δ_{ij}	Kronecker delta	1
η	dynamic viscosity	$kgm^{-1}s^{-1}$
Γ	sharp phase boundary	

κ	curvature of a phase boundary	m^{-1}
λ	heat conductivity	$Wm^{-1}K^{-1}$
Λ_L	lagrangian multiplier in the new model	$Jm^{-3}K^{-1}$
Λ_l	lagrangian multiplier in models from the literature	Jm^{-3}
$\dot{s}_{prod}$	entropy production rate	$JK^{-1}m^{-3}s^{-1}$
$\vec{g}$	gravitational acceleration	ms^{-2}
$\vec{n}$	unit normal vector at a sharp boundary pointing from the solid to the liquid	1
$\vec{p}$	linear momentum	$kgms^{-1}$
$\vec{q}_\xi$	composition flux	$kgm^{-2}s^{-1}$
$\vec{q}_s$	entropy flux	$JK^{-1}m^{-2}s^{-1}$
$\vec{u}$	velocity vector	ms^{-1}
$\mu_{A,i}$	chemical potential of component A in phase i	Jm^{-3}
$\mu_{B,i}$	chemical potential of component B in phase i	Jm^{-3}
Φ	liquid volume fraction	1
ρ	mass density	kgm^{-3}
σ	solid-liquid surface tension of an elemental material	Jm^{-2}
φ	indicator function of the liquid phase of an elemental material	1
φ_1	indicator function of the liquid phase of a binary eutectic alloy	1
φ_2	indicator function of the solid phase α of a binary eutectic alloy	1
φ_3	indicator function of the solid phase β of a binary eutectic alloy	1
ξ	composition of a binary eutectic alloy (mass fraction of component B)	1
$\xi_1^{(1j)}(T)$	composition of the liquid phase of a binary eutectic alloy in equilibrium with the solid phase j, corresponding to the liquid-j liquidus line	1

ξ_e	eutectic composition of a binary eutectic alloy	1
ξ_i	composition of phase i	1
$\xi_j^{(1j)}(T)$	composition of the solid phase j of a binary eutectic alloy in equilibrium with the liquid phase, corresponding to the liquid-j solidus line	1
c	specific heat capacity	$Jkg^{-1}K^{-1}$
D_l	liquid mass diffusion constant	m^2s^{-1}
E	internal energy	J
e	internal energy per volume	Jm^{-3}
e_m	internal energy per mass	Jkg^{-1}
F	free energy	J
f_i	free energy per volume of bulk phase i	Jm^{-3}
f_m	free energy per mass	Jkg^{-1}
H	height of melt pool in effective convectivity model	m
h	sensible enthalpy per mass	Jkg^{-1}
h_i	interpolation function for bulk phase i	1
K	mobility constant in the original phase-field model	Jsm^{-3}
K_0	material dependent porosity parameter	$kgm^{-3}s^{-1}$
$k_{12}(T)$	liquid-α partition coefficient of a binary eutectic alloy corresponding to the ratio of equilibrium compositions of the solid phase α and the liquid phase at temperature T	1
$k_{13}(T)$	liquid-β partition coefficient of a binary eutectic alloy corresponding to the ratio of equilibrium compositions of the solid phase β and the liquid phase at temperature T	1
L	latent heat per mass	Jkg^{-1}
l	liquid phase	

M_{12}	mobility constant of a phase boundary between the liquid phase and solid phase α in the new model	$Jsm^{-3}K^{-1}$
m_{12}	slope of the liquid-α liquidus line in the phase diagram of a binary eutectic alloy	K
M_{13}	mobility constant of a phase boundary between the liquid phase and solid phase β in the new model	$Jsm^{-3}K^{-1}$
m_{13}	slope of the liquid-β liquidus line in the phase diagram of a binary eutectic alloy	K
Nu_{down}	downwards Nusselt number in Steinberner Reineke correlation	1
Nu_{side}	sidewards Nusselt number in Steinberner Reineke correlation	1
Nu_{up}	upwards Nusselt number in Steinberner Reineke correlation	1
p	pressure	Nm^{-2}
p	pressure	Nm^{-2}
Q_V	internal heat source	Wm^{-3}
R	ideal gas constant	$Jmol^{-1}K^{-1}$
Ra	Rayleigh number	1
S	entropy	JK^{-1}
s	entropy per volume	$JK^{-1}m^{-3}$
s_m	entropy per mass	$JK^{-1}kg^{-1}$
T	temperature	K
T_e	eutectic temperature of a binary eutectic alloy	K
T_L	liquidus temperature	K
T_S	solidus temperature	K
u_n	normal velocity of a sharp phase boundary	ms^{-1}
v_m	molar volume	m^3mol^{-1}
W	width of melt pool in effective convectivity model	m
x	spatial coordinate perpendicular to a sharp phase boundary	m

1. Introduction

1.1. Motivation

According to the United Nations, the world population continues to grow and will reach a number of about 9.7 billion by the year 2050 ([1]). Based on this increase and a commonly expected rise in the worldwide standard of living, energy consumption will also grow. In [2], the Organization for Economic Cooperation and Development (OECD) expects that global energy demand will be about 80% higher in 2050 than today. In this context, the role played by nuclear energy as a non-fossile ressource is estimated to rise steadily. Due to this increasing global relevance and the serious consequences which accidents in nuclear power plants may have, it is crucial to intensify efforts in safety research.
This work has been prepared in the context of a core-melting accident in a nuclear power plant. In a late phase of such a scenario, a liquid melt pool may form in the lower head of the reactor pressure vessel. It mainly consists of an oxidic $UO_2 - ZrO_2$ melt, which is covered by a lighter metal layer ([3]). As a consequence of the decay heat being permanently produced in the oxidic part, the reactor pressure vessel may fuse and radioactive material may be released into the containment. A possible strategy to avoid such a scenario is the in-vessel retention concept (IVR) ([4]). Its basic idea is to provide sufficient external water cooling to prohibit a vessel failure, thereby making sure that the corium is retained inside. For a successful IVR design, an exact prediction of the melt pool heat transfer characteristics is of major importance.
In addition to numerous experimental programs, which have been launched so far investigating heat transfer in simulant ([5],[6],[7],[8]) as well as prototypic ([9]) melts, it is also necessary to develop appropriate simulation tools for supporting these investigations. As the models used in published numerical works ([10],[11],[12],[13]), which will be discussed in more detail later, are characterized by a greater or lesser degree of simplification, the task of the present thesis is to improve simulation capabilities by providing a more realistic modelling approach.

1.2. Objective

This thesis focuses on the oxidic part of the core melt pool and aims at providing a detailed modelling of heat transfer and the underlying phenomena. First of all, the $UO_2 - ZrO_2$ system may be described on the basis of a binary eutectic alloy phase diagram. A generic representative is shown in Figure 1.1 with the composition variable ξ denoting the mass

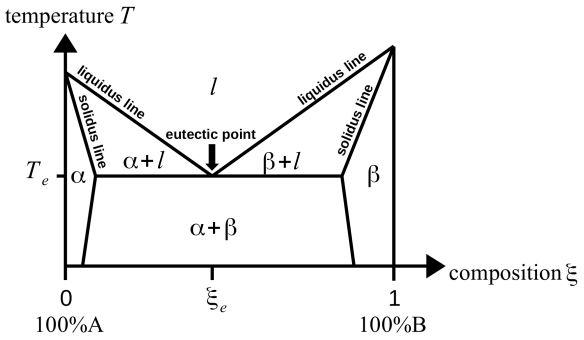

Figure 1.1.: Generic phase diagram of a binary eutectic alloy with components A and B

percentage of component B and ξ_e as well as T_e indicating the eutectic composition and the eutectic temperature, respectively. Note that $UO_2 - ZrO_2$ does not show a miscibility gap in the solid at elevated temperatures ([14]). However, this is not a problem as only minor modifications are necessary in Figure 1.1 to obtain the desired behaviour. Beyond that, a model based on the generic phase diagram presented above allows for an extended scope of application.

According to Figure 1.1, the two components A and B mix homogeneously in the liquid phase l, but they do partly separate in the solid state. As a consequence, two different solid phases α and β can exist with α being predominantly composed of component A and β consisting mainly of component B. For non-eutectic compositions and temperatures above the eutectic temperature, only one of the two solid phases can form as indicated in the phase diagram in Figure 1.1. Consequently, one of the two components A or B is preferably built into the solid crystal lattice while the other one accumulates at the liquid side of the phase boundary.

In contrast to elemental materials with a distinct melting point, solidification occurs here in general over a temperature interval between the composition-dependent liquidus and solidus temperatures. While the former are given by the liquidus lines, the latter are defined by the solidus lines and the eutectic temperature T_e. Inside this temperature interval, the liquid phase coexists with one of the two solid phases ($\alpha + l$ or $\beta + l$ in Figure 1.1) and from a macroscopic point of view, a diffuse interface appears between the entirely liquid and solid regions, the so-called mushy layer. In a more detailed consideration, however, it turns out that phase interfaces between the solid and liquid phases are sharp and that the macroscopic diffuseness is the result of a complex interface morphology in connection with a limited spatial resolution.

In a core melting accident in a nuclear reactor, the formation of a mushy layer between the melt and a completely solid region along the water-cooled vessel wall is a possibility. As solidification proceeds, latent heat is released and one of the components is rejected and accumulates in the melt as well as in the liquid parts of the mushy layer. This leads to density gradients and the resulting buoyancy forces as well as friction forces caused by the mushy layer influence momentum transport. On the other hand, the velocity field transports heat and solute and therefore retroacts on the solidification process by changing temperature and the composition-dependent liquidus and solidus temperatures.

The objective of this thesis is the development of a three-dimensional computational fluid dynamics (CFD) model, which is capable to describe the processes mentioned above as well as their coupling in a thermodynamically consistent manner. With respect to solidification, the model shall be based on the phase-field method as an independent and microscopically well-established description of solid-liquid phase change processes. The idea behind is that if the spatial resolution of the numerical grid is high enough, the final set of implemented

governing equations shall be able to provide a detailed description of the sharp interface solidification microstructure. If, however, the achievable spatial resolution is limited due to a large volume of interest, the model shall give a volume-averaged characterization in the sense of a mushy layer as a diffuse interface between the solid and the liquid.
Additionally, the description of elemental material solidification should be contained in the model as a special case because some experiments in the framework of IVR like BALI ([6]) use water as a core melt simulant.

2. Review of Existing Modelling Approaches

2.1. Models for Melt Pool Heat Transfer Simulation

Apart from system codes like MELCOR ([15]), only a limited number of simulation models have been applied to the description of heat transfer in solidifying core melt pools and corresponding experiments. Especially with respect to a pointwise resolution of the temperature distribution, only two different approaches could be found in the literature. One of them was introduced by C.T. Tran and T.N. Dinh in 2009 and is known as the effective convectivity model ([10],[11],[12]). The other one has been developed by Voller et al. ([16],[17],[18],[19]) around 1990, not especially for the nuclear field. It is a real CFD approach and has been applied to the description of melt pool heat transfer recently in a publication by Zhang et al. from the year 2014 ([13]).
A third method will also be mentioned in this section although it has never been actually used in the framework of IVR. It has been developed by Bennon at al. ([20],[21]) at about the same time as Voller developed his model. In contrast to the latter, it also regards effects related to the composition field and therefore exhibits the potential of a more detailed description of binary alloy solidification.

2.1.1. The Effective Convectivity Model

In the effective convectivity model, the solution of a full set of coupled Navier-Stokes and heat transport equations is circumvented by the use of characteristic velocities for heat transport. As a starting point, the authors in [10] take the empirical heat transfer correlations by Steinberner and Reineke ([22])

$$Nu_{up} = 0.345 Ra^{0.233} \tag{2.1}$$

$$Nu_{side} = 0.85 Ra^{0.19} \tag{2.2}$$

$$Nu_{down} = 1.389 Ra^{0.095} \tag{2.3}$$

with the internal Rayleigh number Ra and the upwards, sidewards and downwards Nusselt numbers Nu_{up}, Nu_{side} and Nu_{down}. Based on this, characteristic velocities for convective heat transport in a rectangular pool of height H and width W with cooled bounding walls and an internal heat source are derived. The derivation assumes the existence of a stratified region with height H_{down} at the bottom and a mixed region with height H_{up}

above and it is demonstrated in [10] that H_{up} and H_{down} can be expressed by the Nusselt numbers and the total height H of the pool according to

$$H_{up} = \frac{H \cdot Nu_{up}}{Nu_{up} + Nu_{side} + Nu_{down}} \tag{2.4}$$

$$H_{down} = H - H_{up}. \tag{2.5}$$

The final result for the characteristic velocities describing convective heat transport to the upper, lateral and lower walls of the pool is given by

$$U_{up} = \frac{\lambda}{\rho c H}(Nu_{up} - \frac{H}{H_{up}}) \tag{2.6}$$

$$U_{side} = \frac{\lambda}{\rho c H}(Nu_{side} - \frac{2H}{W}) \tag{2.7}$$

$$U_{down} = \frac{\lambda}{\rho c H}(Nu_{down} - \frac{H}{H_{down}}) \tag{2.8}$$

with heat conductivity λ , mass density ρ and the specific heat capacity c. The derivation of (2.6)-(2.8) is based on energy balance considerations of the stratified and mixed fluid layers and the expressions subtracted from the Nusselt numbers in the brackets originate in the contribution of heat conduction to the total heat transfer. For details, the reader is refered to [10].
The only transport equation which is solved is that for heat, given by

$$\frac{\partial}{\partial t}(\rho c T) = \vec{\nabla} \cdot (\lambda \vec{\nabla} T) - \frac{\partial}{\partial t}(\rho L \Phi) - \vec{\nabla} \cdot (\rho c T \Phi \vec{u}) + Q_V \tag{2.9}$$

with the latent heat per mass L, temperature T, the velocity field $\vec{u}$ and an internal heat source Q_V. It is important to note here that the convection term $\vec{\nabla} \cdot (\rho c T \Phi \vec{u})$ is treated as an explicit source term on the right hand side of the equation and that it is evaluated by using the characteristic velocities (2.6)-(2.8). Another remarkable aspect is that an additional factor Φ appears in it, which denotes the liquid volume fraction and therefore damps the characteristic velocities to zero in the solid. Finally, the phase change process is considered by the expression $-\frac{\partial}{\partial t}(\rho L \Phi)$ accounting for latent heat production. However, a closure relation is needed as the behaviour of the liquid volume fraction is not known in the mushy layer. In the effective convectivity model, Φ is simply assumed to be a linear function of temperature, given by

$$\Phi = \frac{T - T_S}{T_L - T_S} \tag{2.10}$$

with the solidus and liquidus temperatures T_S and T_L.
As only a simple diffusion equation has to be solved, this model is very efficient and performs quite well despite its simplicity ([11]). But nevertheless, there are discrepancies with experimental measurements and therefore possibilities of improvement. A comparison with experimental data from the COPO experiment ([5]) shows a difference of 30% in the upward heat transfer coefficient ([11]). The results of the model depend on the quality of the underlying heat transfer correlations and it cannot be applied without any preliminary informations. Additionally, the assumption of a linear variation of the liquid fraction with temperature in the mushy layer is quite arbitrary. And last but not least, an effective description like the effective convectivity model is not very satisfying from a fundamental perspective as we know that the flow is actually governed by the Navier-Stokes equations.

2.1.2. Voller's Model

The second approach, which is capable to convey a more complete picture, is the method developed by Voller. In contrast to the effective convectivity model, a full set of Navier-Stokes equations is solved here together with an enthalpy conservation equation. The set of governing equations is given in [16],[17] and [18] by

$$\vec{\nabla} \cdot \vec{u} = 0 \tag{2.11}$$

$$\frac{\partial(\rho\vec{u})}{\partial t} + \vec{\nabla} \cdot (\rho\vec{u} \otimes \vec{u}) = \vec{\nabla} \cdot (\eta\vec{\nabla}\vec{u}) - \vec{\nabla}p + \vec{S}_D + \vec{S}_B \tag{2.12}$$

$$\frac{\partial(\rho h)}{\partial t} + \vec{\nabla} \cdot (\rho h\vec{u}) = \vec{\nabla} \cdot (\frac{\lambda}{c}\vec{\nabla}h) + S_H. \tag{2.13}$$

In the system of equations (2.11)-(2.13), η stands for the dynamic viscosity, p describes pressure, $h = cT$ is the so-called sensible enthalpy per mass and $\vec{S}_D$, $\vec{S}_B$ and S_H are source terms while all other variables have been introduced before.
The term $\vec{S}_D$ is there for damping velocity to zero in the solid. Especially for binary alloy solidification with mushy layers, the latter can be considered to be a porous medium in which the flow is governed by Darcy's law ([23]). In this case, $\vec{S}_D$ may be expressed as

$$\vec{S}_D = -K_0 \frac{(1-\Phi)^2}{\Phi^3}\vec{u} \tag{2.14}$$

with a material-dependent porosity parameter K_0. In practice, a small positive constant is added to Φ^3 in the denominator for avoiding division by zero in the solid.
The second source term in the momentum equation $\vec{S}_B$ accounts for buoyancy effects in the framework of the Boussinesq approximation and is given by

$$\vec{S}_B = \rho\vec{g}\beta_T \frac{h - h_{ref}}{c} \tag{2.15}$$

with the gravitational acceleration $\vec{g}$, the linear thermal expansion coefficient β_T and a reference sensible enthalpy per mass h_{ref}.
The source term S_H in the enthalpy equation represents the influence of phase change. It is derived in [18] by regarding separate transport equations for the solid and liquid phase enthalpies per mass H_s and H_l

$$\frac{\partial}{\partial t}(\rho(1-\Phi)H_s) + \vec{\nabla} \cdot (\rho(1-\Phi)H_s\vec{u}_s) = \vec{\nabla} \cdot [(1-\Phi)\lambda_s\vec{\nabla}T] + [\text{interphase terms}] \tag{2.16}$$

$$\frac{\partial}{\partial t}(\rho\Phi H_l) + \vec{\nabla} \cdot (\rho\Phi H_l\vec{u}_l) = \vec{\nabla} \cdot [\Phi\lambda_l\vec{\nabla}T] - [\text{interphase terms}] \tag{2.17}$$

with the solid and liquid phase velocities $\vec{u}_s$ and $\vec{u}_l$ as well as the solid and liquid phase heat conductivities λ_s and λ_l. Note that the differential formulations in (2.16) and (2.17) arise from integral formulations with volume intergrals $\int dV_k$ and surface integrals $\int dA_k$ over the volume and surface of the corresponding phase k. The factors of Φ and $1-\Phi$ in equations (2.16) and (2.17) result from the assumptions $dV_l = \Phi dV$, $dV_s = (1-\Phi)dV$, $dA_l = \Phi dA$ and $dA_s = (1-\Phi)dA$. The solid and liquid phase enthalpies per mass are defined in [18] by

$$H_s = cT \quad = h \tag{2.18}$$

$$H_l = cT + L = h + L \tag{2.19}$$

and after an addition of equations (2.16) and (2.17), one gets

$$\frac{\partial}{\partial t}(\rho h) + \vec{\nabla} \cdot (\rho\vec{u}h) = \vec{\nabla} \cdot (\lambda\vec{\nabla}T) - \frac{\partial}{\partial t}(\rho L\Phi) - \vec{\nabla} \cdot (\rho L\Phi\vec{u}_l). \tag{2.20}$$

The velocity $\vec{u}$ and heat conductivity λ in (2.20) are defined as mixture quantities according to

$$\vec{u} = (1 - \Phi)\vec{u}_s + \Phi\vec{u}_l \tag{2.21}$$

$$\lambda = (1 - \Phi)\lambda_s + \Phi\lambda_l. \tag{2.22}$$

Assuming the solid phase to be rigid ($\vec{u}_s = \vec{0}$), one gets $\vec{u} = \Phi\vec{u}_l$ and due to

$$\vec{\nabla} \cdot (\rho L \Phi \vec{u}_l) = \vec{\nabla} \cdot (\rho L \vec{u}) = \rho L (\vec{\nabla} \cdot \vec{u}) = 0, \tag{2.23}$$

(2.20) is transformed to

$$\frac{\partial}{\partial t}(\rho h) + \vec{\nabla} \cdot (\rho \vec{u} h) = \vec{\nabla} \cdot (\frac{\lambda}{c} \vec{\nabla} h) - \frac{\partial}{\partial t}(\rho L \Phi). \tag{2.24}$$

A comparison with equation (2.13) then reveals the source term S_H to be

$$S_H = -\frac{\partial}{\partial t}(\rho L \Phi). \tag{2.25}$$

Despite the progress concerning the treatment of mass- and momentum conservation, it is important to note that the phase change process itself is treated here on the same level as in the effective convectivity model. In analogy to (2.10), the liquid volume fraction Φ is simply calculated according to

$$\Phi = \frac{T - T_S}{T_L - T_S} \tag{2.26}$$

as a linear function of temperature and the corresponding latent heat production is considered by a source term $-\frac{\partial}{\partial t}(\rho L \Phi)$. Actually, it has been the other way around and Tran and Dinh were inspired by Voller's enthalpy methodology when they developed their effective convectivity model. I decided for a different order here as I would like to present existing models in a hierarchy of rising complexity.

The model presented in this subsection has been applied recently by Zhang et al.([13]) in connection with a standard $k - \epsilon$ turbulence model to simulate the LIVE L4 experiment. In LIVE-L4, a $20-80\ mol\%\ NaNO_3 - KNO_3$ mixture has been used as a corium simulant and has been heated in a hemispherical vessel with an internal diameter of $1m$ ([24]). In a first phase, $18kW$ of internal electrical heating power have been applied for several hours until a steady-state had established. At the same time, external water cooling induced solidification along the lateral vessel walls.

In [13], this first phase has been simulated by adding an internal heat source S_Q on the right-hand side of equation (2.13) to account for the electrical heating. In particular, the authors compared simulations with and without consideration of phase change, i.e. with and without the source terms $\vec{S}_D$ and S_H in equations (2.12) and (2.13). By comparing maximum flow velocities, temperature profiles along the pool centerline and heat fluxes along the vessel wall at steady state with experimental measurements, Zhang et al. conclude that the phase change process has a significant influence on heat transfer characteristics. Table 2.1 presents selected quantities to support this conclusion.

However, the differences between measurements and the calculations including phase change are still substantial for some quantities. The disagreement in the maximum velocity is large and the average Nusselt number is about 20% higher than the measured value. Due to the pronounced impact of the phase change process, it is possible that a more realistic description of it will lead to further improvements in numerical prediction capabilities.

As mentioned already in the last subsection, the assumption (2.26) of a linear variation of liquid volume fraction in the mushy layer is arbitrary. Its real behaviour will surely be non-linear and besides the temperature dependence, the compostion field will also have an influence on Φ.

	without phase change modelling	with phase change modelling	LIVE-L4
maximum flow velocity	$4.38\frac{cm}{s}$	$2.73\frac{cm}{s}$	$0.3-0.6\frac{cm}{s}$
average Nusselt number	303.5	276.1	229.6

Table 2.1.: Comparison between the simulations of Zhang et al. and LIVE-L4 experiment for selected quantities at steady state

2.1.3. Bennon's Model

The third approach presented here is the model of Bennon. Although the derivation in [20] starts from a very general multiphase picture by regarding conservation equations for mass, momentum, enthalpy and composition for an arbitrary number of individual phases separately, the final set of governing equations presented in [21] for incompressible binary alloy solidification is similar to Voller's equations (2.11)-(2.13):

$$\vec{\nabla}\cdot\vec{u}=0 \tag{2.27}$$

$$\begin{aligned}\frac{\partial(\rho\vec{u})}{\partial t}+\vec{\nabla}\cdot(\rho\vec{u}\otimes\vec{u}) &= \vec{\nabla}\cdot(\eta_l\vec{\nabla}\vec{u})-K_0\frac{(1-\Phi)^2}{\Phi^3}\vec{u} \\ &\quad -\vec{\nabla}p+\rho\vec{g}\{\beta_T(T-T_e)+\beta_\xi(\xi_l-\xi_e)\}\end{aligned} \tag{2.28}$$

$$\frac{\partial(\rho h)}{\partial t}+\vec{\nabla}\cdot(\rho h\vec{u})=\vec{\nabla}\cdot(\lambda\vec{\nabla}T)-\vec{\nabla}\cdot[\rho(h_l-h)\vec{u}] \tag{2.29}$$

$$\frac{\partial(\rho\xi)}{\partial t}+\vec{\nabla}\cdot(\rho\xi\vec{u})=\vec{\nabla}\cdot(\rho\Phi D_l\vec{\nabla}\xi_l)-\vec{\nabla}\cdot[\rho(\xi_l-\xi)\vec{u}]. \tag{2.30}$$

Note that the index l in (2.27)-(2.30) marks quantities related to the liquid phase and that velocity $\vec{u}$, enthalpy per mass h and composition ξ must be interpreted as liquid-solid mixture variables according to

$$\vec{u}=\Phi\vec{u_l}+(1-\Phi)\vec{u_s}=\Phi\vec{u_l} \tag{2.31}$$

$$h=\Phi h_l+(1-\Phi)h_s \tag{2.32}$$

$$\xi=\Phi\xi_l+(1-\Phi)\xi_s. \tag{2.33}$$

As a rigid solid is assumed here as well, the solid velocity $\vec{u_s}$ is set to zero in (2.31).
The main difference to the model of Voller is that the composition field is considered here as an additional state variable. Its evolution equation (2.30) contains the usual unsteady, convective and diffusive contributions whereupon diffusion is explicitly restricted to the liquid phase with the liquid diffusion constant D_l. Additionally, the expression $-\vec{\nabla}\cdot[\rho(\xi_l-\xi)\vec{u}]$ arises on the right-hand side of (2.30) to account for species flux due to relative phase motion. Consideration of the composition field allows for a more detailed description of buoyancy effects in the momentum conservation equation (2.28). In comparison with Voller's equation (2.12), the additional term $\rho\vec{g}\beta_\xi(\xi_l-\xi_e)$ describes buoyancy due to compositional gradients in the liquid with the linear compositional expansion coefficient β_ξ and the eutectic composition ξ_e.
Except for the consideration of compositional influences, the physical content of the models by Bennon and Voller is the same. Although the enthalpy conservation equations look differently at a first glance, (2.29) can be transformed to a form equivalent to Voller's equation (2.13). At first, we realize that Bennon et al. give the solid and liquid phase enthalpies per mass in [21] by

$$h_s=c_sT \tag{2.34}$$

$$h_l=c_lT+(c_s-c_l)T_e+L \tag{2.35}$$

with the eutectic temperature T_e and the constant solid and liquid phase specific heats c_s and c_l. We have to be aware then that Voller's model is formulated for a phase-independent specific heat $c = c_s = c_l$ and that the sensible enthalpy per mass used there corresponds to h_s here. By using (2.32), (2.34) and (2.35) in equation (2.29), setting $c_s = c_l = c$ and rearranging for h_s, we find

$$\frac{\partial(\rho h_s)}{\partial t} + \vec{\nabla} \cdot (\rho h_s \vec{u}) = \vec{\nabla} \cdot (\frac{\lambda}{c} \vec{\nabla} h_s) - \frac{\partial}{\partial t}(\rho \Phi L). \tag{2.36}$$

This is the same as Voller's equation (2.13) for the sensible enthalpy per mass.
Note that by using (2.32), (2.34) and (2.35), the temperature T appearing on the right-hand side in equation (2.29) can be evaluated by

$$T = \frac{h - \Phi(c_s - c_l)T_e - \Phi L}{\Phi c_l + (1 - \Phi)c_s} \tag{2.37}$$

and h_l can then be calculated according to (2.35).
However, there remain two unknown quantities in equations (2.27)-(2.30): the liquid composition ξ_l and the liquid volume fraction Φ. They are determined by making use of the liquidus and solidus lines $\xi_L(T)$ and $\xi_S(T)$ in the equilibrium phase diagram of the binary alloy.
Under the assumption of a local composition equilibrium, the liquid and solid compositions ξ_l and ξ_s are determined by setting

$$\xi_l = \xi_L(T) \tag{2.38}$$

$$\xi_s = \xi_S(T), \tag{2.39}$$

i.e. they are set to their equilibrium values from the phase diagram for a given temperature T.
This fixes the value of the so-far unknown ξ_l and using (2.33), the liquid volume fraction and therefore the phase change process is captured according to

$$\Phi = \Phi(\xi, T) = \frac{\xi - \xi_S(T)}{\xi_L(T) - \xi_S(T)}. \tag{2.40}$$

The phase state is now determined by composition ξ as well as temperature T and is not a linear function of temperature anymore, but also regards compositional effects like e.g. solute rejection.
To the best of my knowledge, the method by Bennon presented in this subsection is the most complete approach in the literature to describe binary alloy solidifiction with convection on macroscopic length scales. Nevertheless, there remain some problematic aspects due to the treatment of phase change and its coupling with the other transport equations. In general, the process of phase change follows its own dynamics and therefore, the phase state does not adapt to the current values of ξ and T instantaneously. Furthermore, the coupling of the Navier-Stokes, heat and composition transport equations with phase change should respect the second law of thermodynamics. For the Bennon model, it is not clear that the entropy in an isolated volume of interest is non-decreasing and consequently, the system of equations (2.27)-(2.30) may be thermodynamically inconsistent.
The model developed in this work aims at closing these remaining gaps by coupling the Navier-Stokes, heat and composition transport equations to an independent and microscopically well-established phase change model in a thermodynamic consistent manner.
As mentioned before, the Bennon model has not been applied so far in the nuclear field. It has been validated in [25] with an experiment investigating the solidification of an aqueous ammonium chloride solution from a cooled vertical wall. Later on, the same experiment will be used as one of three test cases for a validation of the newly developed model and also for a direct performance comparison with Bennon's model.

2.2. Phase-Field Modelling of Solid-Liquid Phase Change

Phase transitions between the solid and liquid state will be described in this work by means of the phase-field method. It has emerged in the 1980s as an alternative to the explicit tracking of sharp interfaces in phase change dynamics and makes use of a smooth phase indicator function instead. Originally developed for solid-liquid phase transitions of elemental materials with static liquid phases, the method has been refined successively. Important steps include the investigation of its relationship to classical sharp interface modelling, assurance of thermodynamic consistency, coupling of phase change with convection and an extension to more than two possible phases. Due to the smoothness of the phase indicator function, the phase-field method necessarily produces interfaces with a certain degree of diffusivity. It is therefore suitable to describe solid-liquid phase change with mushy layers as needed for the description of binary eutectic alloys (see Figure 1.1). Additionally, the phase indicator function is treated on an equal footing with temperature and other state variables and therefore, the phase-field method permits an independent description of the phase change process. In a short summary, I will follow the different steps of development mentioned before by means of an exemplary model to provide an overview of the method and its state of the art.

2.2.1. Origin and Basic Ideas of the Phase-Field Method

We regard a solid-liquid phase change process of an elemental material in a volume $V \in \mathbb{R}^3$. Commonly, it is assumed that the material properties are the same in both phases and that there is no fluid flow in the liquid. Classical sharp interface modelling of this situation ([26]) consists of solving separate heat conduction equations in the two possible phases in compliance with a certain boundary condition at the moving phase interface $\Gamma(t)$

$$\rho c \frac{\partial T}{\partial t} = \lambda \vec{\nabla}^2 T \tag{2.41}$$

$$\rho L u_n = \lambda (\vec{\nabla} T|_s - \vec{\nabla} T|_l) \cdot \vec{n} \quad \text{at } \Gamma(t) \tag{2.42}$$

with density ρ, latent heat per mass L, the normal interface velocity u_n and heat conductivity λ. The vector $\vec{n}$ in (2.42) denotes the unit normal vector at each point on $\Gamma(t)$ pointing from the solid to the liquid and the temperature gradients $\vec{\nabla} T|_s$ and $\vec{\nabla} T|_l$ are calculated from the solid and the liquid side, respectively. Condition (2.42) expresses the conservation of latent heat produced by the moving phase boundary, i.e. it must be balanced by the heat fluxes to the solid and the liquid side. The difficulty originates from the fact that the phase boundary $\Gamma(t)$, on which the boundary condition (2.42) has to be applied, is itself a part of the solution and is not known a priori.
In the most general situation including curvature and kinetic effects, it is given by ([27])

$$\Gamma(t) = \{\vec{x} \in V \quad | \quad T(\vec{x}, t) = T_m - \frac{\sigma \kappa(\vec{x}, t) T_m}{\rho L} - \beta_k u_n\} \tag{2.43}$$

with surface tension σ, interface curvature $\kappa(\vec{x}, t)$ and the linear kinetic coefficient β_k.
A solution of (2.41), (2.42) and (2.43) necessitates an explicit tracking of the phase boundary which may cause numerical difficulties. In particular, topology changes like e.g. coalescence and applications in three spatial dimensions can lead to problems ([28]).
A possible path to an alternative description starts from the observation that (2.41) and (2.42) may be combined to the single equation ([29])

$$\rho c \frac{\partial T}{\partial t} = \lambda \vec{\nabla}^2 T - \rho L \frac{\partial \Theta(\vec{x}, t)}{\partial t}, \tag{2.44}$$

where a step function

$$\Theta(\vec{x},t) = \begin{cases} 1 & (\vec{x},t) \in \text{liquid} \\ 0 & (\vec{x},t) \in \text{solid} \end{cases} \tag{2.45}$$

has been defined to identify the location of latent heat release. However, an evaluation of (2.43) would still be necessary to determine $\Theta(\vec{x},t)$.
The essential idea of the phase-field method is to approximate $\Theta(\vec{x},t)$ by a smooth, sigmoid phase indicator function $\varphi(\vec{x},t)$ (see Figure 2.1) and to replace interface tracking via equation (2.43) by an additional partial differential equation for $\varphi(\vec{x},t)$. A single heat transport equation

$$\rho c \frac{\partial T}{\partial t} = \lambda \vec{\nabla}^2 T - \rho L \frac{\partial \varphi(\vec{x},t)}{\partial t} \tag{2.46}$$

is then solved inside the whole volume V and the additional governing equation for the liquid phase indicator function $\varphi(\vec{x},t)$ is derived from thermodynamic principles. Note that the continuity of the phase indicator function introduces an artificial diffusivity which has no physical correspondence.

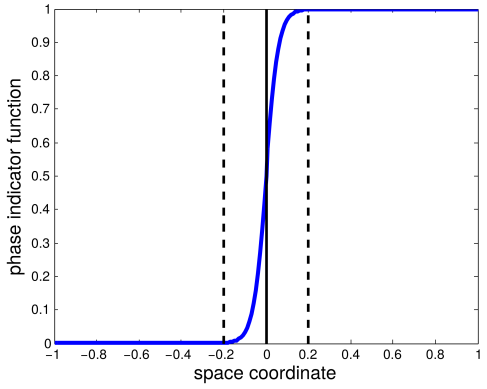

Figure 2.1.: Smooth phase indicator function around a sharp phase boundary Γ

The main ideas about the evolution of $\varphi(\vec{x},t)$ as a non-conserved order parameter date back to the 1970s ([30],[31]). Allen and Cahn investigated in [31] a diffuse interface system in which the phase indicator function $\varphi(\vec{x},t)$ is the only state variable. Based on a phenomenological free energy functional $F[\varphi]$ of the Ginzburg-Landau type, they proposed the governing equation

$$\frac{\partial \varphi(\vec{x},t)}{\partial t} = -K \frac{\delta F[\varphi]}{\delta \varphi}, \quad K > 0, \tag{2.47}$$

with a positive constant K and the first functional derivative $\frac{\delta}{\delta\varphi}$. The reason for this choice is that it assures thermodynamic consistency of the phase change process, i.e. free energy evolves towards a minimum value:

$$\frac{dF[\varphi]}{dt} = \int_V \frac{\delta F[\varphi]}{\delta \varphi} \frac{\partial \varphi}{\partial t} dV = -K \int_V (\frac{\delta F[\varphi]}{\delta \varphi})^2 dV \leq 0. \tag{2.48}$$

In thermodynamic equilibrium, this minimum value is adopted by F and the rate of phase change is zero:

$$\frac{\delta F[\varphi]}{\delta \varphi} = 0 \quad \rightarrow \quad \frac{\partial \varphi(\vec{x},t)}{\partial t} = 0. \tag{2.49}$$

In a non-equilibrium state, the rate of phase change is therefore assumed according to (2.47) to be proportional to the deviation from equilibrium. If the phase change dynamics is not too fast, this is surely a reasonable assumption.

Based on an appropriate free energy functional, the first phase-field models combined equation (2.47) with (2.46) to approximate the sharp interface problem (2.41)-(2.43). Due to the fact that temperature T represents a second state variable next to $\varphi(\vec{x},t)$, these models are not necessarily thermodynamically consistent as changes in temperature also influence the temporal change of free energy.
Examples of these early phase-field models were published by Fix in 1983 ([32]), Collins and Levine in 1985 ([33]), Langer in 1986 ([34]) and also by Kobayashi in 1993 and 1994 ([28],[35]). A representative free energy functional is given by

$$F[\varphi,T] = \int_V (f_{surface} + f_{bulk})dV \tag{2.50}$$

$$f_{surface} = a_1(\vec{\nabla}\varphi)^2 + a_2 g(\varphi) \tag{2.51}$$

$$f_{bulk} = h(\varphi)\rho L\frac{T_m - T}{T_m}, \tag{2.52}$$

where the free energy density is decomposed into a surface part $f_{surface}$ and a bulk part f_{bulk}, a_1 and a_2 are positive constants, $g(\varphi)$ is a symmetric double well function und $h(\varphi)$ is an interpolation function with $h(0) = 0$ and $h(1) = 1$.
The task of $f_{surface}$ is to represent the free energy of phase boundaries. A popular choice for the double well $g(\varphi)$ is the quartic function

$$g(\varphi) = \varphi^2(1-\varphi)^2, \tag{2.53}$$

which is shown in Figure 2.2. The expression $a_2 g(\varphi)$ in $f_{surface}$ leads to a separation of phases and therefore to a tendency to develop sharp phase boundaries because mixture states with $0 < \varphi < 1$ increase the free energy. Moreover, it is required that the transi-

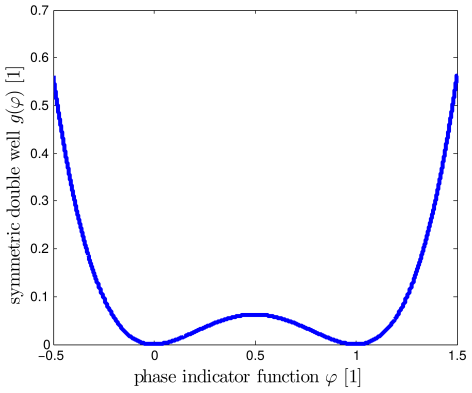

Figure 2.2.: Symmetric double well $g(\varphi)$

tions of φ between 0 and 1 are smooth. Therefore, a certain amount of phase mixing is needed being generated by the expression $a_1(\vec{\nabla}\varphi)^2$ in $f_{surface}$. It produces large positive contributions to the free energy if interfaces are sharp and the corresponding gradients $\vec{\nabla}\varphi$ are steep. The resulting equilibrium profile of the phase indicator function around a sharp interface at $T = T_m$ represents a balance between these two opposing tendencies of phase separation and phase mixing. Using (2.50)-(2.53), one finds

$$\frac{\delta F[\varphi,T_m]}{\delta\varphi} = 0 \quad \leftrightarrow \quad \varphi(x) = \frac{1}{2}(1+\tanh(\frac{x}{2\delta})) \quad \wedge \quad a_1 = a_2\delta^2. \tag{2.54}$$

Note that according to [36] and by using (2.50), the first variational derivative is calculated according to

$$\frac{\delta F[\varphi,T]}{\delta\varphi} = -\vec{\nabla}\cdot\{\frac{\partial(f_{surface}+f_{bulk})}{\partial\vec{\nabla}\varphi}\} + \frac{\partial(f_{surface}+f_{bulk})}{\partial\varphi}. \tag{2.55}$$

In (2.54), x represents a spatial coordinate perpendicular to the sharp phase boundary and δ is a free input parameter governing the width of the transition region between $\varphi = 0$ and $\varphi = 1$. The equilibrium profile from (2.54) is shown in Figure 2.3. In a further step, the

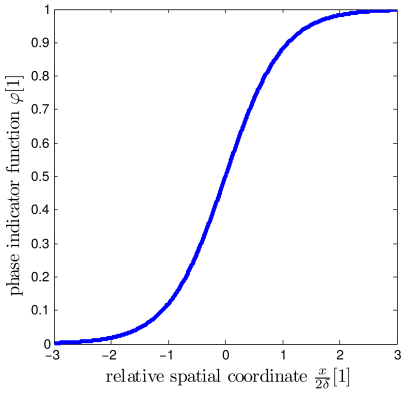

Figure 2.3.: Tangens hyperbolicus equilibrium profile of the phase indicator function

constant a_2 is expressed by surface tension σ as a measurable physical quantity. Surface tension can be defined as the excess free energy of the phase surface divided by the surface area. Consequently, one may calculate for an equilibrium sharp interface with area A at $T = T_m$ using (2.54) as well as the free energy model (2.50) - (2.53):

$$\sigma = \frac{F[\varphi, T_m]}{A} = \frac{1}{3} a_2 \delta \quad \leftrightarrow \quad a_2 = \frac{3\sigma}{\delta}. \tag{2.56}$$

The bulk free energy density f_{bulk} must be interpreted as a superposition of free energy densities of the solid and the liquid phases:

$$f_{bulk} = h(\varphi) f_l(T) + (1 - h(\varphi)) f_s(T) = f_s(T) + h(\varphi)(f_l(T) - f_s(T)). \tag{2.57}$$

By expanding the difference $f_l(T) - f_s(T)$ around the melting point T_m and taking the solid as a reference state ([37])

$$f_l(T) - f_s(T) = \rho L \frac{T_m - T}{T_m} \tag{2.58}$$

$$f_s(T) = 0, \tag{2.59}$$

expression (2.52) is obtained. As indicated in Figure 2.4, the effect of f_{bulk} is to lift or to lower the minimum $\varphi = 1$ of the symmetric double well depending on temperature, which leads to a preference of the solid ($T < T_m$) or the liquid ($T > T_m$) state. The minimum $\varphi = 0$ representing the solid stays unaffected due to $h(0) = 0$.
Based on (2.46), (2.47) and the preceding argumentation, the equations of the phase-field model are

$$\rho c \frac{\partial T}{\partial t} = \lambda \vec{\nabla}^2 T - \rho L \frac{\partial \varphi(\vec{x}, t)}{\partial t} \tag{2.60}$$

$$K^{-1} \frac{\partial \varphi(\vec{x}, t)}{\partial t} = 6\sigma\delta \vec{\nabla}^2 \varphi - \frac{6\sigma}{\delta} \varphi(1 - \varphi)(1 - 2\varphi) - h'(\varphi) \rho L \frac{T_m - T}{T_m}. \tag{2.61}$$

In the earliest investigations ([32],[33],[34]), which deal with analytical studies of the phase-field equations for the most part, the choice $h(\varphi) = \varphi$ was common. The first numerical simulations were published by Kobayashi ([28],[35]). He proposed to use a more general interpolation function $h(\varphi)$. According to his argumentation, the simple choice $h(\varphi) = \varphi$ leads to $h'(\varphi) = 1$ in equation (2.61). Therefore, a temperature change somewhere in a

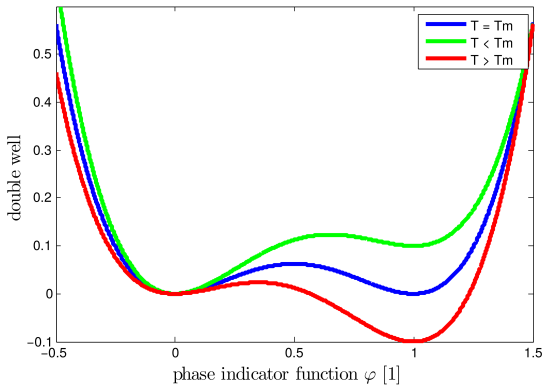

Figure 2.4.: Qualitative effect of f_{bulk} on the symmetric double well

bulk phase with $\varphi = 0$ or $\varphi = 1$ leads to a change of the phase indicator function at that position: $\frac{\partial \varphi}{\partial t} \neq 0$. Consequently, the term $\rho L \frac{\partial \varphi}{\partial t}$ in the temperature equation (2.60) generates an unphysical release of latent heat in the bulk. In contrast to that, usage of

$$h(\varphi) = 3\varphi^2 - 2\varphi^3 \tag{2.62}$$

induces

$$h'(\varphi) = 6\varphi(1 - \varphi) \tag{2.63}$$

and the problem of latent heat release in the bulk is cured. Based on an appropriate choice of the constant K and the introduction of anisotropy in the gradient term of $f_{surface}$, Kobayashi was able to qualitatively reproduce a number of realistic 2D and 3D dendritic crystal patterns. In particular, he replaced (see [28])

$$a_1 \quad \rightarrow \quad a_1 n(\theta) = a_1(1 + q\cos(j(\theta - \theta_0))) \tag{2.64}$$

in (2.51) with θ being the angle between $\vec{\nabla}\varphi$ and the x-direction. This led him to a modified phase-field equation, which can be obtained in two-dimensional form from (2.61) by the modification

$$6\sigma\delta\vec{\nabla}^2\varphi \quad \rightarrow \quad 6\sigma\delta\vec{\nabla} \cdot \{n(\theta)\vec{\nabla}\varphi\} - 3\sigma\delta\{\frac{\partial}{\partial x}(\frac{\partial n}{\partial \theta}\frac{\partial \varphi}{\partial y}) - \frac{\partial}{\partial y}(\frac{\partial n}{\partial \theta}\frac{\partial \varphi}{\partial x})\}. \tag{2.65}$$

Figure 2.5 shows a reproduction of one of Kobayashi's 2D solidification patterns, which I obtained with an implementation of (2.60) and (2.61) utilizing the modification (2.65). The material parameters were chosen as in [28] with the anisotropy parameters $q = 0.04$, $j = 6$ and $\theta_0 = 0.5\pi$.

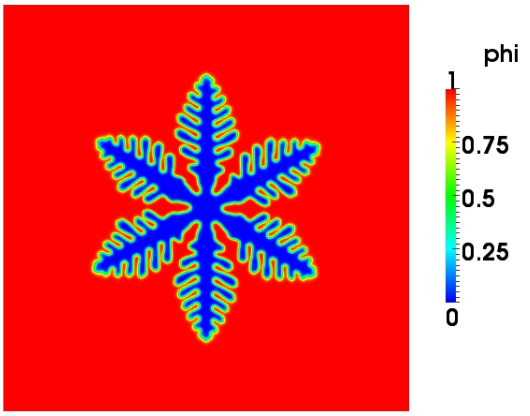

Figure 2.5.: Anisotropic solidification pattern obtained by the phase-field method

2.2.2. Relationship to Classical Sharp Interface Modelling

As mentioned already before, early publications about the phase-field method were mostly of an analytical nature. Besides the search for analytical solutions, investigations of the relationship between the system of equations (2.60)-(2.61) and the sharp interface model (2.41)-(2.43) were a popular topic. One can expect that a connection with the sharp interface model may be possible in the limit $\delta \to 0$ as the free input parameter δ determines the width of the continuous transition region of φ and due to the convergence of the tangens hyperbolicus profile against a sharp interface step function $\Theta(x)$:

$$\lim_{\delta \to 0} \{ \frac{1}{2} (1 + \tanh(\frac{x}{2\delta})) \} = \Theta(x). \tag{2.66}$$

Important contributions come here especially from Caginalp ([38],[39],[29]), who amongst others performed a so-called sharp interface analysis by investigating the limit $\delta \to 0$ of equations (2.60) and (2.61). The basic idea of this procedure is to decompose the volume of interest V into different regions.
The *inner region* is a thin layer around the sharp interface $\Gamma(t)$ with a width proportional to δ, in which the phase-field φ performs its smooth transition from zero to one. In a first step, a local set of curvilinear coordinates (r, s) is introduced in the neighbourhood of Γ. For simplicity, we restrict our considerations here to two dimensions. The coordinate $r(\vec{x}, t)$ measures the signed distance of a point $\vec{x}$ at time t to the sharp phase boundary Γ with $r > 0$ in the liquid and $r < 0$ in the solid. The second coordinate $s(\vec{x}, t)$ represents the corresponding arclength from some fixed point. Furthermore, the stretched coordinate $z = \frac{r}{\delta}$ is introduced to permit a more convenient description of the spatial variations of the phase-field and the temperature field in the inner region. A given value $z = z_0$ corresponds to a normal distance $r = z_0\delta$ to Γ and therefore approaches the sharp interface if δ is decreased. The behaviour of T and φ in the inner region is expressed by the inner expansions

$$T(z, s, t, \delta) = T^{(0)}(z, s, t) + \delta \cdot T^{(1)}(z, s, t) + ... \tag{2.67}$$

$$\varphi(z, s, t, \delta) = \varphi^{(0)}(z, s, t) + \delta \cdot \varphi^{(1)}(z, s, t) + ... \tag{2.68}$$

The *outer region* is defined to be located away from any interface in the bulk phases. The usual coordinate vector $\vec{x}$ can be used here to describe the spatial dependence of T and φ and the broadening of the actually sharp interface induced by a small, but finite value

of δ is considered to represent a small perturbation. Consequently, the outer expansion is given by

$$\tilde{T}(\vec{x},t,\delta) = \tilde{T}^{(0)}(\vec{x},t) + \delta \cdot \tilde{T}^{(1)}(\vec{x},t) + ... \tag{2.69}$$

$$\tilde{\varphi}(\vec{x},t,\delta) = \tilde{\varphi}^{(0)}(\vec{x},t) + \delta \cdot \tilde{\varphi}^{(1)}(\vec{x},t) + ... \tag{2.70}$$

Note that the quantities on the right hand side of (2.69) and (2.70) may adopt a non-smooth behaviour at the sharp interface Γ. The limiting values of the outer variables as Γ is approached from $r > 0$ or $r < 0$ are denoted by $\tilde{T}|_{\Gamma_\pm}$ and $\tilde{\varphi}|_{\Gamma_\pm}$, respectively.
The *intermediate region* is the domain where the inner and outer regions overlap and where the inner and outer expansions must both be valid. Consequently, the inner and outer expansions have to be matched order by order in δ in the intermediate region to achieve consistency. With the unit normal vector $\vec{n}$ on Γ pointing to the liquid side of the interface, this leads to the following matching conditions:

$$\lim_{z\to\pm\infty} \varphi^{(0)} = \tilde{\varphi}^{(0)}|_{\Gamma_\pm} \tag{2.71}$$

$$\lim_{z\to\pm\infty} T^{(0)} = \tilde{T}^{(0)}|_{\Gamma_\pm} \tag{2.72}$$

$$\lim_{z\to\pm\infty} \frac{\partial T^{(1)}}{\partial z} = \vec{\nabla}\tilde{T}^{(0)}|_{\Gamma_\pm} \cdot \vec{n}. \tag{2.73}$$

While (2.71) and (2.72) obviously result from a comparison of the order $O(\delta^0)$ in the inner and outer expansions, relation (2.73) following from the order $O(\delta^1)$ is not immediately clear. One has to be aware that $\tilde{T}^{(i)}(\vec{x},t)$ in the outer expansion can be expressed as a Taylor series

$$\tilde{T}^{(i)}(\vec{x},t) = \tilde{T}^{(i)}|_{\Gamma_\pm} + [\vec{\nabla}\tilde{T}^{(i)}|_{\Gamma_\pm} \cdot \vec{n}]\ z\delta + ..., \tag{2.74}$$

which results in the following order $O(\delta^1)$ contribution to the outer expansion:

$$[\vec{\nabla}\tilde{T}^{(0)}|_{\Gamma_\pm} \cdot \vec{n}]\ z + \tilde{T}^{(1)}|_{\Gamma_\pm}. \tag{2.75}$$

Differentiation with respect to z and equating the resulting expression with $\frac{\partial T^{(1)}(z,s,t)}{\partial z}$ from the inner expansion in the appropriate limit leads then to (2.73).
Applying Caginalp's recipe to our exemplary model, we insert the outer expansions (2.69) and (2.70) into the set of equations (2.60) and (2.61) and find

$$\tilde{\varphi}^{(0)} = 0 \quad \vee \quad \tilde{\varphi}^{(0)} = 1 \tag{2.76}$$

$$\tilde{\varphi}^{(i)} = 0 \quad \text{for} \quad i > 0 \tag{2.77}$$

$$\rho c \frac{\partial \tilde{T}^{(i)}}{\partial t} = \lambda \vec{\nabla}^2 \tilde{T}^{(i)} \quad \text{for} \quad i \geq 0. \tag{2.78}$$

This means that away from interfaces, there are bulk phases and the temperature field is governed by usual heat conduction equation in accordance with equation (2.41) from sharp interface modelling.
With respect to the inner solutions, we have to notice that the differential operators $\vec{\nabla}^2$ and $\frac{\partial}{\partial t}$ must be expressed by the inner variables s and z ([29]). The order $O(\delta^0)$ using the matching conditions (2.71) and (2.72) gives

$$\varphi^{(0)}(z,s,t) = \varphi^{(0)}(z) = \frac{1}{2}(1 + \tanh(\frac{z}{2})) \tag{2.79}$$

$$T^{(0)}(z,s,t) = \tilde{T}^{(0)} = const = \tilde{T}^{(0)}|_{\Gamma_\pm}. \tag{2.80}$$

Consequently, the leading order phase-field performs a tangens hyperbolicus transition in the inner region between the solid and the liquid and the temperature field is continuous

at the sharp interface Γ as $\tilde{T}^{(0)}|_{\Gamma_+} = \tilde{T}^{(0)}|_{\Gamma_-} = \tilde{T}^{(0)}$.
By utilizing the third matching condition (2.73), the order $O(\delta)$ of the temperature equation leads to

$$\lambda(\vec{\nabla}\tilde{T}^{(0)}|_{\Gamma_-} - \vec{\nabla}\tilde{T}^{(0)}|_{\Gamma_+}) \cdot \vec{n} = -\rho L \frac{\partial r}{\partial t}. \tag{2.81}$$

Noting that $\frac{\partial r}{\partial t} = -u_n$ with the normal velocity of the interface u_n, it is easy to confirm that (2.81) represents the same boundary condition for the outer temperature field as we know from equation (2.42) for sharp interface modelling.
Finally, with the interface curvature $\kappa = \vec{\nabla}^2 r$ ([29]), the order $O(\delta)$ of the phase-field equation reproduces condition (2.43) for the interface temperature

$$\tilde{T}^{(0)} = T_m - \frac{\sigma\kappa(\vec{x},t)T_m}{\rho L} - \beta_k u_n, \tag{2.82}$$

if the constant K is chosen according to

$$K^{-1} = \frac{6L\rho\beta_k\delta}{T_m}. \tag{2.83}$$

Consequently, using (2.83) and choosing δ sufficiently small, the set of equations (2.60) and (2.61) is really equivalent to the sharp interface problem.
But what does sufficiently small mean? According to the preceding sharp interface analysis, it means that δ must be smaller than the smallest physical length scale of interest. The latter is given by the capillary length ([40])

$$l_{cap} = \frac{c\sigma T_m}{\rho L^2}. \tag{2.84}$$

The typical order of magnitude of the capillary length is about $10^{-10}m$ (take for example the material properties of usual water). At the same time, the smooth transition of φ must be resolved by the numerical grid resulting in a required grid spacing in the same range of $10^{-10}m$ or even smaller. As typical solidification patterns have characteristic lengths in the micrometer range and above, it becomes immediately clear that quantitative phase-field simulations are impossible on the basis of a sharp interface analysis.
In 1996, Karma and Rappel ([41],[42],[43]) found a remedy to this severe limitation concerning δ and the grid spacing. In their thin interface analysis, they assumed δ to be considerably smaller than the width of the diffusion boundary layer l_{diff} of the temperature field, but it did not have to be smaller than the capillary length l_{cap}. Using the normal velocity u_n of the phase boundary, l_{diff} may be expressed as

$$l_{diff} = \frac{\lambda}{\rho c u_n}. \tag{2.85}$$

In order to determine l_{diff} in practical situations, the normal velocity u_n can usually be extracted from experimental data at hand. If this is not possible, its value can be estimated depending on material properties and undercooling conditions as proposed in [44]. The considered set of generalized equations is given by

$$\rho c \frac{\partial T}{\partial t} = \lambda\vec{\nabla}^2 T - \rho L \frac{\partial w(\varphi(\vec{x},t))}{\partial t} \tag{2.86}$$

$$K^{-1}\frac{\partial\varphi(\vec{x},t)}{\partial t} = 2a\delta\vec{\nabla}^2\varphi - \frac{a}{\delta}g'(\varphi) - h'(\varphi)\rho L\frac{T_m - T}{T_m}, \tag{2.87}$$

where the symmetric double well $g(\varphi)$ as well as the interpolation functions $w(\varphi)$ and $h(\varphi)$ remain unspecified. Note that the value of the constant a is determined by some special choice for $g(\varphi)$.

By expressing all spatial coordinates in units of $l_{diff} = \frac{\lambda}{\rho c u_n}$ and time in units of $\tau_{diff} = \frac{l_{diff}^2 \rho c}{\lambda}$, the equations are non-dimensionalized and the small quantity

$$p = \frac{\delta}{l_{diff}} << 1 \tag{2.88}$$

appears. The inner and outer expansions are then expressed as power series in the small parameter p instead of δ and a procedure similar to the sharp interface analysis presented before is applied.
Karma and Rappel's main result is that even under the condition $l_{cap} < \delta << l_{diff}$, the set of equations (2.86) and (2.87) can be mapped onto the sharp interface problem (2.41)-(2.43) if the functions $g(\varphi)$, $w(\varphi)$ and $h(\varphi)$ obey certain symmetries. Adapted to our description with φ varying between zero and one, these symmetries are

$$g(1-\varphi) = g(\varphi) \tag{2.89}$$
$$w(1-\varphi) = 1 - w(\varphi) \tag{2.90}$$
$$h(1-\varphi) = 1 - h(\varphi). \tag{2.91}$$

It is important to note here that in general, the $O(p^1)$ equation for φ produces corrections in the interface temperature (2.82) to the curvature undercooling term $\frac{\sigma\kappa(\vec{x},t)T_m}{\rho L}$ as well as to the kinetic undercooling term $\beta_k u_n$. Especially the former leads to a non-resolvable discrepancy with the sharp interface problem. If, however, conditions (2.89)-(2.91) are fulfilled, the corrections to the curvature term vanish. The remaining corrections in the kinetic term can then be absorbed into the definition of the constant K.
Choosing

$$g(\varphi) = \varphi^2(1-\varphi)^2 \tag{2.92}$$
$$w(\varphi) = \varphi \tag{2.93}$$
$$h(\varphi) = 3\varphi^2 - 2\varphi^3 \tag{2.94}$$

as our choice from before fulfills conditions (2.89)-(2.91), one finds that (2.82) is recovered if K in (2.83) is modified according to

$$K^{-1} = \frac{6L\rho\delta}{T_m}(\beta_k + r\frac{\rho L\delta}{\lambda}) \tag{2.95}$$

with a numerical constant $0 < r < 1$. Another advantage is that simulations with a negligible kinetic effect are now possible by setting $\beta_k = 0$.
Based on the thin interface analysis, Karma and Rappel were able to reproduce dendritic tip shapes and tip velocities with good agreement ([41],[43]). Around the turn of the millenium, Karma and Rappel's methodology was applied by Almgren ([45]) and McFadden, Wheeler and Anderson ([46]) to the asymmetric case of unequal heat conductivities in the solid and the liquid.
Later on in this work, a thin interface analysis will be performed in detail for the newly developed model.

2.2.3. Thermodynamic Consistency

Concerning thermodynamic consistency, one has to be aware that the phase-field model considered so far contains two different state variables $\varphi(\vec{x},t)$ and $T(\vec{x},t)$ and that both of them influence the temporal evolution of free energy. However, a popular procedure in phase-field modelling has been to regard temperature as a constant at first and to derive the phase-field equation (2.47) according to Allen and Cahn. Afterwards, temperature was

allowed to vary and a heat conduction equation with a latent heat source term containing the phase-field time derivative was added independently from the free energy functional. With this recipe, it is not clear if

$$\frac{dF[\varphi,T]}{dt} = \int_V \{\frac{\delta F[\varphi,T]}{\delta\varphi}\frac{\partial\varphi}{\partial t} + \frac{\delta F[\varphi,T]}{\delta T}\frac{\partial T}{\partial t}\}dV \leq 0. \tag{2.96}$$

A proper way to deal with thermodynamic consistency was presented by Penrose and Fife ([47]) and later by Wang et al. ([48]), who derived a set of equations for temperature and the phase-field from a single functional.
Based on the observation that temperature variations are the result of internal energy flows, a legendre transform leads from the free energy functional $F[\varphi,T]$ to an entropy functional $S[\varphi,e]$ with the internal energy per volume e:

$$F[\varphi,T] = \int_V \{a\delta(\vec{\nabla}\varphi)^2 + f(\varphi,T)\}dV \tag{2.97}$$

$$= \int_V \{a\delta(\vec{\nabla}\varphi)^2 + e - Ts(\varphi,e)\}dV \tag{2.98}$$

$$= E[e] - TS[\varphi,e]. \tag{2.99}$$

The internal energy and entropy functionals E and S are then given by

$$E[e] = \int_V e dV \tag{2.100}$$

$$S[\varphi,e] = \int_V \{s(\varphi,e) - a_s\delta(\vec{\nabla}\varphi)^2\}dV \tag{2.101}$$

with the entropy per volume $s(\varphi,e)$, $a_s = \frac{a}{T}$ and $a = const.$ In general, the non-constant factor $\frac{1}{T}$ makes a_s space-dependent leading to a complication in the further procedure and the resulting final equations. Mainly for analytical reasons, Penrose and Fife and also Wang et al. therefore assume it to be a constant. The newly developed model of this work will resolve this problem by a modification in the definition of free energy.
Penrose and Fife proved that the set of equations

$$\frac{\partial\varphi}{\partial t} = K_1 T\frac{\delta S[\varphi,e]}{\delta\varphi} \quad , \quad K_1 > 0 \tag{2.102}$$

$$\frac{\partial e}{\partial t} = -\vec{\nabla}\cdot[K_2\vec{\nabla}(\frac{\delta S[\varphi,e]}{\delta e})] \quad , \quad K_2 > 0 \tag{2.103}$$

assures thermodynamic consistency:

$$\frac{dS[\varphi,e]}{dt} \geq 0. \tag{2.104}$$

Using

$$\frac{\delta S[\varphi,e]}{\delta e} = \frac{\partial s(\varphi,e)}{\partial e} = \frac{\partial}{\partial e}(\frac{e}{T} - \frac{f(\varphi,T)}{T}) = \frac{1}{T} \tag{2.105}$$

$$\frac{\delta S[\varphi,e]}{\delta\varphi} = -\vec{\nabla}\cdot[\frac{\partial(-a_s\delta(\vec{\nabla}\varphi)^2)}{\partial\vec{\nabla}\varphi}] + \frac{\partial s(\varphi,e)}{\partial\varphi} \tag{2.106}$$

$$= 2a_s\delta\vec{\nabla}^2\varphi + \frac{\partial}{\partial\varphi}(\frac{e}{T} - \frac{f(\varphi,T)}{T}) \tag{2.107}$$

$$= \frac{1}{T}(2a\delta\vec{\nabla}^2\varphi - \frac{\partial f(\varphi,T)}{\partial\varphi}), \tag{2.108}$$

setting $K_2 = \lambda T^2 > 0$ as well as $e(\varphi, T) = \rho c T + \rho L \varphi$ and recovering the tilted double well

$$f(\varphi, T) = \frac{a}{\delta}\varphi^2(1-\varphi)^2 + h(\varphi)\rho L \frac{T_m - T}{T_m}, \tag{2.109}$$

the set of equations resulting from (2.102) and (2.103) is equivalent to the equations (2.60) and (2.61). Consequently, the exemplary model considered so far is really thermodynamically consistent.

2.2.4. Coupling with Convection

There have been two different approaches to couple the phase-field method with the Navier-Stokes equations of hydrodynamics. One of them has been proposed by Beckermann et al. in 1999 ([49]). In order to describe a convective solid-liquid phase change system, the authors in [49] start from a two-phase approach and consider distinct volume-averaged transport equations for the solid and liquid phase. By adding the solid and liquid equations for each transport property Q and defining solid liquid mixture quantities according to

$$Q = \varphi Q_{liquid} + (1-\varphi) Q_{solid}, \tag{2.110}$$

they obain a set of phase-averaged Navier-Stokes, energy and composition transport equations. Viscosity and density are thereby assumed to be constant and phase-independent. The solid is regarded to be rigid by setting the solid velocity to zero

$$\vec{u} = \varphi \vec{u}_{liquid} + (1-\varphi)\vec{u}_{solid} = \varphi \vec{u}_{liquid} \tag{2.111}$$

and an interfacial stress term proportional to

$$\frac{(1-\varphi)}{\delta} |\vec{\nabla}\varphi| \vec{u}_{liquid} \tag{2.112}$$

represents a momentum sink in the transport equation for velocity. It disappears in the liquid with $\varphi = 1$, damps velocity in the diffuse interface region and reproduces the no-slip boundary condition in the sharp interface limit $\delta \to 0$.
However, the derivation of the phase-field equation occurs on the basis of a geometrical argumentation. The disadvantage of this approach is that thermodynamic consistency is not assured as the coupling of the different transport equations with the phase change process does not arise from a single functional in the sense of Penrose and Fife's ideas ([47]) from the last subsection.
Because thermodynamic consistency is an important aspect of this thesis, the second approach proposed by Anderson, McFadden and Wheeler ([50],[51]) is more appropriate as it extends the formalism of irreversible thermodynamics by Penrose and Fife to include the Navier-Stokes equations. They regard both phases as Newtonian fluids with a phase-field dependent viscosity adopting sufficiently large values in the solid to damp velocity to zero.
The derivation is based on the following expressions for mass, momentum, energy and entropy in a subvolume $\Omega \subset V$:

$$M = \int_\Omega \rho dV \tag{2.113}$$

$$\vec{p} = \int_\Omega \rho \vec{u} dV \tag{2.114}$$

$$E = \int_\Omega \{\rho e_m + \frac{1}{2}\rho \vec{u}^2\} dV \tag{2.115}$$

$$S = \int_\Omega \{\rho s_m - a_s \delta (\vec{\nabla}\varphi)^2\} dV \tag{2.116}$$

with linear momentum $\vec{p}$, the internal energy per mass e_m and the entropy per mass s_m. In (2.116), a_s is assumed to be constant again although actually $a_s = \frac{a}{T}$ for the exemplified case considered so far. I note here that in [51], the above expressions are more general by incorporating the possibility of anisotropic behaviour in the entropy gradient term and also by considering an additional gradient contribution to energy. These features are skipped for simplicity. The governing equations corresponding to the introduced quantities are:

$$\frac{dM}{dt} = 0 \qquad \leftrightarrow \qquad \frac{D\rho}{Dt} = -\rho(\vec{\nabla}\cdot\vec{u}) \tag{2.117}$$

$$\frac{d\vec{p}}{dt} = \int_{\partial\Omega} \vec{n}\cdot\boldsymbol{m}dA \qquad \leftrightarrow \qquad \rho\frac{D\vec{u}}{Dt} = \vec{\nabla}\cdot\boldsymbol{m} \tag{2.118}$$

$$\frac{dE}{dt} = -\int_{\partial\Omega} \vec{q_e}\cdot\vec{n}dA + \int_{\partial\Omega} \vec{n}\cdot\boldsymbol{m}\cdot\vec{u}dA \qquad \leftrightarrow \qquad \rho\frac{De_m}{Dt} = -\vec{\nabla}\cdot\vec{q_e} + \boldsymbol{m} : (\vec{\nabla}\vec{u}) \tag{2.119}$$

$$\frac{dS}{dt} = -\int_{\partial\Omega} \vec{q_s}\cdot\vec{n}dA + \int_{\Omega} \dot{s}_{prod}dV \qquad \leftrightarrow \qquad \rho\frac{Ds_m}{Dt} = -\vec{\nabla}\cdot\vec{q_s} + \dot{s}_{prod} + 2a_s\delta Q_G \tag{2.120}$$

In (2.117)-(2.120), the Gaussian theorem was used, $\frac{D}{Dt} = \frac{\partial}{\partial t} + \vec{u}\cdot\nabla$ is the material derivative, $\boldsymbol{m}$ is the stress tensor, $\vec{q_e}$ and $\vec{q_s}$ are the heat and entropy fluxes and $\dot{s}_{prod}$ is the so-called entropy production rate. The quantity Q_G appearing in (2.120) results from the temporal derivative of the gradient term in (2.116) and is given by

$$Q_G = \vec{\nabla}\cdot(\vec{\nabla}\varphi\frac{D\varphi}{Dt}) - \frac{D\varphi}{Dt}\vec{\nabla}^2\varphi - (\vec{\nabla}\vec{u}) : (\vec{\nabla}\varphi\otimes\vec{\nabla}\varphi) + \frac{1}{2}(\vec{\nabla}\varphi)^2(\vec{\nabla}\cdot\vec{u}). \tag{2.121}$$

Note that momentum conservation (2.118) was utilized in (2.119) to eliminate the kinetic terms and to get an equation for the internal energy per mass.
In the framework presented here, thermodynamic consistency means that the entropy production rate is non-negative and the main idea of Anderson et al. is to find constitutive laws for $\boldsymbol{m}$, $\vec{q_e}$, $\vec{q_s}$ and $\frac{D\varphi}{Dt}$ which assure $\dot{s}_{prod} \geq 0$.
An important step is to make use of the thermodynamic relation

$$de_m = Tds_m + \frac{p}{\rho^2}d\rho + \frac{\partial e_m}{\partial\varphi}d\varphi \tag{2.122}$$

with pressure p, which gives

$$\rho\frac{Ds_m}{Dt} = \frac{\rho}{T}\frac{De_m}{Dt} - \frac{p}{\rho T}\frac{D\rho}{Dt} - \frac{\rho}{T}\frac{\partial e_m}{\partial\varphi}\frac{D\varphi}{Dt}. \tag{2.123}$$

The entropy production rate is then

$$\dot{s}_{prod} = \rho\frac{Ds_m}{Dt} + \vec{\nabla}\cdot\vec{q_s} - 2a_s\delta Q_G \tag{2.124}$$

$$= \frac{\rho}{T}\frac{De_m}{Dt} - \frac{p}{\rho T}\frac{D\rho}{Dt} - \frac{\rho}{T}\frac{\partial e_m}{\partial\varphi}\frac{D\varphi}{Dt} + \vec{\nabla}\cdot\vec{q_s} - 2a_s\delta Q_G. \tag{2.125}$$

Replacing $\frac{De_m}{Dt}$ and $\frac{D\rho}{Dt}$ by expressions (2.117) and (2.119) and using $\vec{\nabla}\cdot\vec{u} = \mathbf{1} : (\vec{\nabla}\vec{u})$ as well as $-\frac{1}{T}\vec{\nabla}\cdot\vec{q_e} = -\vec{\nabla}\cdot(\frac{\vec{q_e}}{T}) + \vec{q_e}\cdot\vec{\nabla}(\frac{1}{T})$, we get

$$\dot{s}_{prod} = \vec{\nabla}\cdot(\vec{q_s} - \frac{\vec{q_e}}{T} - 2a_s\delta\vec{\nabla}\varphi\frac{D\varphi}{Dt}) \tag{2.126}$$

$$+ \vec{q_e}\cdot\vec{\nabla}(\frac{1}{T}) + \frac{D\varphi}{Dt}(2a_s\delta\vec{\nabla}^2\varphi - \frac{\rho}{T}\frac{\partial e_m}{\partial\varphi}) \tag{2.127}$$

$$+ \frac{1}{T}\{\boldsymbol{m} + p\mathbf{1} + 2a_s\delta(\vec{\nabla}\varphi\otimes\vec{\nabla}\varphi) - a_s\delta(\vec{\nabla}\varphi)^2\mathbf{1}\} : (\vec{\nabla}\vec{u}). \tag{2.128}$$

The following constitutive laws assure $\dot{s}_{prod} \geq 0$:

$$\vec{q}_s = \frac{\vec{q}_e}{T} + 2a_s\delta\vec{\nabla}\varphi\frac{D\varphi}{Dt} \tag{2.129}$$

$$\vec{q_e} = \lambda(\varphi)T^2\vec{\nabla}(\frac{1}{T}) = -\lambda(\varphi)\vec{\nabla}T \tag{2.130}$$

$$\frac{D\varphi}{Dt} = KT\{2a_s\delta\vec{\nabla}^2\varphi - \frac{\rho}{T}\frac{\partial e_m}{\partial\varphi}\} \quad , \quad K > 0 \tag{2.131}$$

$$\boldsymbol{m} = \boldsymbol{\tau} - p\mathbf{1} - 2a_s\delta\{\vec{\nabla}\varphi\otimes\vec{\nabla}\varphi - \frac{1}{2}(\vec{\nabla}\varphi)^2\mathbf{1}\}. \tag{2.132}$$

In the expressions above, we introduced a phase-dependent heat conductivity $\lambda(\varphi)$ and the viscous stress tensor $\boldsymbol{\tau}$

$$\boldsymbol{\tau} = \eta(\varphi)\{(\vec{\nabla}\vec{u}) + (\vec{\nabla}\vec{u})^T - \frac{2}{3}(\vec{\nabla}\cdot\vec{u})\mathbf{1}\} \tag{2.133}$$

with a phase-dependent viscosity $\eta(\varphi)$. (2.129), (2.130) and (2.132) reduce to their usual form in the bulk phases, but contain additional contributions in the diffuse interface regions.
Putting $\boldsymbol{m}$ and $\vec{q_e}$ into (2.118) and (2.119) realizes a thermodynamically consistent coupling of the phase change process with the Navier-Stokes and heat transport equations. Concerning the phase change process, we note that $e_m = e_m(s_m, \rho, \varphi)$ according to (2.122). A legendre transform leads to the free energy per mass $f_m(T, \rho, \varphi)$ with

$$df_m = d(e_m - Ts_m) = de_m - Tds_m - s_m dT \tag{2.134}$$

$$= Tds_m + \frac{p}{\rho^2}d\rho + \frac{\partial e_m}{\partial\varphi}d\varphi - Tds_m - s_m dT \tag{2.135}$$

$$= -s_m dT + \frac{p}{\rho^2}d\rho + \frac{\partial e_m}{\partial\varphi}d\varphi. \tag{2.136}$$

Consequently, we get

$$\rho\left(\frac{\partial e_m(s_m,\rho,\varphi)}{\partial\varphi}\right)_{s_m,\rho} = \rho\left(\frac{\partial f_m(T,\rho,\varphi)}{\partial\varphi}\right)_{T,\rho} = \frac{\partial(\rho f_m)}{\partial\varphi} = \frac{\partial f}{\partial\varphi} \tag{2.137}$$

with the free energy per volume f and remembering that $a_s = \frac{a}{T}$, the phase-field equation is given by

$$K^{-1}\frac{D\varphi}{Dt} = 2a\delta\vec{\nabla}^2\varphi - \frac{\partial f}{\partial\varphi} \quad , \quad K > 0. \tag{2.138}$$

Inserting the tilted double well (2.109) for f, this equation is equivalent to our previous equation (2.61) except for the material derivative.

2.2.5. Binary Alloys

2.2.5.1. Binary Alloys with Complete Solubility

The first phase-field models for binary alloy solidification were developed by Boettinger, Wheeler and Warren ([52],[53],[54]) and targeted on the description completely soluble systems with simple, lens-shaped phase diagrams. They regarded a free energy functional

$$F[\varphi,\xi,T] = \int_V \{a\delta(\vec{\nabla}\varphi)^2 + f(\varphi,\xi,T)\}dV, \tag{2.139}$$

where the composition variable ξ denotes the mass fraction of component B. The tilted double well $f(\varphi,\xi,T)$ was constructed as a superposition of tilted double wells of the single

components in the sense of an ideal solution:

$$f(\varphi,\xi,T) = \xi f_B(\varphi,T) + (1-\xi)f_A(\varphi,T) + \frac{RT}{v_m}\{\xi\log(\xi) + (1-\xi)\log(1-\xi)\} \tag{2.140}$$

$$f_k(\varphi,T) = \frac{a}{\delta}\varphi^2(1-\varphi)^2 + h(\varphi)\rho_k L_k\frac{T_{m,k}-T}{T_{m,k}}. \tag{2.141}$$

In contrast to the original work by Boettinger et al., we use here a single constant a for simplicity. The last expression of $f(\varphi,\xi,T)$ originates in the entropy of mixing and the ideal gas constant R as well as the molar volume v_m are used. It is usually assumed that temperature variations are negligible and T is set to a constant such that free energy is appropriate for a thermodynamically consistent treatment. The set of equations is then

$$\frac{\partial\varphi}{\partial t} = -K_1\frac{\delta F}{\delta\varphi} \tag{2.142}$$

$$\frac{\partial\xi}{\partial t} = -K_2\vec{\nabla}\cdot\{\xi(1-\xi)\vec{\nabla}(\frac{\delta F}{\delta\xi})\}. \tag{2.143}$$

The factor $\xi(1-\xi)$ is added in (2.143) because it assures a composition-independent diffusion coefficent. Equation (2.143) is the simplest kind of evolution equation assuring thermodynamic consistency for a conserved quantity. It is therefore not a coincidence that it has the same structure as equation (2.103) for internal energy.
In the binary alloy model by Boettinger et al., locally coexisting solid and liquid phases have the same composition: $\xi = \xi_s = \xi_l$. As demonstrated by Kim ([55]), this leads to some severe disadvantages. The authors in [55] assume isothermal conditions and reformulate the tilted double well according to

$$f(\varphi,\xi) = \frac{a}{\delta}\varphi^2(1-\varphi)^2 + h(\varphi)f_l(\xi) + (1-h(\varphi))f_s(\xi), \tag{2.144}$$

where $f_l(\xi)$ and $f_s(\xi)$ denote the liquid and solid phase free energy densities. A connection with the original expression by Boettinger from above can easiliy be obtained by setting

$$f_s(\xi) = \frac{RT}{v_m}\{\xi\log(\xi) + (1-\xi)\log(1-\xi)\} \tag{2.145}$$

$$f_l(\xi) = \frac{RT}{v_m}\{\xi\log(\xi) + (1-\xi)\log(1-\xi)\} \tag{2.146}$$

$$+ \xi\rho_B L_B\frac{T_{m,B}-T}{T_{m,B}} + (1-\xi)\rho_A L_A\frac{T_{m,A}-T}{T_{m,A}}. \tag{2.147}$$

A one-dimensional state of thermodynamic equilibrium is determined by the condition

$$\frac{\delta F}{\delta\varphi} = 0 \quad\leftrightarrow\quad 2a\delta\frac{\partial^2\varphi}{\partial x^2} = \frac{\partial f(\varphi,\xi)}{\partial\varphi} \tag{2.148}$$

$$= \frac{a}{\delta}\frac{\partial}{\partial\varphi}\{\varphi^2(1-\varphi)^2\} + \frac{\partial h(\varphi)}{\partial\varphi}(f_l(\xi) - f_s(\xi)). \tag{2.149}$$

Multiplying both sides with $\frac{\partial\varphi}{\partial x}$, we get

$$a\delta\frac{\partial}{\partial x}\{(\frac{\partial\varphi}{\partial x})^2\} = \frac{\partial}{\partial x}\{\frac{a}{\delta}\varphi^2(1-\varphi)^2 + h(\varphi)(f_l(\xi) - f_s(\xi))\} \tag{2.150}$$

$$\rightarrow \frac{\partial\varphi}{\partial x} = \sqrt{\frac{1}{\delta^2}\varphi^2(1-\varphi)^2 + \frac{1}{a\delta}h(\varphi)(f_l(\xi) - f_s(\xi))}. \tag{2.151}$$

We remember that for elemental materials, we had $f_l(T_m) = f_s(T_m)$ in thermodynamic equilibrium and consequently

$$\frac{\partial\varphi}{\partial x} = \frac{1}{\delta}\varphi(1-\varphi) \quad\leftrightarrow\quad \varphi(x) = \frac{1}{2}(1+\tanh(\frac{x}{2\delta})). \tag{2.152}$$

The equilibrium profile is therefore decoupled from the bulk chemical properties in the case of an elemental material and δ is a free input length. As demonstrated in (2.56), the decoupled equilibrium profile allows a calibration of the model to represent a certain surface tension for arbitrary values of δ by a proper choice for a.
However, for the binary alloy, thermodynamic equilibrium is not characterized by $f_l = f_s$, but rather by the common tangent rule

$$f_l(\xi_l) = f_s(\xi_s) + \frac{\partial f(\varphi,\xi)}{\partial \xi}(\xi_l - \xi_s), \tag{2.153}$$

where the liquid and solid compositions ξ_l and ξ_s have been used. Consequently, the last expression in (2.151) does not vanish and the equilibrium profiles as well as the quantity a depend on the bulk chemical properties. As demonstrated in [55], this leads to a severe restriction concerning the value of δ. For the example of an $Al - 2mol\%Si$ alloy, it is shown that the diffuse interface width must be smaller than about $6nm$, which makes quantitative calculations with large values of δ in the spirit of the thin-interface analysis impossible.
In [56] and [57], Kim et al. present an alternative to get rid of this problem. Their idea is to regard the composition variable ξ as a superposition:

$$\xi = h(\varphi)\xi_l + (1 - h(\varphi))\xi_s \tag{2.154}$$

and to set $f_l = f_l(\xi_l)$ as well as $f_s = f_s(\xi_s)$. In analogy with (2.148), the state of thermodynamic equlibrium is then characterized by

$$2a\delta\frac{\partial^2\varphi}{\partial x^2} = \frac{\partial f(\varphi,\xi)}{\partial\varphi} + \frac{\partial f(\varphi,\xi)}{\partial\xi}\frac{\partial\xi}{\partial\varphi} \tag{2.155}$$

$$= \frac{a}{\delta}\frac{\partial}{\partial\varphi}\{\varphi^2(1-\varphi)^2\} + \frac{\partial h(\varphi)}{\partial\varphi}\{f_l(\xi_l) - f_s(\xi_s) + \frac{\partial f(\varphi,\xi)}{\partial\xi}(\xi_l - \xi_s)\} \tag{2.156}$$

$$= \frac{a}{\delta}\frac{\partial}{\partial\varphi}\{\varphi^2(1-\varphi)^2\} \tag{2.157}$$

and the bulk contributions vanish as in the case of an elemental material. It should be mentioned that this makes the computational effort larger because the quantities ξ_l and ξ_s must be determined from the state variables ξ and φ. This is realized by assuming that there is an instantaneous mass transport between locally coexisting phases, leading to a condition of equal chemical potentials μ_s and μ_l:

$$\mu_s = \frac{\partial f_s(\xi_s)}{\partial\xi_s} = \frac{\partial f_l(\xi_l)}{\partial\xi_l} = \mu_l. \tag{2.158}$$

With (2.154) and (2.158), ξ_l and ξ_s can be determined in principle. However, it is concluded in [56] that a complex numerical solution procedure is necessary in general.

2.2.5.2. Binary Alloys with a Limited Solid Solubility

The next step in phase-field modelling of binary alloys was the consideration of eutectic and peritectic binary alloys, which are characterized by a limited solubility of the two components A and B in the solid state. As there are two different solid phases α and β next to the liquid phase in these cases, it is necessary to introduce more than one phase-field. First attempts in this direction with two phase-fields were presented by Wheeler, McFadden and Boettinger ([58]) in 1996 and subsequently by Lo, Karma and Plapp ([59]). Later on, however, it became common practice to introduce three phase-field functions φ_1 (liquid phase), φ_2 (solid phase α) and φ_3 (solid phase β). It is clear that this necessitates

an extension of those parts of the free energy functional depending on the phase state, i.e. the surface free energy density $f_{surface}$ and the phase interpolation functions. In particular, two problems arise in such a multiphase-field formulation. The first one is that in the spirit of an interpretation of the phase-field φ_i as the volume fraction of phase i, we get the constraint

$$\varphi_1(\vec{x},t) + \varphi_2(\vec{x},t) + \varphi_3(\vec{x},t) = 1. \tag{2.159}$$

The second problem is that equilibrium interfaces between the two bulk phases k and i are in general not completely free of the third phase j and special measures are necessary to avoid the appearance of these so-called ghost phases.

Steinbach's Approach

In principle, there have been two approaches to capture these aspects ([60]). One of them has been proposed by Steinbach and Pezzolla in 1996 ([61]) as a general multiphase-field approach for an arbitrary number N of possible phases and has been coupled to composition transport by Tiaden ([62],[63]) and Kundin ([64]). Steinbach's idea is to decompose the free energy F of the system into a sum of pairwise contributions and to regard the rate of change for the phase-field φ_i as a consequence of pairwise phase interactions:

$$F = \sum_{i,k(i<k)}^{N} F_{ik} \tag{2.160}$$

$$\dot{\varphi}_i = \sum_{i,k(i<k)}^{N} \dot{q}_{ik}. \tag{2.161}$$

The pairwise interactions $\dot{q}_{ik}$ are connected with the pairwise free energies according to the following relaxation ansatz

$$\dot{q}_{ik} = -K_{ik}\frac{\delta F_{ik}}{\delta \varphi_i} \tag{2.162}$$

with a mobility constant K_{ik} for the phase boundary between phases i and k. Finally, the quantities F_{ik} are given by

$$F_{ik} = \int_V \{a_{ik}\delta(\varphi_k\vec{\nabla}\varphi_i - \varphi_i\vec{\nabla}\varphi_k)^2 + \frac{a_{ik}}{\delta}\varphi_i^2\varphi_k^2 + (\frac{1}{2}\varphi_i^3 + \frac{3}{2}\varphi_i^2\varphi_k - \frac{3}{2}\varphi_i\varphi_k^2 - \frac{1}{2}\varphi_k^3)(f_i - f_k)\}dV. \tag{2.163}$$

The above expression has been adapted to our notation, a single value of δ has been used in contrast to Steinbach's δ_{ik} and f_i denotes the free energy per volume of bulk phase i. The extension of the gradient part

$$a\delta(\vec{\nabla}\varphi)^2 \quad \rightarrow \quad a_{ik}\delta(\varphi_k\vec{\nabla}\varphi_i - \varphi_i\vec{\nabla}\varphi_k)^2 \tag{2.164}$$

is according to Steinbach a result of symmetry considerations and the theory of irreducible representations. It is easiliy seen that we get back the original expression for single phase-fields by setting $a_{ik} = a$, $\varphi_i = \varphi$ and $\varphi_k = 1 - \varphi$. The symmetric double well extension to a multiwell is straightforward

$$\frac{a}{\delta}\varphi^2(1-\varphi)^2 \quad \rightarrow \quad \frac{a_{ik}}{\delta}\varphi_i^2\varphi_k^2 \tag{2.165}$$

and gives back the original, single phase-field choice using the same replacements as in the gradient term. The interpolation functions

$$\frac{1}{2}\varphi_i^3 + \frac{3}{2}\varphi_i^2\varphi_k - \frac{3}{2}\varphi_i\varphi_k^2 - \frac{1}{2}\varphi_k^3 \tag{2.166}$$

reduce to $3\varphi^2 - 2\varphi^3 - \frac{1}{2}$, which is shifted compared to the possible choice $3\varphi^2 - 2\varphi^3$ for a single phase-field.
It is clear that multiple phase interactions and triple point as well as higher order point energies are neglected from the very beginning in this approach. A further approximation deals with the constraint (2.159). In the evaluation of (2.162), the following relations are used:

$$\frac{\partial \varphi_k}{\partial \varphi_i} = \frac{\partial}{\partial \varphi_i}(1 - \varphi_i - \varphi_j) \approx -1 \tag{2.167}$$

$$\frac{\partial \vec{\nabla} \varphi_k}{\partial \vec{\nabla} \varphi_i} \approx -1. \tag{2.168}$$

Using (2.161), (2.162), (2.163), (2.167) and (2.168), the resulting governing equation for φ_i is given by

$$\dot{\varphi}_i = \sum_{k=1(k\neq i)}^{N} K_{ik}\{2a_{ik}\delta(\varphi_k \vec{\nabla}^2 \varphi_i - \varphi_i \vec{\nabla}^2 \varphi_k) - \frac{2a_{ik}}{\delta}\varphi_i\varphi_k(\varphi_k - \varphi_i) + 6\varphi_i\varphi_k(f_i - f_k)\}. \tag{2.169}$$

At a binary interface with $\varphi_i = \varphi$ and $\varphi_k = 1 - \varphi$, it reduces to our standard equation (2.61) with $h(\varphi) = 3\varphi^2 - 2\varphi^3$. The presented model respects the constraint (2.159) and avoids the presence of ghost phases.
However, Garcke ([65]) showed that interfacial stresses are not conserved at multi-junctions due to the approximations (2.167) and (2.168). Therefore, Steinbach and Pezzolla proposed a revised version ([66]) of their multiphase approach in 1999 in which the problematic approximations are not necessary anymore and which was utilized by Kim, Kim and Suzuki ([67]) as well as Eiken ([68]) in their phase-field models. The main idea is to introduce interface fields

$$\psi_{ik} = \varphi_i - \varphi_k \tag{2.170}$$

for all possible pairs of phase-fields. The inverse transformation is given by

$$\varphi_i = \frac{1}{n}\{\sum_{k=1(k\neq i)}^{N}(s_i s_k \psi_{ik}) + 1\} \tag{2.171}$$

with the number of locally coexisting phases n and

$$s_i = \begin{cases} 1, & \text{if} \quad \varphi_i > 0 \\ 0, & \text{if} \quad \varphi_i = 0. \end{cases} \tag{2.172}$$

This leads to

$$\frac{\partial \varphi_i}{\partial t} = \frac{1}{n}\sum_{k=1(k\neq i)}^{N}\{s_i s_k \frac{\partial \psi_{ik}}{\partial t}\} \tag{2.173}$$

and for the temporal derivative of the interface fields, they assume

$$\frac{\psi_{ik}}{\partial t} = \frac{\partial \varphi_i}{\partial t} - \frac{\partial \varphi_k}{\partial t} = -K_{ik}(\frac{\delta F}{\delta \varphi_i} - \frac{\delta F}{\delta \varphi_k}). \tag{2.174}$$

Steinbach and Pezzolla demonstrate that the phase-fields can be treated as independent variables in (2.174) and that the interface fields ψ_{ik} can be regarded as generalized coordinates making sure that the constraint (2.159) is respected automatically due to the differences appearing in (2.174). Another new aspect in [66] is that the quite complicated gradient expression was simplified

$$a_{ik}\delta(\varphi_k \vec{\nabla}\varphi_i - \varphi_i \vec{\nabla}\varphi_k)^2 \quad \rightarrow \quad -a_{ik}\delta \vec{\nabla}\varphi_i \cdot \vec{\nabla}\varphi_k. \tag{2.175}$$

Despite the elegant treatment of the constraint (2.159) and the convenient decomposition into pairwise interactions, there remain problems. In particular, the governing equation (2.173) has a singular nature due to the functions s_i and s_k. A consequence of this is that a phase i which is not present at the beginning of a simulation can never be formed because of $s_i = 0$ in the whole domain and therefore $\frac{\partial \varphi_i}{\partial t} = 0$.

Lagrangian Multiplier Approach

The second kind of dealing with multiple phase-fields utilizes the technique of lagrangian multipliers to capture the constraint (2.159). The free energy functional for isothermal conditions is then expressed as

$$F = \int_V \{f_{surface} + f_{bulk} + \Lambda_l \cdot (\varphi_1 + \varphi_2 + \varphi_3 - 1)\} dV \tag{2.176}$$

with the lagrangian multiplier Λ_l. If Λ_l is chosen appropriately, the phase-fields φ_i can be treated as independent variables like in Steinbach's method of interface fields. Assuming a phase-field dependent mobility parameter $K(\varphi_1, \varphi_2, \varphi_3)$ to distinguish between different kinds of interfaces and adopting the well-known evolution equations

$$\frac{\partial \varphi_i}{\partial t} = -K(\varphi_1, \varphi_2, \varphi_3) \frac{\delta F}{\delta \varphi_i}, \tag{2.177}$$

the appropriate choice for Λ_l is characterized by the requirement:

$$\begin{aligned}
\frac{\partial}{\partial t}(\varphi_1 + \varphi_2 + \varphi_3) &= 0 \\
\leftrightarrow -K(\varphi_1, \varphi_2, \varphi_3)\{\frac{\delta F}{\delta \varphi_1} + \frac{\delta F}{\delta \varphi_2} + \frac{\delta F}{\delta \varphi_3}\} &= 0 \\
\leftrightarrow (\frac{\delta}{\delta \varphi_1} + \frac{\delta}{\delta \varphi_2} + \frac{\delta}{\delta \varphi_3}) \int_V \{f_{surface} + f_{bulk}\} dV + 3\Lambda_l &= 0 \\
-\frac{1}{3}(\frac{\delta}{\delta \varphi_1} + \frac{\delta}{\delta \varphi_2} + \frac{\delta}{\delta \varphi_3}) \int_V \{f_{surface} + f_{bulk}\} dV &= \Lambda_l.
\end{aligned} \tag{2.178}$$

In the Lagrangian multiplier approach, there are again two branches which differ in the question about how to avoid the presence of ghost phases at binary equilibrium interfaces. Ghost phases have not been a topic in Steinbach's models as the strictly pairwise decomposition of phase interactions suppresses them automatically.
The first branch is represented by works of Folch and Plapp ([69],[70],[71],[72]), who regard free energy as a smooth landscape above the Gibbs simplex. The latter is presented in Figure 2.6 and denotes an equilateral triangle in $(\varphi_1, \varphi_2, \varphi_3)$-space to which the triple $(\varphi_1, \varphi_2, \varphi_3)$ is constrained due to (2.159). In the spirit of the second law of thermodynamics, the dynamics of $(\varphi_1, \varphi_2, \varphi_3)$ tends to the valleys of this landscape to reduce the free energy of the system. In particular, the free energy functional of Folch and Plapp is especially designed to preserve the tangens hyperbolicus equilibrium profiles and to create minimum values of free energy in the corners of the Gibbs simplex corresponding to the bulk phases as well as free energy valleys along the sides corresponding to binary interfaces. Due to the latter aspect, phase j stays stably at zero at an $i - k$ interface because any perturbation to $\varphi_j > 0$ is linked with a free energy increase. Additionally, the preservation of the tangens hyperbolicus equlibrium profiles is important for the thin-interface analysis because analytical calculations are difficult to perform for an arbitrary sigmoid shape.

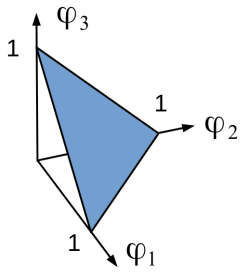

Figure 2.6.: Gibbs simplex for three phase-fields

The expressions proposed by Folch and Plapp are in our notation

$$f_{surface} = a\delta \sum_{i=1}^{3} (\vec{\nabla}\varphi_i)^2 + \frac{a}{\delta} \sum_{i=1}^{3} \varphi_i^2 (1-\varphi_i)^2 \tag{2.179}$$

$$f_{bulk} = X\{\frac{1}{2}[\xi - \sum_{i=1}^{3} h_i A_i(T)]^2 + \sum_{i=1}^{3} h_i B_i(T)\} \tag{2.180}$$

$$h_i = \frac{1}{4}\varphi_i^2\{15(1-\varphi_i)[1+\varphi_i-(\varphi_k-\varphi_j)^2] + \varphi_i(9\varphi_i^2-5)\}. \tag{2.181}$$

The quantity X in f_{bulk} denotes a thermodynamic constant with a unit of energy per volume ([70]) and the functions $A_i(T)$ and $B_i(T)$ represent scaled equilibrium compositions and scaled equilibrium free energies of phase i ([72]), which can be adapted to represent a specific binary alloy phase diagram with two solidus and liquidus lines. The special choices for f_{bulk} and the interpolation functions h_i guarantee a decoupling of the equilibrium profiles from bulk properties. A drawback of this model is that it can only represent a single value of surface tension for all three possible phase interfaces because there is only a single constant a. Further drawbacks of the model are that locally coexisting phases are assumed to have equal compositions and that $\frac{\partial^2 f_{bulk}}{\partial \xi^2} = 1$ independently of the phase being considered. The latter results in a constraint on the ratio of capillary lengths of the two solid-liquid interfaces. In general, this constraint is not fulfilled for an arbitrary material ([70]).
The second branch of Lagrangian multiplier methods consists of models proposed in publications by Garcke, Nestler and others ([73],[74],[75],[76],[77],[78],[79]) which are capable to represent different surface tension values. For a system with N phases, they use the gradient expression

$$\sum_{i,k(i<k)}^{N} a_{ik}\delta(\varphi_k\vec{\nabla}\varphi_i - \varphi_i\vec{\nabla}\varphi_k)^2 \tag{2.182}$$

like Steinbach and a straightforward extension of the symmetric double well

$$\sum_{i,k(i<k)}^{N} \frac{a_{ik}}{\delta}\varphi_i^2\varphi_k^2. \tag{2.183}$$

Ghost phases are avoided by adding a higher order term like

$$\sum_{i,j,k(i<j<k)}^{N} \frac{a_{ijk}}{\delta}\varphi_i^2\varphi_j^2\varphi_k^2. \tag{2.184}$$

In the case of a binary eutectic alloy, the purpose of this higher order additive is to keep the triple $(\varphi_1, \varphi_2, \varphi_3)$ close to the purely binary edges of the Gibbs simplex by increasing free

energy inside without influencing the side lines. The larger the coefficient a_{123} is, the more closely does $(\varphi_1, \varphi_2, \varphi_3)$ stay on a given edge. However, the values of the coefficients a_{ijk} cannot be determined unambiguously and stay a source of uncertainty as they influence the results. Additionally, although (2.184) gives no contribution to the governing equations at purely binary interfaces, the tangens hyperbolicus profile is lost due to additional terms arising from the lagrangian multiplier Λ_l. Consequently, a thin-interface analysis may become difficult here. Variants of this approach replace (2.184) by

$$\sum_{i,k(i<k)}^{N} \frac{a_{ik}}{\delta}\varphi_i^2\varphi_k^2(\sum_{j\neq(i,k)}^{N} a_j\varphi_j) \tag{2.185}$$

([76]) or use the double obstacle potential

$$\sum_{i,k(i<k)}^{N} \frac{a_{ik}}{\delta}\varphi_i\varphi_k \tag{2.186}$$

instead of the double well and utilize a higher order term

$$\sum_{i,j,k(i<j<k)}^{N} \frac{a_{ijk}}{\delta}\varphi_i\varphi_j\varphi_k \tag{2.187}$$

([78],[79]).
Haas developed in his dissertation in mathematics ([80]) a multiphase-field model with N phases using the surface free energy functional

$$F[\vec{\varphi}] = \int_V \{a(\vec{\varphi}, \vec{\nabla}\vec{\varphi})\delta + \frac{1}{\delta}w(\vec{\varphi})\}dV \tag{2.188}$$

with $\vec{\varphi} = (\varphi_1, ..., \varphi_N) = \sum_{i=1}^{N} \varphi_i\vec{e}_i$. The gradient constribution $a(\vec{\varphi}, \vec{\nabla}\vec{\varphi})$ shall be non-negative and positively homogeneous of degree two concerning $\vec{\nabla}\vec{\varphi}$ and $w(\vec{\varphi})$ is a non-negative polynomial vanishing for $\vec{\varphi} = \vec{e}_i$. In the limit $\delta \to 0$, (2.188) describes the surface free energy per unit area at an $i-j$ interface according to

$$\gamma_{ij}(\vec{n}) = \inf_{\vec{p}}\{2\int_{-1}^{1} \sqrt{w(\vec{p}(y))a(\vec{p}(y), \vec{p}\,'(y) \otimes \vec{n})}dy\}. \tag{2.189}$$

In (2.189), $\vec{n}$ is a unit normal vector representing a possible anisotropy, $\vec{p}$ ranges over all Lipschitz continuous functions $\vec{p} : [-1, 1] \to \Sigma$ connecting $\vec{e}_i$ and $\vec{e}_j$ and $\Sigma = \{\vec{\varphi} \in \mathbb{R}^N, \sum_{i=1}^{N} \varphi_i = 1\}$ denotes the Gibbs simplex. Haas constructs possible functions $a(\vec{\varphi}, \vec{\nabla}\vec{\varphi})$ and $w(\vec{\varphi})$ based on the conditions:

1. The minimizer of (2.189) has the form $\vec{p}(y) = h(y)\vec{e}_j + (1 - h(y))\vec{e}_i$.
2. (2.189) coincides with the physically measurable surface tension: $\gamma_{ij} = \sigma_{ij}$.

Assuming in particular that $w(\vec{\varphi})$ reduces to the classical double well along the edges of Σ, he finds

$$w(\vec{\varphi}) = \frac{1}{2}\sum_{i\neq j} a_{ij}\varphi_i^2\varphi_j^2 + \frac{1}{2}\sum_{\substack{i<j \\ i\neq j, i\neq k, j\neq k}} a_{ijk}\varphi_i\varphi_j\varphi_k^2 + \frac{1}{2}\sum_{i<j<k<l} a_{ijkl}\varphi_i\varphi_j\varphi_k\varphi_l \tag{2.190}$$

with $a_{ij} > 0$, $a_{ijkl} > 0$ and

$$a_{ijk} = a_{ik} + a_{jk} - a_{ij}. \tag{2.191}$$

He is able to express the coefficients a_{ij} in terms of the surface tension values σ_{ij} while definite values for the a_{ijkl} cannot be provided. One should note that for the special case $N = 3$, all coefficients are uniquely defined as the terms containing a_{ijkl} are zero then.

2.2.5.3. Binary Alloys and Thin-Interface Analysis

In binary alloy solidification problems, the sharp interface description is given by ([70])

$$\frac{\partial \xi}{\partial t} = D_{l/s} \vec{\nabla}^2 \xi \tag{2.192}$$

$$u_n(\xi_{I,l} - \xi_{I,s}) = \vec{n} \cdot (D_s \vec{\nabla} \xi|_s - D_l \vec{\nabla} \xi|_l) \tag{2.193}$$

$$T_I = T_e + m_l(\xi_{I,l} - \xi_e) - \frac{\sigma T_e}{\rho L} \kappa - \beta_k u_n. \tag{2.194}$$

In the above expressions, the indices l and s indicate the liquid and the solid phase, $\vec{n}$ is the unit normal vector pointing to the liquid, u_n is the normal interface velocity, $D_{l/s}$ stands for the diffusion coefficient in the liquid/solid and $\xi_{I,l}$ as well as $\xi_{I,s}$ represent the composition at the liquid and the solid side of the sharp interface. A comparison with (2.43) from the elemental material sharp interface model reveals that there is now an additional term $m_l(\xi_{I,l} - \xi_e)$ in the expression for the interface temperature T_I with m_l and ξ_e denoting the slope of the liquidus line and the eutectic composition. Because the thermal diffusivity is usually much larger than mass diffusivity $D_{l/s}$, temperature is assumed to be constant and the coupling of the phase change process with the composition field dominates. A special difficulty arising in a thin-interface analysis of a binary alloy phase-field model is that the solid diffusion coefficient D_s is orders of magnitude smaller than the liquid diffusion coefficient D_l whereas Karma and Rappel assumed a phase-independent thermal diffusivity in their original analysis for elemental materials. This asymmetry in the case of binary alloys leads to a number of anomalous terms in the first order equations which caused problems at the beginning. In the meantime, these problems are resolved and the thin-interface analysis technique is also available for binary alloys. For the case of completely soluble binary alloys with only a single phase-field, Karma covered the special case $D_s = 0$ ([81]) and Ohno and Matsuura the more general $D_l >> D_s > 0$ for a dilute alloy ([82]). Concerning multiphase-field models for binary eutectic or peritectic alloys, the approach by Plapp considered before ([70]) is directly equivalent to the original work by Karma and Rappel for elemental materials in the case $D_s = D_l$. However, the authors of [70] do also present a thin-interface analysis for the one-sided case $D_s = 0$. Again, Ohno and Matsuura proposed a procedure for a multiphase-field model with $D_s > 0$ ([83]).

2.2.5.4. Binary Alloys and Convection

The model by Beckermann presented before ([49]) has been used in the literature to describe convective solidification of dilute binary alloys with a single solid phase ([84],[85]). However, no simulations based on a direct extension of Anderson's approach ([51]) to multiple phase-fields with a thermodynamically consistent coupling of phase change with the Navier-Stokes equations as well as transport equations for temperature and composition have been found in the literature. Under isothermal conditions, Nestler and Wheeler treated the case of monotectic solidification with one solid phase and two possible liquid phases ([86]) while fluid flow in a melting porous medium has been simulated by Nestler and others ([87]) based on a coupling of the phase-field and lattice Boltzmann methods.

2.3. Conclusions

In section 2.1, three different modelling approaches for melt pool heat transfer were discussed in an order of rising complexity.
The effective convectivity model by Tran and Dinh is based on correlation-based characteristic velocities and is therefore the least expensive of the three approaches as the Navier-Stokes equations do not have to be solved. Consequently, its applicability is restricted and it can provide only a coarse description without any informations about the

flow field. The latter, however, may have a significant influence on the melt pool heat transfer. In contrast to that, the models of Voller and Bennon describe the flow field in an appropriate manner based on the Navier-Stokes equations. Both methods differ in the treatment of the melt composition, which is assumed to be constant in Voller's approach while it is treated by Bennon as a transport quantity on an equal footing with temperature. Due to the fact that composition inhomogenities influence the local liquidus temperature and therefore the mushy layer thickness, *composition transport will be considered along with heat and momentum transport in the new model developed in this thesis.*
A weak point in all three discussed models is the treatment of phase change. It is captured by calculating the liquid volume fraction as an instantaneous function of either temperature alone or as a function of temperature and composition in the case of Bennon's model. However, the process of phase change commonly follows its own dynamics without instantaneously adapting to any sudden change in the temperature or composition fields. Additionally, its coupling with momentum, heat and composition transport does not assure thermodynamic consistency in the three approaches. *The most important idea of this thesis is to provide an improvement in the modelling of solid-liquid phase change on macroscopic length scales by utilizing the phase-field method and by coupling it with the Navier-Stokes equations as well as the transport equations for heat and composition in a thermodynamically consistent manner.*

The phase-field method originates in attempts to regularize the problem of a moving sharp phase boundary by introducing smooth phase indicator functions. Due to the latter, a certain diffusivity of phase interfaces is inherent in the method and makes it particularly suitable to describe mushy layer solidification. The phase-field method provides independent governing equations for the phase change process and has the capability to correctly reproduce its microscopic details. In section 2.2, the development of the phase-field approach has been reviewed on the basis of an exemplary model.
It has been demonstrated how the sharp interface problem may be regularized, which is necessary to describe phase change by an additional partial differential equation, and under what conditions the regularized problem with a finite interface thickness describes the original sharp interface problem. In particular, a parameter δ exists which governs the diffuse interface width and which has to be smaller than the characteristic length of the dominating diffusion field to reproduce sharp interface dynamics.
Concerning the aspect of a thermodynamically consistent coupling, Anderson et al. ([51]) provide a satisfactory approach for the case of elemental material phase change with just a single phase indicator function. The only problematic aspect has been that the transition from free energy to an entropy functional introduced a non-constant coefficient into the gradient term. *The model developed in this thesis will circumvent the problem of the non-constant prefactor in the gradient term by a modification in the definition of free energy.*
Additionally, the problem under consideration in this thesis necessitates the introduction of more than only one phase indicator function as binary eutectic alloys possess a liquid phase l along with two solid phases α and β. *The new model will generalize the ideas of Anderson to a multiphase setup in order to achieve a thermodynamically consistent coupling between the three phase-field equations, the Navier-Stokes equations and the transport equations for heat and additionally composition.*
The introduction of multiple phase-fields leads to two new difficulties:

- The phase indicator functions of the possible phases must sum up to one at any point and at any time.

- The appearance of ghost phases j at equilibrium interfaces between phases i and k has to be avoided.

Steinbach ([66]) resolves both problems by the introduction of interface fields. However, this approach leads to governing equations with a singular nature. In particular, the formation of phases not being present at the beginning of a simulation is not possible. In order to avoid these drawbacks and as we would like the phase-field dynamics to be based on a smooth free energy landscape, *the method of lagrangian multipliers discussed in paragraph 2.2.5.2 will be used in this thesis to guarantee that the phase indicator functions add up to one.*
Using lagrangian multipliers, Folch and Plapp ([70]) avoid ghost phases by constructing a fine-tuned free energy functional. It makes binary mixture states energetically favourable in comparison with three-phase mixtures and at the same time, it preserves the tangens hyperbolicus profiles from simple phase-field models. However, their model can only represent a single value of surface tension for all three possible phase interfaces. Other approaches do not try a fine-tuning of free energy, but simply add higher order terms containing products of all three phase-fields in order to increase the free energy of three-phase mixtures. These approaches can represent different surface tension values, but the coefficients of the higher order terms can in general not be determined unambiguously and the tangens hyperbolicus equilibrium profiles are destroyed. The work of Haas ([80]) is worthy of special mention as it provides a definite expression for the higher order coefficients in the case of $N = 3$ phases. However, it is developed on a very abstract mathematical level without giving much attention to applicability. In order to stay in touch with engineering practice, *the expression for $f_{surface}$ derived in this work is based on the ideas by Folch and Plapp of a fine-tuned free energy functional. The objective is to make the representation of different surface tension values possible by constructing higher order additions to free energy with uniquely defined coefficients. These additions shall be especially designed to avoid ghost phases and at the same time to preserve the tangens hyperbolicus equilibrium profiles.*
Concerning the modelling of f_{bulk}, the main drawback of the approach by Folch and Plapp is the assumption of locally coexisting phases having equal compositions. *The new model for f_{bulk} is based on the expression proposed by Kim et al. in [67] for dilute alloys under isothermal conditions and generalizes it to non-isothermal and non-dilute setups. In particular, individual composition values are assigned to locally coexisting phases as introduced by Kim et al. in [56] and [57]. In contrast to the speculation made in [56], the individual phase compositions can be determined in an analytical manner in our case and a numerical solution procedure is not necessary.*
The last aspect deals with the diffuse interface width being governed by the parameter δ. So far, the phase-field method has been applied exclusively on length scales of about $10-100$ micrometers being characteristic of the solidification microstructure. The purpose of these applications has been the reproduction of sharp phase boundary dynamics without explicit interface tracking. In this context, δ is usually regarded as a free numerical input parameter which has to be chosen small enough as discussed above. *In the current thesis, the phase-field method is used for the first time also in a volume-averaged setup with the transition regions of the phase-fields corresponding to physically real mushy layers. As the mushy layer width is not a constant, a mechanism is proposed to calculate the diffuse interface width parameter dynamically in space and time.*

3. Model Development

3.1. Free Energy Functional for Isothermal Binary Eutectic Alloys

As the new model shall be capable to describe binary eutectic alloys, I adopt a multiphase-field approach with three phase-fields φ_1 (liquid phase), φ_2 (solid phase α) and φ_3 (solid phase β) for the three possible phases. Tying in with the discussion in paragraph 2.2.5.2 and the conclusions drawn in section 2.3, the constraint

$$\varphi_1(\vec{x},t) + \varphi_2(\vec{x},t) + \varphi_3(\vec{x},t) = 1 \tag{3.1}$$

is handeled by a lagrangian multiplier approach. In accordance with common practice in the literature, the free energy functional is expressed as

$$F[\varphi_1,\varphi_2,\varphi_3,\xi] = \int_V \{f_{surface} + f_{bulk} + \Lambda_L \cdot T \cdot (\varphi_1+\varphi_2+\varphi_3-1)\}dV \tag{3.2}$$

with a surface free energy density $f_{surface}$, a bulk free energy density f_{bulk} and a lagrangian multiplier Λ_L (compare (2.176)). It has been discussed before that a thermodynamically consistent coupling of phase change with momentum, heat and composition transport requires a transition to an entropy functional $S = -\frac{dF}{dT}$. As the constraint (3.1) must also be satisfied if the problem is expressed in terms of entropy, the so far constant factor T has been introduced into the lagrangian multiplier term. The lagrangian contribution would not appear in the corresponding entropy functional otherwise.
In accordance with the literature, Λ_L is determined by the condition (compare (2.178))

$$\begin{aligned} &\frac{\delta F}{\delta\varphi_1} + \frac{\delta F}{\delta\varphi_2} + \frac{\delta F}{\delta\varphi_3} = 0 \\ &\qquad \leftrightarrow \Lambda_L = -\frac{1}{3T}\left(\frac{\delta}{\delta\varphi_1} + \frac{\delta}{\delta\varphi_2} + \frac{\delta}{\delta\varphi_3}\right)\int_V \{f_{surface} + f_{bulk}\}dV. \end{aligned} \tag{3.3}$$

3.1.1. Surface Part of Free Energy Density

For the considerations in this subsection, f_{bulk} is set to zero and the remaining free energy density of phase surfaces represents the action of surface tension. As discussed in section 2.3, the new model shall be based on the ideas by Folch and Plapp who propose the expression

$$f_{surface} = a\delta \sum_{i=1}^{3} (\vec{\nabla}\varphi_i)^2 + \frac{a}{\delta}\sum_{i=1}^{3}\varphi_i^2(1-\varphi_i)^2 \tag{3.4}$$

(compare paragraph 2.2.5.2 for more details). Our objective is to construct a multiphase-field expression $f_{surface}(\vec{\nabla}\varphi_1, \vec{\nabla}\varphi_2, \vec{\nabla}\varphi_3, \varphi_1, \varphi_2, \varphi_3)$ which in analogy to (3.4) preserves the tangens hyperbolicus profiles around binary equilibrium interfaces and which avoids the presence of ghost phases in the transition layers. This is justified because ghost phases are unphysical and the tangens hyperbolicus profiles are important for making a thin-interface analysis feasible.
Furthermore and in contrast to (3.4), the new expression for $f_{surface}$ shall be able to assign different values of surface tension to the three possible phase interfaces. Remembering that the coefficient a makes the connection with surface tension and refering to the multiphase-field models discussed in 2.2.5.2, we use the simplest possibility of generalization for this purpose:

$$a\delta \sum_i (\vec{\nabla}\varphi_i)^2 \quad \rightarrow \quad \sum_{i<j} -a_{ij}\delta \vec{\nabla}\varphi_i \cdot \vec{\nabla}\varphi_j \tag{3.5}$$

$$\frac{a}{\delta} \sum_i \varphi_i^2 (1-\varphi_i)^2 \quad \rightarrow \quad \sum_{i<j} \frac{a_{ij}}{\delta} \varphi_i^2 \varphi_j^2. \tag{3.6}$$

Note that the minus sign enters (3.5) because $\vec{\nabla}\varphi_j = -\vec{\nabla}\varphi_i$ at an i-j interface.
The literature review in paragraph 2.2.5.2 suggests that in order to represent different surface tension values and to avoid the presence of ghost phases at the same time, the addition of higher order terms containing products of all three phase-fields is necessary. However, these higher order terms destroy the tangens hyperbolicus equilibrium profiles in general. The objective is here to derive fine-tuned higher order terms for which the latter is not the case. Consequently, we make the following ansatz for $f_{surface}$:

$$\begin{aligned} f_{surface} = &- a_{12}T\delta\vec{\nabla}\varphi_1 \cdot \vec{\nabla}\varphi_2 - a_{13}T\delta\vec{\nabla}\varphi_1 \cdot \vec{\nabla}\varphi_3 - a_{23}T\delta\vec{\nabla}\varphi_2 \cdot \vec{\nabla}\varphi_3 \\ &+ \frac{a_{12}}{\delta}T\varphi_1^2\varphi_2^2 + \frac{a_{13}}{\delta}T\varphi_1^2\varphi_3^2 + \frac{a_{23}}{\delta}T\varphi_2^2\varphi_3^2 \\ &+ \varphi_1\varphi_2\varphi_3 T f_{123}(\varphi_1, \varphi_2, \varphi_3). \end{aligned} \tag{3.7}$$

The factor T has been included here to generate surface contributions with constant coefficients in the resulting entropy functional.
In the following, we will determine $f_{123}(\varphi_1, \varphi_2, \varphi_3)$ in such a manner that the equilibrium behaviour of the phase-fields around a sharp phase boundary between bulk phases k and i is given by

$$\varphi_i = \frac{1}{2} \cdot (1 + \tanh(\frac{x}{2\delta})) \quad , \quad \varphi_k = 1 - \varphi_i \quad , \quad \varphi_j = 0 \quad , \tag{3.8}$$

i.e. the tangens hyperbolicus profiles are preserved and ghost phases are avoided.
Figure 3.1 gives a graphical representation of the desired behaviour. Using the first and second variational derivatives, the necessary and sufficient conditions of thermodynamic equilibrium are given by ([70])

$$\frac{\delta F}{\delta \varphi_l} = 0 \quad \forall l \tag{3.9}$$

$$\frac{\delta^2 F}{\delta \varphi_l^2} > 0 \quad \forall l. \tag{3.10}$$

The required equilibrium profiles around an interface between solid phase α and the liquid phase are obtained from (3.8) by setting $i = 1, k = 2$ and $j = 3$. In particular, the tangens hyperbolicus profile and the relation $\varphi_2 = 1 - \varphi_1$ imply

$$\vec{\nabla}^2\varphi_1 = \frac{1}{\delta^2}\varphi_1\varphi_2(\varphi_2 - \varphi_1). \tag{3.11}$$

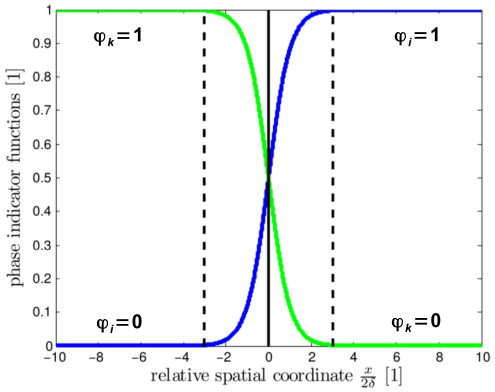

Figure 3.1.: Profile of phase-field functions around a sharp interface

Setting $l = 1$ in the necessary conditions (3.9) and utilizing (3.2) with $f_{bulk} = 0$, we get

$$\frac{\delta F}{\delta \varphi_1} = \frac{\delta}{\delta \varphi_1}\left(\int_V f_{surface} dV\right) + \Lambda_L T = 0. \tag{3.12}$$

Using (3.3) with $f_{bulk} = 0$ and (2.55) to evaluate the functional derivatives, (3.12) gives

$$\left(\frac{2}{3}\frac{\delta}{\delta \varphi_1} - \frac{1}{3}\frac{\delta}{\delta \varphi_2} - \frac{1}{3}\frac{\delta}{\delta \varphi_3}\right)\int_V f_{surface} dV = 0 \tag{3.13}$$

$$\leftrightarrow \frac{2}{3}\{-\vec{\nabla}\cdot\left(\frac{\partial f_{surface}}{\partial \vec{\nabla}\varphi_1}\right) + \frac{\partial f_{surface}}{\partial \varphi_1}\} - \frac{1}{3}\sum_{m=2}^{3}\{-\vec{\nabla}\cdot\left(\frac{\partial f_{surface}}{\partial \vec{\nabla}\varphi_m}\right) + \frac{\partial f_{surface}}{\partial \varphi_m}\} = 0. \tag{3.14}$$

With $f_{surface}$ from (3.7) and by making use of (3.11), this leads to

$$(\varphi_2 - \varphi_1)(-a_{12} - \frac{1}{3}a_{13} + \frac{1}{3}a_{23}) + \frac{4}{3}a_{12}\varphi_2 - \frac{2}{3}a_{12}\varphi_1 - \frac{\delta}{3}f_{123}(\varphi_1, \varphi_2, \varphi_3 = 0) = 0. \tag{3.15}$$

The condition $\frac{\delta F}{\delta \varphi_1} = 0$ and the resulting equation (3.15) are satisfied for

$$f_{123}(\varphi_1, \varphi_2, \varphi_3 = 0) = \frac{a_{12} + a_{13} - a_{23}}{\delta}\varphi_1 + \frac{a_{12} + a_{23} - a_{13}}{\delta}\varphi_2 \tag{3.16}$$

and it turns out that (3.16) is sufficient to satisfy the other two necessary conditions $\frac{\delta F}{\delta \varphi_2} = \frac{\delta F}{\delta \varphi_3} = 0$ as well.
Going through a similar procedure at an interface between the solid phase β and the liquid phase with $\varphi_2 = 0$, one can find

$$\frac{\delta F}{\delta \varphi_1} = 0 \leftrightarrow f_{123}(\varphi_1, \varphi_2 = 0, \varphi_3) = \frac{a_{12} + a_{13} - a_{23}}{\delta}\varphi_1 + \frac{a_{13} + a_{23} - a_{12}}{\delta}\varphi_3. \tag{3.17}$$

$\frac{\delta F}{\delta \varphi_2} = 0$ and $\frac{\delta F}{\delta \varphi_3} = 0$ are again fulfilled without delivering new informations.
Finally, consideration of an $\alpha - \beta$ interface leads to

$$f_{123}(\varphi_1 = 0, \varphi_2, \varphi_3) = \frac{a_{12} + a_{23} - a_{13}}{\delta}\varphi_2 + \frac{a_{13} + a_{23} - a_{12}}{\delta}\varphi_3. \tag{3.18}$$

Hence, a stationary behaviour is assured at all three binary interfaces by combining expressions (3.16), (3.17) and (3.18) to

$$f_{123}(\varphi_1, \varphi_2, \varphi_3) = \frac{a_{12} + a_{13} - a_{23}}{\delta}\varphi_1 + \frac{a_{12} + a_{23} - a_{13}}{\delta}\varphi_2 + \frac{a_{13} + a_{23} - a_{12}}{\delta}\varphi_3. \tag{3.19}$$

It is demonstrated now that the profiles (3.8) do really minimize free energy if f_{123} is chosen according to (3.19). According to [36] and due to

$$\frac{\partial^2 f_{surface}}{\partial\varphi_i \partial\vec{\nabla}\varphi_i} = \frac{\partial^2 f_{surface}}{(\partial\vec{\nabla}\varphi_i)^2} = 0, \tag{3.20}$$

the sufficient conditions (3.10) reduce in our case to

$$\frac{\delta^2 F}{\delta\varphi_l^2} = \frac{\partial^2 f_{surface}}{\partial\varphi_l^2} > 0 \quad \forall l. \tag{3.21}$$

Setting $l = 1$ and using expression (3.7) for $f_{surface}$ with f_{123} according to (3.19), we get

$$\frac{\delta^2 F}{\delta\varphi_1^2} = \frac{\partial^2 f_{surface}}{\partial\varphi_1^2} = \frac{2a_{12}}{\delta}T\varphi_2^2 + \frac{2a_{13}}{\delta}T\varphi_3^2 + 2\frac{a_{12}+a_{13}-a_{23}}{\delta}T\varphi_2\varphi_3. \tag{3.22}$$

At the three possible binary interfaces, (3.22) is given by:

$$\begin{aligned}
\left.\frac{\delta^2 F}{\delta\varphi_1^2}\right|_{\varphi_3=0} &= \frac{2a_{12}}{\delta}T\varphi_2^2 \\
\left.\frac{\delta^2 F}{\delta\varphi_1^2}\right|_{\varphi_2=0} &= \frac{2a_{13}}{\delta}T\varphi_3^2 \\
\left.\frac{\delta^2 F}{\delta\varphi_1^2}\right|_{\varphi_1=0} &= \varphi_2 T\{\frac{2a_{12}}{\delta}\varphi_2 + \frac{a_{12}+a_{13}-a_{23}}{\delta}\varphi_3\} \\
&\quad + \varphi_3 T\{\frac{2a_{13}}{\delta}\varphi_3 + \frac{a_{12}+a_{13}-a_{23}}{\delta}\varphi_2\} \\
&= \varphi_2 T\{\frac{a_{12}+a_{13}-a_{23}}{\delta} + \frac{a_{12}+a_{23}-a_{13}}{\delta}\varphi_2\} \\
&\quad + \varphi_3 T\{\frac{a_{12}+a_{13}-a_{23}}{\delta} + \frac{a_{13}+a_{23}-a_{12}}{\delta}\varphi_3\} \\
&= T\frac{a_{12}+a_{13}-a_{23}}{\delta} + T\varphi_2^2\frac{a_{12}+a_{23}-a_{13}}{\delta} + T\varphi_3^2\frac{a_{13}+a_{23}-a_{12}}{\delta}.
\end{aligned}$$

A similar set of relations can be obtained for the second variations with respect to φ_2 and φ_3 at the three binary interfaces. Altogether, the conditions

$$\begin{aligned}
a_{12} &> 0 \\
a_{13} &> 0 \\
a_{23} &> 0 \\
a_{12}+a_{13} &> a_{23} \\
a_{12}+a_{23} &> a_{13} \\
a_{13}+a_{23} &> a_{12}
\end{aligned} \tag{3.23}$$

are sufficient to assure that the profiles (3.8) minimize free energy if f_{123} is given by (3.19). Hence, an appropriate expression for $f_{surface}$ is given by

$$\begin{aligned}
f_{surface} &= -a_{12}T\delta\vec{\nabla}\varphi_1\cdot\vec{\nabla}\varphi_2 - a_{13}T\delta\vec{\nabla}\varphi_1\cdot\vec{\nabla}\varphi_3 - a_{23}T\delta\vec{\nabla}\varphi_2\cdot\vec{\nabla}\varphi_3 \\
&\quad + \frac{a_{12}}{\delta}T\varphi_1^2\varphi_2^2 + \frac{a_{13}}{\delta}T\varphi_1^2\varphi_3^2 + \frac{a_{23}}{\delta}T\varphi_2^2\varphi_3^2 \\
&\quad + \varphi_1\varphi_2\varphi_3 T\{\frac{a_{12}+a_{13}-a_{23}}{\delta}\varphi_1 + \frac{a_{12}-a_{13}+a_{23}}{\delta}\varphi_2 + \frac{a_{13}-a_{12}+a_{23}}{\delta}\varphi_3\}
\end{aligned} \tag{3.24}$$

with the constraints (3.23) for the numbers a_{ij}.
A comparison of our result for $f_{surface}$ with (2.190) and (2.191) on page 30 reveals that the higher order terms in (3.24) correspond to those proposed by Haas ([80]) for the case of $N = 3$ phases. We can conclude that at least for three phases, the conditions imposed by Haas (see page 30) must be equivalent to ours. While his first condition about the minimizer of (2.189) more or less obviously corresponds to our requirement of suppressing ghost phases, it is not obvious that his second condition $\gamma_{ij} = \sigma_{ij}$ is equivalent to the equilibrium profiles being given by the tangens hyperbolicus function.

3.1.2. Bulk Part of Free Energy Density

The next step is to find a model for the bulk free energy density. As discussed in section 2.3, we use the isothermal model for dilute binary alloys by Kim, Kim and Suzuki ([67]) as a basis. In particular, locally coexisting phases shall be assigned with individual composition values as discussed in paragraph 2.2.5.1 and proposed by Kim et al. also in earlier publications ([56],[57]).
In accordance with [67], we write

$$f_{bulk} = h_1 f_1(\xi_1, T) + h_2 f_2(\xi_2, T) + h_3 f_3(\xi_3, T) \tag{3.25}$$

$$\xi = h_1 \xi_1 + h_2 \xi_2 + h_3 \xi_3 \tag{3.26}$$

with individual phase compositions ξ_i and individual phase free energy densities $f_i(\xi_i, T)$. The functions h_i correspond to appropriate phase interpolation functions and will be determined later.

3.1.2.1. Individual Phase Free Energy Densities

At first, a description of the individual phase free energy densities is provided. As in [67], the individual phases are regarded as ideal solutions of components A and B

$$f_i(\xi_i, T) = \xi_i \mu_{B,i} + (1 - \xi_i)\mu_{A,i} \tag{3.27}$$

and the chemical potentials $\mu_{A,i}$ and $\mu_{B,i}$ of components A and B in phase i are written as

$$\mu_{A,i}(\xi_i, T) = \frac{RT}{v_m} \log(1 - \xi_i) + G_{A,i}(T) \tag{3.28}$$

$$\mu_{B,i}(\xi_i, T) = \frac{RT}{v_m} \log(\xi_i) \qquad + G_{B,i}(T). \tag{3.29}$$

The first summands in (3.28) and (3.29) arise from the entropy of mixture and the ideal gas constant R enters as an abbreviation $R = k_B N_A$ for the product of the Boltzmann constant k_B and Avogadro's number N_A while v_m represents the molar volume. *At this point, we exceed the model in [67] because the dilute solution approximation* $\log(1 - \xi_i) \approx -\xi_i$ *is not appropriate to be used for our purpose.*
We demonstrate now how the functions $G_{A,i}(T)$ and $G_{B,i}(T)$ can be adapted to represent a given binary eutectic alloy. *In order to obtain a suitable temperature dependence of entropy and internal energy in non-isothermal situations, the functions* $G_{A,i}(T)$ *and* $G_{B,i}(T)$ *cannot be chosen as in [67].*
If we take the eutectic temperature T_e as a reference temperature for the liquid state, proper expressions for the liquid entropy density and the liquid internal energy density will be given by

$$s_1 = -\frac{\partial f_1}{\partial T} \stackrel{!}{=} -\frac{R}{v_m}(\xi_1 \log(\xi_1) + (1 - \xi_1)\log(1 - \xi_1)) + \rho c \log(\frac{T}{T_e}) \tag{3.30}$$

$$e_1 = f_1 + T s_1 = f_1 - T\frac{\partial f_1}{\partial T} \stackrel{!}{=} \rho c(T - T_e). \tag{3.31}$$

An expression for the free energy per volume f_1 being consistent with (3.30) and (3.31) is

$$f_1 = \frac{RT}{v_m}(\xi_1 \log(\xi_1) + (1-\xi_1)\log(1-\xi_1)) - \rho c(T\log(\frac{T}{T_e}) - (T-T_e)), \tag{3.32}$$

which suggests

$$G_{A,1}(T) = G_{B,1}(T) = -\rho c(T\log(\frac{T}{T_e}) - (T-T_e)). \tag{3.33}$$

Note that in the isothermal model in [67], the authors set $G_{A,1}(T) = G_{B,1}(T) = 0$.
In analogy to [67], the next step is to regard a state of thermodynamic equilibrium between one of the two solid phases $j \in \{2,3\}$ and the liquid phase at a temperature $T \geq T_e$. In such a situation, the chemical potentials of components A and B in the involved phases must be equal

$$\mu_{A,1} = \mu_{A,j} \tag{3.34}$$
$$\mu_{B,1} = \mu_{B,j} \tag{3.35}$$

and the compositions of the liquid and the solid phase ξ_1 and ξ_j must correspond to their equilibrium values from the phase diagram:

$$\xi_1 = \xi_1^{(1j)}(T) \tag{3.36}$$
$$\xi_j = \xi_j^{(1j)}(T). \tag{3.37}$$

We denote here the composition of the liquid phase in equilibrium with the solid phase j at temperature T by $\xi_1^{(1j)}(T)$ and similarly, the composition of the solid phase j in equilibrium with the liquid phase at temperature T is named $\xi_j^{(1j)}(T)$. Therefore, the functions $\xi_1^{(1j)}(T)$ and $\xi_j^{(1j)}(T)$ correspond to the liquidus and solidus lines in the equilibrium phase diagram (see Figure 1.1).
For $T \geq T_e$ and $j \in \{2,3\}$, this leads to

$$G_{A,j}(T) = \frac{RT}{v_m}\log(\frac{1-\xi_1^{(1j)}(T)}{1-\xi_j^{(1j)}(T)}) - \rho c(T\log(\frac{T}{T_e}) - (T-T_e)) \tag{3.38}$$

$$G_{B,j}(T) = \frac{RT}{v_m}\log(\frac{\xi_1^{(1j)}(T)}{\xi_j^{(1j)}(T)}) \qquad - \rho c(T\log(\frac{T}{T_e}) - (T-T_e)). \tag{3.39}$$

However, we have to be aware that the liquidus and solidus lines end at the eutectic temperature, i.e.

$$\xi_1^{(1j)}(T < T_e) = \xi_1^{(1j)}(T_e) \tag{3.40}$$
$$\xi_j^{(1j)}(T < T_e) = \xi_j^{(1j)}(T_e). \tag{3.41}$$

Suppose we have a volume with a melt of non-eutectic composition which in a first step is cooled down to the eutectic temperature. When a uniform eutectic temperature distribution is approached from above, $T \to T_e^+$, the equilibrium state of the volume will be a mixture of the liquid phase and one of the two solid phases with $\xi_1 = \xi_1^{(1j)}(T_e)$ und $\xi_j = \xi_j^{(1j)}(T_e)$. If more heat is removed in a second step to reduce temperature below T_e, the liquid phase should disappear completely and the final state is expected to consist of a mixture of the two solid phases in general. However, due to (3.40) and (3.41), the chemical potential differences do not change in the second step of heat removal and equilibrium is

retained for arbitrary temperatures $T < T_e$:

$$\mu_{A,1} - \mu_{A,j} = \frac{RT}{v_m}[\log(1 - \xi_1^{(1j)}(T_e)) - \log(1 - \xi_j^{(1j)}(T_e)) - \log(\frac{1 - \xi_1^{(1j)}(T_e)}{1 - \xi_j^{(1j)}(T_e)})] = 0 \quad (3.42)$$

$$\mu_{B,1} - \mu_{B,j} = \frac{RT}{v_m}[\log(\xi_1^{(1j)}(T_e)) - \log(\xi_j^{(1j)}(T_e)) - \log(\frac{\xi_1^{(1j)}(T_e)}{\xi_j^{(1j)}(T_e)})] = 0. \quad (3.43)$$

Consequently, a complete solidification cannot be described for the above scenario with the model for f_{bulk} considered so far. In order to get rid of this problem, we lower the chemical potentials of components A and B in the solid phases α and β for $T < T_e$ proportional to the thermal undercooling $T - T_e$. We use the Heaviside step function

$$\Theta(x) = \begin{cases} 1, \text{falls x}\geq 0 \\ 0, \text{falls x}<0 \end{cases} \quad (3.44)$$

and add an expression

$$\Theta(T_e - T)L\rho\frac{T - T_e}{T_e}. \quad (3.45)$$

to $\mu_{A,j}$ und $\mu_{B,j}$ ($j \in \{2, 3\}$) with the latent heat per mass L. We assume the same value of L for both components in both solid phases because only a single value is usually provided in the literature. However, a generalization to individual latent heat values $L_{A,j}$ and $L_{B,j}$ is not a problem.
With this addition, we obtain for $j \in \{2, 3\}$

$$\begin{aligned} \mu_{A,j} = &\frac{RT}{v_m}\{\log(1 - \xi_j) + \log(\frac{1 - \xi_1^{(1j)}(T)}{1 - \xi_j^{(1j)}(T)})\} \\ &+ \Theta(T_e - T)L\rho\frac{T - T_e}{T_e} - \rho c(T\log(\frac{T}{T_e}) - (T - T_e)) \quad (3.46) \\ \mu_{B,j} = &\frac{RT}{v_m}\{\log(\xi_j) + \log(\frac{\xi_1^{(1j)}(T)}{\xi_j^{(1j)}(T)})\} \\ &+ \Theta(T_e - T)L\rho\frac{T - T_e}{T_e} - \rho c(T\log(\frac{T}{T_e}) - (T - T_e)). \quad (3.47) \end{aligned}$$

Consequently, we get at $T < T_e$, $\xi_1 = \xi_1^{(1j)}(T_e)$ and $\xi_j = \xi_j^{(1j)}(T_e)$ the chemical potential differences

$$\mu_{A,1} - \mu_{A,j} = \mu_{B,1} - \mu_{B,j} = L\rho\frac{T_e - T}{T_e} > 0, \quad (3.48)$$

which increase linearly with thermal undercooling similar to the behaviour of elemental materials and which permit a complete solidification. We summarize the final expressions for the individual phase free energy densities:

$$
\begin{aligned}
f_1(\xi_1,T) &= \frac{RT}{v_m}\{\xi_1\log(\xi_1)+(1-\xi_1)\log(1-\xi_1)\}-\rho c\{T\log(\frac{T}{T_e})-(T-T_e)\}\\
f_2(\xi_2,T) &= \frac{RT}{v_m}\{\xi_2\log(\xi_2)+(1-\xi_2)\log(1-\xi_2)\}-\rho c\{T\log(\frac{T}{T_e})-(T-T_e)\}\\
&\quad+\frac{RT}{v_m}\{\xi_2\log(\frac{\xi_1^{(12)}(T)}{\xi_2^{(12)}(T)})+(1-\xi_2)\log(\frac{1-\xi_1^{(12)}(T)}{1-\xi_2^{(12)}(T)})\}+\Theta(T_e-T)L\rho\frac{T-T_e}{T_e}\\
f_3(\xi_3,T) &= \frac{RT}{v_m}\{\xi_3\log(\xi_3)+(1-\xi_3)\log(1-\xi_3)\}-\rho c\{T\log(\frac{T}{T_e})-(T-T_e)\}\\
&\quad+\frac{RT}{v_m}\{\xi_3\log(\frac{\xi_1^{(13)}(T)}{\xi_3^{(13)}(T)})+(1-\xi_3)\log(\frac{1-\xi_1^{(13)}(T)}{1-\xi_3^{(13)}(T)})\}+\Theta(T_e-T)L\rho\frac{T-T_e}{T_e}
\end{aligned}
\tag{3.49}
$$

3.1.2.2. Determination of Individual Phase Compositions

In analogy with Kim et al. ([67]), we introduced individual phase compositions ξ_i in (3.25) and (3.26). It is important to note, however, that the ξ_i are merely auxiliary variables which have to be determined from the state variables $(\varphi_1,\varphi_2,\varphi_3,\xi,T)$. In this context, Kim et al. propose to assume an instantaneous mass transport between locally coexisting phases and therefore a local equality of the chemical potentials of the three phases:

$$\mu=\frac{\partial f_1(\xi_1,T)}{\partial\xi_1}=\frac{\partial f_2(\xi_2,T)}{\partial\xi_2}=\frac{\partial f_3(\xi_3,T)}{\partial\xi_3}. \tag{3.50}$$

The evaluation of (3.50) is simplified considerably in [67] because the model by Kim et al. is aimed at dilute binary alloys under isothermal conditions $T=T_e$. Introducing the partition coefficients $k_{12}(T)$ and $k_{13}(T)$ according to

$$\xi_2^{(12)}(T)=k_{12}(T)\xi_1^{(12)}(T) \tag{3.51}$$

$$\xi_3^{(13)}(T)=k_{13}(T)\xi_1^{(13)}(T), \tag{3.52}$$

condition (3.50) is evaluated in [67] approximately by setting

$$\xi_2=k_{12}(T_e)\xi_1 \tag{3.53}$$

$$\xi_3=k_{13}(T_e)\xi_1. \tag{3.54}$$

Putting this into (3.26), Kim et al. can calculate ξ_1 and afterwards ξ_2 and ξ_3 by (3.53) and (3.54). *For the general case of a non-dilute alloy, it is concluded in [56] that a complex numerical solution procedure including the Newton-Raphson method is necessary to determine the ξ_i.*
I will demonstrate in the following that for the non-dilute model regarded in this work, the individual phase compositions can be determined exactly in an analytical manner.
We note at first that

$$\frac{\partial f_i(\xi_i,T)}{\partial\xi_i}=\mu_{B,i}-\mu_{A,i}. \tag{3.55}$$

This leads to

$$\begin{aligned}
&\frac{\partial f_1(\xi_1,T)}{\partial \xi_1} = \frac{\partial f_2(\xi_2,T)}{\partial \xi_2} \\
\leftrightarrow &\frac{RT}{v_m}\log(\frac{\xi_1}{1-\xi_1}) + (G_{B,1}(T) - G_{A,1}(T)) = \frac{RT}{v_m}\log(\frac{\xi_2}{1-\xi_2}) + (G_{B,2}(T) - G_{A,2}(T)) \\
\leftrightarrow &\log(\frac{\xi_2}{1-\xi_2}) = \log(\frac{\xi_1}{1-\xi_1}) - \frac{v_m}{RT}(G_{B,2}(T) - G_{A,2}(T)) \\
\leftrightarrow &\frac{\xi_2}{1-\xi_2} = \frac{\xi_1}{1-\xi_1} e^{-\frac{v_m}{RT}(G_{B,2}(T)-G_{A,2}(T))} \\
&= \frac{\xi_1}{(1-\xi_1)Z_2} \\
\leftrightarrow &\xi_2 = \frac{\xi_1}{\xi_1 + (1-\xi_1)Z_2}
\end{aligned} \tag{3.56}$$

and analogously

$$\xi_3 = \frac{\xi_1}{\xi_1 + (1-\xi_1)Z_3} \tag{3.57}$$

with

$$Z_2 = \frac{\xi_1^{(12)}}{\xi_2^{(12)}} \frac{1-\xi_2^{(12)}}{1-\xi_1^{(12)}} \tag{3.58}$$

$$Z_3 = \frac{\xi_1^{(13)}}{\xi_3^{(13)}} \frac{1-\xi_3^{(13)}}{1-\xi_1^{(13)}}. \tag{3.59}$$

Using (3.26), (3.56) and (3.57), we get

$$\begin{aligned}
\xi &= h_1\xi_1 + h_2\xi_2 + h_3\xi_3 \\
&= h_1\xi_1 + h_2\frac{\xi_1}{\xi_1 + (1-\xi_1)Z_2} + h_3\frac{\xi_1}{\xi_1 + (1-\xi_1)Z_3}.
\end{aligned} \tag{3.60}$$

(3.60) can be rearranged to

$$\begin{aligned}
0 &= A\xi_1^3 + B\xi_1^2 + C\xi_1 + D \\
A &= h_1(1 - (Z_2 + Z_3) + Z_2Z_3 \\
B &= h_1(Z_2 + Z_3) - 2h_1Z_2Z_3 + h_2(1 - Z_3) + h_3(1 - Z_2) + \xi(Z_2 + Z_3 - Z_2Z_3 - 1) \\
C &= h_1Z_2Z_3 + h_2Z_3 + h_3Z_2 + \xi(2Z_2Z_3 - Z_2 - Z_3) \\
D &= -\xi Z_2Z_3.
\end{aligned} \tag{3.61}$$

with Z_2 and Z_3 from (3.58) and (3.59).
Equation (3.61) can be solved analytically by using Cardano's formula for cubic equations ([36]). Having obtained ξ_1, ξ_2 and ξ_3 can be calculated with (3.56) and (3.57) and no iterative numerical procedure is necessary.
Due to the dependence of the individual phase compositions on the state variables $V_i \in \{T, \xi, \Phi_1, \Phi_2, \Phi_3\}$, we henceforth express the derivative of a quantity X with respect to one of the state variables V_i according to

$$\frac{dX}{dV_i} = \frac{\partial X}{\partial V_i} + \sum_{k=1}^{3} \frac{\partial X}{\partial \xi_k}\frac{\partial \xi_k}{\partial V_i}. \tag{3.62}$$

3.1.2.3. Interpolation Functions

In (3.25) and (3.26), a consistent set of interpolation functions is needed. As the model by Kim et al. ([67]) is based on Steinbach's multiphase-field approach discussed in paragraph 2.2.5.2, they are able to use the simple choice $h_i = \varphi_i$ in their model. In contrast to that, the triple $(\varphi_1, \varphi_2, \varphi_3)$ moves in continuous free energy landscape in our case as we took the model by Folch and Plapp ([70]) as a basis for $f_{surface}$. This results in several conditions on the functions h_i which necessitate a more complicated choice. The requirements as well as the resulting set of interpolation functions are in accordance with [70], but they are repeated here for the sake of completeness.
According to (3.25), the function h_i shall shift the value of free energy at $\varphi_i = 1$, which is zero by means of $f_{surface}$, to the thermodynamically appropriate value $f_i(\xi_i, T)$ without influencing the other two bulk phases $\varphi_j = 1$ and $\varphi_k = 1$ as well as the $j-k$ interface between them:

$$h_i(\varphi_i = 1) = 1 \quad \wedge \quad h_i(\varphi_i = 0) = 0. \tag{3.63}$$

Additionally, we require for $\varphi_j = 0$ the relation:

$$h_i(\varphi_j = 0) + h_k(\varphi_j = 0) = 1. \tag{3.64}$$

As demonstrated later, this condition induces a connection between the quantities a_{ki} and surface tensions σ_{ki} independently from the equilibrium phase diagram and therefore independently from bulk chemical properties.
Finally, $f_{surface}$ has been constructed to be minimized by the profiles (3.8). As this property shall be maintained for $f_{bulk} \neq 0$, the functions h_i must be designed to make the contribution of f_{bulk} to the first variations in (3.9) vanish in a state of thermodynamic equilibrium provided that the phase-fields are given by (3.8). The above set of conditions is fulfilled by (see [70]):

$$h_i = \varphi_i^5 + 5\varphi_i^4(1-\varphi_i) + 10\varphi_i^3(1-\varphi_i)^2 + \frac{15}{4}\varphi_i^2(1-\varphi_i)^3 - \frac{15}{4}\varphi_i^2(1-\varphi_i)(\varphi_j - \varphi_k)^2. \tag{3.65}$$

(3.65) agrees with (2.181) and leads together with the introduction of individual phase compositions to a complete decoupling of surface effects described by $f_{surface}$ and bulk chemical properties described by f_{bulk}.

3.1.3. Determination of the Model Parameters a_{ki}

Using the recipe provided in [70], we can calculate now the surface tension of a flat $k-i$ equilibrium phase boundary at $T = T_e$ in the framework of the developed model. For a binary eutectic alloy, it is defined to be the surface excess of the grand potential per unit area. Introducing the grand potential per volume $\omega = f - \mu\xi$, we get

$$\begin{aligned} \sigma_{ki} &= \frac{1}{A}\int_V (\omega - \omega_{bulk})dV \\ &= \int_{-\infty}^{+\infty} (\omega - \omega_{bulk})dx. \end{aligned} \tag{3.66}$$

With the equilibrium compositions from the phase diagram $\xi_i = \xi_i^{(ik)}(T_e)$ and $\xi_k = \xi_k^{(ik)}(T_e)$, one obtains

$$\begin{aligned} \omega &= f - \mu\xi \\ &= f_{surface} + h_i f_i(\xi_i^{(ik)}(T_e), T_e) + h_k f_k(\xi_k^{(ik)}(T_e), T_e) - \mu\{h_i\xi_i^{(ik)}(T_e) + h_k\xi_k^{(ik)}(T_e)\} \\ &= f_{surface} + h_i\{f_i(\xi_i^{(ik)}(T_e), T_e) - \mu\xi_i^{(ik)}(T_e)\} + h_k\{f_k(\xi_k^{(ik)}(T_e), T_e) - \mu\xi_k^{(ik)}(T_e)\} \end{aligned} \tag{3.67}$$

as well as

$$\omega(\varphi_i = 1, \varphi_k = 0) = f_i(\xi_i^{(ik)}(T_e), T_e) - \mu\xi_i^{(ik)}(T_e) \tag{3.68}$$

$$\omega(\varphi_i = 0, \varphi_k = 1) = f_k(\xi_k^{(ik)}(T_e), T_e) - \mu\xi_k^{(ik)}(T_e). \tag{3.69}$$

Since a state of thermodynamic equilibrium is regarded, the free energies of the two phases $f_i(\xi_i^{(ik)}(T_e), T_e)$ and $f_k(\xi_k^{(ik)}(T_e), T_e)$ correspond to minimum values of the two free energy functions $f_i(\xi_i, T_e)$ and $f_k(\xi_k, T_e)$. It is well-known in thermodynamics that these minima share a common tangent ([70])

$$f_k(\xi_k^{(ik)}(T_e), T_e) = f_i(\xi_i^{(ik)}(T_e), T_e) + (\xi_k^{(ik)}(T_e) - \xi_i^{(ik)}(T_e))\mu,$$

leading to the relation

$$f_i(\xi_i^{(ik)}(T_e), T_e) - \mu\xi_i^{(ik)}(T_e) = f_k(\xi_k^{(ik)}(T_e), T_e) - \mu\xi_k^{(ik)}(T_e). \tag{3.70}$$

Using (3.70) in (3.68) and (3.69), one can see that the grand potential per volume adopts the same value on both sides of the phase boundary

$$\omega_{bulk} = \omega(\varphi_i = 1, \varphi_k = 0) = \omega(\varphi_i = 0, \varphi_k = 1) = f_i(\xi_i^{(ik)}(T_e), T_e) - \mu\xi_i^{(ik)}(T_e). \tag{3.71}$$

Replacing in (3.66) ω and ω_{bulk} by (3.67) and (3.71), utilizing (3.70) and property (3.64) of the interpolation functions and inserting the derived expression (3.24) for $f_{surface}$ as well as the equilibrium profile $\varphi_i = \frac{1}{2}(1 + \tanh(\frac{x}{2\delta}))$, surface tension is given by

$$\begin{aligned}
\sigma_{ki} &= \int_{-\infty}^{+\infty} \{f_{surface} + [f_i(\xi_i^{(ik)}(T_e), T_e) - \mu\xi_i^{(ik)}(T_e)](h_i + h_k - 1)\}dx \\
&= \int_{-\infty}^{+\infty} \{f_{surface}\}dx \\
&= \int_{-\infty}^{+\infty} \{a_{ki}T_e\delta(\vec{\nabla}\varphi_i)^2 + \frac{a_{ki}T_e}{\delta}\varphi_i^2(1-\varphi_i)^2\}dx \\
&= \frac{2a_{ki}T_e}{\delta}\int_{-\infty}^{+\infty} \{\varphi_i^2(1-\varphi_i)^2\}dx \\
&= 2a_{ki}T_e\int_0^1 \{\varphi_i(1-\varphi_i)\}d\varphi_i \\
&= \frac{a_{ki}T_e}{3} \\
\leftrightarrow a_{ki} &= \frac{3\sigma_{ki}}{T_e}.
\end{aligned} \tag{3.72}$$

3.1.4. Determination of the Lagrangian Multiplier Λ_L

Since the models for $f_{surface}$ and f_{bulk} are complete now, the lagrangian multiplier Λ_L from (3.3) can be calculated explicitly. Using (2.55) to calculate the variation of the surface free energy with respect to an arbitrary phase j, we get

$$\begin{aligned}
&\frac{1}{T}\frac{\delta}{\delta\varphi_j}\int_V f_{surface}dV \\
&= \frac{1}{T}\{-\vec{\nabla}\cdot(\frac{\partial f_{surface}}{\partial\vec{\nabla}\varphi_j}) + \frac{\partial f_{surface}}{\partial\varphi_j}\} \\
&= \vec{\nabla}\cdot(a_{ij}\delta\vec{\nabla}\varphi_i) + \vec{\nabla}\cdot(a_{kj}\delta\vec{\nabla}\varphi_k) + \frac{2a_{ij}}{\delta}\varphi_i^2\varphi_j + \frac{2a_{kj}}{\delta}\varphi_k^2\varphi_j \\
&+ \frac{a_{ij}+a_{ik}-a_{kj}}{\delta}\varphi_i^2\varphi_k + \frac{a_{kj}+a_{ik}-a_{ij}}{\delta}\varphi_k^2\varphi_i + 2\frac{a_{ij}+a_{kj}-a_{ik}}{\delta}\varphi_i\varphi_j\varphi_k
\end{aligned}$$

with $i \neq j \neq k$, $a_{ij}, a_{ik}, a_{kj} \in \{a_{12}, a_{13}, a_{23}\}$ and $a_{ij} = a_{ji}, a_{ik} = a_{ki}, a_{kj} = a_{jk}$.
Additionally, considering (3.62), the bulk part yields

$$\begin{aligned}\frac{1}{T}\frac{\delta}{\delta\varphi_j}\int_V f_{bulk}dV &= \frac{1}{T}\frac{d}{d\varphi_j}\sum_{k=1}^{3} h_k f_k \\ &= \frac{1}{T}\sum_{k=1}^{3}\{\frac{\partial h_k}{\partial\varphi_j}f_k + h_k\frac{\partial f_k}{\partial\xi_k}\frac{\partial\xi_k}{\partial\varphi_j}\}. \end{aligned} \tag{3.73}$$

Due to $\frac{\partial f_k}{\partial\xi_k} = \mu$ and (7.14), we get

$$\frac{1}{T}\frac{\delta}{\delta\varphi_j}\int_V f_{bulk}dV = \frac{1}{T}\sum_{k=1}^{3}\frac{\partial h_k}{\partial\varphi_j}(f_k - \mu\xi_k)$$

and finally, the lagrangian multiplier is given by

$$\begin{aligned}\Lambda_L =& -\frac{1}{3T}(\frac{\delta}{\delta\varphi_1} + \frac{\delta}{\delta\varphi_2} + \frac{\delta}{\delta\varphi_3})\int_V (f_{surface} + f_{bulk})dV \\ =& -\frac{1}{3}\sum_{j=1}^{3}\{\vec{\nabla}\cdot(a_{ij}\delta\vec{\nabla}\varphi_i) + \vec{\nabla}\cdot(a_{kj}\delta\vec{\nabla}\varphi_k) + \frac{2a_{ij}}{\delta}\varphi_i^2\varphi_j + \frac{2a_{kj}}{\delta}\varphi_k^2\varphi_j \\ &+ \frac{a_{ij}+a_{ik}-a_{kj}}{\delta}\varphi_i^2\varphi_k + \frac{a_{kj}+a_{ik}-a_{ij}}{\delta}\varphi_k^2\varphi_i + 2\frac{a_{ij}+a_{kj}-a_{ik}}{\delta}\varphi_i\varphi_j\varphi_k \\ &+ \frac{1}{T}\sum_{k=1}^{3}\frac{\partial h_k}{\partial\varphi_j}(f_k - \mu\xi_k)\}. \end{aligned} \tag{3.74}$$

3.2. Generalization to Macroscopic Length Scales

The phase state of a binary eutectic alloy can fluctuate between the possible bulk phases on a comparably small length scale of several micrometers. In the literature, the phase-field method has been exclusively applied on lengths being representative of the typical solidification microstructure. A generic volume of interest has a side length of about $10 - 100\mu m$ and the phase-fields are used to represent the detailed dynamics of sharp interfaces separating the bulk phases.
If one would like to use the phase-field method for modelling phase change in the context of IVR with characteristic lengths in the range of $1m$, it will not be possible to resolve the detailed phase structure as the necessary number of grid cells will become too large. Additionally, one may assume that the microscopic details are not so important for the overall large-scale behaviour.
From a macroscopic point of view, the mentioned phase state fluctuations are smeared out and appear as mixture states, which according to the phase diagram are purely binary in thermodynamic equilibrium. Examples are the mushy layers, which depending on composition represent a binary mixture of the liquid phase with one of the two solid phases, but also the composite solids as mixtures of the two solid phases α and β.
In this section, I will propose a new approach based on volume-averaging in order to generalize the derived free energy functional to macroscopic length scales. In this framework, the word 'macroscopic' shall be understood as 'being visible to the naked eye'. Furthermore, the generalization will be consistent in the sense that the original expression is recovered if the averaging volume goes to zero.

3.2.1. Free Energy Functional for Volume-Averaged Phase-Fields

In order to render an application of the phase-field method to macroscopic systems possible, we introduce volume-averaged phase-fields

$$\Phi_i(\vec{x},t) = \frac{1}{\Delta V} \int_{-\frac{L}{2}}^{+\frac{L}{2}} \int_{-\frac{L}{2}}^{+\frac{L}{2}} \int_{-\frac{L}{2}}^{+\frac{L}{2}} \varphi_i(\vec{x}+\vec{y},t) dy_1 dy_2 dy_3. \tag{3.75}$$

The integrand of (3.75) is given by the phase-field functions introduced in the last section as an exact description of the phase state. Except for the thin and smooth transition layers around sharp phase boundaries, the integrand of (3.75) therefore adopts a value of one in phase i and a value of zero otherwise. Consequently, the Φ_i correspond to real volume fractions and we get the same constraint as for the φ_i before:

$$\Phi_1(\vec{x},t) + \Phi_2(\vec{x},t) + \Phi_3(\vec{x},t) = 1. \tag{3.76}$$

Note that regions with $0 < \varphi_i < 1$ correspond to an artificial phase mixing generated by the modeling approach while $0 < \Phi_i < 1$ represents a physically real phase mixing.
The task is now to find a phenomenological description of free energy as a functional of the volume-averaged Φ_i instead of the φ_i. The phenomenology of the Φ_i can be read from the phase diagram (see e.g. Figure 1.1). Depending on composition and temperature, there are pure phases α, β and l as well as binary mixtures $\alpha + l$, $\beta + l$ and $\alpha + \beta$. At a given temperature, two bulk phases possessing different compositions are separated by a transition layer consisting of the corresponding binary mixture. The phenomenology is therefore the same as for the small φ_i with the difference that the transition layer width should be described by a dynamical quantity $\Delta(\vec{x},t)$ in the volume-averaged framework instead of the small constant δ needed for sharp interface approximation. This is because the width of macroscopic mixture states may in general vary in space and time.

Consequently, an expression for free energy as a functional of the Φ_i can be obtained from the functional derived in the last section by replacing

$$\varphi_i(\vec{x},t) \to \Phi_i(\vec{x},t) \tag{3.77}$$
$$\delta \to \Delta(\vec{x},t). \tag{3.78}$$

This leads to

$$\begin{aligned} F[\Phi_1,\Phi_2,\Phi_3,\Delta,\xi] &= \int_V \{f + \Lambda_L \cdot T \cdot (\Phi_1+\Phi_2+\Phi_3-1)\} dV \\ f &= f_{surface} + f_{bulk} \\ f_{surface} &= -a_{12}T\Delta\vec{\nabla}\Phi_1\cdot\vec{\nabla}\Phi_2 - a_{13}T\Delta\vec{\nabla}\Phi_1\cdot\vec{\nabla}\Phi_3 - a_{23}T\Delta\vec{\nabla}\Phi_2\cdot\vec{\nabla}\Phi_3 \\ &\quad + \frac{a_{12}}{\Delta}T\Phi_1^2\Phi_2^2 + \frac{a_{13}}{\Delta}T\Phi_1^2\Phi_3^2 + \frac{a_{23}}{\Delta}T\Phi_2^2\Phi_3^2 \\ &\quad + \Phi_1\Phi_2\Phi_3 T\{\frac{a_{12}+a_{13}-a_{23}}{\Delta}\Phi_1 + \frac{a_{12}-a_{13}+a_{23}}{\Delta}\Phi_2 \\ &\qquad + \frac{a_{13}-a_{12}+a_{23}}{\Delta}\Phi_3\} \\ f_{bulk} &= \sum_{i=1}^{3} h_i(\Phi_1,\Phi_2,\Phi_3) f_i(\xi_i,T). \end{aligned} \tag{3.79}$$

The lagrangian multiplier can obtained similarly by applying the replacements (3.77) and (3.78) in (3.74)

$$\begin{aligned} \Lambda_L = &-\frac{1}{3}\sum_{j=1}^{3}\{\vec{\nabla}\cdot(a_{ij}\Delta\vec{\nabla}\Phi_i) + \vec{\nabla}\cdot(a_{kj}\Delta\vec{\nabla}\Phi_k) + \frac{2a_{ij}}{\Delta}\Phi_i^2\Phi_j + \frac{2a_{kj}}{\Delta}\Phi_k^2\Phi_j \\ &+ \frac{a_{ij}+a_{ik}-a_{kj}}{\Delta}\Phi_i^2\Phi_k + \frac{a_{kj}+a_{ik}-a_{ij}}{\Delta}\Phi_k^2\Phi_i + 2\frac{a_{ij}+a_{kj}-a_{ik}}{\Delta}\Phi_i\Phi_j\Phi_k \\ &+ \frac{1}{T}\sum_{k=1}^{3}\frac{\partial h_k}{\partial\Phi_j}(f_k-\mu\xi_k)\} \end{aligned} \tag{3.80}$$

with $i \neq j \neq k$, $a_{ij}, a_{ik}, a_{kj} \in \{a_{12}, a_{13}, a_{23}\}$ and $a_{ij} = a_{ji}, a_{ik} = a_{ki}, a_{kj} = a_{jk}$.

3.2.2. Determination of the Dynamical Parameter $\Delta(\vec{x},t)$

In order to handle the additional degree of freedom $\Delta(\vec{x},t)$, we make use of the fact that we are interested in comparably slow solidification processes. It is therefore possible to assume that the spatial extent of the appearing mixture states is always close to the equilibrium value determined by the other state variables. In this regard, the field $\Delta(\vec{x},t)$ is determined at each point in time based on free energy minimization:

$$\frac{\delta F[\Phi_1,\Phi_2,\Phi_3,\Delta,\xi]}{\delta\Delta} = 0. \tag{3.81}$$

As only $f_{surface}$ depends on Δ and no gradients of Δ appear in it, (3.81) reduces to

$$\frac{\partial f_{surface}}{\partial\Delta} = 0. \tag{3.82}$$

Evaluating (3.82) by using $f_{surface}$ from (3.79) leads to

$$\Delta^2 = \frac{a_{12}\Phi_1^2\Phi_2^2 + a_{13}\Phi_1^2\Phi_3^2 + a_{23}\Phi_2^2\Phi_3^2}{-a_{12}\vec{\nabla}\Phi_1\cdot\vec{\nabla}\Phi_2 - a_{13}\vec{\nabla}\Phi_1\cdot\vec{\nabla}\Phi_3 - a_{23}\vec{\nabla}\Phi_2\cdot\vec{\nabla}\Phi_3} + \frac{\Phi_1\Phi_2\Phi_3\{(a_{12}+a_{13}-a_{23})\Phi_1 + (a_{12}+a_{23}-a_{13})\Phi_2 + (a_{13}+a_{23}-a_{12})\Phi_3\}}{-a_{12}\vec{\nabla}\Phi_1\cdot\vec{\nabla}\Phi_2 - a_{13}\vec{\nabla}\Phi_1\cdot\vec{\nabla}\Phi_3 - a_{23}\vec{\nabla}\Phi_2\cdot\vec{\nabla}\Phi_3}. \tag{3.83}$$

It is important to note that the second derivative of $f_{surface}$ with respect to Δ is always positive. Therefore, the above expression does indeed minimize free energy with respect to Δ. In the following subsections, the physical implications of the volume-averaged description and its consistency in the limit $\Delta V \to 0$ will be investigated.

3.2.3. Equilibrium States of Binary Mixtures

In this subsection, we will investigate the equilibrium states of the volume-averaged model based on (3.79), (3.80) and (3.83). As there is no domain $\alpha+\beta+l$ in the binary eutectic alloy phase diagram (see Figure 1.1), three-phase mixture states do not have to be considered. Note that temperature is still treated as a constant here like in section 3.1. The transition to non-isothermal conditions will be made in section 3.3.
Exemplarily, we regard a binary mixture layer of the liquid phase and solid phase α with $\Phi_3 = 0$. Due to the symmetry of model, the results can be translated to any other combination of two phases. Using (2.55), (3.50), (7.4) from appendix, (3.62) and the free energy model (3.79), the necessary conditions for an equilibrium state are given by

$$\begin{aligned}
\frac{\delta F}{\delta\Phi_1}\Big|_{\Phi_3=0} &= a_{12}T\vec{\nabla}\cdot(\Delta\vec{\nabla}\Phi_2) + \frac{2a_{12}}{\Delta}T\Phi_1\Phi_2^2 \\
&\quad + \sum_{i=1}^{3}\{\frac{\partial h_i}{\partial\Phi_1}\Big|_{\Phi_3=0}(f_i - \mu\xi_i)\} + \Lambda_L T = 0 && (3.84)\\
\frac{\delta F}{\delta\Phi_2}\Big|_{\Phi_3=0} &= a_{12}T\vec{\nabla}\cdot(\Delta\vec{\nabla}\Phi_1) + \frac{2a_{12}}{\Delta}T\Phi_2\Phi_1^2 \\
&\quad + \sum_{i=1}^{3}\{\frac{\partial h_i}{\partial\Phi_2}\Big|_{\Phi_3=0}(f_i - \mu\xi_i)\} + \Lambda_L T = 0 && (3.85)\\
\frac{\delta F}{\delta\Phi_3}\Big|_{\Phi_3=0} &= (a_{13}+a_{23})T\vec{\nabla}\cdot(\Delta\vec{\nabla}\Phi_1 + \Delta\vec{\nabla}\Phi_2) \\
&\quad + \Phi_1\Phi_2 T(\frac{a_{12}+a_{13}-a_{23}}{\Delta}\Phi_1 + \frac{a_{12}-a_{13}+a_{23}}{\Delta}\Phi_2) \\
&\quad + \sum_{i=1}^{3}\{\frac{\partial h_i}{\partial\Phi_3}\Big|_{\Phi_3=0}(f_i - \mu\xi_i)\} + \Lambda_L T = 0. && (3.86)
\end{aligned}$$

In the next step, we replace Λ_L by (3.80), insert the interpolation functions h_i from (3.65) and use $\Phi_2 = 1 - \Phi_1$ to obtain

$$\begin{aligned}
\frac{\delta F}{\delta\Phi_1}\Big|_{\Phi_3=0} &= -(a_{12} - \frac{1}{3}a_{23} + \frac{1}{3}a_{13})T\{\vec{\nabla}\cdot(\Delta\vec{\nabla}\Phi_1) - \frac{1}{\Delta}\Phi_1(1-\Phi_1)(1-2\Phi_1)\} \\
&\quad - 15\Phi_1^2(1-\Phi_1)^2\{f_2 - f_1 - \mu(\xi_2-\xi_1)\} = 0 && (3.87)\\
\frac{\delta F}{\delta\Phi_2}\Big|_{\Phi_3=0} &= (a_{12} + \frac{1}{3}a_{23} - \frac{1}{3}a_{13})T\{\vec{\nabla}\cdot(\Delta\vec{\nabla}\Phi_1) - \frac{1}{\Delta}\Phi_1(1-\Phi_1)(1-2\Phi_1)\} \\
&\quad + 15\Phi_1^2(1-\Phi_1)^2\{f_2 - f_1 - \mu(\xi_2-\xi_1)\} = 0 && (3.88)\\
\frac{\delta F}{\delta\Phi_3}\Big|_{\Phi_3=0} &= -\frac{2}{3}(a_{23}-a_{13})T\{\vec{\nabla}\cdot(\Delta\vec{\nabla}\Phi_1) - \frac{1}{\Delta}\Phi_1(1-\Phi_1)(1-2\Phi_1)\} = 0. && (3.89)
\end{aligned}$$

Setting $\Phi_3 = 0$ in (3.83), the expression for the dynamic Δ simplifies to

$$\Delta = \frac{\Phi_1(1-\Phi_1)}{|\vec{\nabla}\Phi_1|}. \tag{3.90}$$

Regarding (3.90), it is not clear how Δ behaves in the bulk phases with $\Phi_1 = 0$ or $\Phi_1 = 1$ because the numerator as well as the denominator become zero. However, this difficulty can be mitigated by explicitly replacing Δ in the equations. Inserting (3.90) into (3.87)-(3.89), utilizing

$$\vec{\nabla} \cdot \{\frac{\Phi_1(1-\Phi_1)}{|\vec{\nabla}\Phi_1|}\vec{\nabla}\Phi_1\} = \Phi_1(1-\Phi_1)\vec{\nabla} \cdot \frac{\vec{\nabla}\Phi_1}{|\vec{\nabla}\Phi_1|} + (1-2\Phi_1)|\vec{\nabla}\Phi_1| \tag{3.91}$$

and defining curvature κ according to

$$\kappa = \vec{\nabla} \cdot (\frac{\vec{\nabla}\Phi_1}{|\vec{\nabla}\Phi_1|}) = \vec{\nabla} \cdot \vec{n}, \tag{3.92}$$

we end up with the three equations

$$\begin{aligned}
\frac{\delta F}{\delta \Phi_1}\Big|_{\Phi_3=0} &= -(a_{12} - \frac{1}{3}a_{23} + \frac{1}{3}a_{13})T\Phi_1(1-\Phi_1)\kappa \\
&\quad - 15\Phi_1^2(1-\Phi_1)^2\{f_2 - f_1 - \mu(\xi_2 - \xi_1)\} = 0 && (3.93)\\
\frac{\delta F}{\delta \Phi_2}\Big|_{\Phi_3=0} &= \quad (a_{12} + \frac{1}{3}a_{23} - \frac{1}{3}a_{13})T\Phi_1(1-\Phi_1)\kappa \\
&\quad + 15\Phi_1^2(1-\Phi_1)^2\{f_2 - f_1 - \mu(\xi_2 - \xi_1)\} = 0 && (3.94)\\
\frac{\delta F}{\delta \Phi_3}\Big|_{\Phi_3=0} &= -\frac{2}{3}(a_{23} - a_{13})T\Phi_1(1-\Phi_1)\kappa = 0. && (3.95)
\end{aligned}$$

characterizing thermodynamic equilibrium.
Equation (3.95) is solely determined by $f_{surface}$ and it is fulfilled if

$$\Phi_1 = 1 \quad \vee \quad \Phi_1 = 0 \quad \vee \quad \kappa = 0. \tag{3.96}$$

If one of the conditions (3.96) is fulfilled, the contributions from $f_{surface}$ arising in the first lines of (3.93) and (3.94) will vanish as well. We can conclude that with respect to surface tension effects, thermodynamic equilibrium is achieved in the bulk phases $\Phi_1 = 1$ and $\Phi_1 = 0$ and in curvature-free binary mixture layers with $\kappa = 0$. The latter are characterized by the unity vector $\vec{n}$ in (3.92) showing into the same direction at any point of the phase mixture.
In particular, it is important to note that conditions (3.96) characterizing thermodynamic equilibrium with respect to $f_{surface}$ do not specify a certain profile for the phase volume fractions Φ_1 and $\Phi_2 = 1 - \Phi_1$. This is in contrast to the model for the small quantities φ_i and δ. Remember that the expression for $f_{surface}$ has been constructed in subsection 3.1.1 to enforce tangens hyperbolicus profiles in thermodynamic equilibrium. These profiles are lost in the volume-averaged model.
However, the second lines of (3.93) and (3.94) must be zero as well to achieve equilibrium also with respect to f_{bulk}. The resulting condition is

$$f_2(\xi_2, T) = f_1(\xi_1, T) + \mu(\xi_2 - \xi_1) \tag{3.97}$$

at any point in the mixture region. Before this state has not been reached, there will be further phase change processes until (3.97) is fulfilled everywhere. We can conclude that the equilibrium profiles are determined by (3.97) and therefore by the individual phase chemical properties.

3.2.4. Consistency in the Limit $\Delta V \to 0$

In the limit $\Delta V \to 0$, we have by definition

$$\lim_{\Delta V \to 0} \Phi_i(\vec{x}, t) = \varphi_i(\vec{x}, t). \tag{3.98}$$

We know that around sufficiently flat $k-i$ interfaces far from any triple points, the φ_i are given by

$$\begin{aligned} \varphi_i &= \frac{1}{2} \cdot (1 + \tanh(\frac{x}{2\delta})) \\ \varphi_k &= 1 - \varphi_i \\ \varphi_j &= 0. \end{aligned} \tag{3.99}$$

Utilizing (3.98) and (3.99) in (3.83), we get

$$\lim_{\Delta V \to 0} \Delta^2(\vec{x}) = \frac{a_{ki}\varphi_i^2\varphi_k^2}{-a_{ki}\vec{\nabla}\varphi_i \cdot \vec{\nabla}\varphi_k} = \frac{\varphi_i^2(1-\varphi_i)^2}{(\vec{\nabla}\varphi_i)^2} = \delta^2. \tag{3.100}$$

Since Δ and δ are both positive and utilizing (3.98), this means that the original free energy functional for describing sharp interfaces is obtained back:

$$\lim_{\Delta V \to 0} F[\Phi_1, \Phi_2, \Phi_3, \Delta, \xi] = F[\varphi_1, \varphi_2, \varphi_3, \delta, \xi] \equiv F[\varphi_1, \varphi_2, \varphi_3, \xi]. \tag{3.101}$$

It is natural to identify the averaging volume ΔV with the cells of the numerical grid. Strictly speaking, the limit $\Delta V \to 0$ means that the calculation grid is fine enough for $\varphi_i \approx$ *constant* inside a single cell. In practice, it should be sufficient to resolve the continuous transition region between $\varphi_i = 0$ and $\varphi_i = 1$, i.e. to have a handful of cells inside $0 < \varphi_i < 1$ as in usual phase-field simulations.
We can conclude from (3.101) that if the cells of the numerical grid are small enough, the macroscopic governing equations to be derived later based on the generalized free energy functional (3.79) converge to the appropriate microscopic equations describing the detailed sharp interface structure.
Note that at sharp interfaces with a high curvature or close to triple points, the phase-fields cannot adopt the tangens hyperbolicus profiles according to (3.99). The deviation of the resulting expression $\Delta(\varphi_1, \varphi_2, \varphi_3)$ from the constant δ will be regarded as a correction in these cases.

3.2.5. Lower Boundary for Δ

In analogy to subsection 3.2.3, we regard again a binary mixture of phases i and k with Δ being given by

$$\Delta = \frac{\Phi_i(1-\Phi_i)}{|\vec{\nabla}\Phi_i|} = \frac{\Phi_i(1-\Phi_i)}{\sqrt{\vec{\nabla}\Phi_i \cdot \vec{\nabla}\Phi_i}}. \tag{3.102}$$

We investigate here if there is a lower boundary for Δ. A necessary condition for (3.102) adopting a minimum value is

$$\frac{\delta\Delta}{\delta\Phi_i} = 0.$$

An evaluation of this leads to

$$\begin{aligned}
\frac{\delta\Delta}{\delta\Phi_i} &= -\vec{\nabla}\cdot(\frac{\partial\Delta}{\partial\vec{\nabla}\Phi_i}) + \frac{\partial\Delta}{\partial\Phi_i} \\
&= -\vec{\nabla}\cdot(\Phi_i(1-\Phi_i)(-\frac{1}{2})[(\vec{\nabla}\Phi_i)^2]^{-\frac{3}{2}}2\vec{\nabla}\Phi_i) + (1-2\Phi_i)\frac{1}{|\vec{\nabla}\Phi_i|} \\
&= \vec{\nabla}\cdot(\Phi_i(1-\Phi_i)\frac{\vec{\nabla}\Phi_i}{|\vec{\nabla}\Phi_i|^3}) + \frac{1-2\Phi_i}{|\vec{\nabla}\Phi_i|} \\
&= (1-2\Phi_i)\frac{(\vec{\nabla}\Phi_i)^2}{|\vec{\nabla}\Phi_i|^3} + \Phi_i(1-\Phi_i)\frac{\partial}{\partial\vec{\nabla}\Phi_i}(\frac{\vec{\nabla}\Phi_i}{[(\vec{\nabla}\Phi_i)^2]^{\frac{3}{2}}})\vec{\nabla}^2\Phi_i + \frac{1-2\Phi_i}{|\vec{\nabla}\Phi_i|} \\
&= 2\frac{1-2\Phi_i}{|\vec{\nabla}\Phi_i|} + \Phi_i(1-\Phi_i)[\frac{[(\vec{\nabla}\Phi_i)^2]^{\frac{3}{2}} - \vec{\nabla}\Phi_i\cdot\frac{3}{2}[(\vec{\nabla}\Phi_i)^2]^{\frac{1}{2}}2\vec{\nabla}\Phi_i}{[(\vec{\nabla}\Phi_i)^2]^3}]\vec{\nabla}^2\Phi_i \\
&= 2\frac{1-2\Phi_i}{|\vec{\nabla}\Phi_i|} + \Phi_i(1-\Phi_i)\frac{|\vec{\nabla}\Phi_i|^3 - 3|\vec{\nabla}\Phi_i|^3}{|\vec{\nabla}\Phi_i|^6}\vec{\nabla}^2\Phi_i \\
&= 2\{\frac{1-2\Phi_i}{|\vec{\nabla}\Phi_i|} - \Phi_i(1-\Phi_i)\frac{1}{|\vec{\nabla}\Phi_i|^3}\vec{\nabla}^2\Phi_i\}. \qquad (3.103)
\end{aligned}$$

Expression (3.103) vanishes if

$$\Phi_i = \varphi_i = \frac{1}{2}(1+\tanh(\frac{x}{2\delta})). \qquad (3.104)$$

The value adopted by Δ based on the profile (3.104) is according to (3.100) equal to δ. We can conclude

$$\Delta(\vec{x},t) \geq \delta > 0. \qquad (3.105)$$

In addition to the result obtained in subsection 3.2.4, (3.105) demonstrates the consistency of the transition to the volume-averaged model.

3.3. Coupled Governing Equations for Non-Isothermal Conditions

Based on thermodynamic principles, we derive now governing equations for the phase-fields and their coupling with the compressible Navier-Stokes equations as well as with transport equations for heat and composition. *The coupling procedure is based on ideas proposed by Anderson, McFadden and Wheeler ([50],[51]) discussed in subsection 2.2.4 and can be regarded as a generalization for binary alloys including multiple phase-fields, heat and composition transport.* Furthermore, it turns out that due to the special criteria applied in the construction of $f_{surface}$ and f_{bulk}, the final set of equations contains the description of elemental material solid-liquid phase change as a special case.

3.3.1. Binary Eutectic Alloys

The first step is to calculate functionals for entropy and internal energy from the free energy functional (3.79):

$$S = -\frac{dF}{dT} = \int_V \{-\frac{df}{dT} - \Lambda_L(\Phi_1+\Phi_2+\Phi_3-1)\}dV \qquad (3.106)$$

$$E = F + TS = \int_V \{f - T\frac{df}{dT}\}dV. \qquad (3.107)$$

We define an entropy per mass s_m and an internal energy per mass e_m by

$$-\frac{df}{dT} = \sum_{i<j} a_{ij} \Delta \vec{\nabla}\Phi_i \cdot \vec{\nabla}\Phi_j + \rho s_m \tag{3.108}$$

$$f - T\frac{df}{dT} = \rho e_m. \tag{3.109}$$

Note that the coefficients in the gradient term are constants. Considering

$$\frac{df}{dT} = \frac{\partial f}{\partial T} + \sum_{k=1}^{3} \frac{\partial f}{\partial \xi_k}\frac{\partial \xi_k}{\partial T} = \frac{\partial f}{\partial T} + \sum_{k=1}^{3} h_k \frac{\partial f_k}{\partial \xi_k}\frac{\partial \xi_k}{\partial T} = \frac{\partial f}{\partial T} + \mu \frac{\partial \xi}{\partial T} = \frac{\partial f}{\partial T},$$

we get

$$\begin{aligned} \rho s_m = &- \frac{a_{12}}{\Delta}\Phi_1^2\Phi_2^2 - \frac{a_{13}}{\Delta}\Phi_1^2\Phi_3^2 - \frac{a_{23}}{\Delta}\Phi_2^2\Phi_3^2 \\ &- \Phi_1\Phi_2\Phi_3\{\frac{a_{12}+a_{13}-a_{23}}{\Delta}\Phi_1 + \frac{a_{12}-a_{13}+a_{23}}{\Delta}\Phi_2 + \frac{a_{13}-a_{12}+a_{23}}{\Delta}\Phi_3\} \\ &- \sum_{k=1}^{3}\{h_k \frac{\partial f_k}{\partial T}\} \end{aligned} \tag{3.110}$$

and

$$\rho e_m = \sum_{k=1}^{3} h_k \{f_k - T\frac{\partial f_k}{\partial T}\}. \tag{3.111}$$

Furthermore, the following conservation equations for mass, momentum, internal energy and composition shall be valid:

$$\begin{aligned} \frac{D\rho}{Dt} &= -\rho(\vec{\nabla}\cdot\vec{u}) & \rho\frac{De_m}{Dt} &= -\vec{\nabla}\cdot\vec{q_e} + \boldsymbol{m} : (\vec{\nabla}\vec{u}) \\ \rho\frac{D\vec{u}}{Dt} &= \vec{\nabla}\cdot\boldsymbol{m} - K_0\frac{(1-\Phi_1)^2}{\Phi_1^3}\vec{u} + \rho\vec{g} & \rho\frac{D\xi}{Dt} &= -\vec{\nabla}\cdot\vec{q_\xi}. \end{aligned} \tag{3.112}$$

On the left hand sides, the material derivatives $\frac{D}{Dt} = \frac{\partial}{\partial t} + (\vec{u}\cdot\vec{\nabla})$ were used, $\boldsymbol{m}$ represents the stress tensor and the velocity $\vec{u}$ shall be damped in the mushy layer according to Darcy's law with a permeability $K_0 > 0$. Additionally, the quantity $\vec{q_\xi}$ represents the composition flux. The equations for mass, momentum and energy conservation in (3.112) basically correspond to equations (2.117)-(2.119) in subsection 2.2.4 as introduced by Anderson et al. ([51]). The difference to Anderson's model is that we added the Darcy source term in momentum conservation and introduced an additional transport equation for composition.

3.3.1.1. Internal Energy Conservation

At first, we consider internal energy conservation. Applying the chain rule to (3.111), we get

$$\frac{De_m}{Dt} = \frac{\partial e_m}{\partial \rho}\frac{D\rho}{Dt} + \frac{de_m}{dT}\frac{DT}{Dt} + \frac{de_m}{d\xi}\frac{D\xi}{Dt} + \sum_{k=1}^{3}\frac{de_m}{d\Phi_j}\frac{D\Phi_j}{Dt}.$$

The calculations presented in appendix C result in

$$\begin{aligned}
\frac{\partial e_m}{\partial \rho} &= 0 \\
\frac{de_m}{dT} &= -\frac{T}{\rho}\sum_{k=1}^{3} h_k \frac{\partial^2 f_k}{\partial T^2} \\
\frac{de_m}{d\xi} &= \frac{1}{\rho}(\mu - T\frac{d\mu}{dT}) \\
\frac{de_m}{d\Phi_j} &= \frac{1}{\rho}\sum_{k=1}^{3} \frac{\partial h_k}{\partial \Phi_j}[f_k - T\frac{\partial f_k}{\partial T} - \mu\xi_k + T\frac{\partial \mu}{\partial T}\xi_k].
\end{aligned}$$

Using these expressions, the equation for internal energy conservation can be transformed to a transport equation for the temperature field:

$$\begin{aligned}
-T\sum_{k=1}^{3} h_k \frac{\partial^2 f_k}{\partial T^2}\frac{DT}{Dt} = &- \vec{\nabla}\cdot\vec{q_e} + \boldsymbol{m} : (\vec{\nabla}\vec{u}) - (\mu - T\frac{d\mu}{dT})\frac{D\xi}{Dt} \\
&- \sum_{j=1}^{3}\{\sum_{k=1}^{3}\frac{\partial h_k}{\partial \Phi_j}(f_k - \mu\xi_k - T\frac{\partial}{\partial T}(f_k - \mu\xi_k) - T\mu\frac{\partial \xi_k}{\partial T})\}\frac{D\Phi_j}{Dt}.
\end{aligned} \tag{3.113}$$

3.3.1.2. Second Law: Positive Entropy Production Rate

The objective of this paragraph is to find constitutive laws for the quantities $\boldsymbol{m}$, $\vec{q_e}$ and $\vec{q_\xi}$ appearing in the set of equations (3.112) as well as governing equations for the phase volume fractions Φ_j in accordance with the second law of thermodynamics. The resulting constitutive laws will contain non-classical contributions due to the presence of phase interfaces and assure a thermodynamically consistent coupling of phase change with the governing equations (3.112). In analogy to Anderson et al. ([51]), we regard the entropy balance of a control volume $\Omega \subset V$

$$\frac{dS_\Omega}{dt} = \int_\Omega \dot{s}_{prod} d\Omega \quad - \quad \int_{\partial\Omega} \vec{q_s}\cdot\vec{n} dA \tag{3.114}$$

containing a source term $\dot{s}_{prod}$ and an entropy flux $\vec{q_s}$. Utilizing the entropy functional (3.106) with (3.108), the left hand side can be evaluated according to

$$\begin{aligned}
\frac{dS_\Omega}{dt} = &\int_\Omega \{\frac{\partial}{\partial t}(\rho s_m) + \vec{\nabla}\cdot(\rho s_m \vec{u})\} d\Omega \\
&- \int_\Omega \{\Lambda_L(\frac{\partial \Phi_1}{\partial t} + \frac{\partial \Phi_2}{\partial t} + \frac{\partial \Phi_3}{\partial t}) + \Lambda_L \vec{\nabla}\cdot((\Phi_1 + \Phi_2 + \Phi_3 - 1)\vec{u})\} d\Omega \\
&+ \int_\Omega \{\frac{\partial}{\partial t}(\sum_{i<j} a_{ij}\Delta\vec{\nabla}\Phi_i\cdot\vec{\nabla}\Phi_j) + \vec{\nabla}\cdot([\sum_{i<j} a_{ij}\Delta\vec{\nabla}\Phi_i\cdot\vec{\nabla}\Phi_j]\vec{u})\} d\Omega.
\end{aligned}$$

After an application of the continuity equation and the Gaussian theorem, the entropy production rate $\dot{s}_{prod}$ in the subvolume Ω may be expressed as

$$\begin{aligned}
\dot{s}_{prod} = &\rho\frac{Ds_m}{Dt} - \Lambda_L(\frac{D\Phi_1}{Dt} + \frac{D\Phi_2}{Dt} + \frac{D\Phi_3}{Dt}) - \Lambda_L(\Phi_1 + \Phi_2 + \Phi_3 - 1)(\vec{\nabla}\cdot\vec{u}) \\
&+ \frac{\partial}{\partial t}(\sum_{i<j} a_{ij}\Delta\vec{\nabla}\Phi_i\cdot\vec{\nabla}\Phi_j) + \vec{\nabla}\cdot([\sum_{i<j} a_{ij}\Delta\vec{\nabla}\Phi_i\cdot\vec{\nabla}\Phi_j]\vec{u}) + \vec{\nabla}\cdot\vec{q_s}.
\end{aligned} \tag{3.115}$$

In accordance with the second law of thermodynamics, we must assure that expression (3.115) is always non-negative. The first term is evaluated again by using the chain rule

$$\frac{Ds_m}{Dt} = \frac{\partial s_m}{\partial \rho}\frac{D\rho}{Dt} + \frac{ds_m}{dT}\frac{DT}{Dt} + \frac{ds_m}{d\xi}\frac{D\xi}{Dt} + \sum_{j=1}^{3}\frac{ds_m}{d\Phi_j}\frac{D\Phi_j}{Dt} + \frac{\partial s_m}{\partial \Delta}\frac{D\Delta}{Dt}$$

and from the calculations in the appendix D, we get

$$\begin{aligned}
\frac{ds_m}{dT} =& -\frac{1}{\rho}\sum_{k=1}^{3} h_k \frac{\partial^2 f_k}{\partial T^2} \\
\frac{ds_m}{d\xi} =& -\frac{1}{\rho}\frac{d\mu}{dT} \\
\frac{ds_m}{d\Phi_j} =& -\frac{1}{\rho}\{2\frac{a_{ij}}{\Delta}\Phi_i^2\Phi_j + 2\frac{a_{kj}}{\Delta}\Phi_k^2\Phi_j \\
&+ \frac{a_{ij}+a_{ik}-a_{kj}}{\Delta}\Phi_i^2\Phi_k + \frac{a_{kj}+a_{ik}-a_{ij}}{\Delta}\Phi_k^2\Phi_i + 2\frac{a_{ij}+a_{kj}-a_{ik}}{\Delta}\Phi_i\Phi_j\Phi_k \\
&+ \sum_{k=1}^{3}\frac{\partial h_k}{\partial \Phi_j}(\frac{\partial f_k}{\partial T} - \frac{\partial \mu}{\partial T}\xi_k)\} \\
\frac{\partial s_m}{\partial \Delta} =& \frac{1}{\rho}\{\frac{1}{\Delta^2}[a_{12}\Phi_1^2\Phi_2^2 + a_{13}\Phi_1^2\Phi_3^2 + a_{23}\Phi_2^2\Phi_3^2] \\
&+ \frac{1}{\Delta^2}\Phi_1\Phi_2\Phi_3[(a_{12}+a_{13}-a_{23})\Phi_1 + (a_{12}-a_{13}+a_{23})\Phi_2 + (a_{13}-a_{12}+a_{23})\Phi_3]\}.
\end{aligned}$$

It will become clear in the following that the expression for $\frac{\partial s_m}{\partial \rho}$ does not have to be evaluated explicitly. We write in the second line of (3.115)

$$\begin{aligned}
&\frac{\partial}{\partial t}(a_{ij}\Delta\vec{\nabla}\Phi_i\cdot\vec{\nabla}\Phi_j) + \vec{\nabla}\cdot(a_{ij}\Delta\vec{\nabla}\Phi_i\cdot\vec{\nabla}\Phi_j\vec{u}) \\
&= a_{ij}\Delta\vec{\nabla}\Phi_i\cdot\frac{\partial\vec{\nabla}\Phi_j}{\partial t} + a_{ij}\Delta\vec{\nabla}\Phi_j\cdot\frac{\partial\vec{\nabla}\Phi_i}{\partial t} + a_{ij}(\vec{\nabla}\Phi_i\cdot\vec{\nabla}\Phi_j)\frac{\partial\Delta}{\partial t} \\
&+ a_{ij}\Delta(\vec{\nabla}\Phi_i\cdot\vec{\nabla}\Phi_j)(\vec{\nabla}\cdot\vec{u}) + a_{ij}\Delta(\vec{u}\cdot\vec{\nabla})(\vec{\nabla}\Phi_i\cdot\vec{\nabla}\Phi_j) + a_{ij}(\vec{\nabla}\Phi_i\cdot\vec{\nabla}\Phi_j)(\vec{u}\cdot\vec{\nabla})\Delta \\
&= a_{ij}\Delta\vec{\nabla}\Phi_i\cdot\{\frac{\partial\vec{\nabla}\Phi_j}{\partial t} + (\vec{u}\cdot\vec{\nabla})\vec{\nabla}\Phi_j\} + a_{ij}\Delta\vec{\nabla}\Phi_j\cdot\{\frac{\partial\vec{\nabla}\Phi_i}{\partial t} + (\vec{u}\cdot\vec{\nabla})\vec{\nabla}\Phi_i\} \\
&+ a_{ij}(\vec{\nabla}\Phi_i\cdot\vec{\nabla}\Phi_j)\{\frac{\partial\Delta}{\partial t} + (\vec{u}\cdot\vec{\nabla})\Delta\} + a_{ij}\Delta(\vec{\nabla}\Phi_i\cdot\vec{\nabla}\Phi_j)(\vec{\nabla}\cdot\vec{u}) \\
&= a_{ij}\Delta\vec{\nabla}\Phi_i\cdot\frac{D\vec{\nabla}\Phi_j}{Dt} + a_{ij}\Delta\vec{\nabla}\Phi_j\cdot\frac{D\vec{\nabla}\Phi_i}{Dt} + a_{ij}(\vec{\nabla}\Phi_i\cdot\vec{\nabla}\Phi_j)\frac{D\Delta}{Dt} \\
&+ a_{ij}\Delta(\vec{\nabla}\Phi_i\cdot\vec{\nabla}\Phi_j)(\vec{\nabla}\cdot\vec{u}).
\end{aligned} \tag{3.116}$$

We use

$$\begin{aligned}
&\vec{\nabla}\cdot(a_{ij}\Delta\vec{\nabla}\Phi_i\frac{D\Phi_j}{Dt}) \\
&= \frac{D\Phi_j}{Dt}\vec{\nabla}\cdot(a_{ij}\Delta\vec{\nabla}\Phi_i) + a_{ij}\Delta\vec{\nabla}\Phi_i\cdot\vec{\nabla}(\frac{D\Phi_j}{Dt}) \\
&= \frac{D\Phi_j}{Dt}\vec{\nabla}\cdot(a_{ij}\Delta\vec{\nabla}\Phi_i) + a_{ij}\Delta\vec{\nabla}\Phi_i\cdot[\vec{\nabla}(\frac{\partial\Phi_j}{\partial t}) + \vec{\nabla}((\vec{u}\cdot\vec{\nabla})\Phi_j)] \\
&= \frac{D\Phi_j}{Dt}\vec{\nabla}\cdot(a_{ij}\Delta\vec{\nabla}\Phi_i) + a_{ij}\Delta\vec{\nabla}\Phi_i\cdot[\frac{\partial\vec{\nabla}\Phi_j}{\partial t} + (\vec{u}\cdot\vec{\nabla})\vec{\nabla}\Phi_j + (\vec{\nabla}\vec{u})^T\cdot\vec{\nabla}\Phi_j] \\
&= \frac{D\Phi_j}{Dt}\vec{\nabla}\cdot(a_{ij}\Delta\vec{\nabla}\Phi_i) + a_{ij}\Delta\vec{\nabla}\Phi_i\cdot\frac{D\vec{\nabla}\Phi_j}{Dt} + a_{ij}\Delta(\vec{\nabla}\Phi_i\otimes\vec{\nabla}\Phi_j) : (\vec{\nabla}\vec{u})
\end{aligned}$$

and replace in (3.116):

$$a_{ij}\Delta\vec{\nabla}\Phi_i\cdot\frac{D\vec{\nabla}\Phi_j}{Dt}=\vec{\nabla}\cdot(a_{ij}\Delta\vec{\nabla}\Phi_i\frac{D\Phi_j}{Dt})-\frac{D\Phi_j}{Dt}\vec{\nabla}\cdot(a_{ij}\Delta\vec{\nabla}\Phi_i)-a_{ij}\Delta((\vec{\nabla}\Phi_i\otimes\vec{\nabla}\Phi_j):\vec{\nabla}\vec{u}).$$

This leads to

$$\begin{aligned}\dot{s}_{prod}=&\rho\frac{\partial s_m}{\partial\rho}\frac{D\rho}{Dt}-\sum_{k=1}^{3}\{h_k\frac{\partial^2 f_k}{\partial T^2}\}\frac{DT}{Dt}-\frac{d\mu}{dT}\frac{D\xi}{Dt}+\sum_{j=1}^{3}\{\rho\frac{ds_m}{d\Phi_j}\frac{D\Phi_j}{Dt}\}+\rho\frac{\partial s_m}{\partial\Delta}\frac{D\Delta}{Dt}\\&-\Lambda_L\sum_{j=1}^{3}\{\frac{D\Phi_j}{Dt}\}-\Lambda_L(\Phi_1+\Phi_2+\Phi_3-1)(\vec{\nabla}\cdot\vec{u})\\&+\sum_{i<j}\Big\{\vec{\nabla}\cdot(a_{ij}\Delta\vec{\nabla}\Phi_i\frac{D\Phi_j}{Dt})-\frac{D\Phi_j}{Dt}\vec{\nabla}\cdot(a_{ij}\Delta\vec{\nabla}\Phi_i)-a_{ij}\Delta(\vec{\nabla}\Phi_i\otimes\vec{\nabla}\Phi_j):(\vec{\nabla}\vec{u})\\&\quad+\vec{\nabla}\cdot(a_{ij}\Delta\vec{\nabla}\Phi_j\frac{D\Phi_i}{Dt})-\frac{D\Phi_i}{Dt}\vec{\nabla}\cdot(a_{ij}\Delta\vec{\nabla}\Phi_j)-a_{ij}\Delta(\vec{\nabla}\Phi_j\otimes\vec{\nabla}\Phi_i):(\vec{\nabla}\vec{u})\\&\quad+a_{ij}(\vec{\nabla}\Phi_i\cdot\vec{\nabla}\Phi_j)\frac{D\Delta}{Dt}+a_{ij}\Delta(\vec{\nabla}\Phi_i\cdot\vec{\nabla}\Phi_j)(\vec{\nabla}\cdot\vec{u})\Big\}+\vec{\nabla}\cdot\vec{q_s}.\end{aligned}\tag{3.117}$$

In (3.117), we insert the transport equation for the temperature field (3.113) and use $\vec{\nabla}\cdot\vec{u}=\mathbf{1}:(\vec{\nabla}\vec{u})$:

$$\begin{aligned}\dot{s}_{prod}=&\rho\frac{\partial s_m}{\partial\rho}\frac{D\rho}{Dt}-\frac{\mu}{T}\frac{D\xi}{Dt}\\&+\sum_{j=1}^{3}\Big\{-\vec{\nabla}\cdot(a_{ij}\Delta\vec{\nabla}\Phi_i)-\vec{\nabla}\cdot(a_{kj}\Delta\vec{\nabla}\Phi_k)-2\frac{a_{ij}}{\Delta}\Phi_i^2\Phi_j-2\frac{a_{kj}}{\Delta}\Phi_k^2\Phi_j\\&-\frac{a_{ij}+a_{ik}-a_{kj}}{\Delta}\Phi_i^2\Phi_k-\frac{a_{kj}+a_{ik}-a_{ij}}{\Delta}\Phi_k^2\Phi_i-2\frac{a_{ij}+a_{kj}-a_{ik}}{\Delta}\Phi_i\Phi_j\Phi_k\\&-\frac{1}{T}\sum_{k=1}^{3}[\frac{\partial h_k}{\partial\Phi_j}(f_k-\mu\xi_k)]-\Lambda_L\Big\}\frac{D\Phi_j}{Dt}\\&+\{\rho\frac{\partial s_m}{\partial\Delta}+\sum_{i<j}a_{ij}(\vec{\nabla}\Phi_i\cdot\vec{\nabla}\Phi_j)\}\frac{D\Delta}{Dt}-\frac{1}{T}\vec{\nabla}\cdot\vec{q_e}\\&+\Big\{\frac{\boldsymbol{m}}{T}-\sum_{i<j}[a_{ij}\Delta(\vec{\nabla}\Phi_i\otimes\vec{\nabla}\Phi_j+\vec{\nabla}\Phi_j\otimes\vec{\nabla}\Phi_i-(\vec{\nabla}\Phi_i\cdot\vec{\nabla}\Phi_j)\mathbf{1})]\\&-\lambda_L(\sum_{k=1}^{3}\Phi_k-1)\Big\}:(\vec{\nabla}\vec{u})\\&+\vec{\nabla}\cdot(\vec{q_s}+\sum_{i<j}a_{ij}\Delta(\vec{\nabla}\Phi_i\frac{D\Phi_j}{Dt}+\vec{\nabla}\Phi_j\frac{D\Phi_i}{Dt})).\end{aligned}\tag{3.118}$$

Inserting Δ defined in (3.83) into the expression for $\frac{\partial s_m}{\partial\Delta}$, we get:

$$\rho\frac{\partial s_m}{\partial\Delta}+\sum_{i<j}a_{ij}(\vec{\nabla}\Phi_i\cdot\vec{\nabla}\Phi_j)=0.$$

Due to $\frac{\partial e_m}{\partial\rho}=0$, we can write

$$\rho\frac{\partial s_m}{\partial\rho}\frac{D\rho}{Dt}=-\frac{\rho}{T}(\frac{\partial e_m}{\partial\rho}-T\frac{\partial s_m}{\partial\rho})\frac{D\rho}{Dt}=-\frac{\rho}{T}\frac{\partial f_m}{\partial\rho}\frac{D\rho}{Dt}.\tag{3.119}$$

The differential of free energy for a constant quantity of material

$$dF=-SdT-pdV\tag{3.120}$$

can be related to the mass unit, leading to

$$df_m = -s_m dT - pd(\frac{1}{\rho}) = -s_m dT + \frac{p}{\rho^2} d\rho. \tag{3.121}$$

Utilizing this in (3.119) and inserting mass conservation from the set of equations (3.112), we get

$$\rho \frac{\partial s_m}{\partial \rho} \frac{D\rho}{Dt} = -\frac{\rho}{T} \frac{p}{\rho^2} \frac{D\rho}{Dt} = -\frac{p}{\rho T}(-\rho)(\vec{\nabla} \cdot \vec{u}) = \frac{1}{T} p\mathbf{1} : (\vec{\nabla}\vec{u}). \tag{3.122}$$

With

$$-\frac{1}{T}\vec{\nabla} \cdot \vec{q_e} = -\vec{\nabla} \cdot (\frac{\vec{q_e}}{T}) + \vec{q_e} \cdot \vec{\nabla}(\frac{1}{T})$$

and

$$-\frac{\mu}{T}\frac{D\xi}{Dt} = \frac{\mu}{\rho T}\vec{\nabla} \cdot \vec{q_\xi} = \vec{\nabla} \cdot (\frac{\mu}{\rho T}\vec{q_\xi}) - \vec{q_\xi} \cdot \vec{\nabla}(\frac{\mu}{\rho T}),$$

we obtain

$$\begin{aligned}
\dot{s}_{prod} = \sum_{j=1}^{3} \Big\{ & -\vec{\nabla} \cdot (a_{ij}\Delta\vec{\nabla}\Phi_i) - \vec{\nabla} \cdot (a_{kj}\Delta\vec{\nabla}\Phi_k) - 2\frac{a_{ij}}{\Delta}\Phi_i^2\Phi_j - 2\frac{a_{kj}}{\Delta}\Phi_k^2\Phi_j \\
& - \frac{a_{ij} + a_{ik} - a_{kj}}{\Delta}\Phi_i^2\Phi_k - \frac{a_{kj} + a_{ik} - a_{ij}}{\Delta}\Phi_k^2\Phi_i - 2\frac{a_{ij} + a_{kj} - a_{ik}}{\Delta}\Phi_i\Phi_j\Phi_k \\
& - \frac{1}{T}\sum_{k=1}^{3}[\frac{\partial h_k}{\partial \Phi_j}(f_k - \mu\xi_k)] - \Lambda_L \Big\} \frac{D\Phi_j}{Dt} && (3.123) \\
& + \vec{q_e} \cdot \vec{\nabla}(\frac{1}{T}) && (3.124) \\
& - \vec{q_\xi} \cdot \vec{\nabla}(\frac{\mu}{\rho T}) && (3.125) \\
& + \Big\{ \frac{\boldsymbol{m}}{T} + \frac{p}{T}\mathbf{1} - \sum_{i<j}[a_{ij}\Delta(\vec{\nabla}\Phi_i \otimes \vec{\nabla}\Phi_j + \vec{\nabla}\Phi_j \otimes \vec{\nabla}\Phi_i - (\vec{\nabla}\Phi_i \cdot \vec{\nabla}\Phi_j)\mathbf{1})] \\
& - \Lambda_L(\sum_{k=1}^{3}\Phi_k - 1) \Big\} : (\vec{\nabla}\vec{u}) && (3.126) \\
& + \vec{\nabla} \cdot (\vec{q_s} - \frac{\vec{q_e}}{T} + \frac{\mu}{\rho T}\vec{q_\xi} + \sum_{i<j} a_{ij}\Delta(\vec{\nabla}\Phi_i \frac{D\Phi_j}{Dt} + \vec{\nabla}\Phi_j \frac{D\Phi_i}{Dt})). && (3.127)
\end{aligned}$$

The task is now to find expressions for $\boldsymbol{m}$, $\vec{q_e}$, $\vec{q_\xi}$ and $\frac{D\Phi_j}{Dt}$ which keep $\dot{s}_{prod}$ non-negative. It is important to note that the contributions to $\dot{s}_{prod}$ arise from different phenomena like phase change (3.123), heat transport (3.124), composition transport (3.125) or fluid flow (3.126) as well as the corresponding entropy flux (3.127). Additionally, note that the condition of a non-negative entropy production rate must be fulfilled also in special cases in which some of these phenomena are not present and the corresponding terms disappear. This suggests that the different summands must fulfill $\dot{s}_{prod} \geq 0$ individually.
Consider for example a case of purely diffusive heat and composition transport in a solid phase without phase change. In this situation, (3.123) and (3.126) are zero and the expression for $\dot{s}_{prod}$ reduces to

$$\dot{s}_{prod} = \vec{q_e} \cdot \vec{\nabla}(\frac{1}{T}) - \vec{q_\xi} \cdot \vec{\nabla}(\frac{\mu}{\rho T}) + \vec{\nabla} \cdot (\vec{q_s} - \frac{\vec{q_e}}{T} + \frac{\mu}{\rho T}\vec{q_\xi}). \tag{3.128}$$

It is shown in classical irreversible thermodynamics ([88]) that the entropy current may be expressed as

$$\vec{q_s} = \frac{\vec{q_e}}{T} - \frac{\mu}{\rho T}\vec{q_\xi} \tag{3.129}$$

which makes the last term in (3.128) zero. The easiest way to make the two remaining terms non-negative individually is to create a sum of squares by the choices

$$\vec{q_e} = \quad M_e \vec{\nabla}(\frac{1}{T}) \quad , \quad M_e > 0 \tag{3.130}$$

$$\vec{q_\xi} = -M_\xi \vec{\nabla}(\frac{\mu}{\rho T}) \quad , \quad M_\xi > 0. \tag{3.131}$$

This leads to

$$\dot{s}_{prod} = M_e^{-1} \vec{q_e}^2 + M_\xi^{-1} \vec{q_\xi}^2 \geq 0. \tag{3.132}$$

Note that the choices (3.130) and (3.131) represent common practice in classical irreversible thermodynamics. We will demonstrate in the next paragraph that the well-known Fourier and Fick laws for the heat and composition currents can be reproduced by appropriate choices for the constants M_e and M_ξ.
The classical stress tensor $\boldsymbol{m}$ is given by

$$\boldsymbol{m} = \boldsymbol{\tau} - p\mathbf{1} \tag{3.133}$$

with the viscous stress tensor

$$\boldsymbol{\tau} = \eta\{(\vec{\nabla}\vec{u}) + (\vec{\nabla}\vec{u})^T - \frac{2}{3}(\vec{\nabla} \cdot \vec{u})\mathbf{1}\} \tag{3.134}$$

and the dynamic viscosity η. Expressions (3.126) and (3.127) have in common that they contain contributions from the phase volume fractions. In accordance with Anderson et al. ([51]), we modify the classical expressions in (3.129) and (3.133) for $\vec{q_s}$ and $\boldsymbol{m}$ in such a manner that the terms in (3.126) and (3.127) depending on the phase volume fractions are cancelled:

$$\vec{q_s} = \frac{\vec{q_e}}{T} - \frac{\mu}{\rho T}\vec{q_\xi} - \sum_{i<j} a_{ij}\Delta(\vec{\nabla}\Phi_i \frac{D\Phi_j}{Dt} + \vec{\nabla}\Phi_j \frac{D\Phi_i}{Dt}) \tag{3.135}$$

$$\begin{aligned}\boldsymbol{m} = \boldsymbol{\tau} - p\mathbf{1} &+ \sum_{i<j}[a_{ij}T\Delta(\vec{\nabla}\Phi_i \otimes \vec{\nabla}\Phi_j + \vec{\nabla}\Phi_j \otimes \vec{\nabla}\Phi_i - (\vec{\nabla}\Phi_i \cdot \vec{\nabla}\Phi_j)\mathbf{1})] \\ &+ \Lambda_L T(\sum_{k=1}^{3}\Phi_k - 1).\end{aligned} \tag{3.136}$$

By doing so, the influence of the phase volume fractions and their dynamics on $\dot{s}_{prod}$ is limited to the first term (3.123). In order to get thermodynamically consistent governing equations for phase change, we make use of the same idea that has led to equations (3.130) and (3.131). Setting

$$\begin{aligned}M^{-1}\frac{D\Phi_j}{Dt} = &-\vec{\nabla} \cdot (a_{ij}\Delta\vec{\nabla}\Phi_i) - \vec{\nabla} \cdot (a_{kj}\Delta\vec{\nabla}\Phi_k) - 2\frac{a_{ij}}{\Delta}\Phi_i^2\Phi_j - 2\frac{a_{kj}}{\Delta}\Phi_k^2\Phi_j \\ &- \frac{a_{ij} + a_{ik} - a_{kj}}{\Delta}\Phi_i^2\Phi_k - \frac{a_{kj} + a_{ik} - a_{ij}}{\Delta}\Phi_k^2\Phi_i - 2\frac{a_{ij} + a_{kj} - a_{ik}}{\Delta}\Phi_i\Phi_j\Phi_k \\ &- \frac{1}{T}\sum_{k=1}^{3}[\frac{\partial h_k}{\partial \Phi_j}(f_k - \mu\xi_k)] - \Lambda_L \quad , \quad M > 0,\end{aligned} \tag{3.137}$$

three additional square contributions to $\dot{s}_{prod}$ are created. Inserting (3.130), (3.131), (3.135), (3.136) and (3.137) into the expression for $\dot{s}_{prod}$, we obtain

$$\dot{s}_{prod} = M^{-1} \sum_{j=1}^{3} (\frac{D\Phi_j}{Dt})^2 + M_e^{-1} \vec{q_e}^{\,2} + M_\xi^{-1} \vec{q_\xi}^{\,2} + \frac{1}{T} \boldsymbol{\tau} : (\vec{\nabla} \vec{u}). \tag{3.138}$$

While the first three summands are clearly non-negative, the last one must be regarded in more detail:

$$\begin{aligned}
\boldsymbol{\tau} : (\vec{\nabla} \vec{u}) &= \eta \{ (\vec{\nabla} \vec{u}) + (\vec{\nabla} \vec{u})^T - \frac{2}{3} (\vec{\nabla} \cdot \vec{u}) \mathbf{1} \} : (\vec{\nabla} \vec{u}) \\
&= \eta \{ (\vec{\nabla} \vec{u}) + (\vec{\nabla} \vec{u})^T - \frac{2}{3} (\vec{\nabla} \cdot \vec{u}) \mathbf{1} \} : \{ \frac{1}{2} ((\vec{\nabla} \vec{u}) + (\vec{\nabla} \vec{u})^T) + \frac{1}{2} ((\vec{\nabla} \vec{u}) - (\vec{\nabla} \vec{u})^T) \} \\
&= \eta \sum_{i,j=1}^{3} \{ \frac{\partial u_i}{\partial x_j} + \frac{\partial u_j}{\partial x_i} - \frac{2}{3} \frac{\partial u_i}{\partial x_i} \delta_{ij} \} \{ \frac{1}{2} (\frac{\partial u_i}{\partial x_j} + \frac{\partial u_j}{\partial x_i}) + \frac{1}{2} (\frac{\partial u_i}{\partial x_j} - \frac{\partial u_j}{\partial x_i}) \} \\
&= \eta \sum_{i,j=1}^{3} \frac{1}{2} (\frac{\partial u_i}{\partial x_j} + \frac{\partial u_j}{\partial x_i})^2 + \frac{1}{2} (\frac{\partial u_i}{\partial x_j} + \frac{\partial u_j}{\partial x_i}) (\frac{\partial u_i}{\partial x_j} - \frac{\partial u_j}{\partial x_i}) - \frac{2}{3} \frac{\partial u_i}{\partial x_i} \delta_{ij} \frac{\partial u_i}{\partial x_j} \qquad (3.139) \\
&= \eta \sum_{i,j=1}^{3} \frac{1}{2} (\frac{\partial u_i}{\partial x_j} + \frac{\partial u_j}{\partial x_i})^2 - \frac{2}{3} (\frac{\partial u_i}{\partial x_i})^2 \delta_{ij} \qquad (3.140) \\
&= \eta \sum_{i,j=1}^{3} \begin{cases} \frac{1}{2} (\frac{\partial u_i}{\partial x_j} + \frac{\partial u_j}{\partial x_i})^2 \geq 0 & i \neq j \\ \frac{4}{3} (\frac{\partial u_i}{\partial x_i})^2 \geq 0 & i = j \end{cases} \qquad (3.141)
\end{aligned}$$

In the above expression, the Kronecker delta δ_{ij} was utilized and in the step from (3.139) to (3.140), it was used that $(\frac{\partial u_i}{\partial x_j} + \frac{\partial u_j}{\partial x_i})(\frac{\partial u_i}{\partial x_j} - \frac{\partial u_j}{\partial x_i})$ is antisymmetric with respect to an interchange of i and j. In the summation, every pair (i, j) is therefore cancelled by the corresponding (j, i) and the contribution of this expression vanishes.
Based on (3.138) and (3.141), it is clear that

$$\dot{s}_{prod} \geq 0 \tag{3.142}$$

and that our model is in accordance with the second law of thermodynamics.

3.3.1.3. Further Elaboration of the Constitutive Laws

In this paragraph, the constitutive laws found before will be linked with physical experience. In particular, the constants M_e and M_ξ will be determined.

Heat Flux $\vec{q_e}$

Expression (3.130) for $\vec{q_e}$ can be reformulated according to

$$\vec{q_e} = M_e \vec{\nabla} (\frac{1}{T}) = -\frac{M_e}{T^2} \vec{\nabla} T. \tag{3.143}$$

This must be compared with the well-known Fourier law for the heat flux

$$\vec{q_e} = -\lambda \vec{\nabla} T. \tag{3.144}$$

For binary eutectic alloys, we define a mixture heat conductivity of the three phases

$$\lambda = \lambda(\Phi_1, \Phi_2, \Phi_3) = \Phi_1 \lambda_1 + \Phi_2 \lambda_2 + \Phi_3 \lambda_3. \tag{3.145}$$

One can see that the technical choice (3.130) can be made consistent with the Fourier law by setting

$$M_e = \lambda(\Phi_1, \Phi_2, \Phi_3) T^2. \tag{3.146}$$

Composition Flux $\vec{q_\xi}$

Equation (3.131) for the composition flux can be transformed according to

$$\begin{aligned}\vec{q_\xi} &= -M_\xi \vec{\nabla}(\frac{\mu}{\rho T}) \\ &= -M_\xi \{\frac{d}{d\xi}(\frac{\mu}{\rho T})\vec{\nabla}\xi + \frac{d}{dT}(\frac{\mu}{\rho T})\vec{\nabla}T + \sum_{j=1}^{3}\frac{d}{d\Phi_j}(\frac{\mu}{\rho T})\vec{\nabla}\Phi_j + \frac{d}{d\rho}(\frac{\mu}{\rho T})\vec{\nabla}\rho\}\end{aligned}$$

with

$$\begin{aligned}\frac{d}{d\xi}(\frac{\mu}{\rho T}) &= \frac{1}{\rho T}\frac{d\mu}{d\xi} \\ \frac{d}{dT}(\frac{\mu}{\rho T}) &= \frac{1}{\rho T}\frac{d\mu}{dT} - \frac{\mu}{\rho T^2} \\ \frac{d}{d\Phi_j}(\frac{\mu}{\rho T}) &= \frac{1}{\rho T}\frac{d\mu}{d\Phi_j} \overset{(7.8)}{=} -\frac{1}{\rho T}\frac{d\mu}{d\xi}(\sum_{k=1}^{3}\frac{\partial h_k}{\partial \Phi_j}\xi_k) \\ \frac{d}{d\rho}(\frac{\mu}{\rho T}) &= -\frac{\mu}{\rho^2 T}.\end{aligned}$$

The expressions $\frac{d\mu}{d\xi}, \frac{d\mu}{dT}, \frac{d\mu}{d\Phi_j}$ are evaluated in appendix B. In the next step, the factor in front of $\vec{\nabla}\xi$ is compared with the well-known first Fick law describing composition fluxes solely due to composition gradients:

$$\vec{q_\xi} = -\rho D\vec{\nabla}\xi. \tag{3.147}$$

The quantity D represents the mass diffusion coefficient. A comparison leads to

$$M_\xi \frac{1}{\rho T}\frac{d\mu}{d\xi} = \rho D \leftrightarrow M_\xi = \frac{D\rho^2 T}{\frac{d\mu}{d\xi}} \tag{3.148}$$

and with

$$\vec{\nabla}\xi = \vec{\nabla}\sum_{k=1}^{3}h_k\xi_k = \sum_{k=1}^{3}\vec{\nabla}h_k\xi_k + h_k\vec{\nabla}\xi_k = \sum_{k=1}^{3}(\sum_{j=1}^{3}\frac{\partial h_k}{\partial \Phi_j}\vec{\nabla}\Phi_j)\xi_k + h_k\vec{\nabla}\xi_k,$$

we get the following result for the composition flux:

$$\begin{aligned}\vec{q_\xi} &= -\rho D\vec{\nabla}\xi - \rho D\frac{1}{\frac{d\mu}{d\xi}}(\frac{d\mu}{dT} - \frac{\mu}{T})\vec{\nabla}T + \rho D\sum_{j=1}^{3}(\sum_{k=1}^{3}\frac{\partial h_k}{\partial \Phi_j}\xi_k)\vec{\nabla}\Phi_j + \frac{D\mu}{\frac{d\mu}{d\xi}}\vec{\nabla}\rho \\ &= -\rho D\sum_{k=1}^{3}h_k\vec{\nabla}\xi_k - \frac{\rho D}{\frac{d\mu}{d\xi}}(\frac{d\mu}{dT} - \frac{\mu}{T})\vec{\nabla}T + \frac{D\mu}{\frac{d\mu}{d\xi}}\vec{\nabla}\rho.\end{aligned}$$

Phase-Field Equations $\frac{D\Phi_j}{Dt}$

We start with a consistency check concerning the constraint of the phase volume fractions summing up to one. Inserting the lagrangian multiplier (3.80) into the phase-field equations (3.137) and adding the three equations together, one finds:

$$M^{-1}\sum_{j=1}^{3}\frac{D\Phi_j}{Dt} = 0.$$

Due to $M > 0$, this means that the sum of the phase volume fractions is kept constant and a consistent set of initial values will fix this constant value to one.
The inverse mobility M^{-1} is regarded as a superposition of the inverse mobilities M_{12}^{-1} and M_{13}^{-1} corresponding to the two liquid-solid phase boundaries:

$$M^{-1} = \frac{\Phi_2 M_{12}^{-1} + \Phi_3 M_{13}^{-1}}{\Phi_2 + \Phi_3}, \qquad M_{12}^{-1}, M_{13}^{-1} > 0. \tag{3.149}$$

M_{12}^{-1} and M_{13}^{-1} will be determined in section 3.4 in the framework of a thin-interface analysis.

Stress Tensor $\boldsymbol{m}$

Due to $\sum_{j=1}^{3} \Phi_j = 1$, the stress tensor simplifies to

$$\boldsymbol{m} = \boldsymbol{\tau} - p\mathbf{1} + \sum_{i<j} [a_{ij} T \Delta (\vec{\nabla}\Phi_i \otimes \vec{\nabla}\Phi_j + \vec{\nabla}\Phi_j \otimes \vec{\nabla}\Phi_i - (\vec{\nabla}\Phi_i \cdot \vec{\nabla}\Phi_j)\mathbf{1})] \tag{3.150}$$

with $\boldsymbol{\tau}$ being given by (3.134).

Summary

We summarize the constitutive laws and the governing equations for the phase volume fractions assuring a non-negative entropy production rate in their final form

$$\vec{q_e} = \lambda(\Phi_1, \Phi_2, \Phi_3)\vec{\nabla}T \tag{3.151}$$

$$\vec{q_\xi} = -\rho D \sum_{k=1}^{3} h_k \vec{\nabla}\xi_k - \frac{\rho D}{\frac{d\mu}{d\xi}}\left(\frac{d\mu}{dT} - \frac{\mu}{T}\right)\vec{\nabla}T + \frac{D\mu}{\frac{d\mu}{d\xi}}\vec{\nabla}\rho \tag{3.152}$$

$$\begin{aligned} \boldsymbol{m} = {} & \eta\{(\vec{\nabla}\vec{u}) + (\vec{\nabla}\vec{u})^T - \frac{2}{3}(\vec{\nabla}\cdot\vec{u})\mathbf{1}\} - p\mathbf{1} \\ & + \sum_{i<j} [a_{ij} T \Delta (\vec{\nabla}\Phi_i \otimes \vec{\nabla}\Phi_j + \vec{\nabla}\Phi_j \otimes \vec{\nabla}\Phi_i - (\vec{\nabla}\Phi_i \cdot \vec{\nabla}\Phi_j)\mathbf{1})] \end{aligned} \tag{3.153}$$

$$\begin{aligned} M^{-1}\frac{D\Phi_j}{Dt} = {} & -\vec{\nabla}\cdot(a_{ij}\Delta\vec{\nabla}\Phi_i) - \vec{\nabla}\cdot(a_{kj}\Delta\vec{\nabla}\Phi_k) - 2\frac{a_{ij}}{\Delta}\Phi_i^2\Phi_j - 2\frac{a_{kj}}{\Delta}\Phi_k^2\Phi_j \\ & - \frac{a_{ij} + a_{ik} - a_{kj}}{\Delta}\Phi_i^2\Phi_k - \frac{a_{kj} + a_{ik} - a_{ij}}{\Delta}\Phi_k^2\Phi_i - 2\frac{a_{ij} + a_{kj} - a_{ik}}{\Delta}\Phi_i\Phi_j\Phi_k \\ & - \frac{1}{T}\sum_{k=1}^{3}\left[\frac{\partial h_k}{\partial \Phi_j}(f_k - \mu\xi_k)\right] - \Lambda_L \end{aligned} \tag{3.154}$$

with $\lambda(\Phi_1, \Phi_2, \Phi_3)$ being given by (3.145) and M^{-1} by (3.149).

3.3.1.4. Governing Equations

In the momentum equation, the divergence of the stress tensor $\boldsymbol{m}$ appears. In order to evaluate it, we make use of the following relation for component k of the non-classical part

depending on the phase volume fractions:

$$
\begin{aligned}
&(\vec{\nabla}\cdot[\vec{\nabla}\Phi_i\otimes\vec{\nabla}\Phi_j+\vec{\nabla}\Phi_j\otimes\vec{\nabla}\Phi_i-(\vec{\nabla}\Phi_i\cdot\vec{\nabla}\Phi_j)\mathbf{1}])_k\\
&=\frac{\partial}{\partial x_l}\{\frac{\partial\Phi_i}{\partial x_l}\frac{\partial\Phi_j}{\partial x_k}+\frac{\partial\Phi_j}{\partial x_l}\frac{\partial\Phi_i}{\partial x_k}-(\frac{\partial\Phi_i}{\partial x_m}\frac{\partial\Phi_j}{\partial x_m})\delta_{lk}\}\\
&=\frac{\partial^2\Phi_i}{\partial x_l^2}\frac{\partial\Phi_j}{\partial x_k}+\frac{\partial^2\Phi_j}{\partial x_l\partial x_k}\frac{\partial\Phi_i}{\partial x_l}+\frac{\partial^2\Phi_j}{\partial x_l^2}\frac{\partial\Phi_i}{\partial x_k}+\frac{\partial^2\Phi_i}{\partial x_l\partial x_k}\frac{\partial\Phi_j}{\partial x_l}-\frac{\partial}{\partial x_k}(\frac{\partial\Phi_i}{\partial x_m}\frac{\partial\Phi_j}{\partial x_m})\\
&=\vec{\nabla}^2\Phi_i(\vec{\nabla}\Phi_j)_k+\frac{\partial^2\Phi_j}{\partial x_l\partial x_k}\frac{\partial\Phi_i}{\partial x_l}+\vec{\nabla}^2\Phi_j(\vec{\nabla}\Phi_i)_k+\frac{\partial^2\Phi_i}{\partial x_l\partial x_k}\frac{\partial\Phi_j}{\partial x_l}\\
&\quad-\frac{\partial^2\Phi_i}{\partial x_k\partial x_m}\frac{\partial\Phi_j}{\partial x_m}-\frac{\partial^2\Phi_j}{\partial x_k\partial x_m}\frac{\partial\Phi_i}{\partial x_m}\\
&=\vec{\nabla}^2\Phi_i(\vec{\nabla}\Phi_j)_k+\vec{\nabla}^2\Phi_j(\vec{\nabla}\Phi_i)_k
\end{aligned}
$$

This leads to

$$
\begin{aligned}
\vec{\nabla}\cdot\boldsymbol{m}=\vec{\nabla}\cdot(\eta\{(\vec{\nabla}\vec{u})+(\vec{\nabla}\vec{u})^T-\frac{2}{3}(\vec{\nabla}\cdot\vec{u})\mathbf{1}\})-\vec{\nabla}p\\
+\sum_{i<j}\{a_{ij}\Delta T(\vec{\nabla}^2\Phi_i\vec{\nabla}\Phi_j+\vec{\nabla}^2\Phi_j\vec{\nabla}\Phi_i\}\\
+\sum_{i<j}\{a_{ij}(\vec{\nabla}\Phi_i\otimes\vec{\nabla}\Phi_j+\vec{\nabla}\Phi_j\otimes\vec{\nabla}\Phi_i-(\vec{\nabla}\Phi_i\cdot\vec{\nabla}\Phi_j)\mathbf{1})\}\vec{\nabla}(T\Delta).
\end{aligned}
\tag{3.155}
$$

Using the quantity

$$
p_{rgh}=p-\rho\vec{g}\cdot\vec{x}\rightarrow-\vec{\nabla}p+\rho\vec{g}=-\vec{\nabla}p_{rgh}-(\vec{g}\cdot\vec{x})\vec{\nabla}\rho,
$$

we finally summmarize the derived set of coupled governing equations for compressible flows based on equations (3.112) in the box on the next page. Equations (3.156)-(3.160) in combination with (3.83) for the determination of Δ are the main result of this thesis. In the case of incompressible flows, we can set $\vec{\nabla}\cdot\vec{u}=0$ and the term proportional to $\vec{\nabla}\rho$ as well as the factors of ρ can be cancelled in the composition transport equation (3.159). The interpolation functions h_k appear in the system of equations (3.156)-(3.160) in the phase-field equations as well as in the transport equations for composition and temperature. The comparably complicated structure of the h_k given in (3.65) is mainly due to the requirements arising from the phase-field equations, i.e. the condition to retain the desired equilibrium profiles arising from $f_{surface}$. In contrast to that, their task in the transport equations for T and ξ is merely to interpolate between zero and one, which can also be done by the phase-fields Φ_k themselves. If one would like to describe sharp phase boundaries, the different functional behaviour of the interpolation functions $h_k(\Phi_1,\Phi_2,\Phi_3)$ in comparison to the phase-field functions Φ_k will play no role because the phase mixing layers are very thin in comparison to any other length of interest. However, if one would like to describe macroscopically extended mixture states like the mushy layers, the Φ_k as the real volume fractions of the corresponding phases will allow a more realistic interpolation behaviour between the bulk phases. Therefore, in simulations of binary eutectic alloys on macroscopic length scales, we replace the interpolation functions h_k by the phase volume fractions Φ_k in equations (3.158) and (3.159) as well as in equation (3.61) for the determination of individual phase compositions.

$$\frac{D\rho}{Dt} = -\rho(\vec{\nabla}\cdot\vec{u}) \tag{3.156}$$

$$\begin{aligned}\rho\frac{D\vec{u}}{Dt} &= \vec{\nabla}\cdot(\eta\{(\vec{\nabla}\vec{u}) + (\vec{\nabla}\vec{u})^T - \frac{2}{3}(\vec{\nabla}\cdot\vec{u})\mathbf{1}\}) - \vec{\nabla}p_{rgh} \\ &- (\vec{g}\cdot\vec{x})\vec{\nabla}\rho - K_0\frac{(1-\Phi_1)^2}{\Phi_1^3}\vec{u} \\ &+ \sum_{i<j}\{a_{ij}T\Delta(\vec{\nabla}^2\Phi_i\vec{\nabla}\Phi_j + \vec{\nabla}^2\Phi_j\vec{\nabla}\Phi_i)\} \\ &+ \sum_{i<j}\{a_{ij}(\vec{\nabla}\Phi_i\otimes\vec{\nabla}\Phi_j + \vec{\nabla}\Phi_j\otimes\vec{\nabla}\Phi_i - (\vec{\nabla}\Phi_i\cdot\vec{\nabla}\Phi_j)\mathbf{1}\}\cdot\vec{\nabla}(T\Delta)\end{aligned} \tag{3.157}$$

$$\begin{aligned}-T\sum_{k=1}^{3}h_k\frac{\partial^2 f_k}{\partial T^2}\frac{DT}{Dt} &= \vec{\nabla}\cdot(\lambda(\Phi_1,\Phi_2,\Phi_3)\vec{\nabla}T) - (\mu - T\frac{d\mu}{dT})\frac{D\xi}{Dt} \\ &+ \eta\{(\vec{\nabla}\vec{u}) + (\vec{\nabla}\vec{u})^T - \frac{2}{3}(\vec{\nabla}\cdot\vec{u})\mathbf{1}\} : (\vec{\nabla}\vec{u}) \\ &+ \sum_{i<j}\{a_{ij}T\Delta(\vec{\nabla}\Phi_i\otimes\vec{\nabla}\Phi_j + \vec{\nabla}\Phi_j\otimes\vec{\nabla}\Phi_i)\} : (\vec{\nabla}\vec{u}) \\ &- (p + \sum_{i<j}\{a_{ij}T\Delta(\vec{\nabla}\Phi_i\cdot\vec{\nabla}\Phi_j)\})(\vec{\nabla}\cdot\vec{u}) \\ &- \sum_{j=1}^{3}\{\sum_{k=1}^{3}\frac{\partial h_k}{\partial\Phi_j}(f_k - \mu\xi_k - T\frac{\partial}{\partial T}(f_k - \mu\xi_k) - T\mu\frac{\partial\xi_k}{\partial T})\}\frac{D\Phi_j}{Dt}\end{aligned} \tag{3.158}$$

$$\begin{aligned}\rho\frac{D\xi}{Dt} &= \vec{\nabla}\cdot(\rho D\sum_{k=1}^{3}h_k\vec{\nabla}\xi_k) + \vec{\nabla}\cdot(\frac{\rho D}{\frac{d\mu}{d\xi}}(\frac{d\mu}{dT} - \frac{\mu}{T})\vec{\nabla}T) \\ &- \vec{\nabla}\cdot(\frac{D\mu}{\frac{d\mu}{d\xi}}\vec{\nabla}\rho)\end{aligned} \tag{3.159}$$

$$\begin{aligned}M^{-1}\frac{D\Phi_j}{Dt} &= -\vec{\nabla}\cdot(a_{ij}\Delta\vec{\nabla}\Phi_i) - \vec{\nabla}\cdot(a_{kj}\Delta\vec{\nabla}\Phi_k) \\ &- 2\frac{a_{ij}}{\Delta}\Phi_i^2\Phi_j - 2\frac{a_{kj}}{\Delta}\Phi_k^2\Phi_j \\ &- \frac{a_{ij}+a_{ik}-a_{kj}}{\Delta}\Phi_i^2\Phi_k - \frac{a_{kj}+a_{ik}-a_{ij}}{\Delta}\Phi_k^2\Phi_i \\ &- 2\frac{a_{ij}+a_{kj}-a_{ik}}{\Delta}\Phi_i\Phi_j\Phi_k \\ &- \frac{1}{T}\sum_{k=1}^{3}[\frac{\partial h_k}{\partial\Phi_j}(f_k - \mu\xi_k)] - \Lambda_L.\end{aligned} \tag{3.160}$$

3.3.2. The Special Case of Elemental Materials

The system of equations derived in subsection 3.3.1 contains the description of an elemental material as a special case. As the composition field plays no role for elemental materials, we set the individual phase compositions ξ_i as well as the quantities $\xi_i^{(ij)}(T)$ representing the equilibrium compositions from the phase diagram equal to one. Additionally, we identify the eutectic temperature T_e with the elemental material melting temperature T_m. Using $\lim_{x\to 0}\{x\log x\} = 0$, the free energy densities f_2 and f_3 originally representing the two solid phases α and β of a binary eutectic alloy reduce to the same expression. This is consistent with elemental materials having just a single solid phase. We obtain for the free

energy densities of the liquid and the solid phase

$$f_1 = -\rho c(T\log(\frac{T}{T_m}) - (T - T_m))$$
$$f_2 = f_3 = -\rho c(T\log(\frac{T}{T_m}) - (T - T_m)) + \Theta(T_m - T)L\rho(\frac{T - T_m}{T_m})$$

and the chemical potential vanishes:

$$\mu = \frac{\partial f_1}{\partial \xi_1} = \frac{\partial f_2}{\partial \xi_2} = \frac{\partial f_3}{\partial \xi_3} = 0.$$

As there is only a single solid phase, we can set $\Phi_3 \equiv 0$ and we get with $\Phi_1 = \Phi$ as well as $\Phi_2 = 1 - \Phi$ from the interpolation functions (3.65)

$$\begin{aligned}
h_1 &= 6\Phi^5 - 15\Phi^4 + 10\Phi^3 \\
h_2 &= 1 - h_1 \\
h_3 &= 0 \\
\frac{\partial h_1}{\partial \Phi_1} &= \frac{\partial h_2}{\partial \Phi_2} = \frac{90}{4}\Phi^2(1-\Phi)^2 \\
\frac{\partial h_1}{\partial \Phi_2} &= \frac{\partial h_2}{\partial \Phi_1} = -\frac{30}{4}\Phi^2(1-\Phi)^2 \\
\frac{\partial h_1}{\partial \Phi_3} &= \frac{\partial h_2}{\partial \Phi_3} = +\frac{30}{4}\Phi^2(1-\Phi)^2 \\
\frac{\partial h_3}{\partial \Phi_1} &= \frac{\partial h_3}{\partial \Phi_2} = \frac{\partial h_3}{\partial \Phi_3} = 0.
\end{aligned}$$

The lagrangian multiplier Λ_L from (3.80) reduces to

$$\begin{aligned}
\Lambda_L =& \frac{1}{3}\{(a_{23} - a_{13})\vec{\nabla}\cdot(\Delta\vec{\nabla}\Phi) - 3\frac{a_{12}}{\Delta}\Phi(1-\Phi) - \frac{a_{23} - a_{13}}{\Delta}\Phi(1-\Phi)(1-2\Phi) \\
&- \frac{1}{T}\frac{90}{4}\Phi^2(1-\Phi)^2(f_1 + f_2)\}.
\end{aligned}$$

If we insert it into the evolution equation (3.160) for $\Phi_1 = \Phi$, we will get

$$\begin{aligned}
M^{-1}\frac{D\Phi}{Dt} =& (a_{12} - \frac{1}{3}a_{23} + \frac{1}{3}a_{13})\vec{\nabla}\cdot(\Delta\vec{\nabla}\Phi) \\
&- \frac{1}{\Delta}(a_{12} - \frac{1}{3}a_{23} + \frac{1}{3}a_{13})\Phi(1-\Phi)(1-2\Phi) \\
&+ 15\Phi^2(1-\Phi)^2\frac{1}{T}\{f_2 - f_1\}
\end{aligned}$$

while the volume fraction of the solid phase is given by $1 - \Phi$. The phase-field dependent part of equation (3.157) for the velocity field reduces to

$$-2a_{12}T\Delta\vec{\nabla}^2\Phi\vec{\nabla}\Phi - 2a_{12}(\vec{\nabla}\Phi\otimes\vec{\nabla}\Phi - \frac{1}{2}(\vec{\nabla}\Phi)^2\mathbf{1})\vec{\nabla}(T\Delta)$$

and in equation (3.158) for the temperature field, one obtains

$$-T\sum_{k=1}^{3} h_k\frac{\partial^2 f_k}{\partial T^2}\frac{DT}{Dt} = \rho c\frac{DT}{Dt}$$

and on the right-hand side

$$-2a_{12}T\Delta(\vec{\nabla}\Phi\otimes\vec{\nabla}\Phi) : (\vec{\nabla}\vec{u}) - (p - a_{12}T\Delta(\vec{\nabla}\Phi)^2)(\vec{\nabla}\cdot\vec{u}) + 30\Phi^2(1-\Phi)^2(f_2 - f_1 - T\frac{\partial}{\partial T}(f_2 - f_1)).$$

Due to the fact that there is no second solid phase, we set the surface tension values being linked with it to zero: $\sigma_{13} = \sigma_{23} = 0$. This results in $a_{13} = a_{23} = 0$ and with $a_{12} = a = \frac{3\sigma}{T_m}$, we finally obtain

$$\frac{D\rho}{Dt} = -\rho(\vec{\nabla} \cdot \vec{u}) \tag{3.161}$$

$$\rho\frac{D\vec{u}}{Dt} = \vec{\nabla} \cdot (\eta\{(\vec{\nabla}\vec{u}) + (\vec{\nabla}\vec{u})^T - \frac{2}{3}(\vec{\nabla} \cdot \vec{u})\mathbf{1}\}) - \vec{\nabla}p_{rgh} - (\vec{g} \cdot \vec{x})\vec{\nabla}\rho \tag{3.162}$$
$$- 2aT\Delta\vec{\nabla}^2\Phi\vec{\nabla}\Phi - 2a(\vec{\nabla}\Phi \otimes \vec{\nabla}\Phi - \frac{1}{2}(\vec{\nabla}\Phi)^2\mathbf{1}) \cdot \vec{\nabla}(T\Delta)$$

$$\rho c\frac{DT}{Dt} = \vec{\nabla} \cdot (\lambda(\Phi)\vec{\nabla}T) + \boldsymbol{\tau} : (\vec{\nabla}\vec{u}) - 2aT\Delta(\vec{\nabla}\Phi \otimes \vec{\nabla}\Phi) : (\vec{\nabla}\vec{u}) \tag{3.163}$$
$$- (p - aT\Delta(\vec{\nabla}\Phi)^2)(\vec{\nabla} \cdot \vec{u}) - 30\Phi^2(1-\Phi)^2L\rho\frac{D\Phi}{Dt}$$

$$M^{-1}\frac{D\Phi}{Dt} = a\vec{\nabla} \cdot (\Delta\vec{\nabla}\Phi) - \frac{a}{\Delta}\Phi(1-\Phi)(1-2\Phi) \tag{3.164}$$
$$- \frac{1}{T}15\Phi^2(1-\Phi)^2\Theta(T_m - T)L\rho\frac{T_m - T}{T_m}, M^{-1} > 0,$$

$$\Delta = \frac{\Phi(1-\Phi)}{|\vec{\nabla}\Phi|} \tag{3.165}$$

The Darcy term $-K_0\frac{(1-\Phi_1)^2}{\Phi_1^3}\vec{u}$ has been omitted here because we do not expect mushy layers in slow solidification processes of elemental materials. Velocity can be damped by a phase-dependent viscosity assigning a sufficiently large value to the solid phase. Equations (3.161)-(3.165) will be validated later based on an experiment investigating the melting of gallium in a cubic box.

3.3.3. Implementation of the Model Equations

3.3.3.1. General Information

The model has been implemented into the open source CFD software package OpenFoam ([89]). In a given time step of a binary eutectic alloy simulation, the phase-field equations are solved first. After that, the Navier-Stokes equations are treated with a pressure-velocity coupling using the PISO algorithm ([90]) with three pressure corrections. Finally, the transport equations for composition and temperature are solved. An equivalent procedure is used for elemental materials with the difference that there is only a single phase-field equation and that the transport equation for composition drops out.

3.3.3.2. Stability of Numerical Solutions

It has been observed in simulation tests that the phase-field variables Φ_i may move slowly into the direction $\Phi_i < 0$ at some locations due to numerical errors and after a certain point has been passed, a strong decrease to negative values may be observed. This scenario is avoided by adding the expression

$$\Theta(-\Phi_i)C\Phi_i \quad , \quad C > 0, \tag{3.166}$$

with the Θ-function

$$\Theta(-\Phi_i) = \begin{cases} 1, \text{if } \Phi_i \leq 0 \\ 0, \text{if } \Phi_i > 0. \end{cases}$$

to the right-hand side of the equations for Φ_i. In (3.166), the quantity C represents a sufficiently large constant with appropriate units. In this way, the numerical solution is stabilized by the creation of a barrier which increases linearly with the undershooting $\Phi_i < 0$. Note that (3.166) vanishes in the physically reasonable range with $0 \leq \Phi_i \leq 1$ and that the exact value of C therefore does not influence the simulation results.

3.4. Thin-Interface Analysis

We expressed the inverse mobility M^{-1} in (3.149) as a superposition of inverse mobilities M_{12}^{-1} and M_{13}^{-1} representing the individual liquid-solid phase boundaries. In this section, the quantities M_{12}^{-1} and M_{13}^{-1} will be determined based on a thin-interface analysis as discussed in subsection 2.2.2.

3.4.1. Thin-Interface Analysis for Binary Eutectic Alloys

We regard the motion of a sharp phase boundary on a micrometer length scale and assume that convective effects are negligible. As discussed in subsection 2.2.2, Karma and Rappel found that the behaviour of sharp interfaces may be reproduced by a phase-field model with continuous transition layers of finite width between the pure phases if the model functions obey certain symmetries and if the transition layer width parameter δ is significantly smaller than the diffusion length l of the field dominating the phase change process. For many binary materials including metallic alloys, thermal diffusivity is orders of magnitude larger than mass diffusivity and the latent heat produced during phase change is conducted away from the moving phase boundary much faster than the material component rejected by the solid phase. The latter accumulates on the liquid side of the phase boundary and affects the phase change process due its influence on the liquidus temperature and due to the long time it needs to diffuse away. We hence assume that the temperature around the phase boundary is constant, $T \geq T_e$, and concentrate on the interplay of phase change and composition transport. Therefore, the diffusion length is set to $l = \frac{D}{u_n}$ with the mass diffusion constant D and the normal velocity of the sharp phase boundary u_n.
In the following, we take Karma and Rappel's approach ([43]) for elemental materials as a basis and adapt it to the case of a binary alloy. We restrict our considerations to a moving sharp interface between the liquid phase and solid phase α with $M^{-1} = M_{12}^{-1}$ and regard the one-sided case with a solid diffusion constant of zero. On the basis of the assumptions stated above, we can concentrate on a coupled solution of the composition field and the phase-field equation for the solid phase α. In the limit $\Delta V \to 0$, i.e. without volume-averaging, we can replace in equations (3.159) and (3.160) $\Delta \to \delta$, $\Phi_1 \to \varphi_1$, $\Phi_2 \to \varphi_2$ and set $\varphi_1 = 1 - \varphi_2$ as well as $\varphi_3 = 0$:

$$\begin{aligned} M_{12}^{-1}\frac{\partial \varphi_2}{\partial t} =& (a_{12} + \frac{1}{3}a_{23} - \frac{1}{3}a_{13})\delta\vec{\nabla}^2\varphi_2 - \frac{a_{12} + \frac{1}{3}a_{23} - \frac{1}{3}a_{13}}{\delta}\varphi_2(1-\varphi_2)(1-2\varphi_2) \\ & - 15\varphi_2^2(1-\varphi_2)^2\frac{1}{T}\{f_2 - f_1 - \mu(\xi_2 - \xi_1)\} \\ \frac{\partial \xi}{\partial t} =& \vec{\nabla}\cdot\{D(h_1\vec{\nabla}\xi_1 + h_2\vec{\nabla}\xi_2)\}. \end{aligned}$$

As our interest is aimed at comparably slow solidification processes, we assume that ξ_1 and ξ_2 are close to their equilibrium values $\xi_1^{(12)}(T)$ and $\xi_2^{(12)}(T)$ and that in analogy to $\xi_2^{(12)}(T) = k_{12}\xi_1^{(12)}(T)$ with the equilibrium partition coefficient k_{12}, we have $\xi_2 = k_{12}\xi_1$.

This leads to

$$\begin{aligned} f_2 - f_1 - \mu(\xi_2 - \xi_1) &= \mu_{A,2} - \mu_{A,1} \\ &= \frac{RT}{v_m}\{\log(\frac{1-\xi_2}{1-\xi_2^{(12)}}) - \log(\frac{1-\xi_1}{1-\xi_1^{(12)}})\} \\ &= \frac{RT}{v_m}\{\log(1 - \frac{\xi_2 - \xi_2^{(12)}}{1-\xi_2^{(12)}}) - \log(1 - \frac{\xi_1 - \xi_1^{(12)}}{1-\xi_1^{(12)}})\} \\ &\approx -\frac{RT}{v_m}\frac{\xi_2 - \xi_2^{(12)}}{1-\xi_2^{(12)}} + \frac{RT}{v_m}\frac{\xi_1 - \xi_1^{(12)}}{1-\xi_1^{(12)}} \\ &= \frac{RT}{v_m}\{\frac{1}{1-\xi_1^{(12)}} - \frac{k_{12}}{1-\xi_2^{(12)}}\}(\xi_1 - \xi_1^{(12)}) \end{aligned}$$

and

$$h_1\vec{\nabla}\xi_1 + h_2\vec{\nabla}\xi_2 = (1-h_2)\vec{\nabla}\xi_1 + h_2k_{12}\vec{\nabla}\xi_1 = (1-(1-k_{12})h_2)\vec{\nabla}\xi_1.$$

Introducing the substitutes

$$\tau_{12} = \frac{M_{12}^{-1}\delta}{a_{12} + \frac{1}{3}a_{23} - \frac{1}{3}a_{13}} \tag{3.167}$$

$$D = (1-\varphi_2)D_1 \quad , \quad D_1 = \text{diffusion constant in the liquid phase}$$

$$r = (1-(1-k_{12})h_2) \tag{3.168}$$

$$q = (1-\varphi_2)r = (1-\varphi_2)(1-(1-k_{12})h_2) \tag{3.169}$$

$$s = \frac{15R\delta}{v_m(a_{12} + \frac{1}{3}a_{23} - \frac{1}{3}a_{13})}\{\frac{1}{1-\xi_1^{(12)}} - \frac{k_{12}}{1-\xi_2^{(12)}}\} \tag{3.170}$$

the set of governing equations can be expressed as

$$\begin{aligned} \tau_{12}\frac{\partial\varphi_2}{\partial t} &= \delta^2\vec{\nabla}^2\varphi_2 - \varphi_2(1-\varphi_2)(1-2\varphi_2) - s\varphi_2^2(1-\varphi_2)^2(\xi_1 - \xi_1^{(12)}) \\ r\frac{\partial\xi_1}{\partial t} &= D_1\vec{\nabla}\cdot[q\vec{\nabla}\xi_1] - \xi_1\frac{\partial r}{\partial t}. \end{aligned}$$

In the next step, we introduce dimensionless coordinates:

$$\begin{aligned} \vec{x} = l\tilde{\vec{x}} \quad &\rightarrow \quad \vec{\nabla} = \frac{1}{l}\tilde{\vec{\nabla}} \\ t = \frac{l^2}{D_1}\tilde{t} \quad &\rightarrow \quad \frac{\partial}{\partial t} = \frac{D_1}{l^2}\frac{\partial}{\partial\tilde{t}}. \end{aligned}$$

The quantity l describes the diffusion length of the composition field and therefore the typical length scale of the resulting solidification pattern. We assume in the following that the parameter δ, which charaterizes the continuous transition layer width, is chosen considerably smaller than l. Introducing the quantities (compare [43])

$$p = \frac{\delta}{l} << 1 \tag{3.171}$$

$$\alpha = \frac{D_1\tau_{12}}{\delta^2}, \tag{3.172}$$

the governing equations can be rewritten as

$$\begin{aligned} \alpha p^2\frac{\partial\varphi_2}{\partial\tilde{t}} &= p^2\tilde{\vec{\nabla}}^2\varphi_2 - \varphi_2(1-\varphi_2)(1-2\varphi_2) - s(\xi_1 - \xi_1^{(12)})\varphi_2^2(1-\varphi_2)^2 \\ r\frac{\partial\xi_1}{\partial\tilde{t}} &= \tilde{\vec{\nabla}}\cdot[q\tilde{\vec{\nabla}}\xi_1] - \xi_1\frac{\partial r}{\partial\tilde{t}}. \end{aligned}$$

In analogy to Karma and Rappel ([43]), we introduce a set of curvilinear coordinates (χ_1, χ_2, χ_3) which are locally orthogonal and which move with the sharp phase boundary at a normal velocity of u_n. For that matter, χ_1 and χ_2 measure the dimensionless arc lengths along the two principal directions from a given reference point and χ_3 measures the dimensionless signed orthogonal distance from the sharp phase boundary with $\chi_3 > 0$ in the solid. Additionally, an internal coordinate $\eta = \frac{\chi_3}{p}$ is defined as well as the dimensionless normal velocity and a dimensionless curvature

$$\tilde{u_n} = \frac{u_n l}{D_1} \tag{3.173}$$

$$\tilde{\kappa} = l\kappa = l(\frac{1}{R_1} + \frac{1}{R_2}) \tag{3.174}$$

with the two principal radii of curvature R_1 and R_2. According to Caginalp ([29]), the relations

$$|\tilde{\vec{\nabla}}\chi_3| = 1$$
$$\tilde{\vec{\nabla}}^2\chi_3 = \tilde{\kappa}$$

hold in a neighbourhood of the sharp interface.
We rewrite the differential operators in terms of the new coordinates (compare also [45]):

$$\begin{aligned}
\frac{\partial}{\partial \tilde{t}} &= \sum_{k=1}^{3}\{\frac{\partial \chi_i}{\partial \tilde{t}}\frac{\partial}{\partial \chi_i}\} = \sum_{k=1}^{2}\{\frac{\partial \chi_i}{\partial \tilde{t}}\frac{\partial}{\partial \chi_i}\} - \frac{\tilde{u_n}}{p}\frac{\partial}{\partial \eta} \approx -\frac{\tilde{u_n}}{p}\frac{\partial}{\partial \eta} \\
\tilde{\vec{\nabla}} &= \sum_{k=1}^{3}(\tilde{\vec{\nabla}}\chi_k)\frac{\partial}{\partial \chi_k} \\
\tilde{\vec{\nabla}}^2 &= \sum_{k=1}^{3}\{(\tilde{\vec{\nabla}}\chi_k)^2\frac{\partial^2}{\partial \chi_k^2} + \tilde{\vec{\nabla}}^2\chi_k\frac{\partial}{\partial \chi_k}\} \\
&= \sum_{k=1}^{2}\{(\tilde{\vec{\nabla}}\chi_k)^2\frac{\partial^2}{\partial \chi_k^2} + \tilde{\vec{\nabla}}^2\chi_k\frac{\partial}{\partial \chi_k}\} + \frac{1}{p^2}\frac{\partial^2}{\partial \eta^2} + \tilde{\kappa}\frac{1}{p}\frac{\partial}{\partial \eta} \\
&\approx \frac{1}{p^2}\frac{\partial^2}{\partial \eta^2} + \tilde{\kappa}\frac{1}{p}\frac{\partial}{\partial \eta} \\
\tilde{\vec{\nabla}} \cdot [q\tilde{\vec{\nabla}}\xi_1] &= \tilde{\vec{\nabla}}q \cdot \tilde{\vec{\nabla}}\xi_1 + q\tilde{\vec{\nabla}}^2\xi_1 \\
&\approx \frac{1}{p^2}\frac{\partial q}{\partial \eta}\frac{\partial \xi_1}{\partial \eta} + q(\frac{1}{p^2}\frac{\partial^2 \xi_1}{\partial \eta^2} + \frac{\tilde{\kappa}}{p}\frac{\partial \xi_1}{\partial \eta}) \\
&= \frac{1}{p^2}\frac{\partial}{\partial \eta}(q\frac{\partial \xi_1}{\partial \eta}) + \frac{\tilde{\kappa}}{p}q\frac{\partial \xi_1}{\partial \eta}.
\end{aligned}$$

Note that in the expressions above, terms proportional to $\frac{1}{p}$ and $\frac{1}{p^2}$ dominate due to the smallness of p. The equations are then given by

$$p(\alpha\tilde{u_n} + \tilde{\kappa})\frac{\partial \varphi_2}{\partial \eta} + \frac{\partial^2 \varphi_2}{\partial \eta^2} - \varphi_2(1-\varphi_2)(1-2\varphi_2) - s\varphi_2^2(1-\varphi_2)^2(\xi_1 - \xi_1^{(12)}) = 0 \tag{3.175}$$

$$p(\tilde{u_n}r + \tilde{\kappa}q)\frac{\partial \xi_1}{\partial \eta} + \frac{\partial}{\partial \eta}(q\frac{\partial \xi_1}{\partial \eta}) + p\tilde{u_n}\xi_1\frac{\partial r}{\partial \eta} = 0. \tag{3.176}$$

As introduced in subsection 2.2.2, we perform an inner expansion:

$$\varphi_2 = \varphi_2^{(0)}(\eta) + p\varphi_2^{(1)}(\eta) + ... \tag{3.177}$$

$$\xi_1 = \xi_1^{(0)}(\eta) + p\xi_1^{(1)}(\eta) + ... \tag{3.178}$$

3.4.1.1. Order O(1)

Inserting the expansions (3.177) and (3.178) into the governing equations (3.175) and (3.176), we obtain at order $O(p^0) = O(1)$

$$\frac{\partial^2 \varphi_2^{(0)}}{\partial \eta^2} - \varphi_2^{(0)}(1-\varphi_2^{(0)})(1-2\varphi_2^{(0)}) - s{\varphi_2^{(0)}}^2(1-\varphi_2^{(0)})^2(\xi_1^{(0)} - \xi_1^{(12)}) = 0$$

$$\frac{\partial}{\partial \eta}(q\frac{\partial \xi_1^{(0)}}{\partial \eta}) = 0.$$

These equations are solved by

$$\varphi_2^{(0)}(\eta) = \frac{1}{2}(1 + \tanh(\frac{\eta}{2})) \tag{3.179}$$

$$\xi_1^{(0)}(\eta) = \xi_1^{(12)} = const. \tag{3.180}$$

3.4.1.2. Order O(p)

At order O(p), the equation for composition ξ_1 is

$$\begin{aligned} & \frac{\partial}{\partial \eta}[q(\varphi_2^{(0)})\frac{\partial \xi_1^{(1)}}{\partial \eta}] + \tilde{u_n}\xi_1^{(12)}\frac{\partial r(\varphi_2^{(0)})}{\partial \eta} = 0 \\ \leftrightarrow \quad & \frac{\partial}{\partial \eta}[q(\varphi_2^{(0)})\frac{\partial \xi_1^{(1)}}{\partial \eta} + \tilde{u_n}\xi_1^{(12)} r(\varphi_2^{(0)})] = 0 \\ \leftrightarrow \quad & q(\varphi_2^{(0)})\frac{\partial \xi_1^{(1)}}{\partial \eta} + \tilde{u_n}\xi_1^{(12)} r(\varphi_2^{(0)}) = A = const \quad \forall \eta \end{aligned} \tag{3.181}$$

In the limit $\eta \to \infty$, we get

$$\lim_{\eta \to +\infty} r(\varphi_2^{(0)}) = r(1) = k_{12}$$

$$\lim_{\eta \to +\infty} q(\varphi_2^{(0)}) = q(1) = 0$$

$$\lim_{\eta \to +\infty} \frac{\partial \xi_1^{(1)}}{\partial \eta} = \lim_{\chi_3 \to 0^+} \frac{\partial \xi_1}{\partial \chi_3}$$

and therefore

$$A = \tilde{u_n} k_{12} \xi_1^{(12)}. \tag{3.182}$$

In the limit $\eta \to -\infty$, we get

$$\lim_{\eta \to -\infty} r(\varphi_2^{(0)}) = r(0) = 1$$

$$\lim_{\eta \to -\infty} q(\varphi_2^{(0)}) = q(0) = r = 1$$

$$\lim_{\eta \to -\infty} \frac{\partial \xi_1^{(1)}}{\partial \eta} = \lim_{\chi_3 \to 0^-} \frac{\partial \xi_1}{\partial \chi_3}$$

and hence

$$\lim_{\chi_3 \to 0^-} \frac{\partial \xi_1}{\partial \chi_3} = \tilde{u_n}(k_{12} - 1)\xi_1^{(12)}.$$

Replacing $\tilde{u_n} = \frac{u_n l}{D_1}$, this leads to

$$D_1 \hat{\vec{n}} \cdot \vec{\nabla} \xi \big|_{liquid} = u_n(\xi_2^{(12)} - \xi_1^{(12)}) \tag{3.183}$$

with the unit normal vector pointing into the liquid phase and $\vec{\nabla}\xi\big|_{liquid}$ representing the composition gradient at the sharp phase boundary calculated from the liquid side. This is the well-known boundary condition for the composition field from sharp interface modelling in the special case of zero diffusion in the solid. It corresponds to expression (2.193) if we set $D_s = 0$.
Combining (3.181) and (3.182), we get

$$\begin{aligned} q(\varphi_2^{(0)})\frac{\partial \xi_1^{(1)}}{\partial \eta} &= \tilde{u_n}(k_{12} - r(\varphi_2^{(0)}))\xi_1^{(12)} \\ &= -\tilde{u_n}(1-k_{12})(1-h_2)\xi_1^{(12)} \\ \leftrightarrow \frac{\partial \xi_1^{(1)}}{\partial \eta} &= -\frac{\tilde{u_n}(1-k_{12})(1-h_2)\xi_1^{(12)}}{q(\varphi_2^{(0)})}. \end{aligned}$$

We integrate this equation from η to ∞ and specify the integration constant by ${\xi_1^{(1)}}^*$:

$${\xi_1^{(1)}}^* - \xi_1^{(1)}(\eta) = -\tilde{u_n}\xi_1^{(12)}(1-k_{12})\int_\eta^\infty \frac{1-h_2(\varphi_2^{(0)})}{q(\varphi_2^{(0)})}d\eta.$$

Based on (3.179), the integration variable can be changed according to

$$d\eta = \frac{d\varphi_2^{(0)}}{\varphi_2^{(0)}(1-\varphi_2^{(0)})},$$

and one obtains with $q(\varphi_2^{(0)})$ from (3.169)

$$\xi_1^{(1)}(\eta) = {\xi_1^{(1)}}^* - \tilde{u_n}(1-k_{12})\xi_1^{(12)}F(\varphi_2^{(0)}) \tag{3.184}$$

$$F(\varphi_2^{(0)}) = \int_1^{\varphi_2^{(0)}} \frac{1-h_2(\varphi_2)}{[1-(1-k_{12})h_2(\varphi_2)]\varphi_2(1-\varphi_2)^2}d\varphi_2. \tag{3.185}$$

The phase-field equation of order O(p) is given by

$$[\frac{\partial^2}{\partial \eta^2} - (1 - 6\varphi_2^{(0)} + 6{\varphi_2^{(0)}}^2)]\varphi_2^{(1)} = s{\varphi_2^{(0)}}^2(1-\varphi_2^{(0)})^2\xi_1^{(1)}(\eta) - (\alpha\tilde{u_n} + \tilde{\kappa})\frac{\varphi_2^{(0)}}{\partial \eta} \tag{3.186}$$

and it will be used to determine ${\xi_1^{(1)}}^*$ in (3.184). We multiply both sides of (3.186) with $\frac{\partial \varphi_2^{(0)}}{\partial \eta}$ and by inserting the tangens hyperbolicus according to (3.179) for $\varphi_2^{(0)}$, we find

$$[\frac{\partial^2}{\partial \eta^2} - (1 - 6\varphi_2^{(0)} + 6{\varphi_2^{(0)}}^2)]\frac{\partial \varphi_2^{(0)}}{\partial \eta} = 0.$$

Integrating from $-\infty$ to $+\infty$, we get the equation

$$\int_{-\infty}^{+\infty}[s{\varphi_2^{(0)}}^2(1-\varphi_2^{(0)})^2\xi_1^{(1)}(\eta) - (\alpha\tilde{u_n} + \tilde{\kappa})\frac{\varphi_2^{(0)}}{\partial \eta}]\frac{\partial \varphi_2^{(0)}}{\partial \eta}d\eta = 0. \tag{3.187}$$

Replacing $\xi_1^{(1)}(\eta)$ with (3.184), the following integrals arise which can be evaluated by utilizing the tangens hyperbolicus profiles $\varphi_2^{(0)}(\eta)$ from (3.179) again and $F(\varphi_2^{(0)})$ from

(3.185):

$$\int_{-\infty}^{+\infty} \frac{\partial \varphi_2^{(0)}}{\partial \eta} \frac{\partial \varphi_2^{(0)}}{\partial \eta} d\eta = \int_0^1 \{\varphi_2^{(0)}(1-\varphi_2^{(0)})\} d\varphi_2^{(0)} = \frac{1}{6}$$

$$\int_{-\infty}^{+\infty} {\varphi_2^{(0)}}^2 (1-\varphi_2^{(0)})^2 \frac{\partial \varphi_2^{(0)}}{\partial \eta} d\eta = \int_0^1 \{{\varphi_2^{(0)}}^2 - 2{\varphi_2^{(0)}}^3 + {\varphi_2^{(0)}}^4\} d\varphi_2^{(0)} = \frac{1}{30}$$

$$\int_{-\infty}^{+\infty} {\varphi_2^{(0)}}^2 (1-\varphi_2^{(0)})^2 F(\varphi_2^{(0)}) \frac{\partial \varphi_2^{(0)}}{\partial \eta} d\eta$$

$$= \int_0^1 \{\frac{\partial}{\partial \varphi_2^{(0)}} [\frac{1}{3}{\varphi_2^{(0)}}^3 - \frac{1}{2}{\varphi_2^{(0)}}^4 + \frac{1}{5}{\varphi_2^{(0)}}^5] F(\varphi_2^{(0)})\} d\varphi_2^{(0)}$$

$$= [\frac{1}{3}{\varphi_2^{(0)}}^3 - \frac{1}{2}{\varphi_2^{(0)}}^4 + \frac{1}{5}{\varphi_2^{(0)}}^5] F(\varphi_2^{(0)})\Big|_0^1 - \int_0^1 [\frac{1}{3}{\varphi_2^{(0)}}^3 - \frac{1}{2}{\varphi_2^{(0)}}^4 + \frac{1}{5}{\varphi_2^{(0)}}^5] \frac{dF(\varphi_2^{(0)})}{d\varphi_2^{(0)}} d\varphi_2^{(0)}$$

$$= -\int_0^1 \frac{[\frac{1}{3}{\varphi_2^{(0)}}^3 - \frac{1}{2}{\varphi_2^{(0)}}^4 + \frac{1}{5}{\varphi_2^{(0)}}^5](1-h_2(\varphi_2^{(0)}))}{\varphi_2^{(0)}(1-\varphi_2^{(0)})^2[1-(1-k_{12})h_2(\varphi_2^{(0)})]} d\varphi_2^{(0)}$$

$$= -\zeta_{12}$$

One obtains

$$s{\xi_1^{(1)}}^* \frac{1}{30} + s\tilde{u_n}\xi_1^{(12)}(1-k_{12})\zeta_{12} - (\alpha\tilde{u_n} + \tilde{\kappa})\frac{1}{6} = 0$$

and after recovering the original quantities from the substitutes defined in (3.170), (3.167), (3.172), (3.173) and (3.174) according to

$$\begin{aligned} s &= \frac{15R\delta}{v_m(a_{12} + \frac{1}{3}a_{23} - \frac{1}{3}a_{13})} \{\frac{1}{1-\xi_1^{(12)}} - \frac{k_{12}}{1-\xi_2^{(12)}}\} \\ \alpha &= \frac{D_1 M_{12}^{-1}}{\delta(a_{12} + \frac{1}{3}a_{23} - \frac{1}{3}a_{13})} \\ \tilde{u_n} &= \frac{u_n l}{D_1} \\ \tilde{\kappa} &= l\kappa, \end{aligned}$$

the result is

$${\xi_1^{(1)}}^* = -30\frac{u_n l}{D_1}\xi_1^{(12)}(1-k_{12})\zeta_{12} + \frac{v_m}{3R(\frac{1}{1-\xi_1^{(12)}} - \frac{k_{12}}{1-\xi_2^{(12)}})} \frac{M_{12}^{-1}u_n l}{\delta^2} + \frac{v_m(a_{12} + \frac{1}{3}a_{23} - \frac{1}{3}a_{13})}{3R\delta(\frac{1}{1-\xi_1^{(12)}} - \frac{k_{12}}{1-\xi_2^{(12)}})} l\kappa. \tag{3.188}$$

Figures 3.2 and 3.3 illustrate the composition profiles for the case of a continuous transition layer of finite thickness between the bulk phases and in the limit $\chi_{3,0} \to 0$ of a sharp phase boundary. Note that due to the fact that a slow solidification process with a zero solid diffusion constant is regarded, the composition variables adopt constant values in the bulk solid ([67]).

It is possible now to express the composition at the liquid side of the sharp phase boundary $\xi_{I,l}$ used in sharp interface modelling (compare equation (2.194)) by quantities which are available in our thin-interface analysis of the phase-field approach. As shown in Figure 3.3, $\xi_{I,l}$ matches the constant value of ξ_1 in the solid. This constant value, in turn, agrees with $\xi_1(\chi_3 \geq \chi_{3,0})$ in Figure 3.2 which can be obtained as the limit $\eta \to \infty$ of the inner

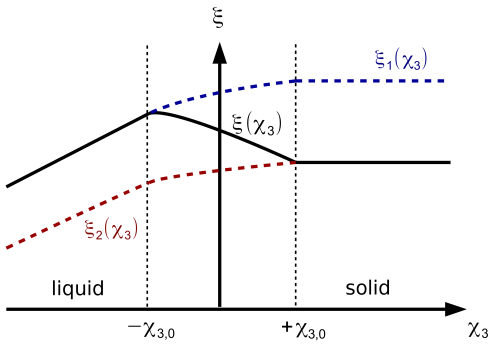

Figure 3.2.: Composition profile for a phase boundary with finite thickness

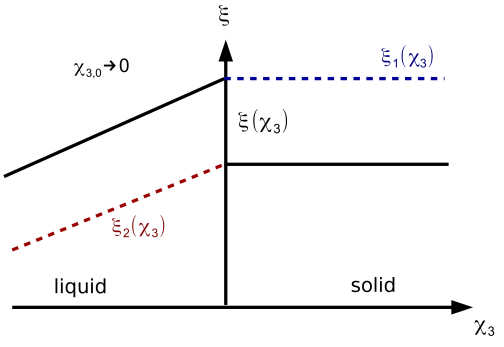

Figure 3.3.: Composition profile for a sharp interface

expansion. Using (3.178), (3.180) and (3.184), we get

$$\begin{aligned}\xi_{I,l} &= \xi_1(\chi_3 \geq \chi_{3,0}) \\ &= \lim_{\eta\to\infty} \xi_1(\eta) \\ &= \lim_{\eta\to\infty} \{\xi_1^{(12)} + p[\xi_1^{(1)^*} - \tilde{u_n}\xi_1^{(12)}(1-k_{12})F(\varphi_2^{(0)}(\eta))]\} \\ &= \xi_1^{(12)} + p\xi_1^{(1)^*} - p\tilde{u_n}\xi_1^{(12)}(1-k_{12})F(1) \\ &= \xi_1^{(12)} + p\xi_1^{(1)^*}. \end{aligned} \tag{3.189}$$

Assuming a straight liquidus line in the phase diagram, we can write

$$T_L(\xi) = T_e + m_{12}(\xi - \xi_e) \tag{3.190}$$

with the eutectic temperature T_e, the eutectic composition ξ_e and the slope m_{12} . By transforming (3.190), we can express the corresponding equilibrium composition $\xi_1^{(12)}$ as a function of temperature

$$\xi_1^{(12)} = \xi_e - \frac{T_e - T}{m_{12}}. \tag{3.191}$$

(3.189) can be rearranged after inserting (3.191) for $\xi_1^{(12)}$ according to

$$T = T_e + m_{12}(\xi_{I,l} - \xi_e) - m_{12}p\xi_1^{(1)^*}.$$

Repacing p according to its defintion in (3.171), $p = \frac{\delta}{l}$, and using (3.188), we get

$$\begin{aligned} T =& T_e + m_{12}(\xi_{I,l} - \xi_e) + m_{12}[30\frac{\xi_1^{(12)}(1-k_{12})\zeta_{12}}{D_1}\delta - \frac{v_m M_{12}^{-1}}{3R(\frac{1}{1-\xi_1^{(12)}} - \frac{k_{12}}{1-\xi_2^{(12)}})\delta}]u_n \\ &- \frac{v_m m_{12}(a_{12} + \frac{1}{3}a_{23} - \frac{1}{3}a_{13})}{3R(\frac{1}{1-\xi_1^{(12)}} - \frac{k_{12}}{1-\xi_2^{(12)}})}\kappa. \end{aligned} \tag{3.192}$$

This must be compared to expression (2.194) for the interface temperature from sharp interface theory

$$T = T_e + m_{12}(\xi_{I,l} - \xi_e) - d_\kappa\kappa - \beta_{12}u_n \tag{3.193}$$

with the linear kinetic coefficient β_{12} and the Gibbs-Thomson coefficient

$$d_\kappa = \frac{\sigma_{12}T_e}{\rho L_{12}}. \tag{3.194}$$

In the expression for the Gibbs-Thomson coefficient, σ_{12} describes surface tension between the phases α and l and L_{12} represents the corresponding latent heat.
Obviously, an expression proportional to curvature κ representing the Gibbs-Thomson effect does also appear in our model according to (3.192). However, the corresponding Gibbs-Thomson coefficient d_κ is different from (3.194). Therefore, a numerical investigation will be performed in section 4.3 which clarifies that the effect may nevertheless be reproduced quantitatively correctly.
The mobility of the phase boundaries can be determined by a comparison of the velocity-dependent terms in (3.192) and (3.193):

$$M_{12}^{-1} = \frac{3R(\frac{1}{1-\xi_1^{(12)}} - \frac{k_{12}}{1-\xi_2^{(12)}})\delta}{v_m}\{\frac{\beta_{12}}{m_{12}} + \frac{30\xi_1^{(12)}(1-k_{12})\zeta_{12}}{D_1}\delta\}.$$

For the validation cases to be consisdered in chapter 5, we can neglect the kinetic effect and set $\beta_{12} = 0$. The mobility of a phase boundary between the liquid phase and one of the two solid phases $i \in \{2, 3\}$ is hence given by

$$M_{1i}^{-1} = \frac{90R(\frac{1}{1-\xi_1^{(1i)}} - \frac{k_{1i}}{1-\xi_i^{(1i)}})\xi_1^{(1i)}(1-k_{1i})\zeta_{1i}}{v_m D_1}\delta^2 \tag{3.195}$$

$$\zeta_{1i} = \frac{1}{30}\int_0^1 \frac{h_i(\varphi_i^{(0)})(1-h_i(\varphi_i^{(0)}))}{\varphi_i^{(0)}(1-\varphi_i^{(0)})^2[1-(1-k_{1i})h_i(\varphi_i^{(0)})]} d\varphi_i^{(0)}. \tag{3.196}$$

3.4.2. Thin-Interface Analysis for Elemental Materials

We also perform a thin-interface analysis based on the analysis by Karma and Rappel in [43] for the special case of elemental materials. We neglect again convective effects and regard a moving sharp interface between the solid and the liquid phase. In the limit $\Delta V \to 0$, we replace $\Delta \to \delta$ and $\Phi \to \varphi$ in (3.163) and (3.164) and obtain the coupled set of equations

$$\begin{aligned} M^{-1}\frac{\partial\varphi}{\partial t} &= a\delta\vec{\nabla}^2\varphi - \frac{a}{\delta}\varphi(1-\varphi)(1-2\varphi) - 15\varphi^2(1-\varphi)^2\frac{1}{T}L\rho\frac{T_m - T}{T_m} \\ \rho c\frac{\partial T}{\partial t} &= \lambda\vec{\nabla}^2 T - 30\varphi^2(1-\varphi)^2 L\rho\frac{\partial\varphi}{\partial t}. \end{aligned}$$

The heat conductivity λ is assumed to be constant here. If we replace temperature by the new coordinate $\psi = \frac{T-T_m}{T_m}$, we get after some minor transformations

$$\begin{aligned} \frac{M^{-1}\delta}{a}(1+\psi)\frac{\partial\varphi}{\partial t} &= (1+\psi)\delta^2\vec{\nabla}^2\varphi - (1+\psi)\varphi(1-\varphi)(1-2\varphi) + 15\varphi^2(1-\varphi)^2\frac{L\rho\delta}{aT_m}\psi \\ \rho c\frac{\partial\psi}{\partial t} &= \lambda\vec{\nabla}^2\psi - 30\varphi^2(1-\varphi)^2\frac{L\rho}{T_m}\frac{\partial\varphi}{\partial t}. \end{aligned}$$

The next step is to introduce dimensionless coordinates

$$\begin{aligned} \vec{x} = l\tilde{\vec{x}} \quad &\to \quad \vec{\nabla} = \frac{1}{l}\tilde{\vec{\nabla}} \\ t = \frac{l^2\rho c}{\lambda}\tilde{t} \quad &\to \quad \frac{\partial}{\partial t} = \frac{D_1}{l^2}\frac{\partial}{\partial\tilde{t}}, \end{aligned}$$

with l being the diffusion length of the temperature field now. Using $p = \frac{\delta}{l} << 1$ as well as

$$\alpha = \frac{M^{-1}\lambda}{a\rho c\delta} \qquad \beta = \frac{L\rho\delta}{2T_m a}$$
$$\gamma = \frac{L}{cT_m} \qquad h = 6\varphi^5 - 15\varphi^4 + 10\varphi^3$$
$$g = \frac{1}{2}\varphi^2(1-\varphi)^2,$$

we obtain

$$\alpha p^2 \frac{\partial \varphi}{\partial \tilde{t}} = p^2 \tilde{\vec{\nabla}}^2 \varphi - \frac{\partial g}{\partial \varphi} + \beta \frac{\partial h}{\partial \varphi} \frac{\psi}{1+\psi} \tag{3.197}$$
$$\frac{\partial \psi}{\partial \tilde{t}} = \tilde{\vec{\nabla}}^2 \psi - \gamma \frac{\partial h}{\partial \tilde{t}}. \tag{3.198}$$

Aside from the factor $\frac{\psi}{(1+\psi)}$ in (3.197), which however does not induce any significant changes, equations (3.197) and (3.198) are the same as equations (26) and (27) in [43]. Concerning the following calculation steps, I therefore refer to [43] and only the final result for the inverse mobility is presented here. Assuming $\delta << l$, the temperature at the phase boundary is given by

$$T = T_m - \frac{\sigma\kappa T_m}{L\rho} - \beta_k u_n \tag{3.199}$$

with the linear kinetic coefficient β_k and the normal velocity of the phase boundary u_n if

$$M^{-1} = \frac{3L\rho\delta}{T_m^2}\{\beta_k + \frac{209}{420}\frac{L\rho\delta}{\lambda}\}. \tag{3.200}$$

The elemental material model will be validated with an experiment investigating the melting of gallium for which the kinetic effect can be neglected. Setting $\beta_k = 0$, we obtain

$$M^{-1} = \frac{627}{420}\frac{L^2\rho^2\delta^2}{\lambda T_m^2}. \tag{3.201}$$

4. Model Verification

In this chapter, we will investigate if the implemented model reproduces the properties resulting from our analytical considerations before. On the one hand, we will examine if the surface and bulk parts of free energy $f_{surface}$ and f_{bulk} manifest themselves in the simulation results by generating the desired behaviour at phase surfaces and by representing a given phase diagram. On the other hand, the transition to neighbouring modelling appoaches will be checked. In particular, on a sufficiently fine grid, the large-scale equations (3.156)-(3.160) for Φ_i and the dynamic Δ should converge to a classical phase-field model with a constant δ. Additionally, the results of sharp-interface modelling should be reproduced by the classical phase-field model if δ is sufficiently small, i.e. much smaller than the boundary layer width of the dominating diffusion field. Finally, there should also be a connection of the developed model with the volume-of-fluid method ([91]) by Hirt and Nichols if the elemental material equations of subsection 3.3.2 are taken and the solid phase is fitted with material properties corresponding to a fluid.

4.1. Surface Part of Free Energy Density

4.1.1. Tangens Hyperbolicus Profile

The surface part of free energy density has been constructed to generate tangens hyperbolicus equilibrium profiles for the phase-fields φ_i around flat sharp interfaces for constant values of δ. We verify this by simulating the formation of an equilibrium phase boundary

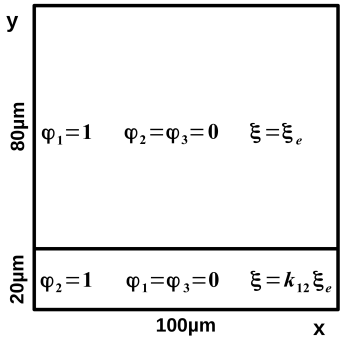

Figure 4.1.: Simulation setup with initial values

between the liquid phase and solid phase α of $CBr_4 - C_2Cl_6$ (material properties in appendix E) in a two-dimensional volume of interest under isothermal conditions $T = T_e$. The

dimensions of the volume are $100\mu m \times 100\mu m$ with a grid spacing of $0.5\mu m$ and the compositions of the two phases correspond to their equilibrium values $\xi_1^{(12)}(T_e) = \xi_e = 0.118$ and $\xi_2^{(12)}(T_e) = k_{12}\xi_e = 0.0885$. The volume of interest and the initial values of the phase-fields and the composition field are shown in Figure 4.1. The gradients of all fields were set to zero at all boundaries.
The resulting profile of the phase-field φ_1 in a simulation with $\delta = 0.6 \cdot 10^{-6} m$ is presented in Figure 4.2 and agrees very well with the tangens hyperbolicus profile. Note that the simulated profile has been shifted in y-direction to be centered around $y = 0$ for a comparison with the standard tangens hyperbolicus. Further calculations reveal that the width of the continuous transition layer between the bulk phases depends linearly on δ (see Figure 4.3).

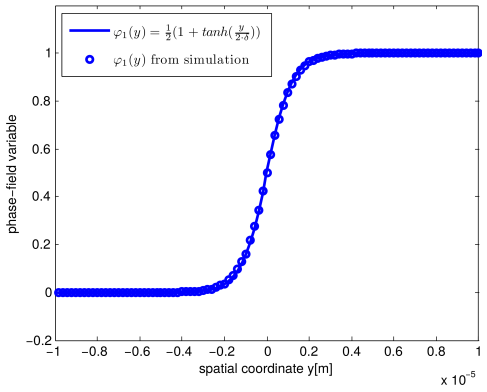

Figure 4.2.: Equilibrium Profile of the phase-field φ_1

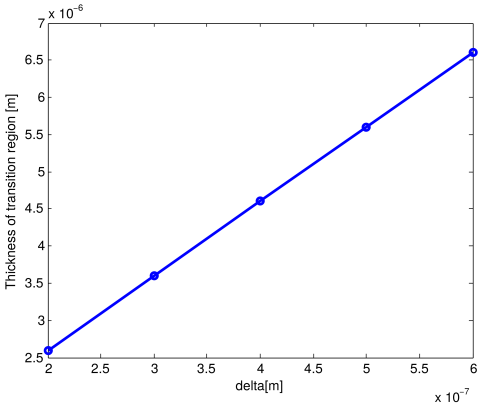

Figure 4.3.: Dependence of transition layer width on δ

4.1.2. Convergence of $\Delta \to \delta$ on Small Length Scales

We keep the simulation setup from Figure 4.1 using the material properties of $CBr_4 - C_2Cl_6$, but we leave the state of equilibrium by changing the initial composition of the melt from $\xi_e = 0.118$ to $k_{12}\xi_e = 0.0885$. Furthermore, a constant temperature gradient $G = 10^5 \frac{K}{m}$ is applied in positive y-direction which generates the eutectic temperature $T_e = 357.6K$ at the starting position of the phase boundary at $y = 20\mu m$. The liquidus temperature of the melt is given by $T_L(0.0885) = 359.99K$, which is $2.39K$ higher than the temperature at the phase boundary. Consequently, solidification is initiated and the phase boundary indicated in Figure 4.1 moves upwards. The simulations are performed with a constant $\delta = 10^{-6} m$ and with dynamically calculated values of Δ according to (3.83) with $\Delta \geq \delta$. Note that in order to generate a tangens hyperbolicus profile in phase-field simulations, the contribution of $f_{surface} \propto \frac{1}{\delta}$ to the phase-field equations must dominate over the contribution of f_{bulk}. The choice $\delta = 10^{-6} m$ is small enough to fulfill this condition. Additionally, it is important for the convergence $\Delta \to \delta$ that the grid is fine enough to permit a resolution of the tangens hyperbolicus profile. For $\delta = 10^{-6} m$, the transition layer width is $l_t \approx 10\delta = 10\mu m$. Therefore, a grid spacing of $1\mu m$ has been chosen such that a sufficient resolution is achieved with 10 grid cells in the transition layer.
As Figure 4.4 shows by means of a profile along the central vertical line $x = 50\mu m$, the dynamically calculated Δ values are larger than $\delta = 10^{-6} m$ at first. However, the phase-field profiles tend towards the tangens hyperbolicus shape with increasing time and Δ approaches the constant value of $\delta = 10^{-6} m$. For $t \geq 1s$, $\Delta = \delta$ is realized everywhere and permanently. Figure 4.5 presents the phase-field profiles for both cases along the same line $x = 50\mu m$ after 1s and illustrates a good agreement. The statement of subsection 3.2.4 that Δ gives back δ at flat binary interfaces on a sufficiently fine grid is therefore

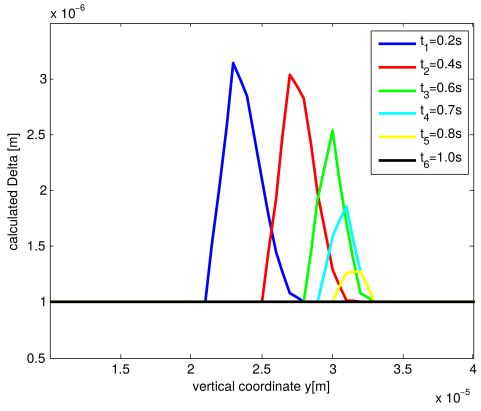

Figure 4.4.: Calculated Δ-values at different times along $x = 50\mu m$

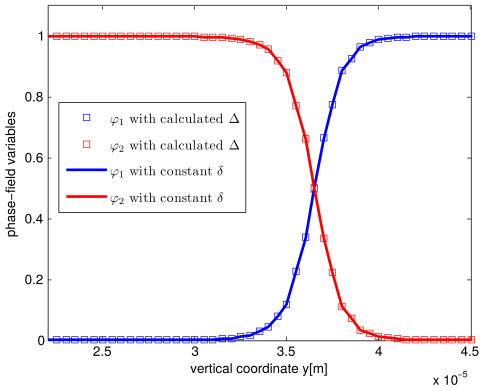

Figure 4.5.: Profiles of the phase-field functions at $t = 1s$

confirmed numerically.

4.1.3. Binary Mixtures on Large Length Scales

4.1.3.1. Curved Binary Mixtures

We have seen that $f_{surface}$ enforces tangens hyperbolicus profiles around sharp interfaces on small length scales. Concerning macroscopic length scales, it has been shown analytically in subsection 3.2.3 that $f_{surface}$ in combination with the Δ-model works on minimizing the curvature of binary mixture states. In order to verify this, we stretch the volume of interest in Figure 4.1 by a factor of 1000, leading to a square with a side length of $0.1m$ and bend the lower boundary. The grid spacing is $1mm$. On the basis of a preceding calculation, a curved mixture of the liquid phase and solid phase α of $CBr_4 - C_2Cl_6$ is created and used as the initial state for this paragraph (see Figure 4.6). Starting from this initial state, the phase-field equations are solved utilizing the Δ-model with the contributions from f_{bulk} being set to zero. The resulting dynamics is therefore solely due to the surface part in the governing equations and we expect that according to equations (3.93)-(3.95), the final equilibrium state is free of curvature. As Figure 4.7 shows, this is indeed the case.

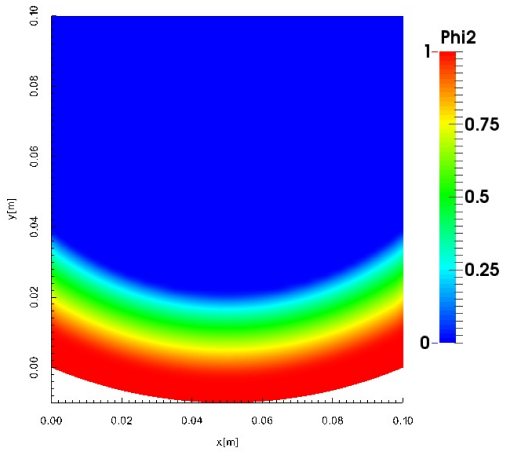

Figure 4.6.: Curved α-l mixture used as initial state

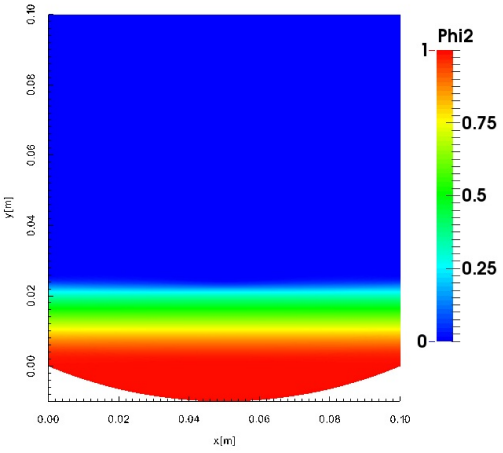

Figure 4.7.: Final equilibrium state due to the action of $f_{surface}$

4.1.3.2. Flat Binary Mixtures

In this paragraph, we withdraw the bending of the lower boundary and regard a square with a side length of $0.1m$ filled with $CBr_4 - C_2Cl_6$. The starting position of the liquid-α phase boundary with $T = T_e$ shall be located at $y = 0.02m$ and a temperature gradient of $G = 100\frac{K}{m}$ shows in the positive y-direction. The initial values and boundary conditions of the phase-fields and the composition field correspond to those in subsection 4.1.2 and we expect the formation of a mushy layer between the solidus temperature $T = T_e = 357.6K$ at $y = 0.02m$ and the liquidus temperature $T = T_L(0.0885) = 359.99K$ at $y = 0.044m$. The simulations are performed again with the two variants of subsection 4.1.2, i.e. with a constant $\delta = 10^{-6}m$ and with dynamically calculated values of Δ under the condition $\Delta \geq \delta$. A comparison of Figures 4.8 and 4.9 shows that the mushy layer fully develops in the latter simulation while this is not the case for the constant δ. The constant value of $\delta = 10^{-6}m$ attaches an oversized importance to the surface terms being proportional to $\frac{1}{\delta}$ which prevents a complete formation of the mushy layer. Additionally, it is shown

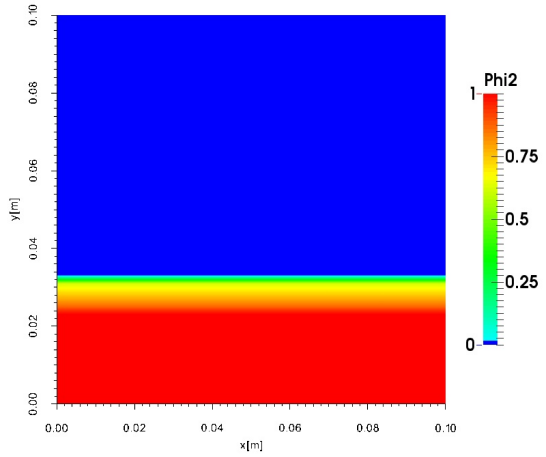

Figure 4.8.: Equilibrium state of Φ_2 for $\delta = 10^{-6}m$

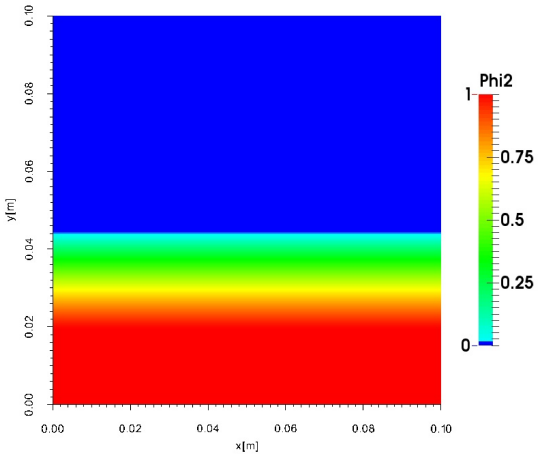

Figure 4.9.: Equilibrium state of Φ_2 for dynamically calculated Δ

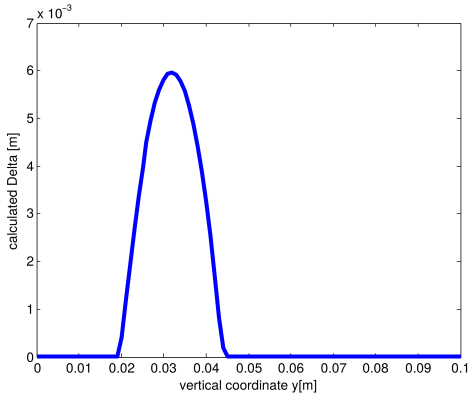

Figure 4.10.: Calculated Δ-values along $x = 0.05m$ in Figure 4.9

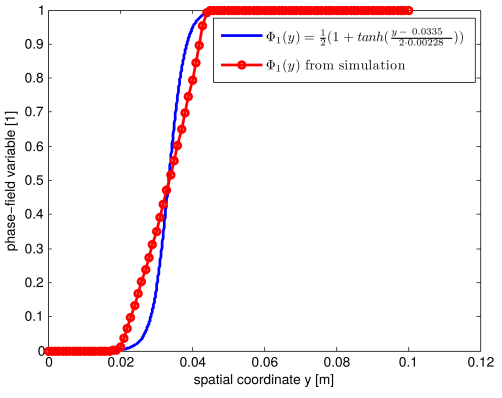

Figure 4.11.: Equilibrium profile of Φ_1 along $x = 0.05m$ in Figure 4.9

in Figure 4.10 that the calculated Δ's do not converge against δ here as in subsection 4.1.2, but adopt values in the mm range. The profile of Φ_1 corresponding to Figure 4.9 along $x = 0.05m$ is presented in Figure 4.11. It is obvious that the profile is not a tangens hyperbolicus anymore as in subsection 4.1.2, but that it is determined instead by the thermodynamic properties of the involved phases represented by f_{bulk}. We can therefore

conclude that based on the dynamical calculation of Δ, the phase-field equations can be applied independently from the spatial dimensions of interest. While the equilibrium profiles are determined by $f_{surface}$ on small length scales (see the tangens hyperbolicus profiles in Figure 4.5) and the phase mixing regions are thin layers between the bulk phases, the model for $f_{surface}$ in combination with the Δ-model allows the profiles to develop according to the requirements of f_{bulk} to form mushy layers of appropriate thickness on large lengths. As Figure 4.8 shows, a transition between different length scales is not possible with a single constant value of δ. The Δ-model therefore assigns an appropriate magnitude to phase surface effects represented by $f_{surface}$ in comparison with f_{bulk}.

4.1.3.3. Binary Mixtures With a Non-Uniform Thickness

The examples considered so far in subsection 4.1.3 exhibited binary mixture layers with uniform thicknesses. The original reason for introducing the dynamic $\Delta(\vec{x}, t)$ has been that the thickness of macroscopic binary mixture states may be non-uniform, which makes a constant $\Delta(\vec{x}, t) = \Delta_0$ inappropriate. The objective of this paragraph is to demonstrate numerically that the proposed model for the dynamic calculation of $\Delta(\vec{x}, t)$ based on equation (3.83) is able to characterize mixture states with spatially-dependent thicknesses. Additionally, it is shown that the same results cannot be reproduced with a constant Δ_0. To create a mushy layer with a non-uniform thickness, we regard a more general scenario including convection, heat and composition transport. The investigation is done by means of an aqueous ammonium chloride solution (material properties in appendix G) as the thermal and compositional linear expansion coefficients of $CBr_4 - C_2Cl_6$, the material considered so far, could not be found in the literature. The simulation volume stays the same square with a side length of $0.1m$ and a grid spacing of $1mm$, but the left wall is cooled to a constant temperature $T = 243.15K < T_e = 257.75K$ and the right wall is kept at $T = 313.15K$ as indicated in Figure 4.12. At the beginning of the simulation, the

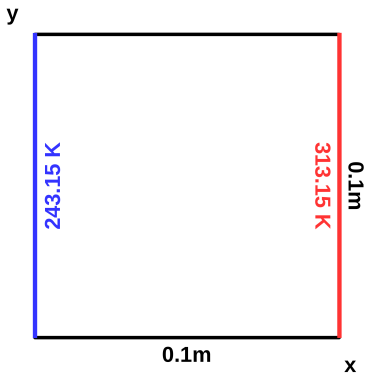

Figure 4.12.: Simulation setup

square is completely filled with a melt of composition $\xi = 0.7$ with $T = 313.15K$. As time goes by, a solid phase with a mushy layer grows from the left wall which is influenced by the heat and composition transport of the velocity field. Figures 4.13 and 4.14 show Φ_2 and Δ at $t = 600s$. The width of the mushy layer is non-uniform here and adopts a value of about $5mm$ at the top and an about 2.6 times larger value of $13mm$ at the bottom. The dynamically calculated Δ values do not directly represent these thicknesses, but the Δ-model is capable to provide a measure for them and to reflect the non-uniformity. The values calculated at the bottom of about $8mm$ are also approximately 2.6 times larger than the values of $3mm$ calculated at the top. In order to make clear that the results cannot be reproduced by simply choosing a constant value of about an appropriate magnitude, Figures 4.15 and 4.16 show the results of corresponding simulations with constant values

$\Delta = 3mm$ and $\Delta = 8mm$. In the calculation with $\Delta = 3mm$, the mushy layer thickness is $6mm$ on top (+20%) and $11mm$ at the bottom (-15%) while the corresponding values are $7mm$ (+40%) and $11mm$ (-15%) for the case $\Delta = 8mm$. Additionally, without the preceding calculation of Figures 4.13 and 4.14, it would not have been clear in which range the constant values shall be chosen.

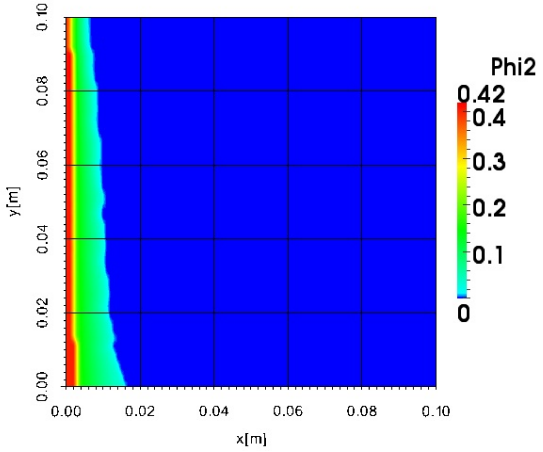

Figure 4.13.: Phase-field Φ_2 at $t = 600s$ with dynamically calculated values of Δ

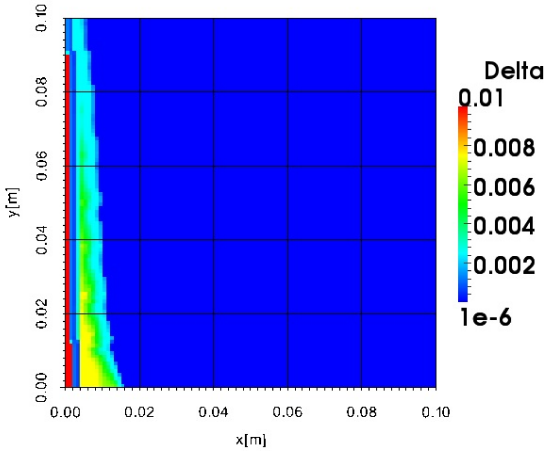

Figure 4.14.: Calculated values of Δ at $t = 600s$

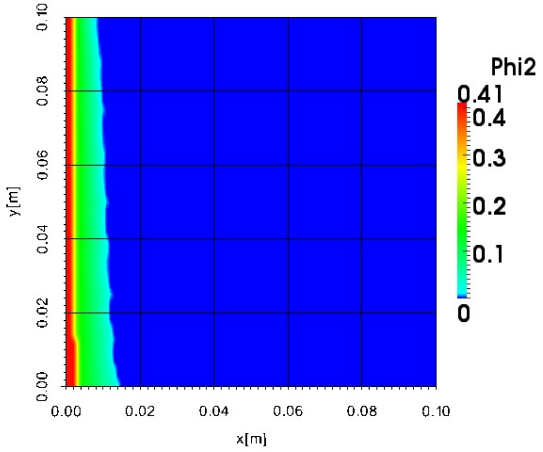

Figure 4.15.: Phase-field Φ_2 at $t = 600s$ with $\Delta = 3mm$

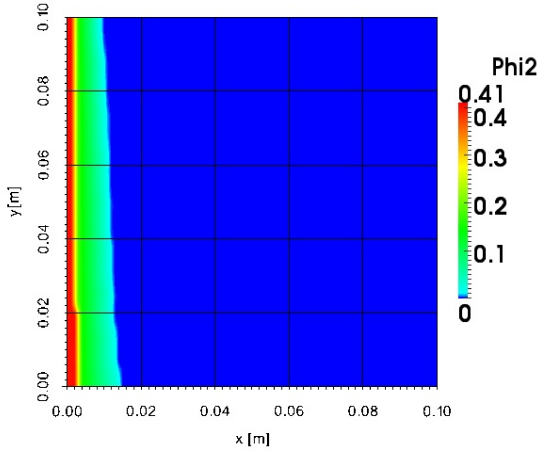

Figure 4.16.: Phase-field Φ_2 at $t = 600s$ with $\Delta = 8mm$

4.2. Bulk Part of Free Energy Density

The implemented model should reproduce the characteristic properties of the equilibrium phase diagram in slow solid-liquid phase change processes. In this section, the material properties of the binary eutectic alloy $CBr_4 - C_2Cl_6$ (see appendix E) are utilized again.

4.2.1. Reproduction of Equilibrium Compositions from the Phase Diagram

In order to investigate the reproduction of equilibrium compositions in accordance with the phase diagram, we go back to the small square with dimensions $100\mu m \times 100\mu m$ and solve the phase-field equations and the composition equation for different constant values T_0 of temperature with initial melt compositions $\xi_0 < \xi_1^{(12)}(T_0)$ and $\xi_0 > \xi_1^{(13)}(T_0)$, respectively. The simulation setup with the corresponding boundary conditions and inital values is presented in Figure 4.17. Note that solidification starts at the lower boundary and that the system decides itself which of the two solid phases is formed. δ is set to $0.3\mu m$ as this choice generates continuous transition layers between the pure phases which are sufficiently thin to approximate sharp interfaces in the current setup. The grid spacing of $0.5\mu m$ assures an appropriate resolution with 6 cells in the transition layer. Tables 4.1 and

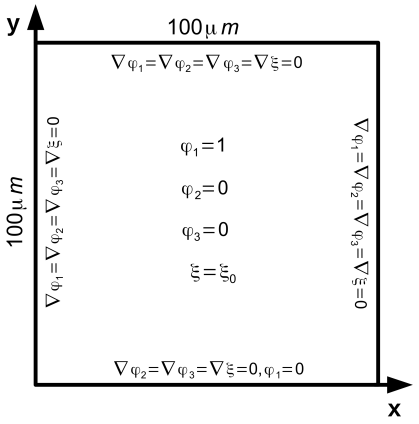

Figure 4.17.: Simulation setup with initial values and boundary conditions

4.2 specify the chosen inital values of composition ξ_0 and the corresponding temperatures T_0 of the simulations. For that matter, the values of ξ_0 have been chosen slightly below (if $\xi_0 < \xi_e$) and above (if $\xi_0 > \xi_e$) the equilibrium composition of the liquid phase at temperature T_0 in order to guarantee a sufficiently slow solidification rate. Consequently, the phase boundary stays close to equilibrium and the compositions of the adjacent liquid phase and the solid should correspond to the equilibrium values $\xi_j^{(1j)}(T_0)$ and $\xi_1^{(1j)}(T_0)$ from the phase diagram.

T_0	ξ_0	$\xi_1^{(12)}(T_0)$
$357.6K$	0.116	0.118
$360.0K$	0.086	0.088
$362.0K$	0.062	0.064
$364.0K$	0.037	0.039
$366.0K$	0.0138	0.0143

Table 4.1.: Initial values of composition ($\xi_0 < \xi_e$) for different constant temperatures T_0

T_0	ξ_0	$\xi_1^{(13)}(T_0)$
$357.6K$	0.120	0.118
$395.0K$	0.347	0.345
$430.0K$	0.559	0.557
$475.0K$	0.832	0.830

Table 4.2.: Initial values of composition ($\xi_0 > \xi_e$) for different constant temperatures T_0

A first result of the simulations is that in accordance with the phase diagram, simulations with $\xi_0 < \xi_e$ lead to the formation of solid phase α while solid phase β is generated in simulations with $\xi_0 > \xi_e$. On the small length scale considered here, $f_{surface} \propto \frac{1}{\delta}$ separates coexisting bulk phases up to thin transition layers. Figures 4.18 and 4.19 show the phase-field function φ_2 and the corresponding composition profile in y-direction from the simulation ($T_0 = 360.0K, \xi_0 = 0.086$) at $t = 4s$. One can see in Figure 4.19 that there

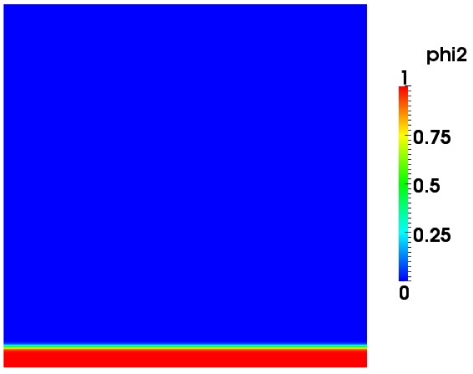

Figure 4.18.: Phase-field φ_2 indicating solid phase α for ($T_0 = 360.0K, \xi_0 = 0.086$) at $t = 4s$

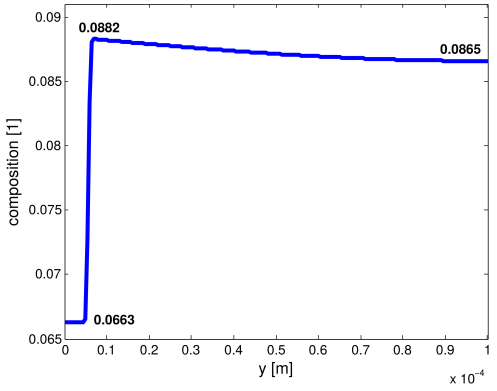

Figure 4.19.: Composition profile in y-direction at $t = 4s$

is a constant composition of 0.0663 in the solid phase α and a composition maximum of 0.0882 in the liquid adjacent to the phase boundary due to the rejection of component B by the solid. Going further into the liquid, composition approaches its initial value of 0.086. Therefore, the equilibrium compositions of solid phase α and the liquid phase at temperature $T_0 = 360.0K$ resulting from the phase diagram, $\xi_1^{(12)}(T_0) = 0.088$ and $\xi_2^{(12)}(T) = 0.066$, are reproduced well by the simulation. Figures 4.20 and 4.21 show systematic comparisons between the simulation results and the specifications of the phase diagram and reveal a good agreement.

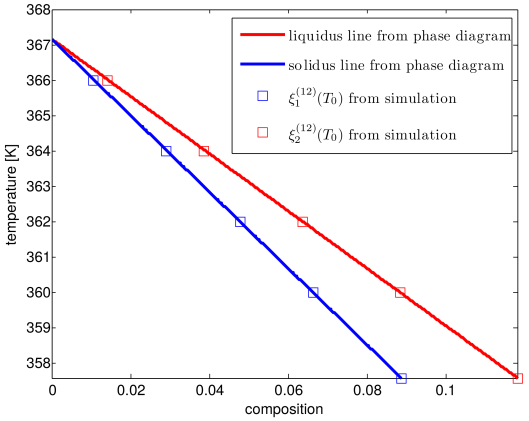

Figure 4.20.: Comparison of simulated equilibrium compositions with the liquidus and solidus lines of $CBr_4 - C_2Cl_6$ for $\xi_0 < \xi_e$

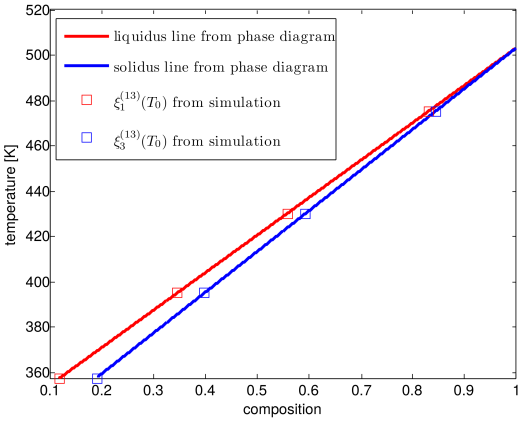

Figure 4.21.: Comparison of simulated equilibrium compositions with the liquidus and solidus lines of $CBr_4 - C_2Cl_6$ for $\xi_0 > \xi_e$

4.2.2. Reproduction of Stability Properties from the Phase Diagram

In this subsection, we investigate the instability of phase boundaries, which manifests itself on macroscopic length scales in the formation of a mushy layer between the bulk liquid and solid phases. For a given value of ξ_0, one can read from the phase diagram if and in what temperature interval a mushy layer should develop and which of the two solid phases should coexist with the liquid therein. In order to further verify the developed model, we adopt the simulation setup from Figure 4.17 with the same initial and boundary conditions. However, the side length is increased by a factor of 1000 to $0.1m$ and a uniform grid with a spacing of $1mm$ is utilized. The simulations are performed for different constant values ξ_0 of the melt composition in a temperature gradient G which shows upwards in Figure 4.17.

The isotherm representing the solidus temperature $T_S(\xi_0)$ corresponding to composition ξ_0 is located at the lower boundary of the simulation volume at the beginning and moves upwards with all other isotherms with a small constant velocity $v = 0.5\frac{\mu m}{s}$. We expect the formation of a completely solid phase below the isotherm $T_S(\xi_0)$ and a purely binary mushy layer in the region $T_S(\xi_0) < T < T_L(\xi_0)$. Because the width of the temperature interval $[T_s(\xi_0), T_l(\xi_0)]$ is much smaller for $\xi_0 < \xi_e$ than for $\xi_0 > \xi_e$, different temperature gradients $G = 100\frac{K}{m}$ $(\xi_0 < \xi_e)$ and $G = 200\frac{K}{m}$ $(\xi_0 > \xi_e)$ were used to keep the mushy layer width in a reasonable scope compared to the dimensions of the simulation volume.

As an example, simulation results for the eutectic composition $\xi_0 = \xi_e = 0.118$ and for the non-eutectic composition $\xi_0 = 0.09$ are presented in Figures 4.22 and 4.23. One can see that the phase boundary does indeed stay sharp in the eutectic case, whereas a mushy layer develops for $\xi_0 = 0.09$. According to the profiles in Figure 4.24, this mushy layer is really a purely binary liquid-α mixture as the phase diagram requires. We mention here that the solid being formed in the region $T \leq T_e$ is in general a mixture of solid phases α and β. In Figure 4.22, the solid contains a phase α volume fraction of $\Phi_2 = 0.706$ and correspondingly $\Phi_3 = 0.294$. In Figure 4.23, the values are $\Phi_2 = 0.985$ and $\Phi_3 = 0.015$. This will be discussed in more detail in the next subsection. A systematic comparison of the mushy layer extents with the phase diagram is provided in Figures 4.25 and 4.26. It shows a good agreement.

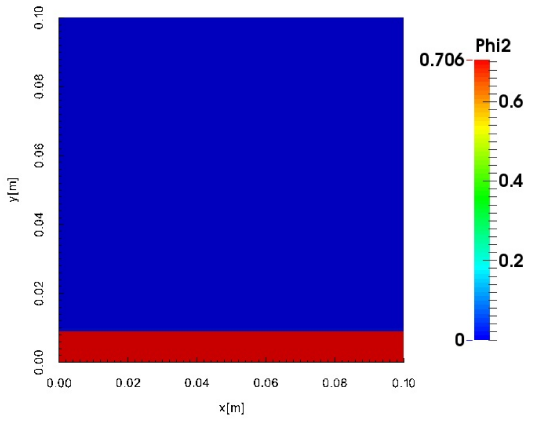

Figure 4.22.: Steady-State at eutectic composition $\xi_0 = \xi_e = 0.118$

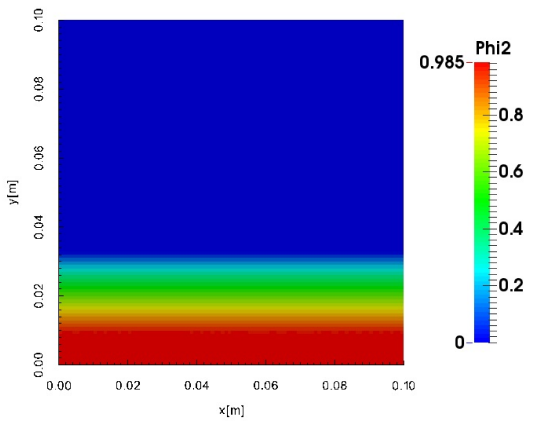

Figure 4.23.: Steady-State at composition $\xi_0 = 0.09$

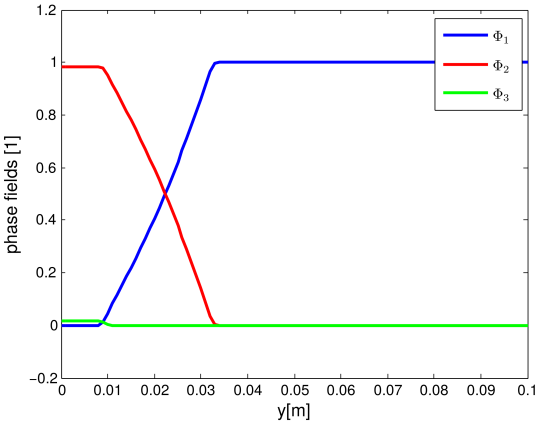

Figure 4.24.: Profiles of the phase-fields in Figure 4.23 along the line $x = 0.05m$

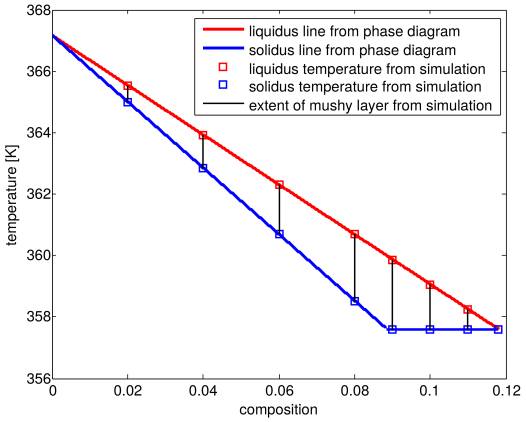

Figure 4.25.: Comparison of simulation results with the liquidus and solidus lines of the phase diagram for $\xi_0 < \xi_e$

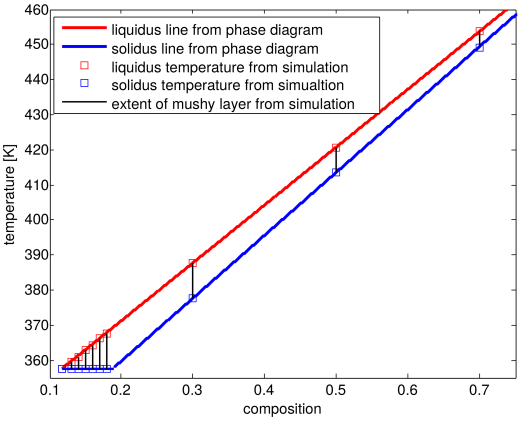

Figure 4.26.: Comparison of simulation results with the liquidus and solidus lines of the phase diagram for $\xi_0 > \xi_e$

4.2.3. Composite Solids

As mentioned before and indicated in Figures 4.22 and 4.23, the formation of composite solids is possible. The latter will occur if the initial composition of the melt lies within the eutectic plateau, i.e. if

$$\xi_2^{(12)}(T_e) \leq \xi_0 \leq \xi_3^{(13)}(T_e). \tag{4.1}$$

Under condition (4.1), mass conservation leads to

$$\xi_0 = \Phi_2 \xi_2^{(12)}(T_e) + (1-\Phi_2)\xi_3^{(13)}(T_e) \quad \leftrightarrow \quad \Phi_2 = \frac{\xi_0 - \xi_3^{(13)}(T_e)}{\xi_2^{(12)}(T_e) - \xi_3^{(13)}(T_e)} \tag{4.2}$$
$$\Phi_3 = 1 - \Phi_2.$$

According to (4.2), the volume fraction of solid phase α in the composite solid approaches 1 for $\xi_0 \to \xi_2^{(12)}(T_e)$ and 0 for $\xi_0 \to \xi_3^{(13)}(T_e)$. For $\xi_0 < \xi_2^{(12)}(T_e)$, a pure α-solid is obtained and analogously for $\xi_0 > \xi_3^{(13)}(T_e)$ a pure β-solid. On the basis of the simulations presented in the preceding subsection, Figure 4.27 compares the phase volume fractions of the composite solid with the expectations according to mass conservation. Again, we find a good agreement.

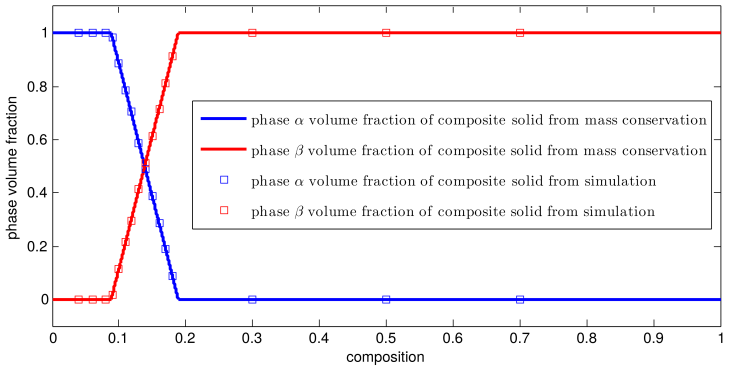

Figure 4.27.: Comparison of the phase volume fractions in the solid resulting from mass conservation with simulation results

4.3. Transition to a Sharp-Interface Model

In this section, we consider the non-averaged model based on the phase indicator functions φ_i with a constant δ and verify its capability to numerically reproduce results from sharp interface modelling if δ is sufficiently small. In particular, it has been demonstrated analytically in the thin-interface analysis in subsection 3.4.1 that the new model is able to describe the undercooling at phase boundaries due to curvature. It will be shown here that the implemented model is able to reproduce this so-called Gibbs-Thomson effect quantitatively correctly. The verification setup has been adopted by Kim et al. ([67]) and will be described in more detail below.

The setup consists of two α-grains of the binary eutectic alloy $CBr_4 - C_2Cl_6$ (material properties in appendix E) which are separated by each other and the adjacent liquid phase by sharp phase boundaries. The sample is placed in a constant external temperature gradient $G = 8000\frac{K}{m}$, which shows upwards in Figure 4.28.

In the framework of sharp-interface modelling, the equilibrium shape of the phase boundary can be calculated in the following manner. If θ is the angle between the x-direction

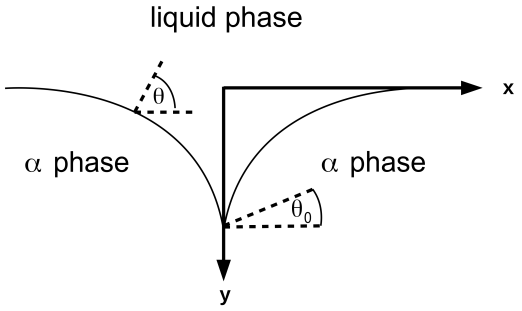

Figure 4.28.: Simulation Setup

and the unit normal on the phase boundary, its value θ_0 at the triple point can be obtained from the force balance

$$\sigma_{22} - 2\sigma_{12}\cos(\theta_0) = 0 \leftrightarrow \theta_0 = \arccos(\frac{\sigma_{22}}{2\sigma_{12}}). \tag{4.3}$$

Therefore, the final contact angle is determined by the ratio of the surface tensions σ_{22} between the two α-grains and σ_{12} between the liquid phase and solid phase α. This angle is related to a certain curvature κ and according to (3.192) to a certain curvature undercooling at the phase boundary. Consequently, the triple point moves downwards in the external temperature gradient G until the necessary undercooling is realized. Based on the boundary conditions $\theta = \theta_0$ at $x = 0$ and $\theta = \frac{\pi}{2}$ at $y = 0$, the points (x, y) defining the position of the sharp equilibrium phase boundary can be obtained by ([67])

$$\begin{aligned} x &= \frac{1}{aG}\int_{\theta_0}^{\theta} \sigma_{12}\frac{\sin(\theta)}{y}d\theta \\ y^2 &= \frac{2}{aG}\sigma_{12}(1-\sin(\theta)) \\ a &= \frac{RT_e}{v_m}\frac{k_{12}-1}{m_{12}}. \end{aligned}$$

In order to investigate the capability of the newly developed model to numerically reproduce sharp interface behaviour and in order to check the reproduction of the Gibbs-Thomson effect in particular, we simulate the above situation for different ratios $\frac{\sigma_{22}}{\sigma_{12}}$. In this context, only the phase-field and composition equations are solved and the phase-field φ_2 is assigned to the right α-grain and φ_3 to the left one. Additionally, the material properties of solid phases α and β appearing in the governing equations are set equal as both solid phases shall represent phase α of $CBr_4 - C_2Cl_6$ in the calculations considered here. The calculations are performed with a constant $\delta = 0.12\mu m$ and a grid spacing of $0.1\mu m$. The results for different ratios $\frac{\sigma_{22}}{\sigma_{12}}$ are presented in Figures 4.29, 4.30 and 4.31.
One can see that the phase-field simulations show a good agreement with the sharp interface solutions. As curvature undercooling plays a vital role here, we can conclude that the Gibbs-Thomson effect can be represented by the model sufficiently well.

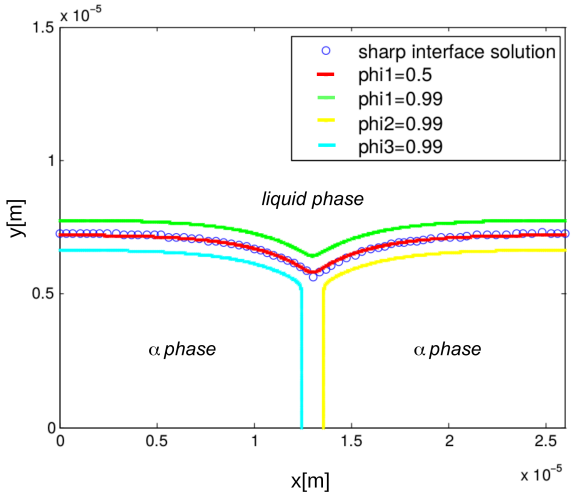

Figure 4.29.: Equilibrium phase boundary for $\sigma_{22} = \sigma_{12}$

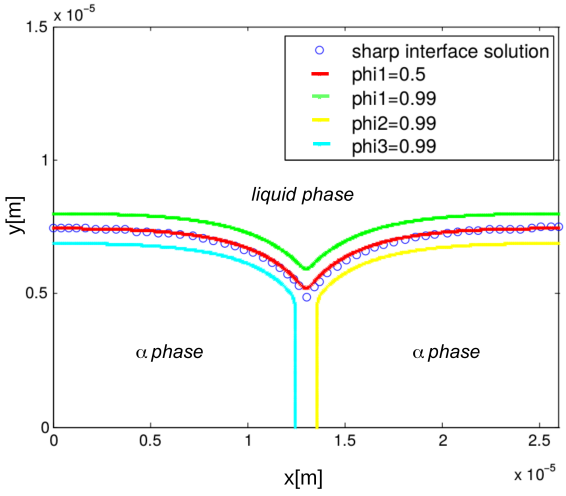

Figure 4.30.: Equilibrium phase boundary for $\sigma_{22} = 1.5\sigma_{12}$

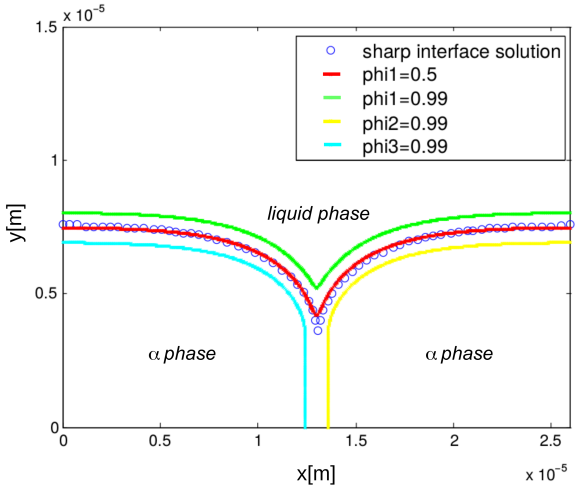

Figure 4.31.: Equilibrium phase boundary for $\sigma_{22} = 1.95\sigma_{12}$

4.4. Relationship to the Volume-of-Fluid Method

The volume-of-fluid method presented by Hirt and Nichols ([91]) allows an efficient description of two-phase flows. They introduce a step-like phase indicator function γ, which adopts a constant value of 1 in one of the two phases and a constant value of 0 in the other one. Consequently, grid cells with values of γ between 0 and 1 indicate the sharp phase boundary between both fluids. In the case of an incompressible flow, γ is transported according to the advection equation

$$\frac{\partial \gamma}{\partial t} + \vec{\nabla} \cdot (\gamma \vec{u}) = 0 \tag{4.4}$$

with the velocity field $\vec{u}$. However, it turns out that special measures are necessary in order to keep the phase interface sharp and to avoid a smearing. In the following, the version of the volume-of-fluid method implemented in OpenFOAM ([89]) in the framework of the InterFoam solver for incompressible flows is taken as a basis. The corresponding equations are

$$\vec{\nabla} \cdot \vec{u} = 0 \tag{4.5}$$

$$\frac{\partial (\rho \vec{u})}{\partial t} + \vec{\nabla} \cdot (\rho \vec{u} \vec{u}) - \vec{\nabla} \cdot (\eta \vec{\nabla} \vec{u}) = -\vec{\nabla} p + \rho \vec{g} + \sigma \kappa \vec{\nabla} \gamma \tag{4.6}$$

$$\frac{\partial \gamma}{\partial t} + \vec{\nabla} \cdot (\gamma \vec{u}) + \vec{\nabla} \cdot (\gamma (1-\gamma) \vec{u_r}) = 0. \tag{4.7}$$

The coupling of γ with the Navier-Stokes equations is realized on the one hand via the velocity field $\vec{u}$ and on the other hand via an additional source term $\sigma \kappa \vec{\nabla} \gamma$ in the momentum equation to describe surface effects with curvature

$$\kappa = -\vec{\nabla} \cdot \frac{\vec{\nabla} \gamma}{|\vec{\nabla} \gamma|}.$$

The so-called compression term $\vec{\nabla} \cdot (\gamma (1-\gamma) \vec{u_r})$ appearing in (4.7) avoids the smearing of phase boundaries and is discretized in the following manner:

$$\vec{\nabla} \cdot (\gamma (1-\gamma) \vec{u_r}) = \sum_f \gamma_f (1-\gamma_f) \vec{u}_{r,f} \vec{S}_f \tag{4.8}$$

$$\vec{u}_{r,f} = \frac{(\vec{\nabla} \gamma)_f}{|(\vec{\nabla} \gamma)_f + \epsilon|} \min\{C_\gamma \frac{|F_f|}{|\vec{S}_f|}, \max\{\frac{|F_f|}{|\vec{S}_f|}\}\}.$$

For that matter, it is summed over the surface areas f of a grid cell, $\vec{S}_f$ is the area vector being perpendicular to f and F_f is the volume flow. The maximum is evaluated considering all cells of the grid, ϵ is a small stabilizing quantity and C_γ is set to one in the following. Consequently, the compression term has the form

$$\vec{\nabla} \cdot (\gamma (1-\gamma) \frac{\vec{\nabla} \gamma}{|\vec{\nabla} \gamma|} K) \tag{4.9}$$

with a quantity K in accordance with (4.8) and it vanishes in a continuous consideration as $\gamma(1-\gamma)$ is always zero then.
We compare this now with the model developed in this work for the special case of elemental materials (equations (3.161)-(3.164)) because only two possible phases are needed here. In order to see the close connection between the volume-of-fluid method and the phase-field model, some simplifications and rearrangements in the equations derived in Chapter 3 are necessary. These will be presented in the following.

As the volume-of-fluid method is not capable to describe phase change, we set $T = T_m$ in the phase-field equation to switch off f_{bulk} and the corresponding thermodynamic driving forces. This leads to

$$\frac{D\Phi}{Dt} = \frac{\partial \Phi}{\partial t} + (\vec{u} \cdot \vec{\nabla})\Phi = Ma\vec{\nabla}(\Delta\vec{\nabla}\Phi) - \frac{Ma}{\Delta}\Phi(1-\Phi)(1-2\Phi). \tag{4.10}$$

Note that all specifics of the liquid-solid system have vanished in (4.10) and that the remaining part merely represents surface tension forces between two arbitrary phases. As the influence of f_{bulk}, which is usually the dominant factor in the phase-field equations on macroscopic length scales, is not present here, we choose a constant δ in (4.10) and obtain

$$\frac{\partial \Phi}{\partial t} = -(\vec{u} \cdot \vec{\nabla})\Phi + Ma\{\delta\vec{\nabla}^2\Phi - \frac{1}{\delta}\Phi(1-\Phi)(1-2\Phi)\}. \tag{4.11}$$

For sufficiently small values of δ, the second summand on the right-hand side dominates over $-(\vec{u} \cdot \vec{\nabla})\Phi$ and enforces a tangens hyperbolicus profile

$$\Phi(x_n) = \frac{1}{2}(1 + \tanh(\frac{x_n}{2\delta})) \tag{4.12}$$

with

$$|\vec{\nabla}\Phi| = \frac{\partial \Phi}{\partial x_n} = \frac{1}{\delta}\Phi(1-\Phi) \tag{4.13}$$

$$\vec{\nabla}^2\Phi = \frac{\partial^2 \Phi}{\partial x_n^2} = \frac{1}{\delta^2}\Phi(1-\Phi)(1-2\Phi). \tag{4.14}$$

Note that the profile (4.12) makes the expression in the brackets $\{\}$ vanish, but as soon as there is a deviation from (4.12), a large contribution proportional to $\frac{1}{\delta}$ drives the disturbed profile back towards the tangens hyperbolicus. Especially in the limit $\delta \to 0$, the tangens hyperbolicus converges against the step function of the volume-of-fluid method and assuming incompressibility $\vec{\nabla} \cdot \vec{u} = 0$, we obtain the analogue of equation (4.4):

$$\frac{\partial \Phi}{\partial t} + \vec{\nabla} \cdot (\Phi\vec{u}) = 0. \tag{4.15}$$

Additionally, it is possible to extract a term from the phase-field equation (4.11) which corresponds to the compression term (4.9) of the volume-of-fluid method and which in analogy to (4.9) is analytically zero in the limit $\delta \to 0$. For that manner, we use (4.13) to make the following transformations:

$$\begin{aligned}
\frac{Ma}{\delta}\Phi(1-\Phi)(1-2\Phi) &= Ma|\vec{\nabla}\Phi|(1-2\Phi) \\
&= Ma\vec{\nabla}(\Phi(1-\Phi)) \cdot \frac{\vec{\nabla}\Phi}{|\vec{\nabla}\Phi|} \\
&= \vec{\nabla} \cdot (Ma\Phi(1-\Phi)\frac{\vec{\nabla}\Phi}{|\vec{\nabla}\Phi|}) - \Phi(1-\Phi)\vec{\nabla} \cdot (Ma\frac{\vec{\nabla}\Phi}{|\vec{\nabla}\Phi|}) \\
&= \vec{\nabla} \cdot (Ma\Phi(1-\Phi)\frac{\vec{\nabla}\Phi}{|\vec{\nabla}\Phi|}) - \delta|\vec{\nabla}\Phi|\vec{\nabla} \cdot (Ma\frac{\vec{\nabla}\Phi}{|\vec{\nabla}\Phi|}).
\end{aligned} \tag{4.16}$$

Based on this, we obtain from (4.11) with $\vec{\nabla} \cdot \vec{u} = 0$ the equation

$$\frac{\partial \Phi}{\partial t} + \vec{\nabla} \cdot (\Phi\vec{u}) = Ma\delta\vec{\nabla}^2\Phi - \vec{\nabla} \cdot (Ma\Phi(1-\Phi)\frac{\vec{\nabla}\Phi}{|\vec{\nabla}\Phi|}) + \delta|\vec{\nabla}\Phi|\vec{\nabla} \cdot (Ma\frac{\vec{\nabla}\Phi}{|\vec{\nabla}\Phi|}), \tag{4.17}$$

which adopts in the sharp interface limit $\delta \to 0$ the form

$$\frac{\partial \Phi}{\partial t} + \vec{\nabla} \cdot (\Phi \vec{u}) = -\vec{\nabla} \cdot (Ma\Phi(1-\Phi)\frac{\vec{\nabla}\Phi}{|\vec{\nabla}\Phi|}). \tag{4.18}$$

In the phase-field model, the term $\frac{Ma}{\delta}\Phi(1-\Phi)(1-2\Phi)$ results from the double well potential and its task is to separate coexisting phases. A comparison of (4.18) with (4.7) shows that an expression can be extracted from it which has the same structure as the compression term of the volume-of-fluid method. At the same time, the mobility M of the phase-field can be determined by comparing (4.18) with (4.9):

$$Ma = K \leftrightarrow M = \frac{K}{a}. \tag{4.19}$$

The discretization of the resulting expression $\vec{\nabla} \cdot (K\Phi(1-\Phi)\frac{\vec{\nabla}\Phi}{|\vec{\nabla}\Phi|})$ may be conducted in analogy to (4.8). Note that in the framework of the thin-interface analysis presented in subsection 3.4.2, the phase-field mobility M has already been determined for phase boundaries moving due to phase change. In the situation considered here, phase change plays no role and it is therefore natural to find an alternative expression for M.
The last point is the coupling with the Navier-Stokes equations. The thermodynamically consistent coupling leads in the case $T = T_m$, $\Delta = \delta$ and $a = \frac{3\sigma}{T_m}$ regarded here to an expression

$$-6\sigma\delta\vec{\nabla}^2\Phi\vec{\nabla}\Phi \tag{4.20}$$

on the right-hand side of the momentum equation (3.162). In the following, we will try to express $\vec{\nabla}^2\Phi$ by $\vec{\nabla} \cdot (\frac{\vec{\nabla}\Phi}{|\vec{\nabla}\Phi|})$ plus a correction term. Using $\partial_i = \frac{\partial}{\partial x_i}$, we start by evaluating

$$\begin{aligned}
&\partial_1(\frac{\partial_1\Phi}{|\vec{\nabla}\Phi|}) \\
&= \partial_1(\frac{\partial_1\Phi}{\sqrt{(\partial_1\Phi)^2+(\partial_2\Phi)^2+(\partial_3\Phi)^2}}) \\
&= \frac{\partial_1^2\Phi\sqrt{(\partial_1\Phi)^2+(\partial_2\Phi)^2+(\partial_3\Phi)^2}}{(\sqrt{(\partial_1\Phi)^2+(\partial_2\Phi)^2+(\partial_3\Phi)^2})^2} \\
&- \frac{\partial_1\Phi\frac{1}{2}\{(\partial_1\Phi)^2+(\partial_2\Phi)^2+(\partial_3\Phi)^2\}^{-\frac{1}{2}}(2\partial_1\Phi\partial_1^2\Phi+2\partial_2\Phi\partial_1\partial_2\Phi+2\partial_3\Phi\partial_1\partial_3\Phi)}{(\sqrt{(\partial_1\Phi)^2+(\partial_2\Phi)^2+(\partial_3\Phi)^2})^2} \\
&= \frac{\partial_1^2\Phi}{|\vec{\nabla}\Phi|} - \frac{\partial_1\Phi}{|\vec{\nabla}\Phi|^3}(\partial_1\Phi\partial_1^2\Phi+\partial_2\Phi\partial_1\partial_2\Phi+\partial_3\Phi\partial_1\partial_3\Phi).
\end{aligned} \tag{4.21}$$

In analogy, one obtains

$$\partial_2(\frac{\partial_2\Phi}{|\vec{\nabla}\Phi|}) = \frac{\partial_2^2\Phi}{|\vec{\nabla}\Phi|} - \frac{\partial_2\Phi}{|\vec{\nabla}\Phi|^3}(\partial_1\Phi\partial_2\partial_1\Phi+\partial_2\Phi\partial_2^2\Phi+\partial_3\Phi\partial_2\partial_3\Phi) \tag{4.22}$$

$$\partial_3(\frac{\partial_3\Phi}{|\vec{\nabla}\Phi|}) = \frac{\partial_3^2\Phi}{|\vec{\nabla}\Phi|} - \frac{\partial_3\Phi}{|\vec{\nabla}\Phi|^3}(\partial_1\Phi\partial_3\partial_1\Phi+\partial_2\Phi\partial_3\partial_2\Phi+\partial_3\Phi\partial_3^2\Phi). \tag{4.23}$$

Using (4.21)-(4.23), one can write

$$\begin{aligned}
\vec{\nabla} \cdot (\frac{\vec{\nabla}\Phi}{|\vec{\nabla}\Phi|}) &= \sum_{i=1}^{3}\partial_i(\frac{\partial_i\Phi}{|\vec{\nabla}\Phi|}) \\
&= \frac{\vec{\nabla}^2\Phi}{|\vec{\nabla}\Phi|} - \frac{1}{|\vec{\nabla}\Phi|^3}(\vec{\nabla}\Phi)^T \cdot (\vec{\nabla}\otimes\vec{\nabla}\Phi)\cdot\vec{\nabla}\Phi \\
\leftrightarrow \vec{\nabla}^2\Phi &= |\vec{\nabla}\Phi|\vec{\nabla} \cdot (\frac{\vec{\nabla}\Phi}{|\vec{\nabla}\Phi|}) + (\frac{\vec{\nabla}\Phi}{|\vec{\nabla}\Phi|})^T \cdot (\vec{\nabla}\otimes\vec{\nabla}\Phi)\cdot(\frac{\vec{\nabla}\Phi}{|\vec{\nabla}\Phi|}).
\end{aligned} \tag{4.24}$$

Introducing the curvature $\kappa = -\vec{\nabla} \cdot (\frac{\vec{\nabla}\Phi}{|\vec{\nabla}\Phi|})$ and using $\delta|\vec{\nabla}\Phi| = \Phi(1-\Phi)$, we obtain the expression

$$6\Phi(1-\Phi)\sigma\kappa\vec{\nabla}\Phi - 6\sigma\frac{\Phi(1-\Phi)}{|\vec{\nabla}\Phi|}\{(\frac{\vec{\nabla}\Phi}{|\vec{\nabla}\Phi|})^T \cdot (\vec{\nabla}\otimes\vec{\nabla}\Phi)\cdot(\frac{\vec{\nabla}\Phi}{|\vec{\nabla}\Phi|})\}\vec{\nabla}\Phi \tag{4.25}$$

on the right-hand side of the momentum equation. The similarity with the corresponding term in the volume-of-fluid method becomes even more pronounced if we replace $\Phi(1-\Phi)$ by its average value in the transition region $0 < \Phi < 1$ due to the small spatial extent of the latter:

$$\int_0^1 \Phi(1-\Phi)d\Phi = \frac{1}{6}. \tag{4.26}$$

This leads to

$$-6\sigma\delta\vec{\nabla}^2\Phi\vec{\nabla}\Phi = \sigma\kappa\vec{\nabla}\Phi - \sigma\{\frac{1}{|\vec{\nabla}\Phi|}(\frac{\vec{\nabla}\Phi}{|\vec{\nabla}\Phi|})^T \cdot (\vec{\nabla}\otimes\vec{\nabla}\Phi)\cdot(\frac{\vec{\nabla}\Phi}{|\vec{\nabla}\Phi|})\}\vec{\nabla}\Phi \tag{4.27}$$

on the right-hand side of the momentum equation. (4.27) contains the same expression as in (4.6) plus an additional correction.
In the following, we will compare the results of the phase-field method (PFM) with those of the volume-of-fluid method (VOF) represented by the InterFoam algorithm taking the example of the dam break test case prepared in OpenFOAM. In this test case, a water column surrounded by air rushes down onto a solid obstacle. In the phase-field calculations, (4.26) has not been utilized as this average does not naturally arise in the framework of the phase-field method. Possible differences with the InterFoam algorithm may therefore be rooted in the factors $6\Phi(1-\Phi)$ as well as in the correction term in (4.27). The results are presented in Figures 4.32 - 4.35 and show a good agreement. We can therefore conclude that on the one hand, the correction term is not too important on a macroscopic length scale. On the other hand, the coupling procedure with the Navier-Stokes equations is justified as there are no major discrepancies with the well-established volume-of-fluid method. In Table 4.3, we additionally compare both methods with respect to the conservation of the phase volume. One can see that the volume fraction of water decreases in both methods. The phase-field method, however, performs slightly better.

Time	Phase-Field Method	Volume-of-Fluid Method
$0.0s$	0.124769	0.124769
$1.0s$	0.123248	0.122835

Table 4.3.: Volume fraction of water at the beginning and at the end of the simulations

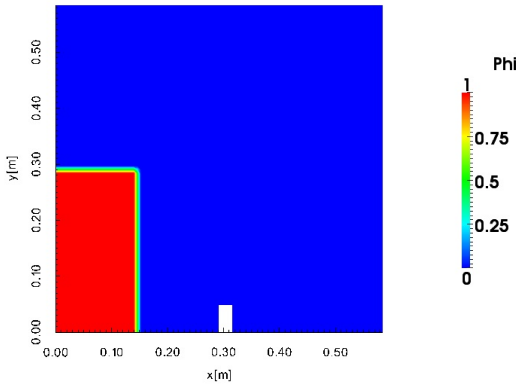

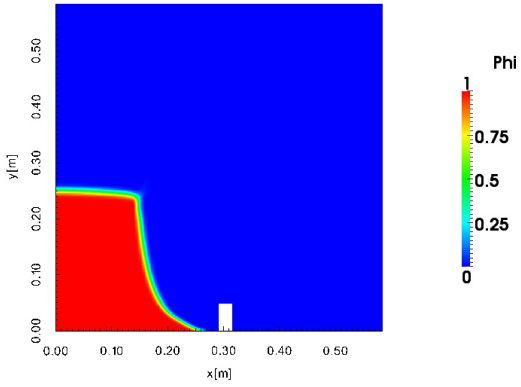

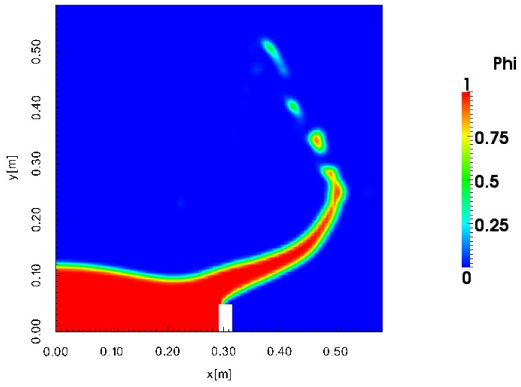

Figure 4.32.: PFM at $t = 0.0s, t = 0.1s$ and $t = 0.3s$

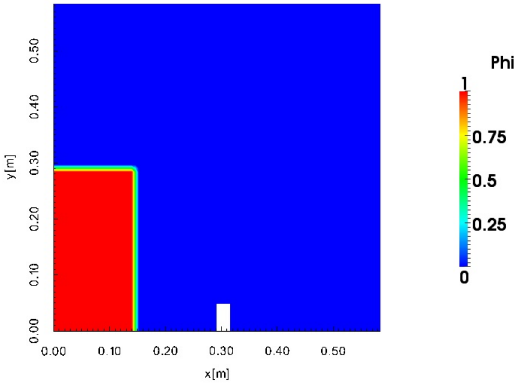

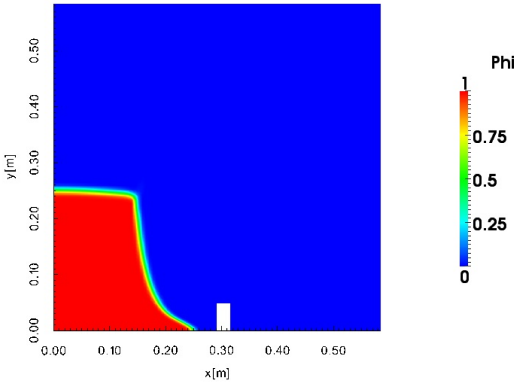

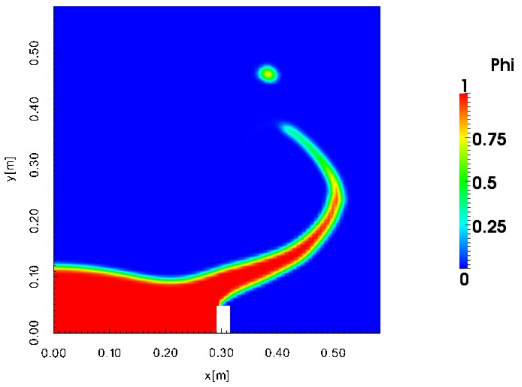

Figure 4.33.: VOF at $t = 0.0s, t = 0.1s$ and $t = 0.3s$

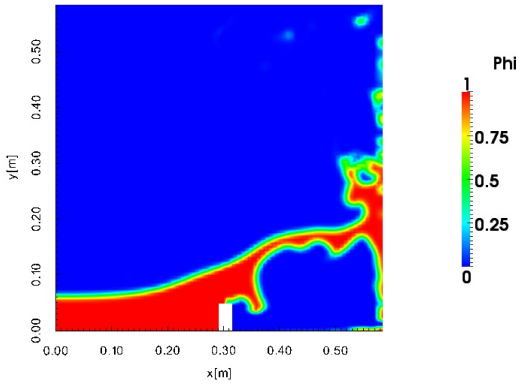

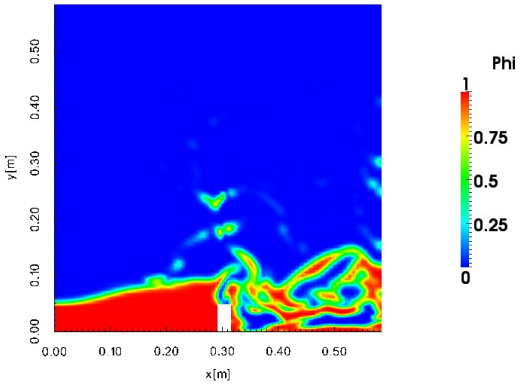

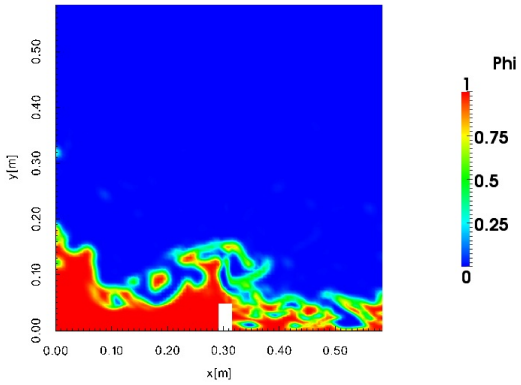

Figure 4.34.: PFM at $t = 0.5s, t = 0.75s$ and $t = 1.0s$

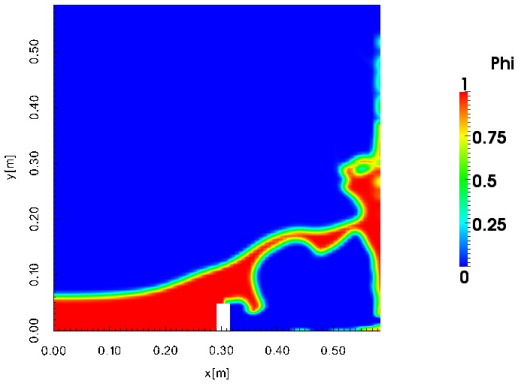

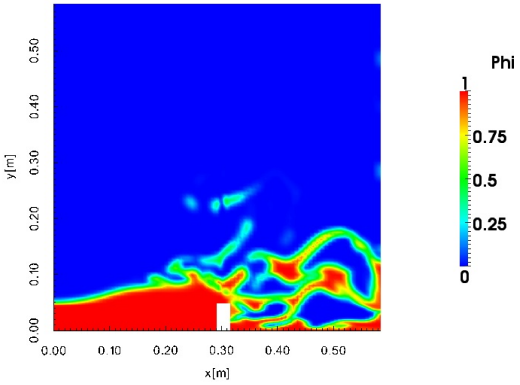

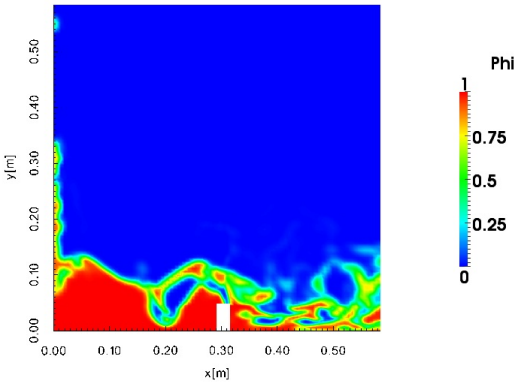

Figure 4.35.: VOF at $t = 0.5s, t = 0.75s$ and $t = 1.0s$

5. Model Validation

In this chapter, the results of CFD simulations using the developed model will be compared with experimental data. In particular, three different cases will be considered which have been chosen to cover a wide scope of possible applications.
The first case treats a solidifying microstructure of $CBr_4 - C_2Cl_6$ with alternating lamella of solid phases α and β, which are separated from each other and the eutectic melt by sharp phase boundaries. The objective is to show that the developed model is really capable to reproduce the details of sharp interface solidification if it is applied on a sufficiently fine grid. The corresponding experimental data have been published by Ginibre et al. ([92]).
After that, a second simulation on a macroscopic length scale treats elemental material phase change under thermal natural convection, a scenario being contained in the derived model as a special case (see subsection 3.3.2). As the dynamics of phase change can be described in both directions, a melting process of elemental gallium in a box-shaped container published by Gau and Viskanta ([93]) is considered here. Another notable aspect is that this second simulation treats the dynamics of sharp phase boundaries on a macroscopic scale in contrast to the microscopic sharp interface dynamics of $CBr_4 - C_2Cl_6$ treated in the first case.
Finally, a macroscopic experiment by Christenson et al. ([94],[25]) investigating the solidification of an aqueous ammonium chloride solution under thermosolutal natural convection is simulated. In this last setup, the full scope of our model including heat and composition transport as well as mushy layer formation is covered.

5.1. Microscopic Lamellae Solidification of $CBr_4 - C_2Cl_6$

As mentioned before, we turn towards the description of the exact sharp interface structure on a small length scale at first. For a validation of the developed model, an experiment by Ginibre et al. ([92]) is used in which the solidification dynamics of the binary eutectic alloy $CBr_4 - C_2Cl_6$ is investigated on a length scale of several micrometers. A sketch of the experiment is presented in Figure 5.1. For that matter, a $12\mu m$ thick sample is enclosed between two glass plates and placed in fixed external temperature gradient $G = 8000\frac{K}{m}$. Starting from an inital equilibrium state with alternating lamellae of the two solid phases α and β in the region with $T \leq T_e$ and a eutectic melt in the area with $T > T_e$, the sample is moved with a constant velocity $V = 0.5\frac{\mu m}{s}$ to the cold side of the temperature gradient. Further details about the experimental procedure may be found in [92]. As demonstrated in Figure 5.2, the resulting solidification pattern is characterized by oscillating phase boundaries between the two solid phases α and β. This experiment has been

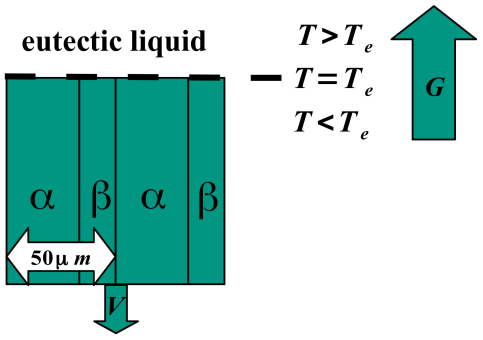

Figure 5.1.: Sketch of Ginibre's experiment

simulated with the model developed in this work. In the simulations, only the phase-field equations and the transport equation for the composition field have been solved because effects of natural convection are negligible on the small length scale considered here and because the temperature field is dominated by the external gradient despite the latent heat being released. The equations have been discretized on a uniform grid in two dimensions

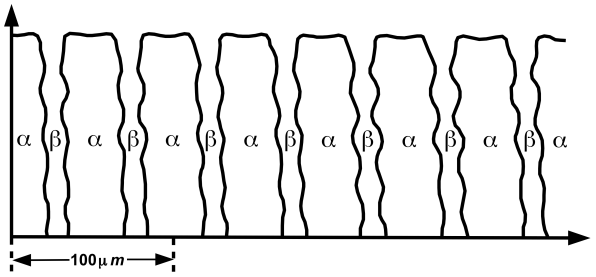

Figure 5.2.: Solidification pattern of the sample moving with $V = 0.5\frac{\mu m}{s}$

with a grid spacing of $0.5\mu m$. Only two pairs of lamellae have been considered and cyclic boundary conditions have been utilized at the left and right boundaries. Figures 5.3 and 5.4 show the resulting solidification pattern for the case of dynamically calculated values $\Delta(\vec{x}, t)$ as well as for the case of a constant $\delta = 3 \cdot 10^{-7} m$. The calculated values $\Delta(\vec{x}, t)$ corresponding to Figure 5.3 are presented in Figure 5.5 and were subjected to the condition $\Delta(\vec{x}, t) \geq \delta$. Obviously, the case of Figure 5.3 leads to a more realistic result. Figure 5.5 makes clear that only small corrections to the constant $\delta = 3 \cdot 10^{-7} m$ are calculated with maximum values at the triple points connecting the solid phases α and β as well as the liquid phase. These corrections seem to be crucial in order to obtain a realistic result for the setup considered here.
How can this be understood? The phase-field model with a small and constant δ to describe the microscopic sharp-interface dynamics is based on the free energy functional developed in section 3.1. It has been constructed to keep the continuous transition region between two bulk phases purely binary and to impose a tangens hyperbolicus profile on the involved phase-fields in or close to a state of thermodynamic equilibrium. Thereby, the existence of triple points has not been considered and the implicit assumption was that triple points follow the motion of neighbouring binary interfaces without having a large influence. In the spirit of considering free energy as a landscape above the Gibbs simplex, its values in the interior of the simplex result in our model from a superposition of expressions which provide the desired behaviour along the edges. Therefore, triple points may not be represented entirely correctly and the constant $\delta = 3 \cdot 10^{-7} m$ seems to be too large to suppress their influence on the result. As all three phases are present at triple points

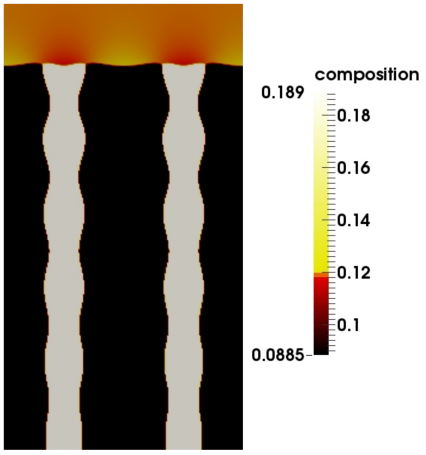

Figure 5.3.: Solidification pattern for dynamically calculated values $\Delta(\vec{x}, t)$

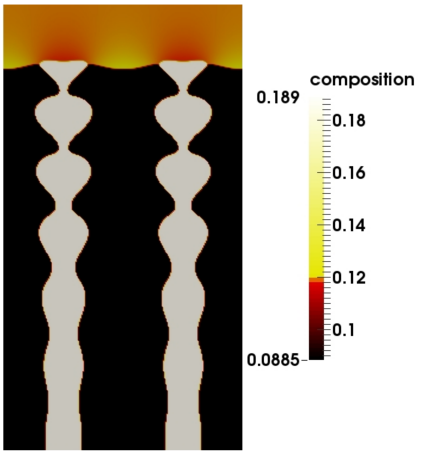

Figure 5.4.: Solidification pattern for a constant $\delta = 3 \cdot 10^{-7} m$

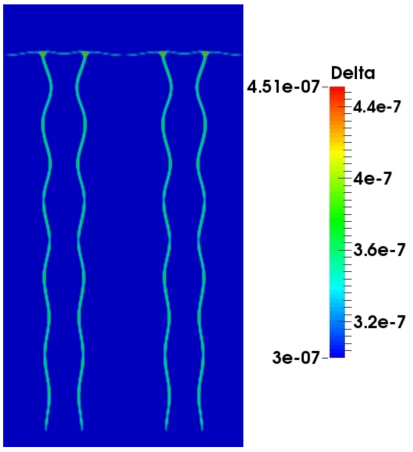

Figure 5.5.: Dynamically calculated $\Delta(\vec{x}, t)$ corresponding to Figure 5.3

by definition, the profiles of the phase-fields deviate from the tangens hyperbolicus shape and the Δ model provides small corrections to the constant δ there. As Figure 5.5 shows, these corrections trace the path of the triple points and neutralize their bad influence on the results.
The oscillation wavelength is constant in Figure 5.3 and adopts a value of about $30\mu m$. A comparison with the experimental result shows a quite good agreement (Figure 5.6). However, the oscillations get out of step after some time because the experimental wavelength is not a constant and fluctuates around $30\mu m$. A reason for this deviation may be that as pointed out by Ginibre et al. ([92]), the pulling velocity V was subjected to periodic oscillations of $\pm 4\%$ around its average value $0.5\frac{\mu m}{s}$ which has not been considered in the simulations. We can conclude that the developed model is capable to correctly reproduce the solidification microstructure of binary eutectic alloys on a small length scale.

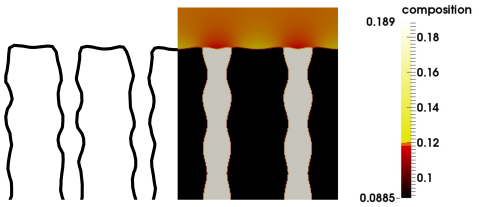

Figure 5.6.: Comparison of the experimental result with the simulation result from Figure 5.3

5.2. Melting of Gallium Under Thermal Natural Convection

We investigate in this section the melting of elemental gallium in a box-shaped container of dimensions $0.0889m \times 0.0635m \times 0.0381m$. The corresponding experiments are described in [93] and have been performed by Gau and Viskanta in 1986. According to the authors, the inital temperature of the solid gallium block and all bounding walls has generally been $1K-2K$ below the melting point $T_m = 302.93K$ before the melting process was started. As no further specifications are given, we assume an initial temperature of $T_c = 301.45K$ and therefore an undercooling of $1.5K$ in the following. The melting process was initialized by raising the temperature of a wall with dimensions $0.0635m \times 0.0381m$ to the fixed value $T_h = 311.15K > T_m$ while the opposing wall was kept at the initial temperature of $T_c = 301.45K$. All other walls were isolated. A sketch of the experimental setup is shown in Figure 5.7. During the series of experiments, the phase change process was stopped in

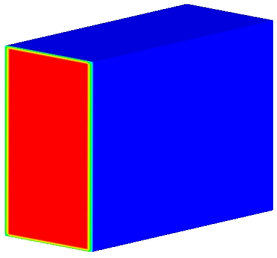

Figure 5.7.: Experimental setup from Gau and Viskanta with the heated wall in red

each case at a certain point in time and the position of the phase boundary was determined after a quick removal of the residual melt. The experimental results presented by Gau and Viskanta in [93] are shown in Figure 5.8. The results are presented in two dimensions as no noteworthy changes were observed in the perpendicular direction. One can see that melting is stronger at the top and that the difference increases with time. The reason for this behaviour is that due to thermal buoyancy effects, the melt rises along the heated wall, absorbs heat along the way and transports it to the phase boundary. The heat is spent there to transform the solid phase into the liquid state and the melt falls down due to the heat loss and the associated density increase. On its way down, the induced melting becomes weaker and weaker as more heat has been spent before. In the course of these events, the phase boundary bulges as shown in Figure 5.8 and the distance covered by the melt during heat release increases, leading to an even more pronounced difference between the top and the bottom of the cavity.
The considered experimental series was simulated with the special case of the developed model for elemental materials, i.e. by solving the system of equations (3.161)-(3.165)

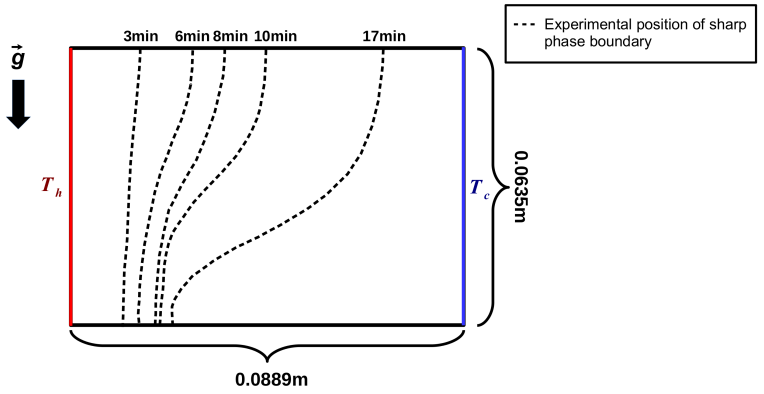

Figure 5.8.: Experimentally determined position of the sharp phase boundary at different points in time

with the assumption of incompressibility. The material properties of gallium used in the simulation are specified in appendix F. The Grashof number is

$$Gr = \frac{g\rho^2\beta_T\Delta T L^3}{\eta^2} = \frac{9.81\frac{m}{s^2}\cdot(6111\frac{kg}{m^3})^2\cdot 1.3\cdot 10^{-4}\frac{1}{K}\cdot 9.7K\cdot(0.0635m)^3}{(2.045\cdot 10^{-3}\frac{kg}{ms})^2} = 2.8\cdot 10^7$$

and therefore smaller than the critical value $Gr_{krit} = 10^9$ for flows along heated vertical plates ([95]) which indicates the onset of turbulence.
The simulations have been performed in three dimensions with a grid distance of $1mm$. Although the characteristics of the phase boundary are determined by the two spatial dimensions specified in Figure 5.8, the velocity field has a non-negligible component in the third direction especially at the beginning of the simulation when the liquid volume fraction is small. A comparison of the simulated positions of the sharp phase boundary with the experimental results from Figure 5.8 is shown in Figure 5.9.

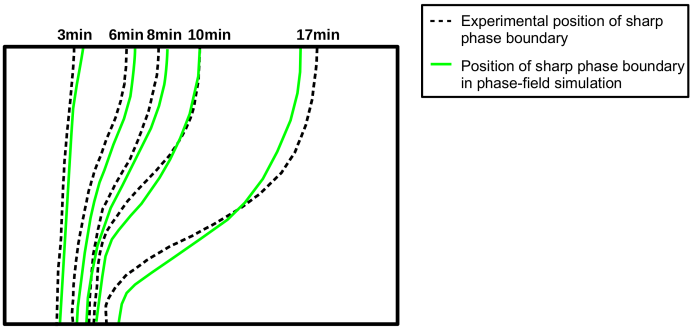

Figure 5.9.: Comparison of simulation results with experiment

All in all, the temporal evolution as well as the form of the phase boundary agree well. The small discrepancies in the temporal development may be explained by uncertainties concerning the temperature T_c of the cold wall. As mentioned before, T_c is specified with $1K - 2K$ below the melting point for every run. As the experiment was executed anew for every curve shown in Figure 5.8, it is probable that there were certain variations of T_c which have not been considered in the numerical simulations with a fixed $T_c = 301.45K$ corresponding to an undercooling of $1.5K$.
Additionally, Figures 5.10 and 5.11 show the temperature field and the magnitude of the

velocity field after 17 minutes. At this point in time, there is a single, two-dimensional convection cell which transports heat from the heated wall to the phase boundary.

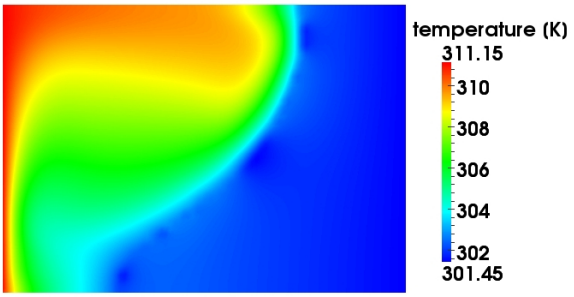

Figure 5.10.: Simulated temperature field after 17 minutes

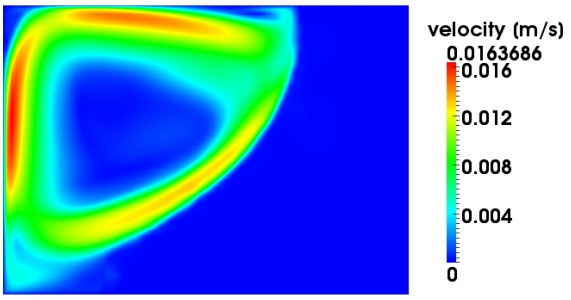

Figure 5.11.: Simulated velocity field (magnitude) after 17 minutes

5.3. Solidification of NH_4Cl-H_2O Under Thermo-Solutal Natural Convection

In this section, the developed model is validated by means of the solidification of an aqueous ammonium chloride solution $NH_4Cl - H_2O$ in a box-shaped volume with dimensions $0.036m \times 0.144m \times 0.2m$. The material properties of $NH_4Cl - H_2O$ and the model parameters to be calculated by them are specified in appendix G. In the corresponding experiment presented by Christenson et al. in [94] and [25], the mentioned box-shaped volume is filled with an aqueous ammonium chloride solution with an initial composition $\xi = 0.7 < \xi_e$ and an initial temperature $T = 313.15K$. One of the two walls with dimensions $0.144m \times 0.2m$ is held at a constant temperature $T_c = 243.15K$ and the opposing wall is held at $T_h = 313.15K$. The Grashof number is

$$Gr = \frac{g\rho^2\beta_T\Delta T L^3}{\eta^2} = \frac{9.81\frac{m}{s^2}\cdot(1078\frac{kg}{m^3})^2\cdot 3.832\cdot 10^{-4}\frac{1}{K}\cdot 4.518K\cdot(0.144m)^3}{(1.3\cdot 10^{-3}\frac{kg}{ms})^2} = 3.5\cdot 10^7, \tag{5.1}$$

which means that it is below the critical value $Gr_{krit} = 10^9$ for flows along vertical plates marking the transition to turbulence (see [95]). Because only the liquid part must be taken into consideration for possible turbulent motions, ΔT in (5.1) has been calculated from the difference between the heated wall temperature T_h and the temperature at the boundary between the mushy layer and completely liquid regions, which has been estimated to be given by the liquidus temperature:

$$\begin{aligned}\Delta T &= T_h - T_l(\xi)\\ &= T_h - T_e - m_{12}\cdot(\xi - \xi_e)\\ &= 313.15K - 257.75K - (-494K)\cdot(0.7 - 0.803)\\ &= 4.518K.\end{aligned}$$

We mention here that even if the temperature difference between the heated and the cooled wall $\Delta T = T_h - T_c = 70K$ is used, the resulting Grashof number $Gr = 5.4\cdot 10^8$ is still smaller than Gr_{krit}.
We can therefore assume the flow to be laminar and due to the large container depth of $0.2m$, it can also be regarded as being essentially two-dimensional. In the following, the depicted experiment will be described in the sense of Figure 5.12.

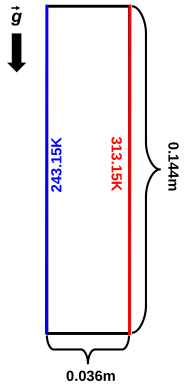

Figure 5.12.: Experimental setup in two dimensions

At first, Figure 5.13 shows the experimentally determined solidification behaviour presented by Christenson et al. in [25]. Note that small dendritic tips at the boundary between the mushy layer and the liquid phase have been taken out by the authors of [25] such that the data represent the smoothed behaviour. One can see that a solid phase grows

from the cooled wall, which due to the non-eutectic composition of the melt is separated by a mushy layer from the liquid phase. The temperature and composition dependence of density generates buoyancy forces, which manifest themselves in a transport of heat and the lighter water to the upper part of the container. This leads to a temperature increase and due to the higher mass fraction of water to a decrease of the liquidus temperature there. Consequently, the process of solidification is attenuated in the upper part of the box and the solidification behaviour presented in Figure 5.13 is observed.

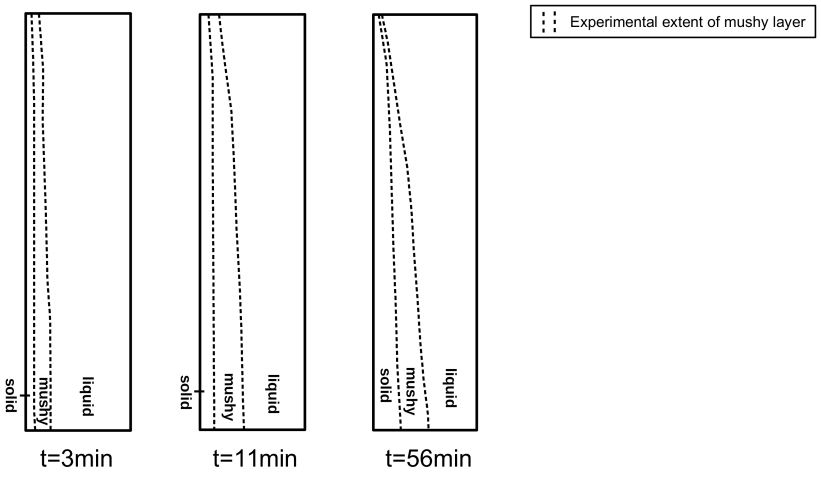

Figure 5.13.: Experimentally determined solidification behaviour

In the numerical simulation based on Figure 5.12, a uniform grid with a cell size of $1mm$ was used and the full system of equations (3.156)-(3.160) was solved under the incompressibility assumption $\vec{\nabla} \cdot \vec{u} = 0$. The temperature and composition dependence of density has been considered in the framework of the Boussinesq approximation.
In Figure 5.14, the simulation results of the developed model concerning the extent of the mushy layer (green lines) is compared on the one hand with the experimental results from Figure 5.13 and on the other hand with the simulation results which Christenson et al. ([25]) obtained with Bennon's model (see subsection 2.1.3).

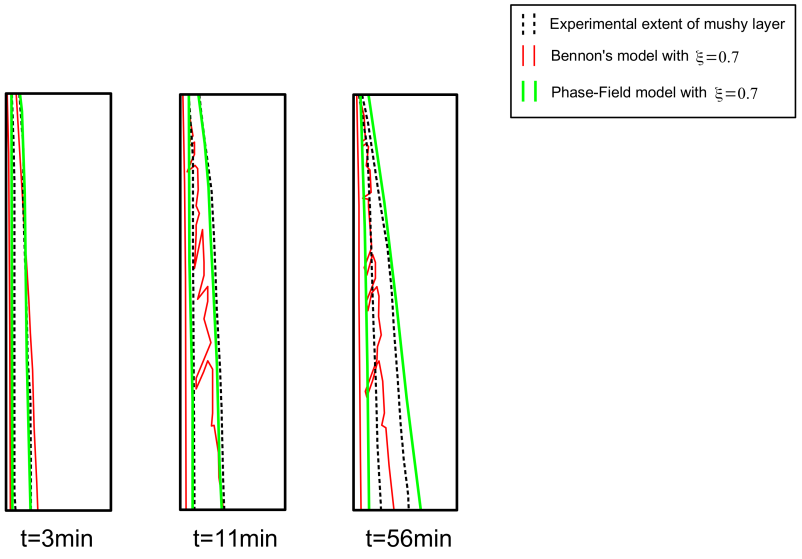

Figure 5.14.: Comparison of experimental results with numerical simulations (1)

Note that small tips between the mushy layer and the liquid phase appeared in the simulations as well and have been removed to be consistent with the data presented in [25] and in Figure 5.13. One can see that the newly developed model is capable to give a good reproduction of the experimental results and that it improves the results of Bennon's model. Remember that in Bennon's model, the phase state is calculated as an instantaneous function of temperature and composition according to equation (2.40). In contrast to that, the model developed in this work solves additional governing equations describing phase change. Furthermore, the assurance of thermodynamic consistency generates additional phase-field dependent coupling terms in the other transport equations in the new model which are not present in Bennon's approach.
It must be mentioned that Christenson et al. ([25]) present a second simulation which has been obained tentatively with an initial melt composition $\xi = 0.69$ and which is compared with the experimental results and our simulation results in Figure 5.15.

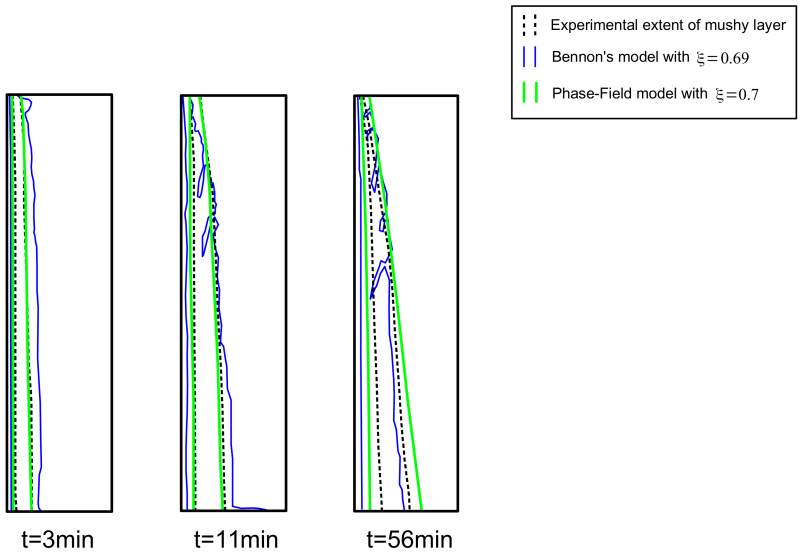

Figure 5.15.: Comparison of experimental results with numerical simulations (2)

However, as the uncertainty of the composition measurement is given by at most ± 0.005 in the experimental paper ([94]), this second simulation with $\xi = 0.69$ is actually not consistent with the experiment. The comparison of the newly developed model with Bennon's model should therefore be based on Figure 5.14.
Additionally, temperature measurements at different positions are available. A selection of these measurements is presented in Figures 5.16 to 5.21 together with the simulated temperature distributions based on the phase-field model as well as Bennon's model. One can see that the new model leads to a better agreement with the measurements here as well. Note that the red and blue lines in Figures 5.16 to 5.21 end in each case at the time when a steady-state has established in the corresponding simulations. The experimentally determined steady state after about 56 minutes occurs much later than the in the simulations with the Bennon model and is nearly reproduced by the phase-field model. Note that the temperature measurements end after 40 minutes when the experimental steady state has not established yet.

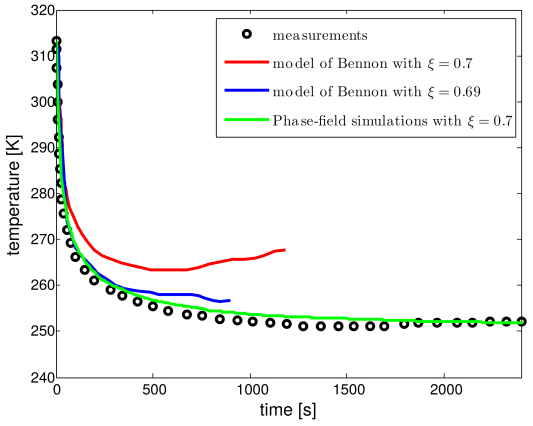

Figure 5.16.: Temperature at $x = 0.0022m$, $y = 0.09m$

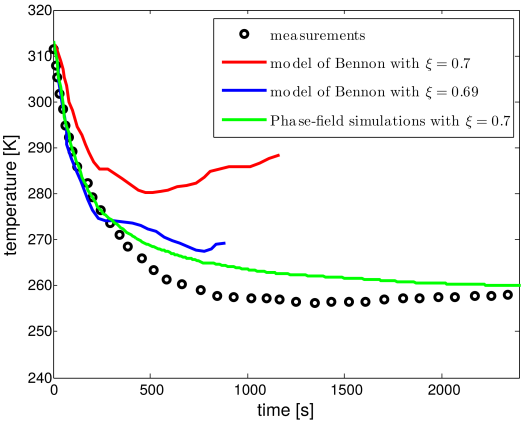

Figure 5.17.: Temperature at $x = 0.0044m$, $y = 0.09m$

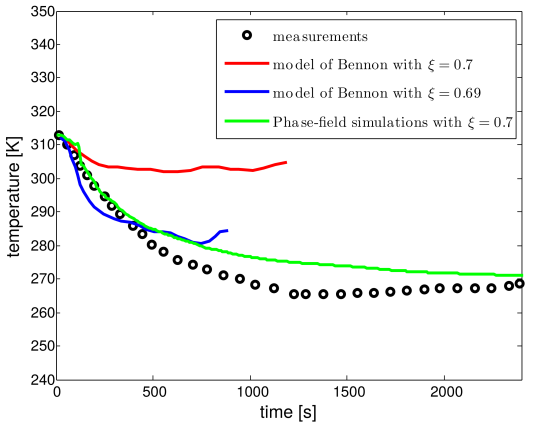

Figure 5.18.: Temperature at $x = 0.0066m$, $y = 0.09m$

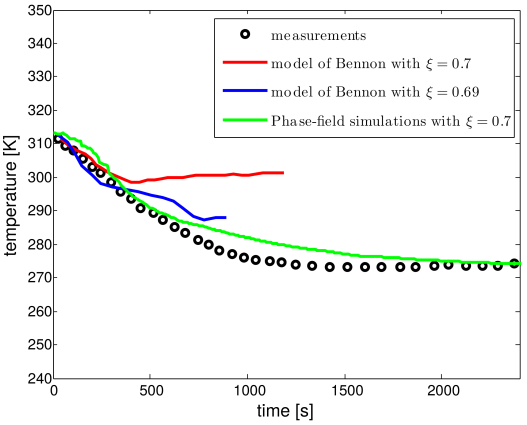

Figure 5.19.: Temperature at $x = 0.0087m$, $y = 0.065m$

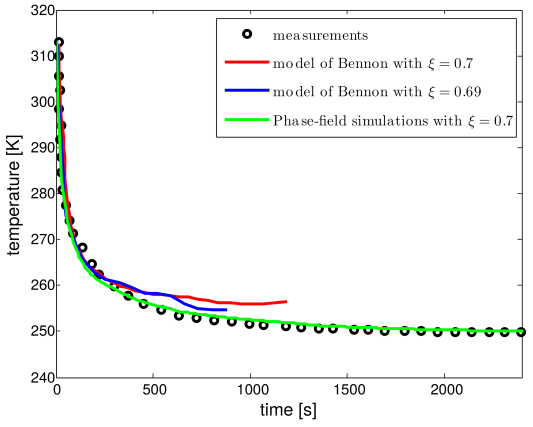

Figure 5.20.: Temperature at $x = 0.0022m$, $y = 0.045m$

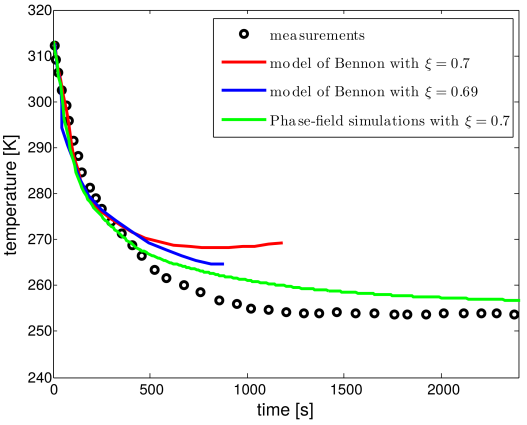

Figure 5.21.: Temperature at $x = 0.0044m$, $y = 0.045m$

6. Conclusion and Outlook

6.1. Conclusion

In this thesis, a three-dimensional computational fluid dynamics model has been developed which couples the Navier-Stokes equations and transport equations for heat and composition with an independent phase change model in a thermodynamically consistent manner. The phase change model is based on the phase-field method, which is a well-known diffuse interface approach to represent the dynamics of sharp solid-liquid phase boundaries with the help of smooth phase indicator functions.
The *model development* is based on the construction of a phenomenological functional for the free energy of binary eutectic alloys. After a generalization of the free energy functional to a volume-averaged framework, it is used to achieve a thermodynamically consistent coupling of phase change with momentum, heat and composition transport. In particular, this thesis can contribute the following new aspects:

- The modelling of surface free energy density generalizes the approach by Folch and Plapp ([70]) by the introduction of an especially designed higher-order term, which additionally to the avoidance of ghost phases and the preservation of the tangens hyperbolicus equlibrium profiles as considered by the model in [70] allows to assign different surface tension values to different interfaces. While the avoidance of ghost phases is in accordance with physical experience and the tangens hyperbolicus profiles are important for the feasibility of a thin-interface analysis, the representation of different surface tension values is requested as the new model shall provide a realistic microscopic description. It has turned out that the resulting expression for $f_{surface}$ corresponds to a special case of a model proposed by Haas ([80]) for N phases derived from a different perspective.
- The modelling of bulk free energy density is based on an expression provided by Kim et al. ([67]) for dilute binary eutectic alloys under isothermal conditions. It has been generalized to non-isothermal conditions and arbitrary composition values. In particular, individual phase compositions are introduced and in contrast to some speculations in the literature ([56]), it has been demonstrated that no numerical solution procedure is necessary for their determination. Rather, they can be calculated in an analytical manner by using Cardano's formula.
- Due to the potential appearance of complicated and, depending on the size of the volume of interest, non-resolvable microstructures in binary eutectic alloy solidification problems, the free energy functional has been generalized and expressed by the

volume averages of the phase indicator functions, i.e. the phase volume fractions. In this regard, a dynamic calculation procedure for the parameter Δ characterizing the diffuse interface width has been proposed based on free energy minimization. Additionally, it has been demonstrated that the generalization to the volume-averaged description is consistent in the sense that the original free energy functional can be obtained back when the averaging volume goes to zero.

- In order to find governing equations for the phase volume fractions and a thermodynamically consistent coupling of phase change with the Navier-Stokes equations and transport equations for heat and composition, the method proposed by Anderson et al. ([51]) for elemental materials has been extended based on the generalized free energy functional for binary eutectic alloys constructed before. The main differences to the original approach are the presence of three phases and the necessity of including composition transport into the coupling procedure. The description of elemental materials is contained in the resulting set of governing equations as a special case.

Concerning the *model verification*, it has been examined if the desired behaviour is reproduced numerically by the implemented code. Additionally, the agreement of numerical results with related approaches like sharp-interface modelling and the volume-of-fluid method have been investigated in appropriate limits. In particular, the following steps have been performed:

- Concerning phase surfaces, it has been demonstrated that the tangens hyperbolicus profiles are reproduced numerically by the non-averaged model on small length scales. In a volume-averaged setup, it has been shown that the profiles are determined by the chemcial properties of the involved phases and that the effect of surface free energy density is to minimize the curvature of mixture layers. Furthermore, it has been illustrated that the volume-averaged model utilizing the dynamical calculation procedure for Δ is capable to reproduce the results of the non-averaged model if the numerical grid is sufficiently fine. Consequently, the dynamic calculation procedure for Δ allows an application of the phase-field equations independently from the spatial dimensions of interest. This is not possible if Δ is set to a single constant value. Finally, it has been demonstrated that the dynamic model for Δ is able to characterize spatially varying thicknesses of binary mixture layers and that the results cannot be reproduced with a constant Δ_0 even if it is chosen in the same range as the dynamically calculated values.
- The modelling of f_{bulk} has been verified by illustrating that the equilibrium compositions as well as the stability properties of phase boundaries including the resulting mushy layer thicknesses are in accordance with a given binary eutectic alloy phase diagram.
- It has been verified that the new model is capable to reproduce the results of sharp interface modelling. In particular, the Gibbs-Thomson effect is represented quantitatively correctly.
- It has been shown that there is a close relationship of the new model with the well-known volume-of-fluid method if the possibility for phase change is switched off and if the mobility constant is chosen appropriately. In the framework of the standard dam break test case prepared in OpenFOAM, the results of the two methods agree well. Notably, this provides a verification of the coupling between the phase-field and Navier-Stokes equations.

The *model validation* has been performed with the help of three test cases:

- The sharp interface solidification microstructure of the binary eutectic alloy $CBr_4 - C_2Cl_6$ resulting from an experiment by Ginibre et al. ([92]) could be reproduced

successfully by applying the model on a micrometer length scale. The dynamic calculation procedure concerning the transition layer width between pure phases has led to an improvement here in comparison to another simulation utilizing a fixed value as it could neutralize the bad influence of triple points.

- The second validation case treats the sharp interface melting of elemental gallium in a rectangular cavity on a centimeter length scale as presented by Gau and Viskanta ([93]). The results of the developed model have shown a good agreement with the experimentally determined position of the sharp phase boundary at different points in time.
- The third test case examines the mushy layer solidification of the binary eutectic alloy $NH_4Cl - H_2O$ in a rectangular box on a centimeter length scale on the basis of investigations by Christenson et al. ([94],[25]). The numerical results concerning the mushy layer width at different points in time as well as temporal temperature variations at different positions have reproduced the experimental measurements with a satisfactory agreement. Additionally, this last validation case has been used to compare the model with Bennon's model, which to the best of my knowledge represents the most complete modelling approach for macroscopic binary alloy solidification with convection. It has been demonstrated that the new model is capable to improve the results from Bennon's method and therefore, the additional effort related to the solution of two more partial differential equations for phase change has been justified.

6.2. Outlook

There remains some work to be done until the present model is ready for an application in the field of core melt in-vessel retention. The most important aspect is an appropriate treatment of turbulence as the typical Rayleigh numbers of corium melt pools are in the range of $10^{15} - 10^{17}$. As a direct resolution of the smallest eddies is not possible considering typical volume sizes of IVR experiments, the present model must be coupled with a turbulence model. Due to the spirit of the model development in this thesis aiming at delivering a picture as complete as possible and due to the fact that volume-averaging has been incroporated already in the phase change process, a large eddy simulation approach seems to be appropriate in order to close the gaps. A recently developed subgrid-scale model for turbulent heat flux in flows with a significant influence of buoyancy may be helpful here ([96]). A minor point is the introduction of an internal heat source representing decay heat production on the right-hand side of the temperature equation, which has not been necessary in the scenarios considered so far.

Bibliography

[1] *World Population Prospects - Key findings & advance tables*. United Nations, Department of Economic and Social Affairs, Population Division, New York, 2015.

[2] T. Manders et al. Socio-economic Developments in OECD Environmental Outlook to 2050: The Consequences of Inaction. *OECD Publishing*, 2012.

[3] A.A. Gubaidullin, B.R. Sehgal. Simeco Tests in a melt stratified pool. *Proceedings of ICONE10*, 2002.

[4] C.G. Theofanus et al. In-vessel coolability and retention of a core melt. *Nuclear Engineering and Design*, 169:1–48, 1997.

[5] O. Kymalainen, H. Tuomisto, O. Hongisto, T.G. Theofanus. Heat flux distribution from a volumetrically heated pool with high Rayleigh number. *Nuclear Engineering and Design*, 149:401–408, 1994.

[6] J.M. Bonnet, J.M. Seiler. Thermal hydraulic phenomena in corium pools: The BALI experiment. *7th International Conference on Nuclear Engineering, Tokyo, Japan*, ICONE-7057, 1999.

[7] B.R. Sehgal, V.A. Bui, T.N. Dinh, J.A. Green, G. Kolb. SIMECO experiments on in-vessel melt pool formation and heat transfer with and without a metallic layer. *OECD/CSNI Workshop on 'In-Vessel Core Debris Retention and Coolability', Garching, Germany*, 1998.

[8] X. Gaus-Liu, A. Miassoedov, T. Cron, T. Wenz. In-vessel melt pool coolability test-Description and results of LIVE experiments. *Nuclear Engineering and Design*, 240:3898–3903, 2010.

[9] V. Asmolov, N.N. Ponomarev-Stepnoy, V. Strizhov, B.R. Sehgal. Challenges left in the area of in-vessel melt retention. *Nuclear Engineering and Design*, 209:87–96, 2001.

[10] C.-T. Tran, T.-N. Dinh. The effective convectivity model for simulation of melt pool heat transfer in a light water reactor pressure vessel lower head. Part 1: Physical processes, modeling and model implementation. *Progress in Nuclear Energy*, 51:849–859, 2009.

[11] C.-T. Tran, T.-N. Dinh. The effective convectivity model for simulation of melt pool heat transfer in a light water reactor pressure vessel lower head. Part 2: Model assessment and application. *Progress in Nuclear Energy*, 51:860–871, 2009.

[12] C.-T. Tran, T.-N. Dinh. Simulation of core melt pool formation in a reactor pressure vessel lower head using an effective convectivity model. *Nuclear Engineering and Technology*, 41:929–944, 2009.

[13] Y.P. Zhang et al. Numerical study on the heat transfer characteristics of LIVE-L4 melt pool with a partial solidification process. *Progress in Nuclear Energy*, 74:213–221, 2014.

[14] K. H. Desai, R. W. Grimes, D. Parfitt, T. Wiss, P. van Uffelen. Atomic-scale simulation of soluble fission products in UO_2. *Joint Research Center, European Comission, EUR Report ISSN 1018-5593*, 2009.

[15] MELCOR Computer Code Manuals. *Primer and User's Guides, NUREG/CR-6119*.

[16] V.R. Voller, M. Cross and N.C. Markatos. An enthalpy method for convection/diffusion phase change. *International Journal for Numerical Methods in Engineering*, 24:271–284, 1987.

[17] V.R. Voller and C. Prakash. A fixed grid numerical modelling methodology for convection-diffusion mushy region phase-change problems. *International Journal of Heat and Mass Transfer*, 30:1709–1719, 1987.

[18] V.R. Voller and A.D. Brent. Modelling the mushy region in a binary alloy. *Applied Mathematical Modelling*, 14:320–326, 1990.

[19] V.R. Voller and C.R. Swaminathan. General source-based method for solidification phase change. *Numerical Heat Transfer, Part B*, 19:175–189, 1991.

[20] W.D. Bennon and F.P. Incropera. A continuum model for momentum, heat and species transport in binary solid-liquid phase change systems-I. Model formulation. *International Journal of Heat and Mass Transfer*, 30:2161–2170, 1987.

[21] W.D. Bennon and F.P. Incropera. A continuum model for momentum, heat and species transport in binary solid-liquid phase change systems-II. Application to solidification in a rectangular cavity. *International Journal of Heat and Mass Transfer*, 30:2171–2187, 1987.

[22] U. Steinberner, H.H. Reineke. Turbulent buoyancy convection heat transfer with internal heat sources. *Proceedings of the 6th International Heat Transfer Conference, Toronto, Canada*, 2:305–310, 1978.

[23] P.C. Carman. Fluid flow through granular beds. *Chemical Engineering Research and Design*, 75:S32–S48, 1997.

[24] X. Gaus-Liu, A. Miassoedov, T. Cron, J. Foit, B. Fluhrer, S. Schmidt-Stiefel, T. Wenz. Test and simulation results of LIVE-L4 + LIVE-L5L. *KIT Scientific Publishing*, KIT Scientific Reports 7593, 2011.

[25] M.S. Christenson, W.D. Bennon and F.P. Incropera. Solidification of an aqueous ammonium chloride solution in a rectangular cavity-II. Comparison of predicted and measured results. *International Journal of Heat and Mass Transfer*, 32:69–79, 1989.

[26] H.S. Udaykumar, R. Mittal and W. Shyy. Computation of solid-liquid phase fronts in the sharp interface limit on fixed grids. *Journal of Computational Physics*, 153:535–574, 1999.

[27] R. F. Sekerka. Morphology: from sharp interface to phase field models. *Journal of Crystal Growth*, 264:530–540, 2004.

[28] R. Kobayashi. Modeling and numerical simulations of dendritic crystal growth. *Physica D*, 63:410–423, 1993.

[29] G. Caginalp. Stefan and Hele-Shaw type models as asymptotic limits of the phase-field equations. *Physical Review A*, 39:5887–5896, 1989.

[30] P.C. Hohenberg, B.I. Halperin. Theory of dynamic critical phenomena. *Review of Modern Physics*, 49:435–479, 1977.

[31] S.M. Allen and J.W. Cahn. A microscopic theory for antiphase boundary motion and its application to antiphase domain coarsening. *Acta Metallurgica*, 27:1085–1095, 1979.

[32] G. Fix. Phase field models for free boundary problems. *Free Boundary Problems, edited by A. Fassano and M. Primicero, Pitman,New York*, pages 580–589, 1983.

[33] J.B. Collins and H. Levine. Diffuse interface model of diffusion-limited crystal growth. *Physical Review B*, 31:6119–6122, 1985.

[34] J. S. Langer. Models of pattern formation in first-order phase transitions. *Directions in Condensed Matter Physics, edited by G. Grinstein and G. Mazenko, World Scientific, Singapore and Philadelphia*, pages 165–186, 1986.

[35] R. Kobayashi. A numerical approach to three-dimensional dendritic solidification. *Experimental Mathematics*, 3:59–81, 1994.

[36] Bronstein, Semendjajew, Musiol, Mühlig. Taschenbuch der Mathematik. *Verlag Harri Deutsch*, page 582, 2005.

[37] W.J. Boettinger, J.A. Warren, C. Beckermann, A. Karma. Phase-Field Simulation of Solidification. *Annu. Rev. Mater. Res.*, 32:163–194, 2002.

[38] G. Caginalp. An analysis of a phase field model of a free boundary. *Archive for Rational Mechanics and Analysis*, 92:205–245, 1986.

[39] G. Caginalp, P.C. Fife. Dynamics of layered interfaces arising from phase boundaries. *SIAM Journal on Applied Mathematics*, 48:506–518, 1988.

[40] R. Gonzales-Cinca, R. Folch, R. Benitez, L. Ramirez-Piscina, J. Casademunt, A. Hernandez-Machado. Phase-field models in interfacial pattern formation out of equilibrium. *Advances in Condensed Matter and Statistical Physics*, pages 203–236, 2004.

[41] A. Karma, W.-J. Rappel. Phase-field method for computationally efficient modeling of solidification with arbitrary interface kinetics. *Physical Review E*, 53:R3017–R3020, 1996.

[42] A. Karma, W.-J. Rappel. Numerical Simulation of three-dimensional dendritic growth. *Physical Review Letters*, 77:4050–4053, 1996.

[43] A. Karma, W.-J. Rappel. Quantitative phase-field modeling of dendritic growth in two and three dimensions. *Physical Review E*, 57:4323–4349, 1998.

[44] J.J. Hoyt, M. Asta, A. Karma. Atomistic and continuum modeling of dendritic solidification. *Materials Science and Engineering*, R41:121–163, 2003.

[45] R.F. Almgren. Second-order phase field asymptotics for unequal conductivities. *SIAM Journal on Applied Mathematics*, 59:2086–2107, 1999.

[46] G.B. McFadden, A.A. Wheeler, D.M. Anderson. Thin interface asymptotics for an energy/entropy approach to phase-field models with unequal conductivities. *Physica D*, 144:154–168, 2000.

[47] O. Penrose, P.C. Fife. Thermodynamically consistent models of phase-field type for the kinetics of phase transitions. *Physica D*, 43:44–62, 1990.

[48] S.-L. Wang, R.F. Sekerka, A.A. Wheeler, B.T. Murray, S.R. Coriell, R.J. Braun and G.B. McFadden. Thermodynamically-consistent phase-field models for solidification. *Physica D*, 69:189–200, 1993.

[49] C. Beckermann, H.J. Diepers, I. Steinbach, A. Karma, X. Tong. Modeling melt convection in phase-field simulations of solidification. *Journal of Computational Physics*, 154:468–496, 1999.

[50] D.M. Anderson and G.B. McFadden. Diffuse-interface methods in fluid mechanics. *Annual Review of Fluid Mechanics*, 30:139–165, 1998.

[51] D.M. Anderson, G.B. McFadden and A.A. Wheeler. A phase-field model of solidification with convection. *Physica D*, 135:175–194, 2000.

[52] A.A. Wheeler, W.J. Boettinger, G.B. McFadden. Phase-field model for isothermal phase transitions in binary alloys. *Physical Review A*, 45:7424–7439, 1992.

[53] J.A. Warren and W.J. Boettinger. Predicition of dendritic growth and microsegregation patterns in a binary alloy using the phase-field method. *Acta Metallurgica et Materialia*, 43:689–703, 1995.

[54] W.J. Boettinger and J.A. Warren. The phase-field method: Simulation of alloy dendritic solidification during recalescence. *Metallurgical and Materials Transactions A*, 27A:657–669, 1996.

[55] S.G. Kim, W.T. Kim, T. Suzuki. Interfacial compositions of solid and liquid in a phase-field model with finite interface thickness for isothermal solidification in binary alloys. *Physical Review E*, 58:3316–3323, 1998.

[56] S.G. Kim, W.T. Kim, T. Suzuki. Phase-field model for binary alloys. *Physical Review E*, 60:7186–7197, 1999.

[57] M. Ode, T. Suzuki, S.G. Kim, W.T. Kim. Phase-field model for solidification of Fe-C alloys. *Science and Technology of Advanced Materials*, 1:43–49, 2000.

[58] A.A. Wheeler, G.B. McFadden and W.J. Boettinger. Phase-field model for solidification of a eutectic alloy. *Proceedings of the Royal Society of London A*, 452:495–525, 1996.

[59] T.S. Lo, A. Karma and M. Plapp. Phase-field modeling of microstructural pattern formation during directional solidification of peritectic alloys without morphological instability. *Physical Review E*, 63:031504–1–15, 2001.

[60] E. Pogorelov, J. Kundin, H. Emmerich. General phase-field model with stability requirements on interfaces in N-dimensional phase-field space. *arxiv.org*, page arXiv:1304.6549, 2013.

[61] I. Steinbach, F. Pezzolla, B. Nestler, M. Seeßelberg, R. Prieler, G.J. Schmitz, J.L.L. Rezende. A phase field concept for multiphase systems. *Physica D*, 94:135–147, 1996.

[62] J. Tiaden, B. Nestler, H.J. Diepers and I. Steinbach. The multiphase-field model with an integrated concept for modelling solute diffusion. *Physica D*, 115:73–86, 1998.

[63] M. Zanotello, M.C.C. Cunha and R. Caram. Evaluation of lamellar spacing selection in eutectic alloys using phase field model. *Computational Materials Science*, 44:695–701, 2008.

[64] J. Kundin and R. Siquieri. Phase-field model for multiphase systems with different thermodynamic factors. *Physica D*, 240:459–469, 2011.

[65] H. Garcke, B. Nestler and B. Stoth. On anisotropic order parameter models for multi-phase systems and their sharp interface limits. *Physica D*, 115:87–108, 1998.

[66] I. Steinbach and F. Pezzolla. A generalized field method for multiphase transformations using interface fields. *Physica D*, 134:385–393, 1999.

[67] S.G. Kim, W.T. Kim, T. Suzuki and M. Ode. Phase-field modeling of eutectic solidification. *Journal of Crytsal Growth*, 261:135–158, 2004.

[68] J. Eiken, B. Böttger and I. Steinbach. Multiphase-field approach for multicomponent alloys with extrapolation scheme for numerical application. *Physical Review E*, 73:066122, 2006.

[69] R. Folch and M. Plapp. Towards a quantitative phase-field model of two-phase solidification. *Physical Review E*, 68:010602, 2003.

[70] R. Folch and M. Plapp. Quantitative phase-field modeling of two-phase growth. *Physical Review E*, 72:011602, 2005.

[71] A. Parisi and M. Plapp. Stability of lamellar eutectic growth. *Acta Materialia*, 56:1348–1357, 2008.

[72] J. Kundin, R. Kumar, A. Schlieter, M.A. Choudhary, T. Gemming, U. Kühn, J. Eckert, H. Emmerich. Phase-field modeling of eutectic Ti-Fe alloy solidification. *Computational Materials Science*, 63:319–328, 2012.

[73] H. Garcke, B. Nestler and B. Stoth. A multiphase field concept: Numerical simulations of moving phase boundaries and multiple junctions. *SIAM Journal on Applied Mathematics*, 60:295–315, 1999.

[74] B. Nestler and A.A. Wheeler. A multi-phase-field model of eutectic and peritectic alloys: numerical simulation of growth structures. *Physica D*, 138:114–133, 2000.

[75] H. Garcke, B. Nestler and B. Stinner. A diffuse interface model for alloys with multiple components and phases. *SIAM Journal on Applied Mathematics*, 64:775–799, 2004.

[76] B. Nestler, H. Garcke and B. Stinner. Multicomponent alloy solidification: Phase-field modeling and simulations. *Physical Review E*, 71:041609, 2005.

[77] D. Danilov and B. Nestler. Phase-field simulations of solidification in binary and ternary systems using a finite element method. *Journal of Crystal Growth*, 275:e177–e182, 2005.

[78] H. Garcke, B. Nestler, B. Stinner and F. Wendler. Allen-Cahn systems with volume constraints. *Universität Regensburg, Preprint Nr. 14*, 2007.

[79] B. Nestler, F. Wendler, M. Selzer, B. Stinner and H. Garcke. Phase-field model for multiphase systems with preserved volume fractions. *Physical Review E*, 78:011604, 2008.

[80] R. Haas. Modeling and analysis for general non-isothermal convective phase field systems. *PHD thesis at the faculty of mathematics at University of Regensburg, http://epub.uni-regensburg.de/10538/1/diss_robert_haas.pdf*, 2005.

[81] A. Karma. Phase-field formulation for quantitative modeling of alloy solidification. *Physical Review Letters*, 87:115701, 2001.

[82] M. Ohno, K. Matsuura. Quantitative phase-field modeling for dilute alloy solidification involving diffusion in the solid. *Physical Review E*, 79:031603, 2009.

[83] M. Ohno, K. Matsuura. Quantitative phase-field modeling for two-phase solidification process involving diffusion in the solid. *Acta Materialia*, 58:5749–5758, 2010.

[84] H.-J. Diepers, C. Beckermann and I. Steinbach. Simulation of convection and ripening in a binary alloy mush using the phase-field method. *Acta Metallurgica*, 47:3663–3678, 1999.

[85] M.X. Liu, K. Wang, D. Xia, T. Jiang. Phase field simulation of Al-Si binary dendritic growth and micro-segregation patterns under convection. *Journal of Alloys and Compounds*, 589:431–435, 2014.

[86] B. Nestler, A.A. Wheeler, L. Ratke and C. Stöcker. Phase-field model for solidification of a monotectic alloy with convection. *Physica D*, 141:133–154, 2000.

[87] B. Nestler, A. Aksi, M. Selzer. Combined lattice Boltzmann and phase-field simulations for incompressible fluid flow in porous media. *Mathematics and Computers in Simulation*, 80:1458–1468, 2010.

[88] R. Mauri. *Non-Equilibrium Thermodynamics in Multiphase Flows*. Springer, 2013.

[89] The OpenFOAM Foundation. *www.openfoam.org*.

[90] R.I. Issa. Solution of the Implicitly Discretised Fluid Flow Equations by Operator-Splitting. *Journal of Computational Physics*, 62:40–65, 1985.

[91] C.W. Hirt, B.D. Nichols. Volume of Fluid (VOF) Method for the Dynamics of Free Boundaries. *Journal of Computational Physics*, 39:201–225, 1979.

[92] M. Ginibre, S. Akamatsu, G. Faivre. Experimental determination of the stability diagram of a lamellar eutectic growth front. *Physical Review E*, 56:780–796, 1997.

[93] C. Gau, R. Viskanta. Melting and solidification of a pure metal on a vertical wall. *Journal of Heat Transfer*, 108:174–181, 1986.

[94] M.S. Christenson and F.P. Incropera. Solidification of an aqueous ammonium chloride solution in a rectangular cavity-I. Experimental study. *International Journal of Heat and Mass Transfer*, 32:47–68, 1989.

[95] M. Rathore, R. Kapuno. *Engineering Heat Transfer*. Jones and Bartlett Publ., 2nd edition, 2009.

[96] D. Morar. Subgrid-scale heat flux modeling for large eddy simulation of turbulent mixed convection. *PHD thesis at the faculty of mechanical engineering at Karlsruhe Institute of Technology, http://d-nb.info/1065732139/34*, 2014.

[97] J. Mergy, G. Faivre, C. Guthmann and R. Mellet. Quantitative determination of the physical parameters relevant to the thin-film directional solidification of the $CBr_4 - C_2Cl_6$ eutectic alloy. *Journal of Crystal Grwoth*, 134:353–368, 1993.

[98] S. Bottin-Rousseau, M. Perrut, C. Picard, S. Akamatsu and G. Faivre. An experimental method for the in-situ observation of eutectic growth patterns in bulk samples of transparent alloys. *Journal of Crystal Growth*, 306:465–472, 2007.

[99] M.A. Rady, S.A. Nada. Solidification of hypereutectic and hypoeutectic binary alloys with buoyancy and surface tension driven natural convection. *Heat and Mass Transfer*, 34:337–347, 1998.

[100] R.L. Blokhra, S.K. Agarwal and S.S. Thakur. Molar volumes of ammonium chloride-ammonium salt solutions. *Proceedings of the Indian Academy of Sciences*, 89:193–200, 1980.

[101] C. M. Oldenburg and F. J. Spera. Hybrid model for solidification and convection. *Numerical Heat Transfer, Part B*, 21:217–229, 1992.

[102] D. Morvan, M. E. Ganaoui and P. Bontoux. Numerical simulation of a 2-D crystal growth problem in vertical Bridgman-Stockbarger furnace: latent heat effect and crytsal-melt interface morphology. *International Journal of Heat and Mass Transfer*, 42:573–579, 1999.

[103] D. Turnbull. Formation of Crystal Nuclei in Liquid Metals. *Journal of Applied Physics*, 21:1022–1028, 1950.

7. Appendix

A. Derivatives of Individual Phase Compositions ξ_i

Regard the chemical potential function

$$\mu(T, \xi, \Phi_1, \Phi_2, \Phi_3) = \frac{\partial f_1(\xi_1, T)}{\partial \xi_1} = \frac{\partial f_2(\xi_2, T)}{\partial \xi_2} = \frac{\partial f_3(\xi_3, T)}{\partial \xi_3}.$$

A.1. Derivative with Respect to Temperature

We have

$$\frac{d\mu}{dT} = \frac{\partial^2 f_1}{\partial \xi_1 \partial T} + \frac{\partial^2 f_1}{\partial \xi_1^2}\frac{\partial \xi_1}{\partial T} = \frac{\partial^2 f_2}{\partial \xi_2 \partial T} + \frac{\partial^2 f_2}{\partial \xi_2^2}\frac{\partial \xi_2}{\partial T} = \frac{\partial^2 f_3}{\partial \xi_3 \partial T} + \frac{\partial^2 f_3}{\partial \xi_3^2}\frac{\partial \xi_3}{\partial T}$$

and therefore

$$\frac{\partial \xi_j}{\partial T} = \frac{\frac{\partial^2 f_i}{\partial \xi_i \partial T} - \frac{\partial^2 f_j}{\partial \xi_j \partial T}}{\frac{\partial^2 f_j}{\partial \xi_j^2}} + \frac{\frac{\partial^2 f_i}{\partial \xi_i^2}}{\frac{\partial^2 f_j}{\partial \xi_j^2}}\frac{\partial \xi_i}{\partial T}.$$

Due to

$$\frac{d\xi}{dT} = 0 = \sum_{k=1}^{3} h_k \frac{\partial \xi_k}{\partial T},$$

we get

$$h_i\frac{\partial \xi_i}{\partial T} + (\frac{\frac{\partial^2 f_i}{\partial \xi_i \partial T} - \frac{\partial^2 f_j}{\partial \xi_j \partial T}}{\frac{\partial^2 f_j}{\partial \xi_j^2}} + \frac{\frac{\partial^2 f_i}{\partial \xi_i^2}}{\frac{\partial^2 f_j}{\partial \xi_j^2}}\frac{\partial \xi_i}{\partial T})h_j + (\frac{\frac{\partial^2 f_i}{\partial \xi_i \partial T} - \frac{\partial^2 f_k}{\partial \xi_k \partial T}}{\frac{\partial^2 f_k}{\partial \xi_k^2}} + \frac{\frac{\partial^2 f_i}{\partial \xi_i^2}}{\frac{\partial^2 f_k}{\partial \xi_k^2}}\frac{\partial \xi_i}{\partial T})h_k = 0$$

and consequently

$$\frac{\partial \xi_i}{\partial T} = \frac{h_j \frac{\partial^2 f_k}{\partial \xi_k^2}(\frac{\partial^2 f_j}{\partial \xi_j \partial T} - \frac{\partial^2 f_i}{\partial \xi_i \partial T})}{h_1 \frac{\partial^2 f_2}{\partial \xi_2^2}\frac{\partial^2 f_3}{\partial \xi_3^2} + h_2 \frac{\partial^2 f_1}{\partial \xi_1^2}\frac{\partial^2 f_3}{\partial \xi_3^2} + h_3 \frac{\partial^2 f_1}{\partial \xi_1^2}\frac{\partial^2 f_2}{\partial \xi_2^2}} \tag{7.1}$$

A.2. Derivative with Respect to Composition

We have

$$\frac{d\mu}{d\xi} = \frac{\partial^2 f_1}{\partial \xi_1^2}\frac{\partial \xi_1}{\partial \xi} = \frac{\partial^2 f_2}{\partial \xi_2^2}\frac{\partial \xi_2}{\partial \xi} = \frac{\partial^2 f_3}{\partial \xi_3^2}\frac{\partial \xi_3}{\partial \xi}$$

and hence

$$\frac{\partial \xi_j}{\partial \xi} = \frac{\frac{\partial^2 f_i}{\partial \xi_i^2}}{\frac{\partial^2 f_j}{\partial \xi_j^2}}\frac{\partial \xi_i}{\partial \xi}.$$

From

$$\frac{d\xi}{d\xi} = 1 = \sum_{k=1}^{3} h_k \frac{\partial \xi_k}{\partial \xi},$$

it follows that

$$\frac{\partial \xi_i}{\partial \xi}\{h_i + \frac{\frac{\partial^2 f_i}{\partial \xi_i^2}}{\frac{\partial^2 f_j}{\partial \xi_j^2}}h_j + \frac{\frac{\partial^2 f_i}{\partial \xi_i^2}}{\frac{\partial^2 f_k}{\partial \xi_k^2}}h_k\} = 1. \tag{7.2}$$

Consequently,

$$\frac{\partial \xi_i}{\partial \xi} = \frac{\frac{\partial^2 f_j}{\partial \xi_j^2}\frac{\partial^2 f_k}{\partial \xi_k^2}}{h_1\frac{\partial^2 f_2}{\partial \xi_2^2}\frac{\partial^2 f_3}{\partial \xi_3^2} + h_2\frac{\partial^2 f_1}{\partial \xi_1^2}\frac{\partial^2 f_3}{\partial \xi_3^2} + h_3\frac{\partial^2 f_1}{\partial \xi_1^2}\frac{\partial^2 f_2}{\partial \xi_2^2}}. \tag{7.3}$$

A.3. Derivative with Respect to the Phase-Fields

Due to

$$\frac{d\mu}{d\Phi_l} = \frac{\partial^2 f_1}{\partial \xi_1^2}\frac{\partial \xi_1}{\partial \Phi_l} = \frac{\partial^2 f_2}{\partial \xi_2^2}\frac{\partial \xi_2}{\partial \Phi_l} = \frac{\partial^2 f_3}{\partial \xi_3^2}\frac{\partial \xi_3}{\partial \Phi_l},$$

we have

$$\frac{\partial \xi_j}{\partial \Phi_l} = \frac{\frac{\partial^2 f_i}{\partial \xi_i^2}}{\frac{\partial^2 f_j}{\partial \xi_j^2}}\frac{\partial \xi_i}{\partial \Phi_l}.$$

Using

$$\frac{d\xi}{d\Phi_l} = 0 = \sum_{k=1}^{3} h_k \frac{\partial \xi_k}{\partial \Phi_l} + \frac{\partial h_k}{\partial \Phi_l}\xi_k \leftrightarrow \sum_{k=1}^{3} h_k \frac{\partial \xi_k}{\partial \Phi_l} = -\sum_{k=1}^{3} \frac{\partial h_k}{\partial \Phi_l}\xi_k, \tag{7.4}$$

we get

$$\frac{\partial \xi_i}{\partial \Phi_l}\{h_i + \frac{\frac{\partial^2 f_i}{\partial \xi_i^2}}{\frac{\partial^2 f_j}{\partial \xi_j^2}}h_j + \frac{\frac{\partial^2 f_i}{\partial \xi_i^2}}{\frac{\partial^2 f_k}{\partial \xi_k^2}}h_k\} = -\xi_1\frac{\partial h_1}{\partial \Phi_l} - \xi_2\frac{\partial h_2}{\partial \Phi_l} - \xi_3\frac{\partial h_3}{\partial \Phi_l}$$

and therefore

$$\frac{\partial \xi_i}{\partial \Phi_l} = \frac{-\xi_1\frac{\partial h_1}{\partial \Phi_l} - \xi_2\frac{\partial h_2}{\partial \Phi_l} - \xi_3\frac{\partial h_3}{\partial \Phi_l}}{h_1\frac{\partial^2 f_2}{\partial \xi_2^2}\frac{\partial^2 f_3}{\partial \xi_3^2} + h_2\frac{\partial^2 f_1}{\partial \xi_1^2}\frac{\partial^2 f_3}{\partial \xi_3^2} + h_3\frac{\partial^2 f_1}{\partial \xi_1^2}\frac{\partial^2 f_2}{\partial \xi_2^2}} \cdot \frac{\partial^2 f_j}{\partial \xi_j^2}\frac{\partial^2 f_k}{\partial \xi_k^2} \tag{7.5}$$

B. Derivatives of Chemical Potential μ

B.1. Derivative with Respect to Temperature

We can calculate

$$\frac{d\mu}{dT} = \frac{d}{dT}(\frac{\partial f_i}{\partial \xi_i}) = \frac{\partial^2 f_i}{\partial \xi_i \partial T} + \frac{\partial^2 f_i}{\partial \xi_i^2}\frac{\partial \xi_i}{\partial T}.$$

Using (7.1), one gets

$$\frac{d\mu}{dT} = \frac{h_1 \frac{\partial^2 f_2}{\partial \xi_2^2}\frac{\partial^2 f_3}{\partial \xi_3^2}\frac{\partial^2 f_1}{\partial \xi_1 \partial T} + h_2 \frac{\partial^2 f_1}{\partial \xi_1^2}\frac{\partial^2 f_3}{\partial \xi_3^2}\frac{\partial^2 f_2}{\partial \xi_2 \partial T} + h_3 \frac{\partial^2 f_1}{\partial \xi_1^2}\frac{\partial^2 f_2}{\partial \xi_2^2}\frac{\partial^2 f_3}{\partial \xi_3 \partial T}}{h_1 \frac{\partial^2 f_2}{\partial \xi_2^2}\frac{\partial^2 f_3}{\partial \xi_3^2} + h_2 \frac{\partial^2 f_1}{\partial \xi_1^2}\frac{\partial^2 f_3}{\partial \xi_3^2} + h_3 \frac{\partial^2 f_1}{\partial \xi_1^2}\frac{\partial^2 f_2}{\partial \xi_2^2}}. \tag{7.6}$$

B.2. Derivative with Respect to Composition

Based on

$$\frac{d\mu}{d\xi} = \frac{d}{d\xi}(\frac{\partial f_i}{\partial \xi_i}) = \frac{\partial^2 f_i}{\partial \xi_i^2}\frac{\partial \xi_i}{\partial \xi}$$

and using (7.3), we obtain

$$\frac{d\mu}{d\xi} = \frac{\frac{\partial^2 f_1}{\partial \xi_1^2}\frac{\partial^2 f_2}{\partial \xi_2^2}\frac{\partial^2 f_3}{\partial \xi_3^2}}{h_1 \frac{\partial^2 f_2}{\partial \xi_2^2}\frac{\partial^2 f_3}{\partial \xi_3^2} + h_2 \frac{\partial^2 f_1}{\partial \xi_1^2}\frac{\partial^2 f_3}{\partial \xi_3^2} + h_3 \frac{\partial^2 f_1}{\partial \xi_1^2}\frac{\partial^2 f_2}{\partial \xi_2^2}}. \tag{7.7}$$

B.3. Derivative with Respect to the Phase-Fields

We have

$$\frac{d\mu}{d\Phi_l} = \frac{d}{d\Phi_l}(\frac{\partial f_i}{\partial \xi_i}) = \frac{\partial^2 f_i}{\partial \xi_i^2}\frac{\partial \xi_i}{\partial \Phi_l}.$$

Using (7.5) and (7.7), one gets

$$\frac{d\mu}{d\Phi_l} = -\frac{d\mu}{d\xi}\sum_{k=1}^{3}\frac{\partial h_k}{\partial \Phi_l}\xi_k. \tag{7.8}$$

C. Derivatives of Internal Energy per Mass e_m

C.1. Derivative with Respect to Density

Internal energy per mass e_m is given by

$$e_m = \frac{1}{\rho}\sum_{k=1}^{3} h_k\{f_k - T\frac{\partial f_k}{\partial T}\}.$$

If we express the molar volume v_m appearing in the individual phase free energy densities f_k as

$$v_m = \frac{M_m}{\rho}$$

with the molar mass M_m, the quantities f_k will be composed of terms with prefactors $\frac{\rho RT}{M_m}$, ρL as well as ρc. Hence, ρ is cancelled in e_m, leading to

$$\frac{\partial e_m}{\partial \rho} = 0. \tag{7.9}$$

C.2. Derivative with Respect to Temperature

$$\begin{aligned}\frac{de_m}{dT} &= \frac{\partial e_m}{\partial T} + \sum_{k=1}^{3} \frac{\partial e_m}{\partial \xi_k}\frac{\partial \xi_k}{\partial T} \\ &= \frac{1}{\rho}\sum_{k=1}^{3}\{h_k(\frac{\partial f_k}{\partial T} - \frac{\partial f_k}{\partial T} - T\frac{\partial^2 f_k}{\partial T^2}\} + \frac{1}{\rho}\sum_{k=1}^{3}\{h_k(\frac{\partial f_k}{\partial \xi_k} - T\frac{\partial^2 f_k}{\partial \xi_k \partial T})\frac{\partial \xi_k}{\partial T}\}\end{aligned}$$

We use

$$\begin{aligned}\frac{1}{\rho}\sum_{k=1}^{3}\{h_k(\frac{\partial f_k}{\partial \xi_k} - T\frac{\partial^2 f_k}{\partial \xi_k \partial T})\frac{\partial \xi_k}{\partial T}\} &= \frac{1}{\rho}\mu\sum_{k=1}^{3}\{h_k\frac{\partial \xi_k}{\partial T}\} - \frac{T}{\rho}\sum_{k=1}^{3}\{h_k[\frac{\partial}{\partial T}(\frac{\partial f_k}{\partial \xi_k}\frac{\partial \xi_k}{\partial T}) - \frac{\partial f_k}{\partial \xi_k}\frac{\partial^2 \xi_k}{\partial T^2}]\} \\ &= \frac{\mu}{\rho}\frac{\partial \xi}{\partial T} - \frac{T}{\rho}\frac{\partial}{\partial T}(\mu\frac{\partial \xi}{\partial T}) + \frac{T}{\rho}\mu\frac{\partial^2 \xi}{\partial T^2} = 0 \end{aligned} \tag{7.10}$$

because ξ and T are state variables, which are independent from each other by definition:

$$\frac{\partial \xi}{\partial T} = \frac{\partial^2 \xi}{\partial T^2} = 0.$$

We end up with

$$\frac{de_m}{dT} = -\frac{T}{\rho}\sum_{k=1}^{3} h_k\frac{\partial^2 f_k}{\partial T^2}. \tag{7.11}$$

C.3. Derivative with Respect to Composition

$$\begin{aligned}\frac{de_m}{d\xi} &= \frac{\partial e_m}{\partial \xi} + \sum_{k=1}^{3}\frac{\partial e_m}{\partial \xi_k}\frac{\partial \xi_k}{\partial \xi} \\ &= \frac{1}{\rho}\sum_{k=1}^{3} h_k(\frac{\partial f_k}{\partial \xi_k} - T\frac{\partial^2 f_k}{\partial \xi_k \partial T})\frac{\partial \xi_k}{\partial \xi} \\ &= \frac{\mu}{\rho}\sum_{k=1}^{3} h_k\frac{\partial \xi_k}{\partial \xi} - \frac{T}{\rho}\sum_{k=1}^{3} h_k\frac{\partial^2 f_k}{\partial \xi_k \partial T}\frac{\partial \xi_k}{\partial \xi}\end{aligned}$$

We use

$$\sum_{k=1}^{3} h_k\frac{\partial \xi_k}{\partial \xi} = \frac{\partial \xi}{\partial \xi} = 1,$$

insert $\frac{\partial \xi_k}{\partial \xi}$ from (7.3) and compare with(7.6):

$$\sum_{k=1}^{3} h_k\frac{\partial^2 f_k}{\partial \xi_k \partial T}\frac{\partial \xi_k}{\partial \xi} = \frac{d\mu}{dT}. \tag{7.12}$$

This leads to

$$\frac{de_m}{d\xi} = \frac{1}{\rho}(\mu - T\frac{d\mu}{dT}). \tag{7.13}$$

C.4. Derivative with Respect to the Phase-Fields

$$\begin{aligned}\frac{de_m}{d\Phi_j} &= \frac{\partial e_m}{\partial \Phi_j} + \sum_{k=1}^{3} \frac{\partial e_m}{\partial \xi_k}\frac{\partial \xi_k}{\partial \Phi_j} \\ &= \frac{1}{\rho}\sum_{k=1}^{3}\frac{\partial h_k}{\partial \Phi_j}(f_k - T\frac{\partial f_k}{\partial T}) + \frac{1}{\rho}\sum_{k=1}^{3} h_k(\frac{\partial f_k}{\partial \xi_k} - T\frac{\partial^2 f_k}{\partial \xi_k \partial T})\frac{\partial \xi_k}{\partial \Phi_j} \\ &= \frac{1}{\rho}\sum_{k=1}^{3}\frac{\partial h_k}{\partial \Phi_j}(f_k - T\frac{\partial f_k}{\partial T}) + \frac{\mu}{\rho}\sum_{k=1}^{3} h_k\frac{\partial \xi_k}{\partial \Phi_j} - \frac{T}{\rho}\sum_{k=1}^{3} h_k\frac{\partial^2 f_k}{\partial \xi_k \partial T}\frac{\partial \xi_k}{\partial \Phi_j}\end{aligned}$$

Due to

$$\frac{\partial \xi}{\partial \Phi_j} = \sum_{k=1}^{3}\frac{\partial h_k}{\partial \Phi_j}\xi_k + h_k\frac{\partial \xi_k}{\partial \Phi_j} = 0 \leftrightarrow \sum_{k=1}^{3} h_k\frac{\partial \xi_k}{\partial \Phi_j} = -\sum_{k=1}^{3}\frac{\partial h_k}{\partial \Phi_j}\xi_k \tag{7.14}$$

and

$$\begin{aligned}\sum_{k=1}^{3} h_k\frac{\partial^2 f_k}{\partial \xi_k \partial T}\frac{\partial \xi_k}{\partial \Phi_j} &= \sum_{k=1}^{3} h_k\{\frac{\partial}{\partial T}(\frac{\partial f_k}{\partial \xi_k}\frac{\partial \xi_k}{\partial \Phi_j}) - \frac{\partial f_k}{\partial \xi_k}\frac{\partial^2 \xi_k}{\partial \Phi_j \partial T}\} \\ &= \frac{\partial}{\partial T}(\sum_{k=1}^{3} h_k\frac{\partial f_k}{\partial \xi_k}\frac{\partial \xi_k}{\partial \Phi_j}) - \mu\frac{\partial}{\partial T}(\sum_{k=1}^{3} h_k\frac{\partial \xi_k}{\partial \Phi_j}) \\ &= \frac{\partial}{\partial T}(-\mu\sum_{k=1}^{3}\frac{\partial h_k}{\partial \Phi_j}\xi_k) + \mu\frac{\partial}{\partial T}(\sum_{k=1}^{3}\frac{\partial h_k}{\partial \Phi_j}\xi_k) \\ &= -\frac{\partial \mu}{\partial T}\sum_{k=1}^{3}\frac{\partial h_k}{\partial \Phi_j}\xi_k,\end{aligned} \tag{7.15}$$

one obtains

$$\frac{de_m}{d\Phi_j} = \frac{1}{\rho}\sum_{k=1}^{3}\frac{\partial h_k}{\partial \Phi_j}[f_k - T\frac{\partial f_k}{\partial T} - \mu\xi_k + T\frac{\partial \mu}{\partial T}\xi_k]. \tag{7.16}$$

D. Derivatives of Entropy per Mass s_m

D.1. Derivative with Respect to Temperature

$$\begin{aligned}\frac{ds_m}{dT} &= \frac{\partial s_m}{\partial T} + \sum_{k=1}^{3}\frac{\partial s_m}{\partial \xi_k}\frac{\partial \xi_k}{\partial T} \\ &= -\frac{1}{\rho}\sum_{k=1}^{3} h_k\frac{\partial^2 f_k}{\partial T^2} - \frac{1}{\rho}\sum_{k=1}^{3} h_k\frac{\partial^2 f_k}{\partial \xi_k \partial T}\frac{\partial \xi_k}{\partial T}.\end{aligned}$$

Using (7.10), we get

$$\sum_{k=1}^{3} h_k \frac{\partial^2 f_k}{\partial \xi_k \partial T} \frac{\partial \xi_k}{\partial T} = 0$$

and hence

$$\frac{ds_m}{dT} = -\frac{1}{\rho} \sum_{k=1}^{3} h_k \frac{\partial^2 f_k}{\partial T^2}. \tag{7.17}$$

D.2. Derivative with Respect to Composition

$$\frac{ds_m}{d\xi} = \frac{\partial s_m}{\partial \xi} + \sum_{k=1}^{3} \frac{\partial s_m}{\partial \xi_k} \frac{\xi_k}{\partial \xi} = -\frac{1}{\rho} \sum_{k=1}^{3} h_k \frac{\partial^2 f_k}{\partial \xi_k \partial T} \frac{\partial \xi_k}{\xi}$$

Utilizing (7.12), we get

$$\frac{ds_m}{d\xi} = -\frac{1}{\rho} \frac{d\mu}{dT}. \tag{7.18}$$

D.3. Derivative with Respect to the Phase-Fields

$$\begin{aligned}
\frac{ds_m}{d\Phi_j} =& -\frac{1}{\rho}\{2\frac{a_{ij}}{\Delta}\Phi_i^2\Phi_j + 2\frac{a_{kj}}{\Delta}\Phi_k^2\Phi_j \\
&+ \frac{a_{ij}+a_{ik}-a_{kj}}{\Delta}\Phi_i^2\Phi_k + \frac{a_{kj}+a_{ik}-a_{ij}}{\Delta}\Phi_k^2\Phi_i + 2\frac{a_{ij}+a_{kj}-a_{ik}}{\Delta}\Phi_i\Phi_j\Phi_k \\
&+ \sum_{k=1}^{3} \frac{\partial h_k}{\partial \Phi_j}\frac{\partial f_k}{\partial T} + \sum_{k=1}^{3} h_k \frac{\partial^2 f_k}{\partial \xi_k \partial T}\frac{\partial \xi_k}{\partial \Phi_j}\}
\end{aligned}$$

Using (7.15) leads to

$$\begin{aligned}
\frac{ds_m}{d\Phi_j} =& -\frac{1}{\rho}\{2\frac{a_{ij}}{\Delta}\Phi_i^2\Phi_j + 2\frac{a_{kj}}{\Delta}\Phi_k^2\Phi_j \\
&+ \frac{a_{ij}+a_{ik}-a_{kj}}{\Delta}\Phi_i^2\Phi_k + \frac{a_{kj}+a_{ik}-a_{ij}}{\Delta}\Phi_k^2\Phi_i + 2\frac{a_{ij}+a_{kj}-a_{ik}}{\Delta}\Phi_i\Phi_j\Phi_k \\
&+ \sum_{k=1}^{3} \frac{\partial h_k}{\partial \Phi_j}(\frac{\partial f_k}{\partial T} - \frac{\partial \mu}{\partial T}\xi_k)\}.
\end{aligned} \tag{7.19}$$

D.4. Derivative with Respect to Δ

$$\begin{aligned}
\frac{\partial s_m}{\partial \Delta} =& \frac{1}{\rho}\{\frac{1}{\Delta^2}[a_{12}\Phi_1^2\Phi_2^2 + a_{13}\Phi_1^2\Phi_3^2 + a_{23}\Phi_2^2\Phi_3^2] \\
&+ \frac{1}{\Delta^2}\Phi_1\Phi_2\Phi_3[(a_{12}+a_{13}-a_{23})\Phi_1 + (a_{12}-a_{13}+a_{23})\Phi_2 + (a_{13}-a_{12}+a_{23})\Phi_3]\}
\end{aligned} \tag{7.20}$$

E. Material Properties of $CBr_4 - C_2Cl_6$

The phase diagram of the binary eutectic alloy $CBr_4 - C_2Cl_6$ is presented in Figure E.1. According to this, the liquidus and solidus lines can be modeled as straight lines. The material properties used in this work are as follows (mainly taken from [67]):

Quantity	Symbol	Value	Unit
eutectic composition	ξ_e	0.118	1
eutectic temperature	T_e	357.6	K
partition coefficient $\alpha - l$	k_{12}	0.75	1
partition coefficient $\beta - l$ at $T = T_e$	k_{13e}	1.6	1
slope of liquidus line $\alpha - l$	m_{12}	-81	K
slope of liquidus line $\beta - l$	m_{13}	165	K
liquidus line $\alpha - l$	$\xi_1^{(12)}(T)$	$\xi_e - \frac{T_e - T}{m_{12}}$	1
liquidus line $\beta - l$	$\xi_1^{(13)}(T)$	$\xi_e - \frac{T_e - T}{m_{13}}$	1
solidus line $\alpha - l$	$\xi_2^{(12)}(T)$	$k_{12}\xi_1^{(12)}(T)$	1
solidus line $\beta - l$	$\xi_3^{(13)}(T)$	$\frac{1-k_{13e}\xi_e}{m_{13}(1-\xi_e)}(T - T_e) + k_{13e}\xi_e$	1
diffusion coefficient of the liquid phase	D_1	$5 \cdot 10^{-10}$	$\frac{m^2}{s}$
diffusion coefficient of the solid phase	$D_2 = D_3$	0	$\frac{m^2}{s}$
diffusion coefficient	D	$\Phi_1 D_1$	$\frac{m^2}{s}$
surface tension $\alpha - l$	σ_{12}	$6.6 \cdot 10^{-3}$	$\frac{J}{m^2}$
surface tension $\beta - l$	σ_{13}	$5.8 \cdot 10^{-3}$	$\frac{J}{m^2}$
surface tension $\alpha - \beta$	σ_{23}	$11.5 \cdot 10^{-3}$	$\frac{J}{m^2}$
molar volume	v_m	$1.12 \cdot 10^{-4}$	$\frac{m^3}{mol}$
latent heat per volume	ρL	$3 \cdot 10^7$	$\frac{J}{m^3}$

Table E.1.: Material properties of $CBr_4 - C_2Cl_6$

Diffusion in the solid phase is neglected here. The value for the latent heat per volume is based on data presented in [97] and [98]. The constants ζ_{12} and ζ_{13} appearing in (3.195) as a result of the thin-interface analysis are obtained by numerically evaluating the integral (3.196):

$$\zeta_{12} = 0.0483$$
$$\zeta_{13} = 0.0298.$$

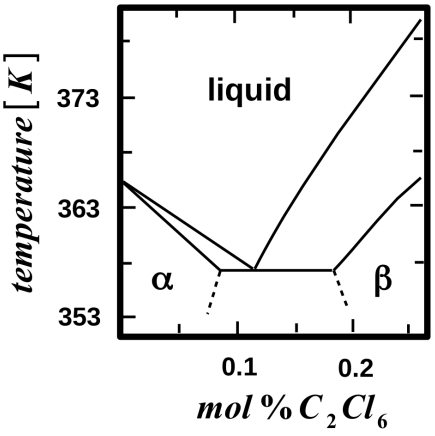

Figure E.1.: Phase diagram of $CBr_4 - C_2Cl_6$

F. Material Properties of Gallium

The elemental material gallium is described by the following material properties:

Quantity	Symbol	Value	Unit
melting temperature	T_m	302.93	K
latent heat per mass	L	80160	$\frac{J}{kg}$
surface tension	σ	0.056	$\frac{J}{m^2}$
liquid density	ρ_l	$6327.23\frac{kg}{m^3} - 0.73743\frac{kg}{m^3K}T + 1.37767 \cdot 10^{-4}\frac{kg}{m^3K^2}T^2$	$\frac{kg}{m^3}$
solid density	ρ_s	5094	$\frac{kg}{m^3}$
density	ρ	$(6\Phi^2-15\Phi^4+10\Phi^3)\rho_l+(1-6\Phi^2+15\Phi^4-10\Phi^3)\rho_s$	$\frac{kg}{m^3}$
heat conductivity	λ	$0.11\frac{W}{mK^2}T - 5\frac{W}{mK}$	$\frac{W}{mK}$
heat capacity	c	360	$\frac{J}{kgK}$
linear thermal expansion coefficient	β_T	$1.3 \cdot 10^{-4}$	$\frac{1}{K}$
liquid viscosity	η_l	$4.359 \cdot 10^{-4}\frac{kg}{ms} \cdot e^{\frac{481K}{T}}$	$\frac{kg}{ms}$
solid viscosity	η_s	90	$\frac{kg}{ms}$
viscosity	η	$(6\Phi^2-15\Phi^4+10\Phi^3)\eta_l+(1-6\Phi^2+15\Phi^4-10\Phi^3)\eta_s$	$\frac{kg}{ms}$

Table F.2.: Material properties of gallium

The viscosity of the solid phase has been regarded as a fitting parameter.

G. Material Properties of $NH_4Cl - H_2O$

The phase diagram of the binary eutectic alloy $NH_4Cl - H_2O$ is shown in Figure G.2. The material properties are listed in the following table (mostly from [99]):

Quantity	Symbol	Value	Unit
eutectic composition	ξ_e	0.803	1
eutectic temperature	T_e	257.75	K
partition coefficient $\alpha - l$	k_{12}	0.3	1
partition coefficient $\beta - l$ at $T = T_e$	k_{13e}	1.23	1
slope of liquidus line $\alpha - l$	m_{12}	-494	K
slope of liquidus line $\beta - l$	m_{13}	78	K
liquidus line $\alpha - l$	$\xi_1^{(12)}(T)$	$\xi_e - \frac{T_e - T}{m_{12}}$	1
liquidus line $\beta - l$	$\xi_1^{(13)}(T)$	$\xi_e - \frac{T_e - T}{m_{13}}$	1
solidus line $\alpha - l$	$\xi_2^{(12)}(T)$	$k_{12}\xi_1^{(12)}(T)$	1
solidus line $\beta - l$	$\xi_3^{(13)}(T)$	$\frac{1-k_{13e}\xi_e}{m_{13}(1-\xi_e)}(T - T_e) + k_{13e}\xi_e$	1
diffusion coefficient of the liquid phase	D_1	$5 \cdot 10^{-10}$	$\frac{m^2}{s}$
diffusion coefficient of the solid phase	$D_2 = D_3$	0	$\frac{m^2}{s}$
diffusion coefficient	D	$\Phi_1 D_1$	$\frac{m^2}{s}$
surface tension $\alpha - l$	σ_{12}	0.04	$\frac{J}{m^2}$
surface tension $\beta - l$	σ_{13}	0.04	$\frac{J}{m^2}$
surface tension $\alpha - \beta$	σ_{23}	0.04	$\frac{J}{m^2}$
molar volume	v_m	$3.9 \cdot 10^{-5}$	$\frac{m^3}{mol}$
latent heat per mass	L	$3.138 \cdot 10^5$	$\frac{J}{kg}$
liquid heaet conductivity	λ_1	0.468	$\frac{W}{mK}$
solid heat conductivity	$\lambda_2 = \lambda_3$	0.393	$\frac{W}{mK}$
heat conductivity	λ	$\Phi_1\lambda_1 + \Phi_2\lambda_2 + \Phi_3\lambda_3$	$\frac{W}{mK}$
density	ρ	1078	$\frac{kg}{m^3}$
liquid specific heat capacity	c_1	3269	$\frac{J}{kgK}$
solid specific heat capacity	$c_2 = c_3$	1870	$\frac{J}{kgK}$
specific heat capacity	c	$\Phi_1 c_1 + \Phi_2 c_2 + \Phi_3 c_3$	$\frac{J}{kgK}$
linear thermal expansion coefficient	β_T	$3.832e - 4$	$\frac{1}{K}$
linear compositional expansion coefficient	β_ξ	0.257	1
liquid viscosity	η_1	$1.3 \cdot 10^{-3}$	$\frac{kg}{ms}$
permeability constant	K_0	$2.338 \cdot 10^7$	$\frac{kg}{m^3 s}$

Table G.3.: Material properties of $NH_4Cl - H_2O$

The quantities k_{13}, m_{12} and m_{13} have been deduced from the phase diagram. The molar volume v_m has been chosen according to [100]. The damping of the velocity field in the mushy layer is achieved with a hybrid model in analogy to [101] and [102], which combines the Darcy law with a phase-dendent viscosity as the former is only valid for liquid volume fractions $\Phi_1 \leq 0.5$ ([101]). As no measured values of surface tension could be found in the literature, they were estimated as follows: The molar masses of NH_4Cl and water are given by

$$M_{mol}^{NH_4Cl} = 14\frac{g}{mol} + 4 \cdot 1\frac{g}{mol} + 35.5\frac{g}{mol} = 53.5\frac{g}{mol}$$
$$M_{mol}^{H_2O} = 2 \cdot 1\frac{g}{mol} + 16\frac{g}{mol} = 18\frac{g}{mol}.$$

For a solution with $70\% H_2O$, this leads to

$$< M_{mol} >= 0.7 \cdot 18 \frac{g}{mol} + 0.3 \cdot 53.5 \frac{g}{mol} = 28.65 \frac{g}{mol} = 4.7576 \cdot 10^{-26} kg \quad \text{per molecule.}$$

Therefore, one can assign the following value for latent heat to a single molecule:

$$L_{molecule} = L \cdot < M_{mol} >= 3.138 \cdot 10^5 \frac{J}{kg} \cdot 4.7576 \cdot 10^{-26} kg = 1.493 \cdot 10^{-20} J.$$

The average number density of molecules is

$$n = \frac{\rho}{< M_{mol} >} = \frac{1078 \frac{kg}{m^3}}{4.7576 \cdot 10^{-26} kg} = 2.266 \cdot 10^{28} \frac{1}{m^3}.$$

Surface tension can then be estimated using the empirical relation by Turnbull ([103]) in the form presented in [44]:

$$\begin{aligned} \sigma n^{-\frac{2}{3}} &= 0.32 \cdot L_{molecule} \\ \leftrightarrow \sigma &= n^{\frac{2}{3}} \cdot 0.32 \cdot L_{molecule} \approx 0.04 \frac{J}{m^2}. \end{aligned} \tag{7.21}$$

As microscopic details like contact angles are not an issue in the simulation with $NH_4Cl - H_2O$, we use the same value (7.21) for all three quantities σ_{ij}. The quantities ζ_{12} and ζ_{13} appearing in the thin-interface analysis result from a numerical evaluation of the integral (3.196) and are given by

$$\begin{aligned} \zeta_{12} &= 0.0818 \\ \zeta_{13} &= 0.0354. \end{aligned}$$

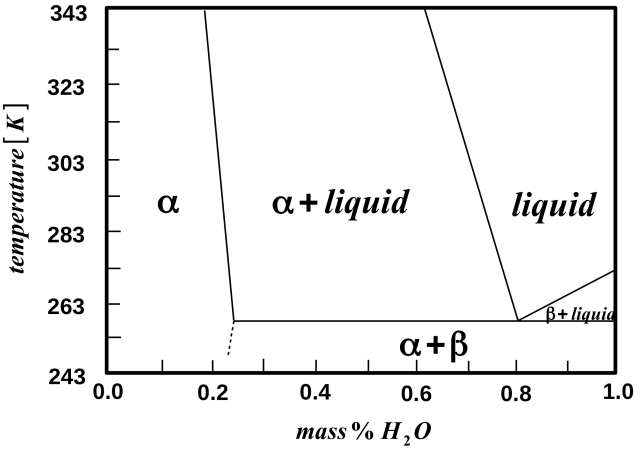

Figure G.2.: Phase diagram of $NH_4Cl - H_2O$